National Technical University of Athens
School of Naval Architecture and Marine Engineering
Division of Ship and Marine Hydrodynamics

Interdisciplinary Postgraduate Program
Marine and Ocean Technology and Science

Master Diploma Thesis

"WECs over general bathymetry A novel approach for performance evaluation and optimization"

Author
Markos I. Bonovas

Supervisor
Prof. Konstantinos A. Belibassakis

Athens 2019

National Technical University of Athens
School of Naval Architecture and Marine Engineering
Division of Ship and Marine Hydrodynamics

Interdisciplinary Postgraduate Program
Marine and Ocean Technology and Science

Master Diploma Thesis
"WECs over general bathymetry A novel approach for performance evaluation and optimization"

Author
Markos I. Bonovas

Supervisor
Prof. Konstantinos A. Belibassakis

Athens 2019

Front page Image:
Screenshot from https://bit.ly/2Cp7mr9

National Technical University of Athens
School of Naval Architecture and Marine Engineering
Division of Ship and Marine Hydrodynamics

"WECs over general bathymetry A novel approach for performance evaluation and optimization"

Interdisciplinary Postgraduate Program (Course): Marine and Ocean Technology and Science (I)

Master Candidate: Markos I. Bonovas
Email: markosbonovas@hotmail.com
Phone: +30 6979141006

Supervisor: **Prof. Konstantinos A. Belibassakis**
School of Naval Architecture & Marine Engineering
National Technical University of Athens
Heroon Polytechniou 9, 15780, Athens, Greece
Email: kbel@fluid.mech.ntua.gr
Phone: 210 772 1061

Examination Committee

- **Prof. Konstantinos A. Belibassakis**
  School of Naval Architecture & Marine Engineering
  National Technical University of Athens
  Heroon Polytechniou 9, 15780, Athens, Greece
  Email: kbel@fluid.mech.ntua.gr

- **Prof. George G. Zaraphonitis**
  School of Naval Architecture and Marine Engineering,
  National Technical University of Athens
  Heroon Polytechniou 9, 15780, Athens, Greece
  Email: zar@deslab.ntua.gr

- **Prof. Spyridon Mavrakos**
  President and Director of HCMR
  School of Naval Architecture and Marine Engineering,
  National Technical University of Athens
  Heroon Polytechniou 9, 15780, Athens, Greece
  Email: mavrakos@naval.ntua.gr

Athens, 18 / 02 / 2019

Athens, January 2019

"Obsessed by a fairytale, we spend our lives searching …"

Eugene O'Neil

Acknowledgements

The author would like to gratefully acknowledge Prof. Dr. K.A. Belibassakis who gave the opportunity for a very interesting thesis project. Through his continuous support and valuable supervision the research was always enjoyable and at the end commensurate of the expectations.

Withal the professor, family and friends, through their ceaseless support, have been vital for accomplishing this challenge.

Introduction

Completed my studies as a Mechanical Engineer at the National Technical University of Athens, the present thesis come as the capstone of my efforts for acquiring the Master Diploma in Marine and Ocean Technology and Science, coordinated by the School of Naval Architecture and Marine Engineering of the same university.

New horizons, relevant to the marine technology, have opened during my studies for the last eighteenth months. New inspirational professors have contributed in many ways on my scientific growth. New colleagues were part of my everyday life, being friends and advisors and together we widen the breadth of our knowledge and experience. In a life learning professional environment, this might be the end of an era inside the educational sector and the beginning of my career, or may declare a decision for another more demanding period of education.

Fate might be sealed, but destiny come as a matter of choice. Whatever the next steps of mine will be, all these personalities and all this experience will certainly be present in the endeavor to fulfill my dreams.

The author,
Markos I. Bonovas

Abstract

Power emerging from the oceans is a form of renewable energy increasingly attracting the interest of the scientific and industrial society. A brief review of wave energy technologies and an attempt for their categorization is initially presented in this thesis. The performance of Wave Energy Converters (WECs) in nearshore and coastal areas, where the bottom topography may present significant variation, is examined in this work by means of a Boundary Element Method, capable of treating hydrodynamic interaction between multiple floating bodies and general bathymetry. The methodology is based on a novel Boundary Element Method, combined with the Coupled Mode System and Perfectly Matched Layer model, for the treatment of the propagation/diffraction/radiation problems and, following its validation in 2D and 3D problems, the research focuses in the evaluation of flow details at the local scale of the energy absorbers. An important feature of the methodology is that it is free of mild-slope assumptions and restrictions. Numerical results are presented and discussed concerning the details of the wave field and the power output of a single floater with vertical cylindrical body over a region of general topography. The optimization of the device performance is examined by considering generally-shaped axisymmetric bodies and power take-off values for heaving motion. Interactions among cylindrical heaving WECs in an array layout are also examined. Finally, shape and PTO optimization are carried through for heave power mode and one additional degree of freedom, this of pitch mode of oscillation.

Keywords: Wave energy; Point absorber; Frequency-domain; Boundary Element Method; Coupled Mode System; Perfectly Matched Layer; Variable depth effects; Wave Energy Converter; WEC Arrays; Multi-DOF WEC; Design optimization;

Περίληψη

Η ωκεάνια ενέργεια είναι μια μορφή ανανεώσιμης ενέργειας η οποία όλο και περισσότερο προσελκύει το ενδιαφέρον της επιστημονικής κοινότητας και της βιομηχανίας. Αρχικά γίνεται μια παρουσίαση των διαθέσιμων τεχνολογιών κυματικής ενέργειας καθώς και μια προσπάθεια κατηγοριοποίησής τους. Η απόδοση των συσκευών εκμετάλλευσης της κυματικής ενέργειας σε παράκτιες περιοχές, όπου η τοπογραφία του πυθμένα μπορεί να παρουσιάζει έντονη διακύμανση, εξετάζεται στην παρούσα μελέτη με όρους της Μεθόδου Συνοριακών Στοιχείων, μεθόδου ικανής να αντιμετωπίσει περιπτώσεις υδροδυναμικής αλληλεπίδρασης πολλαπλών επιπλεόντων σωμάτων και γενικού βαθυμετρικού προφίλ. Η καινοτόμος αριθμητική μεθοδολογία βασίζεται στο συνδυασμό BEM-CMS-PML για την αντιμετώπιση των γενικών προβλημάτων διάδοσης/περίθλασης/ακτινοβολίας και, αφού επικυρωθεί σε 2D και 3D προβλήματα, θα χρησιμοποιηθεί στον υπολογισμό των χαρακτηριστικών της ροής στην τοπική κλίμακα των ενεργειακών απορροφητών. Σημαντικό χαρακτηριστικό της μεθοδολογίας είναι η έλλειψη οποιωνδήποτε παραδοχών και περιορισμών για τις μέσες κλίσεις. Τα αριθμητικά αποτελέσματα παρουσιάζονται και σχολιάζονται σύμφωνα με τις λεπτομέρειες του κυματικού πεδίου και της παραγόμενης ισχύος για μια συσκευή με μορφή κατακόρυφου κυλίνδρου, η οποία λειτουργεί πάνω από περιοχή γενικής βαθυμετρίας. Η βελτιστοποίηση της απόδοσης γίνεται με την υπόθεση σωμάτων γενικού αξονοσυμμετρικού σχήματος και διαφόρων τιμών των παραμέτρων του συστήματος απορρόφησης ενέργειας κατά την κατακόρυφη ταλάντωση της συσκευής. Η αλληλεπίδραση μεταξύ όμοιων κυλινδρικών συσκευών σε διάταξη συστοιχίας εξετάζεται επίσης. Τέλος, η βελτιστοποίηση του σχήματος και των παραμέτρων του συστήματος απορρόφησης της ισχύος μελετάται και για συσκευή με περισσότερων του ενός βαθμών ελευθερίας, συγκεκριμένα λαμβάνοντας υπόψη την κατακόρυφη ταλάντωση και την περιστροφή περί τον εγκάρσιο άξονα, κίνηση γνωστή και ως προνευτασμός.

Table of Contents

List of Figures

List of Tables

Abbreviations

ALC	Articulated Loading Column
BC	Boundary Condition
BEM	Boundary Element Method
BIE	Boundary Integral Equation
BNM	Boundary Node Method
BVP	Boundary Value Problem
CAE	Computer Aided Engineering
CALM	Catenary Anchor Leg Mooring
CFD	Computational Fluid Dynamics
CMS	Coupled-Mode System
CWR	Capture Width Ratio
DOF	Degree Of Freedom
EFM	Edge-Function Method
FDM	Finite Difference Method
FEA	Finite Element Analysis
FEM	Finite Element Method
FK	Froude-Krylov
FS	Free Surface
GRP	Glass Reinforced Plastic
LCOE	Levelized Cost Of Energy
LDP	Lower Dead Point
MIMO	Multiple Input Multiple Output
MOO	Multi Objective Optimization
ODE	Ordinary Differential Equation
OWC	Oscillating Water Column
PDE	Partial Differential Equation
PML	Perfectly Matched Layer
PTO	Power Take off
RAO	Response Amplitude Operator
RK 4th	Runge-Kutta 4th Order
R&D	Research & Development
SALM	Single Anchor Leg Mooring
SOO	Single Objective Optimization
SPAR	Single Point Mooring & Reservoir
St-L	Sturm-Liouville
SWH	Significant Wave Height
SWL	Standard Water Level
TRL	Technology Readiness Level
UDP	Upper Dead Point
WEC	Wave Energy Converter
2D	Two-Dimensional
3D	Three-Dimensional

1

Ocean energy: A brief review

1.1 Facts and policies for climate change

1.1.1 The crucial indexes

The prosperity of our societies is measured by the energy consumption (**Figs 1**, **2**). More specifically, a country which is growing and attempting to establish a well-living for its citizens, is at the same time a powerful energy consumer and therefore a severe reason for environmental pollution, due to the reliance of the energy sector on conventional fuels. The energy consumption and the environmental impacts are a field of harsh diplomatic negotiations, especially among the growth and the growing countries, with apparent competitive affairs.

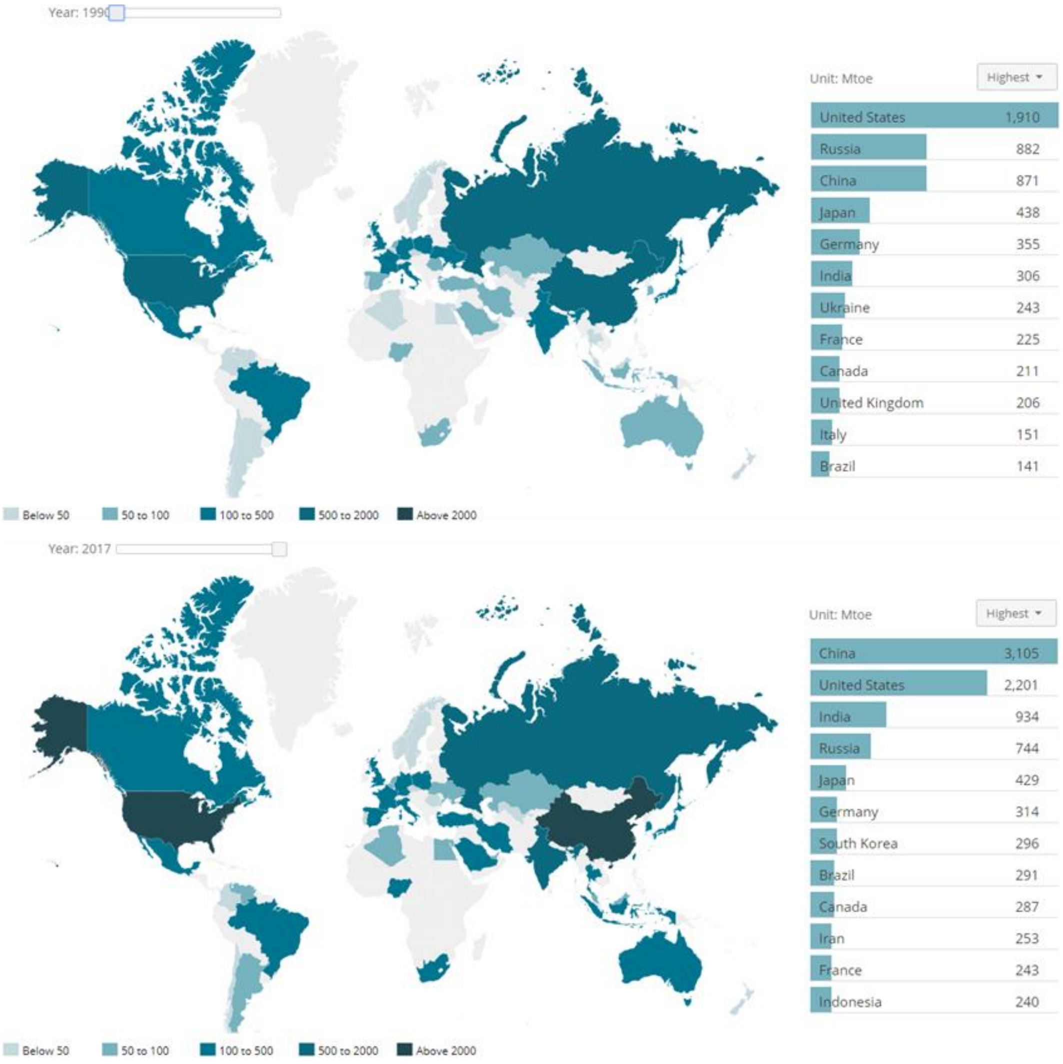

Figure 1: Total energy consumption (1990-2017) [1]

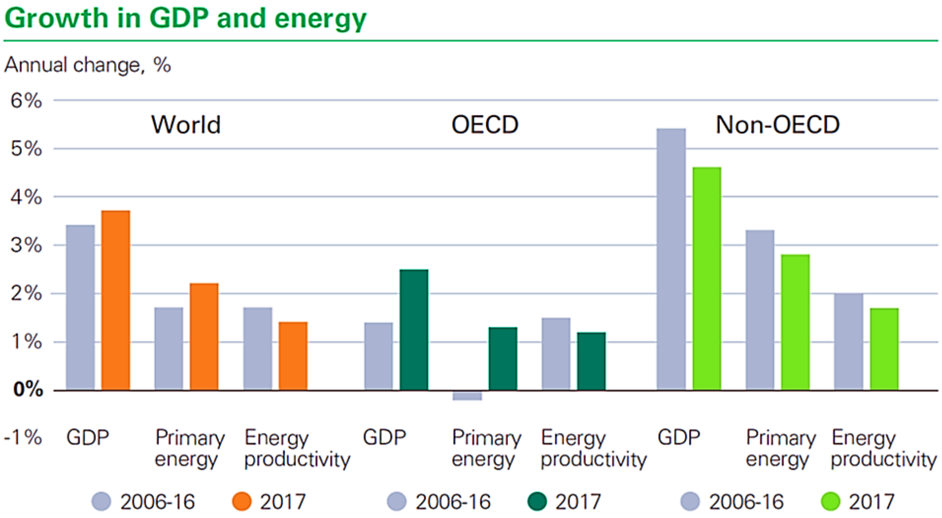

Figure 2: Energy consumption and GDP annual growth change (2006-2017) [2]

However, this global activity has many fallouts on our planet. The September of 2016, according to many researches, was the turning point in human history and its relation with the environment. The CO_2 concentration in the atmosphere, and as a result the temperature levels on planet Earth, climbed to their highest levels, as shown in **Fig. 3** and this demands the immediate fundamental transformation of the global energy mix in just few years [3]. One of the significant outcomes is that the annual ice covering of Arctic is dramatically reducing (**Fig. 4**) and subsequently the sea level increases, as pointed out by the measurements of **Table 1** and the relevant **Figs 5**, **6** and **7**, facts manifesting the climate crisis.

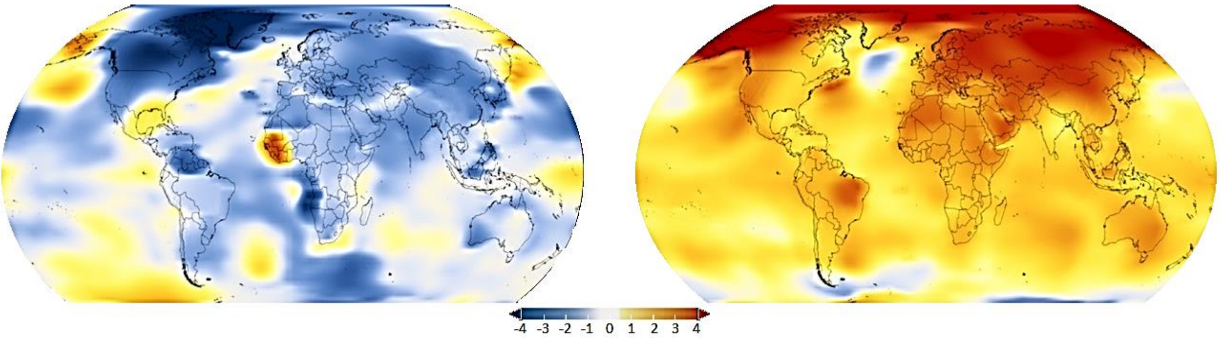

Figure 3: Global temperature difference (1884-2017) [4]

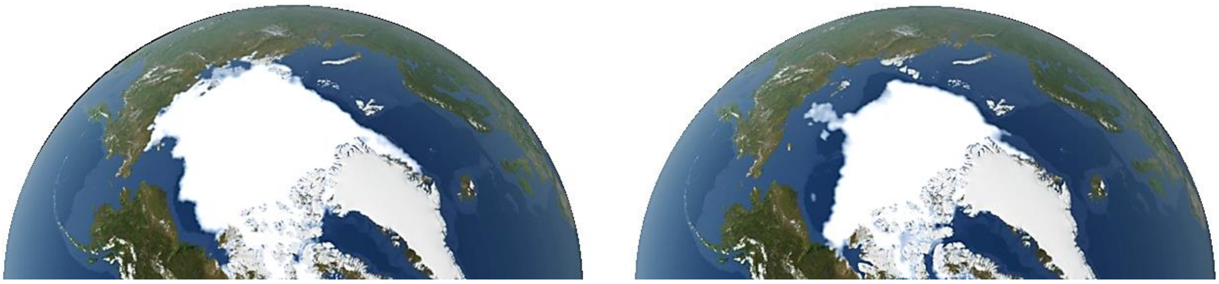

Figure 4: Arctic sea ice covering (1979-2018) [4]

Now, more than ever before, this issue demands a solution, under the prescience alleging that humanity has almost twelve years to prevent a non-reversible climate change. The data by the

National Air & Space Administration are ringing the bell and the following facts and stats are a proof [4]. The main evidences of this rapid climate change are namely: the global temperature rise, the warming oceans, the shrinking ice sheets, the retreating glacial, the decreased snow cover, the rising sea level, the declining Arctic sea ice, the frequent extreme events and the ocean acidification. Another reason justifying this concern is that during United Nations Climate Change Conference in Paris on 2015 was predicted a total mean temperature increase of 1.5^{o}C by 2050, while in most recent studies humanity surpasses itself and this prediction is now almost 2^{o}C, if the man continues to reject CO_2 with the same tempo.

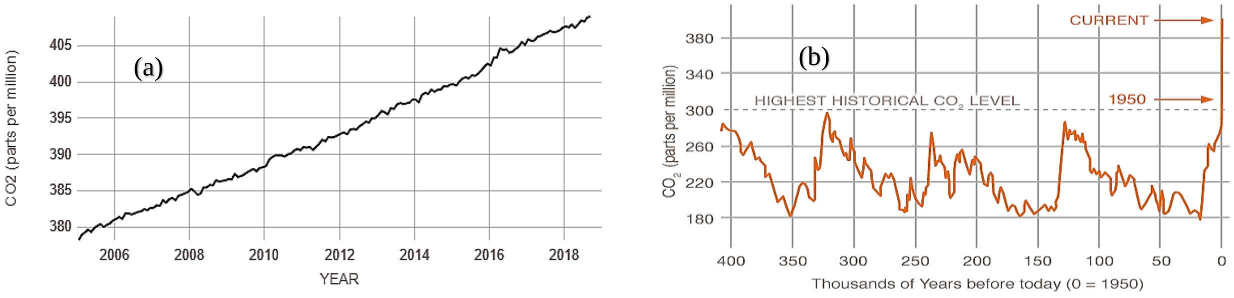

Figure 5: CO2 emissions: (a) 2005-2020, (b) Last 400 millennium̄s [4]

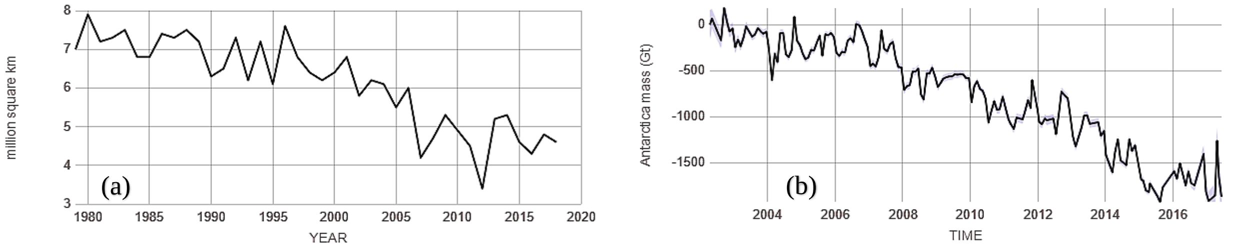

Figure 6: Arctic ice: (a) Covering in square km, (b) Mass in Gt [4]

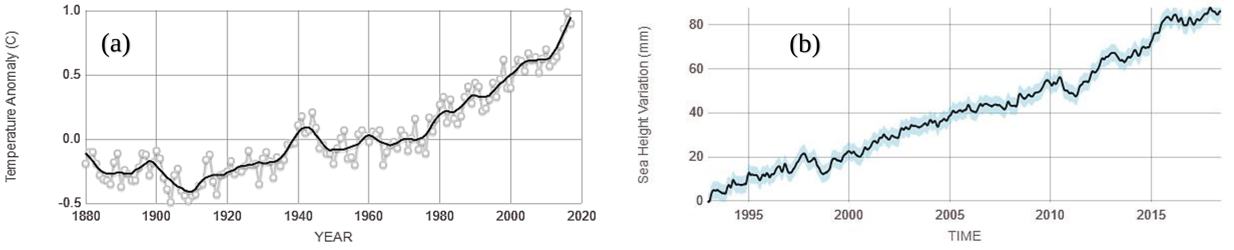

Figure 7: (a) Temperature anomaly, (b) Sea level variation [4]

Table 1
The climate change in numbers [4]

Variable	Trends	Facts
$[CO_2]_{atm}$	↗7.6% (17th Sep 2017-17th Sep 2018)	The highest levels of air CO_2 for the past 650.000 years.
Global Temperature	↗1.8°C (Since 1880)	Eighteen of the warmest years occurred from 2001
Arctic Ice	↘12.8% per decade	In 2012 the Arctic sea ice shrank to its lowest recorded levels
Ice Sheets	↘413 Gtn per year	Rapidly losing mass
Sea Level	↗3.2 mm per year	Global average sea level has risen to almost 178 mm in the past century

On the other hand, there are many scientists supporters of the opinion that this whole variation of the climate is a natural circle and at some time the dynamic ecosystem of Earth will overcome and will balance again. If anyone study evidences, similar to those described in the above **Figs 5**, **6** and **7**, he will probably come up with a different conclusion, because above any questioning, critical indexes of equilibrium are showing ominous ratios for the last decades.

1.1.2 Redirecting to eco-policies

Pursuant to those foreboding facts the countries are changing their policies and redirecting their efforts towards eco-friendly energy production activities and carbon neutrality. The pressure for more regulations regarding the emissions are intense, referring to a total decrease of the Greenhouse Effect Gases up to 40-70% until 2050. The European Schedule of "20-20-20" is one among others that stands out and sets strategy and targets of environmental policy adaptation for every member until 2020 (**Fig. 8**), while more strict regulations are scheduled for 2030. Every member of the EU institutes laws and regulations in order to assign partial targets in specific fields and meet the strategic goals. Moreover, emission pricing tariffs are also proposed and applied all over the world. A characteristic example of this effort and its results is the China, which contributed in the decline of coal sharing in primary energy consumption of about 60.4% during 2017. However, the industrial growth led to surging energy demands and thus to an increase of 3% in coal consumption during 2017-2018, proving that this transition should be restlessness.

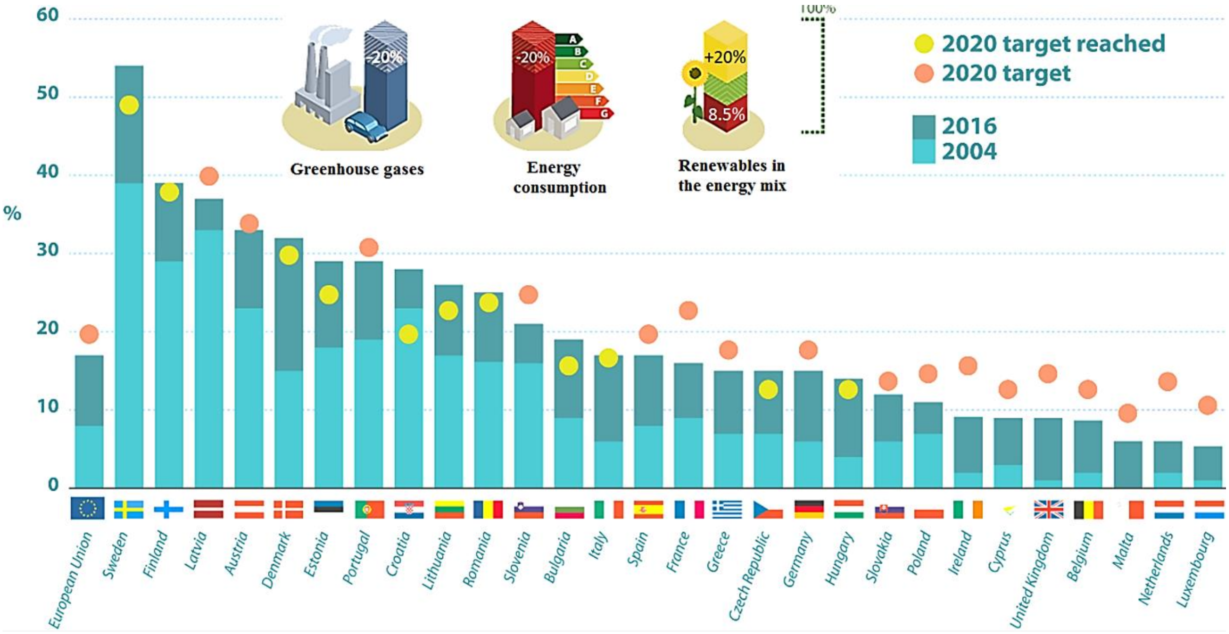

Figure 8: The EU 2020 Schedule and the member statistics for renewable energy sources in percentage of gross energy consumption [5,6]

Therefore, the green technology emerges more ambitiously than ever before and progressively dominates more quota of the energy production market. This forms of energy sources can be categorized based on their origins as:

- Wind energy
- Solar energy
- Hydropower
- Biomass
- Hydrogen and fuels cells
- Geothermal energy
- Ocean (Blue) energy

The most significant advantages of the renewables are:

- Eco-friendly
- Inexhaustible sources
- A way for power self-sufficiency
- Low operating costs
- State funded programs
- Employment opportunities
- High geographical distribution
- High density near urban areas
- Significant prospects for technological evolution

As every proposed solution, even this one has its disadvantages. The majority of them are related with the physical form of this type of energy, but also with the human way of living and the ordinary public perception and beliefs, i.e. Not In My Back Yard (NIMBY), impeding their commercial establishment.

The main drawbacks of exploiting renewable forms of energy are:

- The geographical distribution is not advantageous in cases of high power concentration demands in a specific area.
- Low power density
- Intense geographical and seasonal power fluctuations
- High investment cost due to its immaturity as technology and demand for R&D funds
- Low capacity factors because of their reduced temporal availability
- Impact on the environment and the ecosystems of flora and fauna
- Property issues for the potential grounds among stakeholders and owners
- Unpropitious operational conditions
- High cost of power transfer
- Deterioration of the optical surroundings
- Noise pollution

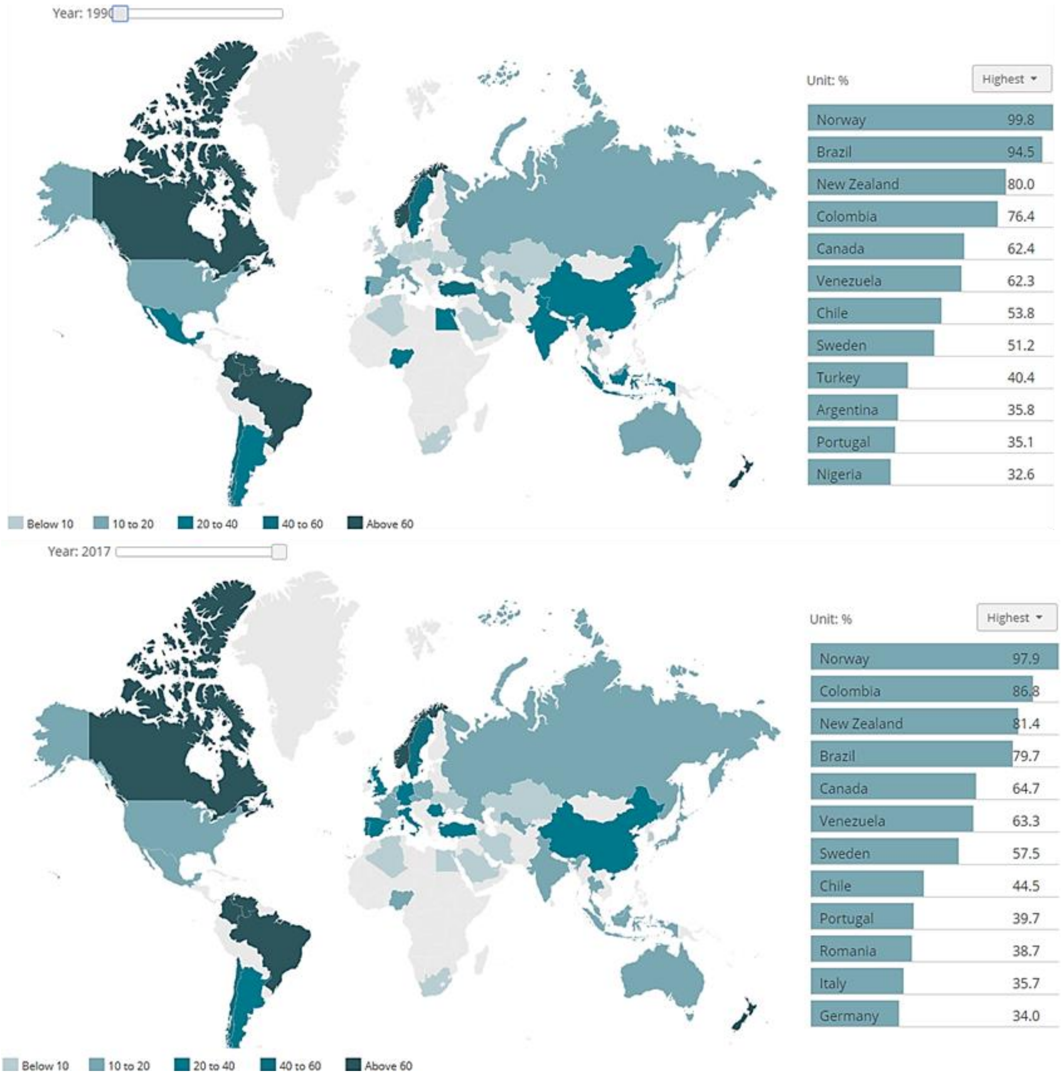

Figure 9: Renewable energy electricity production (1990-2017) [1]

The investments in renewable energy sector is the only way to become independent from the conventional fuels. In addition, it is also the way for the countries to become self-sufficient in the energy sector by the geographical distribution of its sources and the ensuing decentralization of the power system. Retrieving stats again for China's case, this colossus in carbon consumption is struggling to become more "green" and this effort is reflected from the increased share of renewables in total power generation from 16.2% in 2011 to 26.5% in 2017 [7] and the record breaking investments percentage of 45% of the global investments in renewables sector for 2017, up from 35% during 2016 and followed by Europe (15%) [8]. In conclusion the past year of 2017 was a mark in renewables power capacity scale up, reaching the highest numbers of all times. In 2017, the estimations of new investments in renewable energy technologies were 279.8 bn$, increased by 2.1% from 2016. The power capacity from renewable sources was 2017 GW in 2016 and 2195 GW in 2017, including the hydro plants. At the same time, the renewable sector holds almost 20.5% of total energy consumption globally, while the sharing of this amount is shaped as the 27% for heat production out of 48% in total energy spending in this specific field, 25% in power production out of 20% and 3% on transports out of 32% [8]. The efforts are focusing primarily in the power sector, and secondly in heat-cooling and transportation, while besides this fact, the electric passenger vehicles sales increased up to 58% in comparison with 2016 and the appreciation of modern renewables participation in heating and cooling is growing rapidly beyond 10.3% for 2017.

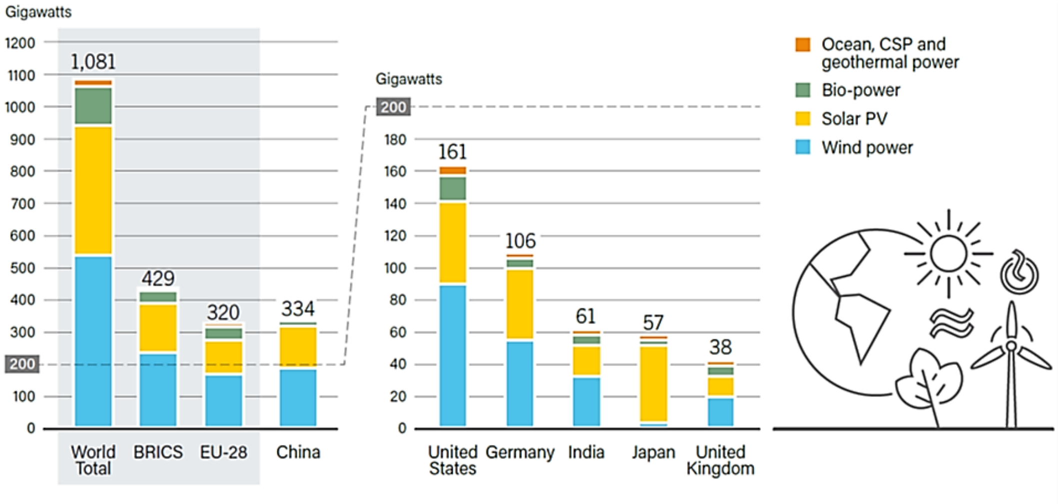

Note: BRICS = Brazil, the Russian Federation, India, China and South Africa. *Not including hydropower.

Figure 10: Renewable power capacities and top six countries (2017) [8]

At the present, the transition towards renewables is shown to be possible, but the results in its sectors individually are unequal. Nevertheless, efforts and innovative technologies attempt to exploit the most prosperous forms of renewables, striving for a more promising future. Many companies at first, counted to almost five hundreds so far, cities secondly, and even whole nations attempt and being committed to go 100% on renewables, as members of RE100 initiative, always in terms of energy production footprint and not of energy sources, for example Facebook, Microsoft, BMW Group and Coca Cola until 2020. Over 1.8 billion people have decided to go totally "green" in the following decades, at least in one sector and in this direction a great paradigm is Copenhagen setting the goal to be the first carbon neutral capital by 2025. As of now, fifty seven countries are targeting on a 100% renewable electricity production [8]. A change also in the way of thinking is essential if humanity wants to meet her goals and, along this path of transforming to more eco-friendly society, skepticism and concerns about the accompanying impacts of green technologies should be critiqued.

1.2 An ocean of potential

1.2.1 *Power emerging from the seas*

The ocean energy, also called as "blue" energy, is another form of renewable energy, with its dawning dating back to two centuries, however still commercially "young" in the energy market. More than a thousand patents were registered up to 1980 and this number has of course been multiplied nowadays. Even today, with the technological evolution and R&D activity in this area of interest to their highest levels there is still no validation for the most efficient way of harnessing the energy from the seas and many of the proposals are still in labs and experimental tanks, while the currently operating devices have specifications at best of TRL 6-7 out of 9 (Technology Readiness Level) (**Fig. 11**). This is the main difference among this renewable source and others like solar and wind, fields where the way, the deployment risk and the machines of producing power has come to a final crystallization.

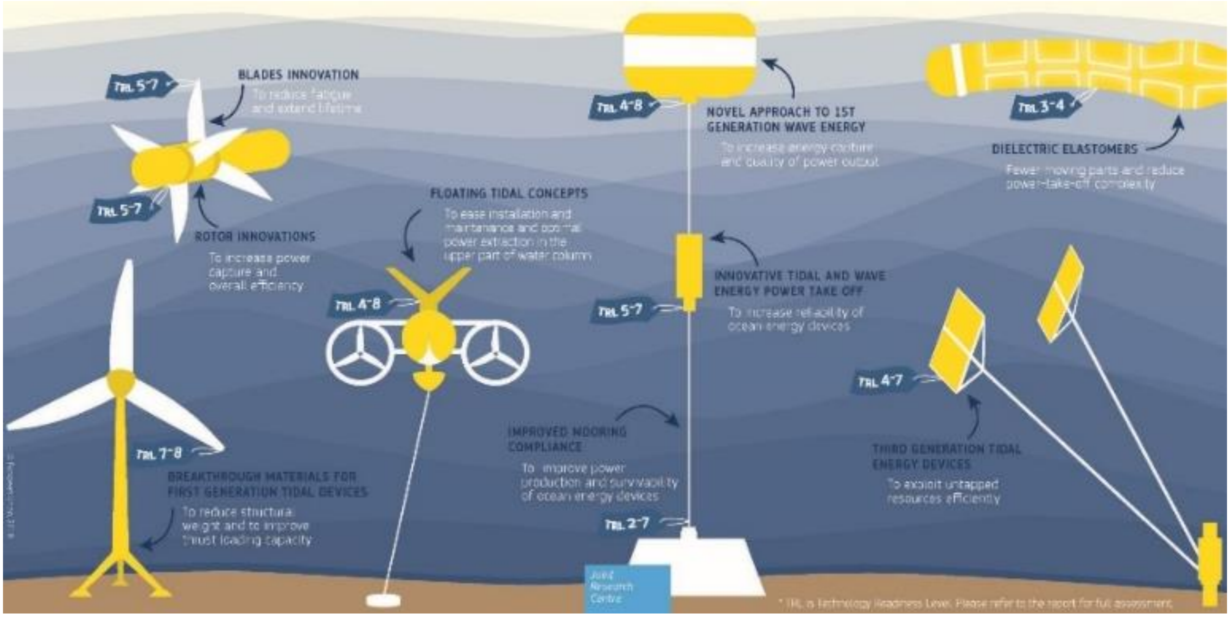

Figure 11: Current ocean energy technologies [9]

The ocean can provide a proportion of their energy, primarily absorbed by the sun, with one of the following forms:

- Tidal energy
- Wave energy
- Marine current energy
- Osmotic energy
- Ocean thermal energy

Estimations about the potential of these forms as a possible answer for eco-friendly power production are more than encouraging, as the values in **Table 2** reveal:

Table 2
Ocean energy potential [10]

Form	Annual global potential
Tidal energy	>300 TWh
Marine current power	>800 TWh
Osmotic power (salinity gradient)	2,000 TWh
Ocean thermal energy (thermal gradient)	10000 TWh
Wave energy	8000–80000 TWh

The wide range in assessing the wave energy has to do with the point of view of each researcher and the strongly dynamic physics of the waves. The results are proving the high prospects of exploiting such a powerful source. Focusing on wave energy, the great density of this form, measured up to 3 KW/m^2 [11], comparing it with the 0.3 KW/m^2 of solar energy, in combination with the coastal distribution of the population, with the 37% of people living in only 60 miles of coastline, drive the estimations for the energy capacities from the waves to very big scales. The total electric grid power is at the moment almost 3.5 TW and theoretical assessment only on wave energy suggests that more than 2 TW can be extracted from the waves. The exploitation of 15% of wave energy in USA can provide the same amount of energy as the total conventional hydro plants all over the world. The total theoretical wave energy potential is estimated up to 32 PWh/yr [12]. However, this potential is mainly distributed in Atlantic Ocean and in North Sea while in the Mediterranean Sea, which is mainly dominated by short crested waves and small fetch lengths, is by far less exploitable [13]. Their time availability is another advantageous feature, exceeding up to 90% of time, compared to the 20-30% of wind and solar energy devices [14]. More than a hundred companies operate in this field and set the goals for the near future. Here are presented some really interesting facts in this sector of power production [15]:

- World’s largest tidal energy plant is launched in Scotland
- Tidal energy is turning commercial
- China plans a foundation of marine energy center
- USA invests 40 m$ in wave center
- World largest tidal turbine is under test in Orkney. The Orbital O2 2MW have recently completed a very successful test year at the European Marine Energy Centre (EMEC) generating over 3 GWh (**Fig. 12**).
- The relevant market is estimated to cost up to 460 bn$ in the period 2010-2050
- If the ocean energy deployment reaches 748 GW by 2050 this could create 160.000 employment opportunities by 2030.

Figure 12: The Orbital O2 (2 MW) tidal turbine by Orbital Marine Power (ex Scotrenewables) [16]

The areas with potential interest around the world are geographically gathered in latitudes of 30^o-60^o, because the wind generates waves and in this area the wind presents the following features:

- High wind velocities
- Long fetch lengths
- Long lasting blows

Waves of high amplitudes can occurred also in cases on canals due to more complicated potential phenomena.

Source: GlobalData

Figure 13: Global wave potential

Figure 14: Global marine power installations (2018)

On the opposite of this "ocean of potential" is the still expensive energy technological units for ocean power exploitation. Many predictions refer to two different scenarios for the upcoming years regarding the commercialization of the wave energy: one optimistic and one pessimistic [17]. Estimations of the Levelized Cost Of Energy (LCOE) for wave energy are approximately 500 \$/MWh and 440 \$/MWh for tidal [15]. Furthermore, economical separation of the scenarios, can be applied and, in more details, the scenarios are divided in low (279 \$/MWh), medium (486 \$/MWh) and high (1038 \$/MWh) cost [18]. This may be one of the reasons why tidal projects and the relevant installed capacity are dominant over wave energy projects. The cost of ocean energy is still extremely high compared with other renewables such as offshore wind (174 $/MWh), onshore wind (83 $/MWh), crystalline silicon solar PV (122 $/MWh), large hydro (70 $/MWh) and geothermal applications (271 $/MWh). Despite its current economic defect, longtime studies identified that it could lead to savings up to 1.38 bn$/year by replacing other intermittent renewable power generation sources like solar and wind [15]. The new wave power systems, with the implementation of the knowledge acquired from R&D studies, scheduled for 2022–2040, are promising reduce of the costs for power take-off (PTO) by 22%, for installation 18%, for operation and maintenance 17%, for foundation and mooring 6% and for grid connection 5% [18]. The cost predictions with the commercial experience of the near future, in case of economies of scale and farms are 131-261 $/MWh for 2030 for installed power levels above 2 GW [19].

1.2.2 The wave energy technologies

Going back and recalling the Girard's and his son's patent in Royan, France (1799), the Bochaux-Praceique oscillating water column (OWC) device of 1 KW (1910), Yoshio Masuda research projects in Japan for devices with different principals of function (1940), C.C Mei's projects in M.I.T. (1973), Stephen Salter's Duck with the really impressing efficiency of 81% (1974) and many other concepts, patents and theories of the past century, developed mainly during the oil crisis of 80's in the Gulf of Mexico, when waves physics were deeply studied and described, these are the true reasons behind today's experience and knowledge, deployed day by day in harvesting the oceans more efficiently.

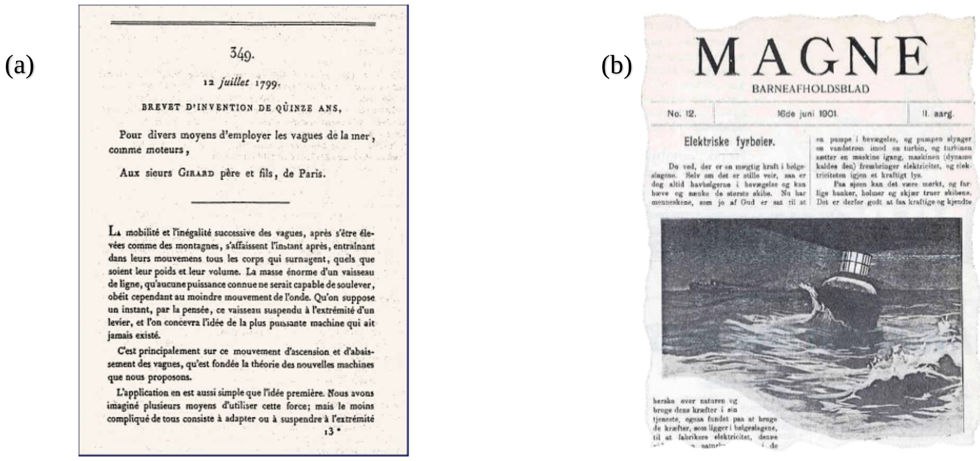

349.

12 *juillet* 1799.

BREVET D'INVENTION DE QÙINZE ANS,

Pour divers moyens d'employer les vagues de la mer, comme moteurs,

Aux sieurs GIRARD père et fils, de Paris.

La mobilité et l'inégalité successive des vagues, après s'être élevées comme des montagnes, s'affaissent l'instant après, entraînant dans leurs mouvemens tous les corps qui surnagent, quels que soient leur poids et leur volume. La masse énorme d'un vaisseau de ligne, qu'aucune puissance connue ne serait capable de soulever, obéit cependant au moindre mouvement de l'onde. Qu'on suppose un instant, par la pensée, ce vaisseau suspendu à l'extrémité d'un levier, et l'on concevra l'idée de la plus puissante machine qui ait jamais existé.

C'est principalement sur ce mouvement d'ascension et d'abaissement des vagues, qu'est fondée la théorie des nouvelles machines que nous proposons.

L'application en est aussi simple que l'idée première. Nous avons imaginé plusieurs moyens d'utiliser cette force; mais le moins compliqué de tous consiste à adapter ou à suspendre à l'extrémité

13 *

MAGNE

BARNEAFHOLDSBLAD

No. 12. 16de juni 1901. II. aarg.

Elektriske fyrbøier.

Du ved, der er en mægtig kraft i bølgeslagene. Selv om det er stille veir, saa er dog altid havbølgerne i bevægelse og kan hæve og sænke de største skibe. Nu har menneskene, som jo af Gud er sat til at herske over naturen og bruge dens kræfter i sin tjeneste, ogsaa fundet paa at bruge de kræfter, som ligger i bølgeslagene, til at fabrikere elektricitet, denne

en pumpe i bevægelse, og pumpen slynger en vandstrøm imod en turbin, og turbinen sætter en maskine igang, maskinen (dynamo kaldes den) frembringer elektricitet, og elektriciteten igjen et kraftigt lys.

Paa sjøen kan det være mørkt, og farlige banker, holmer og skjær truer skibene. Det er derfor godt at faa kraftige og kjendte

Figure 15: (a) Girard's patent (1799), (b) Cover page of Norwegian magazine proposal for autonomous electrical signaling buoys [20].

There are six key features for every wave energy device rendering its design and operation principals and making possible the energy absorption by the oceans. These are:

- Structure and prime mover
- Foundation and mooring
- Power Take Off
- Control
- Installation
- Connection to the grid

As stated previously, there is still no definition for the most efficient way of power production by the oceans and therefore there is still no optimized device, even regarding its main aspects and design, while state of the art concepts show up, being funded and tested constantly. Nevertheless, some categorization is feasible, according to their characteristics.

1.2.2.1 1st Categorization criterion: Type

There are three predominant types of wave energy converters and every single concept design can be classified as [14]:

- *Attenuator*: Devices with their principal axis parallel to the dominant wave direction, giving the impression of "riding" them.
- *Point absorber*: Devices with small dimensions in comparison to the incident wavelength. Due to their small dimension and their very common axisymmetric design the direction of the wave has no impact. Numerous examples of different approaches and technologies are making this class the most widely used and studied. A different type of converters is discussed in [21], the quasi-point absorber, which is a point absorber with bigger dimensions, compared to the wavelength, than typical point-absorbers.
- *Terminator*: Their main feature is that their principal axis is parallel to the wavefront and therefore perpendicular to the wave direction, intercepting the waves.

Despite the lack of a determined efficient technology, there are some leaders in this market. Some of the most known commercialized products with their categorization and power capacity are included in **Table 3**.

Table 3
Wave energy types and relevant commercial products [18]

Category	**Device**	**Capacity (kW)**
Point Absorber	Pontoon Power Converter (PPC)	3619
	Ocean Energy Buoy (OE)	2880
	Wavebob	1000
	CETO	260
	Seabased AB	15
Attenuator	Sea Power	3587
	Wave Star	2709
	Oceantec	500
Terminator	Wave Dragon	5900

1.2.2.2 2nd Categorization criterion: Operation

A further attempt for categorization of the above main types of Wave Energy Converters (WECs) lead to this second level of classification according to the mode of operation [14,22]. The most significant classes are:

- **Oscillating water column (OWC)**: It can be further categorized in:

  - *Fixed-structure OWC*: Based on different principals of extracting energy from the waves many prototypes have been proposed, but only few full-scale models were deployed. They are named as first generation devices and they are located in coastal or nearshore spots, making their installation, even in seaport structures and breakwaters, their maintenance and the power transfer effortless. However, the available potential for capture is limited. The principal of their function is trapping the air inside a concrete structure above sea level. The incoming wave will raise the water level inside this man-made cave and cause the air to flow through a turbine, commonly a Wells turbine, which is ideal for exploiting low velocities without rectifying valves and without being exposed in seawater and corrosion.

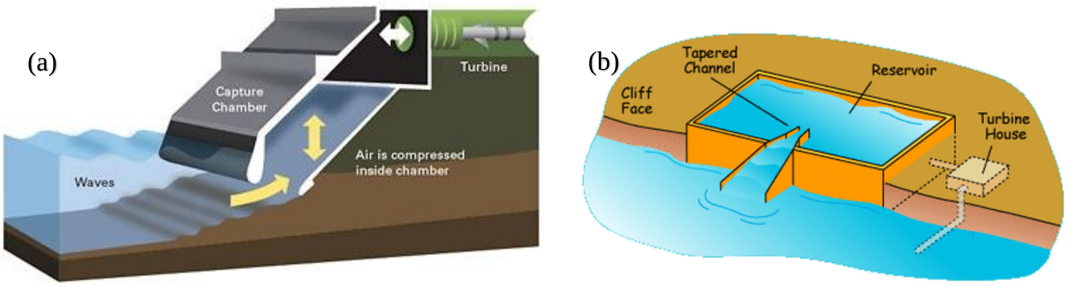

Figure 16: Fixed structure OWC: (a) The Limpet project [23], (b) The Tapchan project [24]

  - *Floating-structure OWC*: The first types of this technology were deployed during 1960s and 1970s by Yoshio Masuda. The mode of operation is similar to that of the Fixed-structure OWC: again air is trapped inside a chamber on a floating platform and through its interaction with the oscillating water is guided to a Wells turbine, coupled with a generator, and then escapes to the atmosphere. As the water retreats air is suctioned back and refills the chamber. The platforms are slack-moored and free to oscillate maximizing the flow of the air towards the turbine. In most of the cases, one platform has installed many OWC devices, probably with different resonance frequencies to optimize the operation.

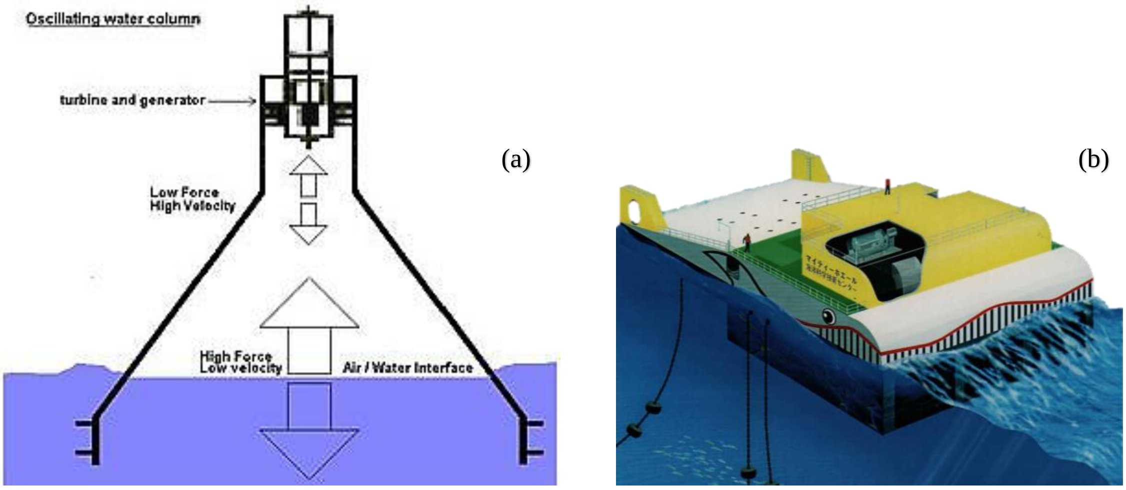

Figure 17: Floating structure OWC: (a) Operation principal, (b) The Mighty Whale device [25]

- **Oscillating body systems**: Can be either floating or fully submerged, located in offshore spots. They are exposed to the highest wave energy potential and this is the reason behind their evolution. On the other hand issues arising from the extreme sea states occurring at these locations, related to mooring, maintenance, power transfer and survival are reasoning why only few technologies have reached full-scale and commercialization. They can be categorized as:

    - *Single body heaving buoys*: The most common and simplest oscillating wave devices, also conceived generally as point absorbers. They are capturing energy from the most dense power mode, the heave motion. The oscillating part of the buoy reacts against a fixed or large-inertia component and this relative motion is converted to power from the PTO. The number of proposed technologies is really impressing, introducing different ways of power production from piston-pump-turbine systems to autonomous wave-to-wire circuits.

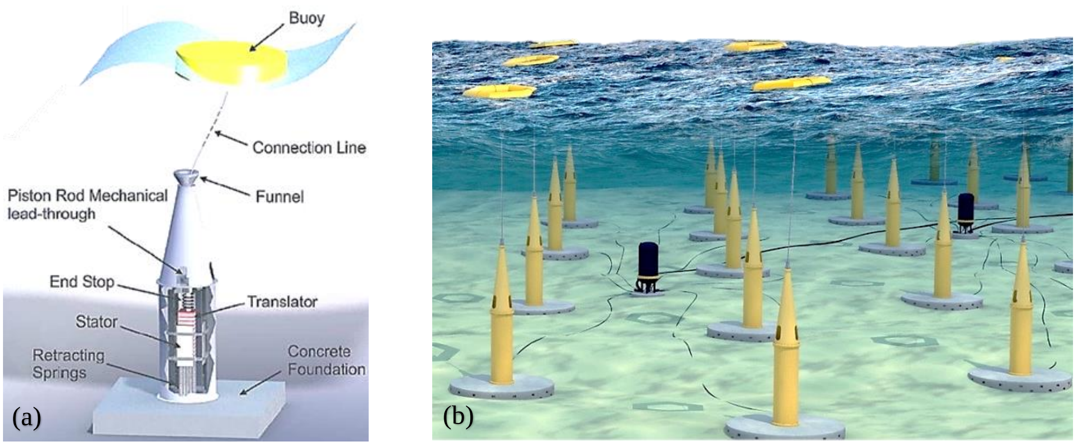

Figure 18: Single body heaving buoys with linear generator PTO: The Seabased AB device [26,27]: (a) Device description, (b) Farm arrangement

    - *Two-body heaving systems*: The distance between free surface where the floating part of the WEC operates and sea bottom, where the fixed component is located is causing problems from wave induced forces and strength against failure of the mechanical components. The two-body system, with a component acting like the fixed one and located in a mid-distance such as a heaving plate, is an alternative, aiming to the power conversion of the relative motion between this component and the floating one. This relative motion is achieved through causing phase difference between the oscillations of the two components with inertia appliance techniques.

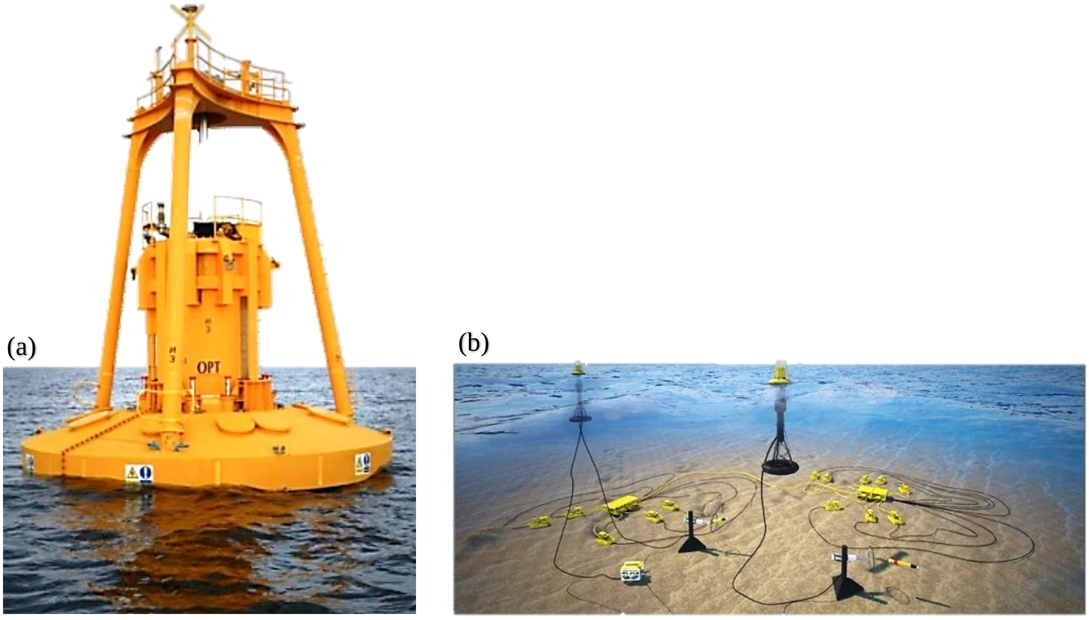

Figure 19: Two-body heaving buoy: The OPT PB3 device [28,29]:
(a) The device, (b) Two-WECs array

- *Fully submerged pressure differential*: Mainly a submerged point absorber using the difference of pressure above itself between crests and troughs of the wave. A typical configuration comprise a sea-based fixed cylinder and a piston connected with the oscillating part of the WEC, moving inside this cylinder, pumping fluid and producing power. The main advantage of this device is that since it is fully submerged is not exposed in the extreme conditions of the free surface, such as slamming events, while at the same time has no visual impact. On the other hand, maintenance is an issue. They are typically installed nearshore and can also be combined with desalination pumped-water units.

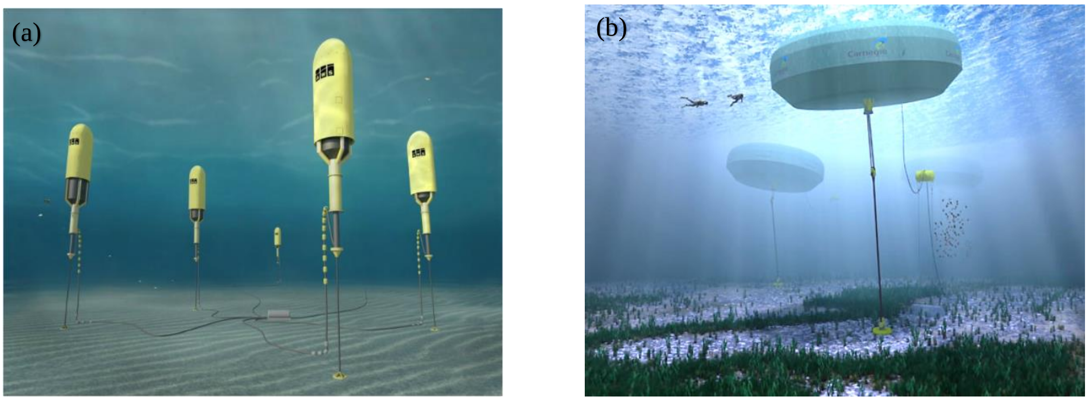

Figure 20: Submerged pressure differential: (a) The AWS device [30], (b) The CETO device [31]

- *Pitching devices*: This converters, unlike the above heaving systems associated with a relative translational oscillation, absorb energy through the pitch-rotation. In late 1970s the first device of this type was the Salter's Duck or Duck of Edinburgh, which unfortunately never reached a full-scale model. The power capturing mechanism constitutes from a section hinged with joints parallel to the wave direction. These joints may pump fluid, typically oil though hydraulic motors and drive electrical generators. This principal can also be applied with small modifications in two-body devices with one component in the water and the other outside of it. In this models the component in the water takes a paddle-shape. The non-wet component can also be enclosed inside the component in the water along with the PTO which will take advantage of their relative motion.

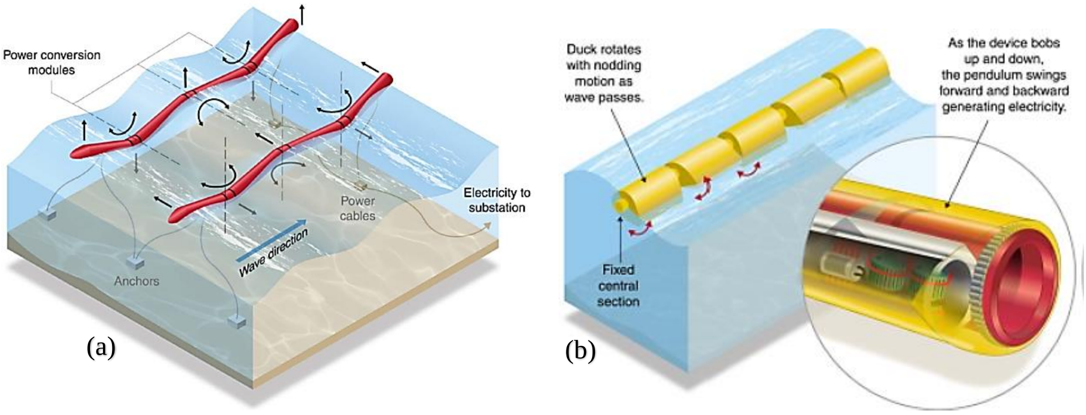

Figure 21: Pitching devices [32]: (a) The Pelamis device [33], (b) The Salter's Duck

- *Bottom hinged systems*: They are also mentioned as oscillating wave surge converters. Again, based on the rotational relative movement, many devices have been proposed hinged at the sea bed. The pitch-oscillation of a paddle engaged with joints to the fixed bottom component is the main principal of the PTO, which can be a water-pump and a sub-sea pipeline leading to a conventional hydro plant or produce electricity on the spot and transfer it to shore with an underwater cable, exploiting mainly the horizontal velocity field induced by the wave. The upper part of this device can be above sea water and visible in nearshore installations.

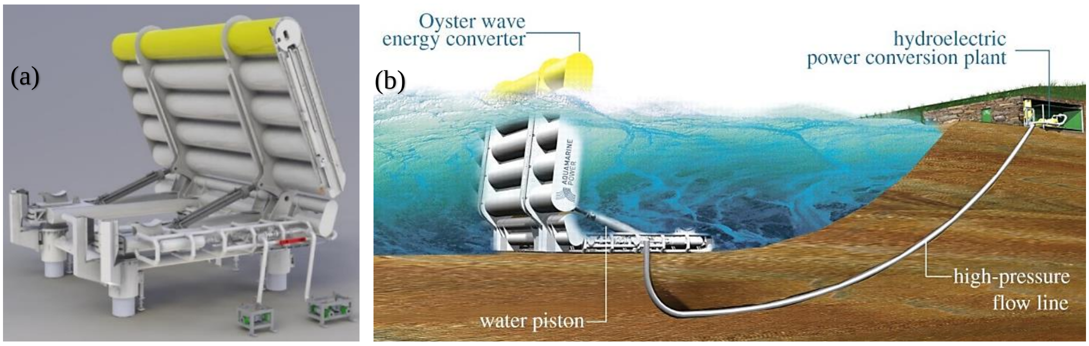

Figure 22: Bottom hinged systems: The AMP Oyster device:
(a) The device, (b) Oyster Plant configuration [34,35]

- *Many body systems*: The idea of scaling-up and deploying a number of heaving point absorbers sharing the same platform in an offshore environment is a trend in modern industry, leading the projects for larger power capacities.

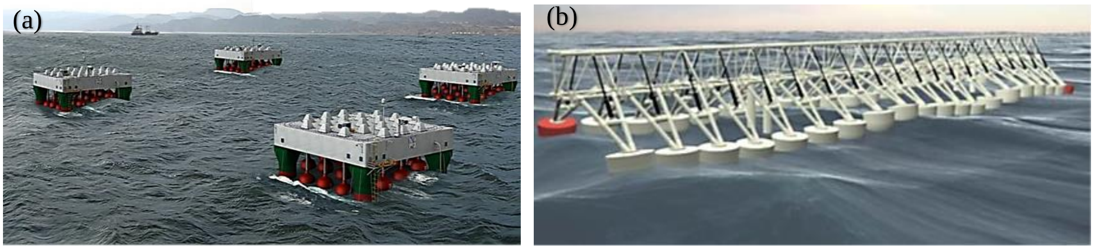

Figure 23: Multi-body systems: (a) The SEEWEC project [36], (b) The Wavestar project [37,38]

- **Overtopping converters**: A whole different way of extracting energy from the waves is the overtopping systems, aiming at this time to capture the wave crest water volume by breakwaters, curved-reflectors and ramps to a raised reservoir, and drive it to a low-head hydro turbine. The study of these devices cannot be addressed by hydrodynamics of OWC and oscillating body converters. This proposal is ideal even for energy storage as hydraulic potential. They can be either onshore or offshore deployed, where the turbine is located commonly under the sea water level. Many concepts combine more than one reservoirs and multi-stage turbines.

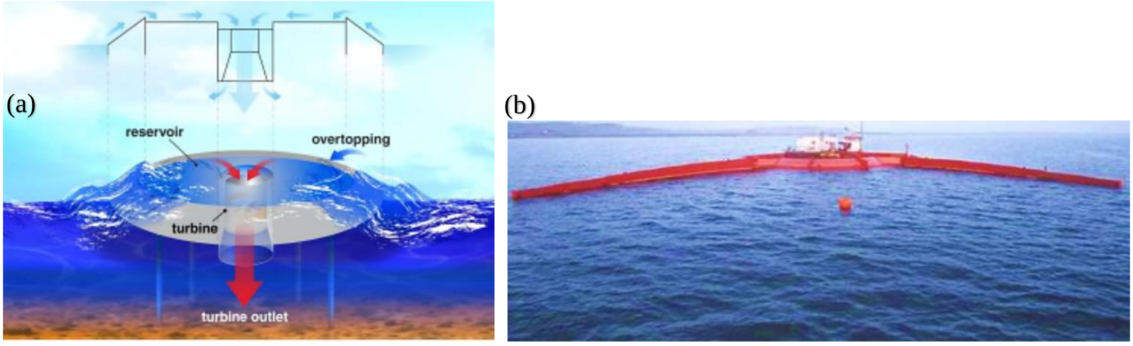

Figure 24: Overtopping systems: (a) Operation principals [32], (b) The Wavedragon device [39,40]

- **Other concepts**: This field of research is really active with new state of the art concepts and ideas arising very often. Here are presented some of these devices:

  - *Bulge wave device*: Water enters due to the wave to a flexible floating tube near the free surface. As it travels through this tube it accelerates and increases its amplitude and finally goes through a micro-turbine at the end of the tube, producing power.

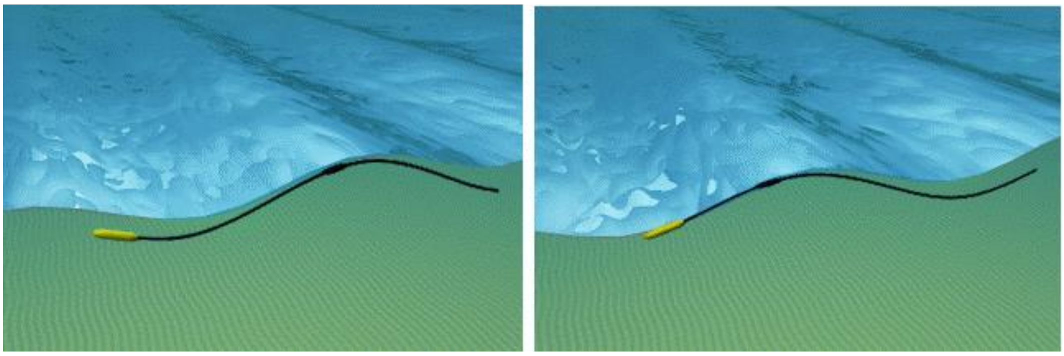

Figure 25: The bulge wave device (motion snapshots) [41]

- *<u>Rotating mass converters</u>*: These devices are taking advantage of the rotational degrees of freedom, mainly of the pitch and roll, of a floating body. This movement causes the rotation of an eccentric mass inside their axisymmetric body, which drives an electrical generator.

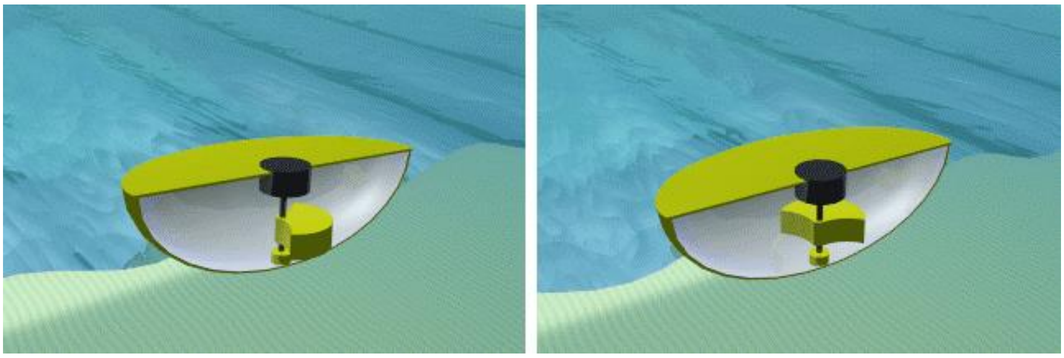

Figure 26: The rotating mass device (motion snapshots) [41]

- *<u>Membrane devices</u>*: A floating flexible membrane follows the wave motion, with the appropriate PTO, which can be turbine or piezoelectric, producing finally electricity.

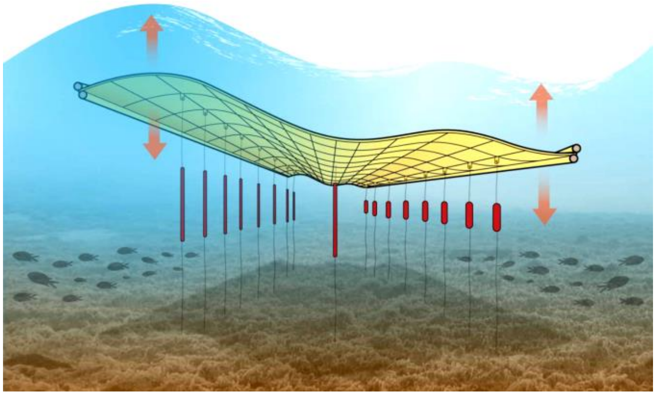

Figure 27: The membrane device [32]

Table 4
Wave energy technologies [18]

Technology	System	Principle	Project
Oscillating Water Column	Fixed Floating	Isolated; In breakwaters; Nearshore -	Pico; Limpet; Sakata Mighty Whale; Oceanlinx
Oscillating Bodies	Fixed-shoreline Floating Submerged	- Translation (heave) Rotation Translation (heave) Rotation	Eco Wave Power AquaBuoy; Wavebob SEAREV AWS Oyster; Waveroller
Overtopping	Fixed Floating	Shoreline -	TAPCHAN; SSG Wave Dragon

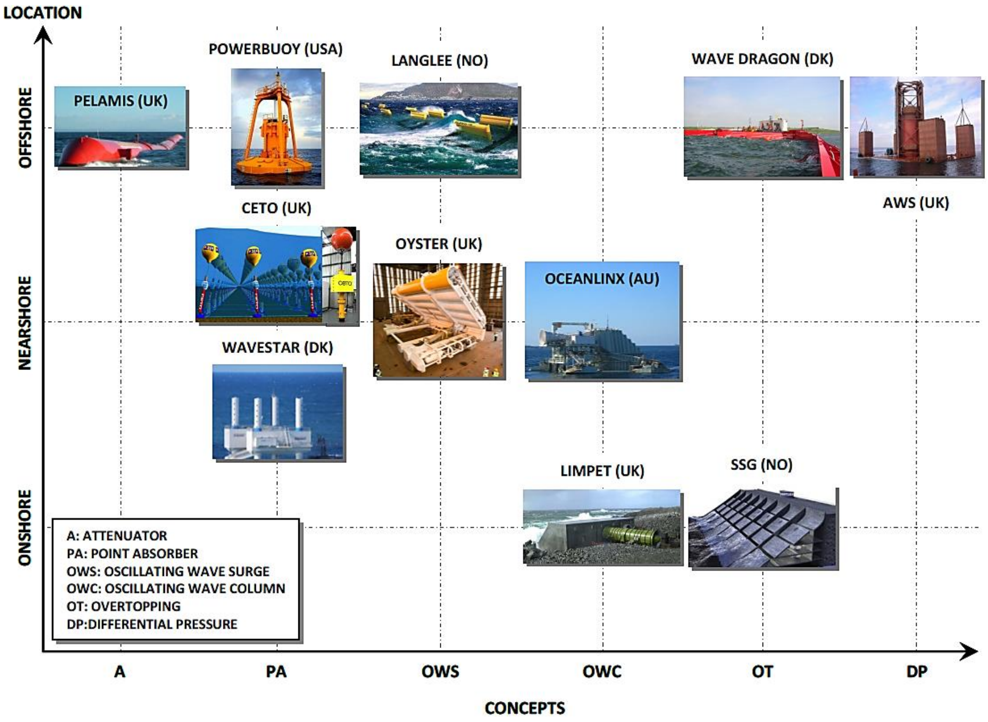

Figure 28: Wave energy concepts and their categorization (2018) [42]

1.2.2.3 3rd *Categorization criterion: Location*

According to the device distance from the shoreline there are three types of installations, described in detail in **Fig. 29** [15]:

- *Shoreline devices*: With their foundations in a natural rock or in a man-made structure they are closely located to the grid and easy to maintain with lower risks of being damaged, however with reduced available potential to be captured.
- *Near-shore devices*: Operating in shallow waters and mainly fixed on the bottom, able to oscillate against a stationery rod. The potential is again limited in low levels.
- *Offshore devices*: The high depth of the spot demands their mooring and sets challenges for construction, maintenance, installation and survivability. Along with the harming extreme conditions comes the much higher amount of energy potential. In environmental terms, is predicted to have the lowest impacts.

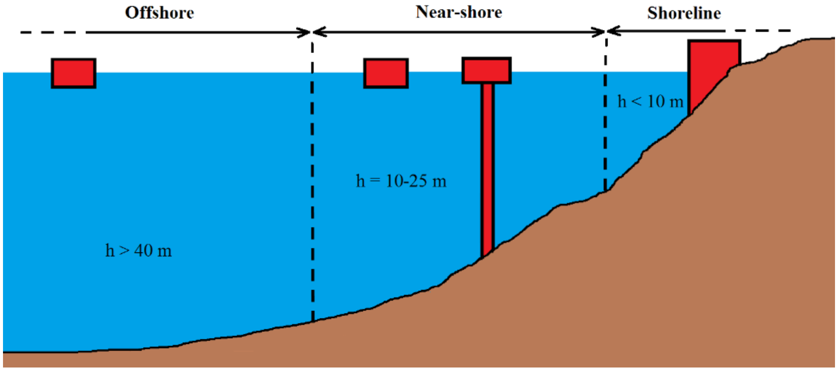

Figure 29: Shore distance categorization for WECs

1.2.2.4 4th Categorization criterion: Power Take Off

The method for capturing the energy is varying among devices. The most common idea is the power production by the coupling of a rotary component to a high-speed electrical generator, as depicted in **Fig. 30**, frequently in combination with appropriate transmission systems to convert linear oscillation into rotary motion. A brief description for each type of this Power Take Off (PTOs) follows [14]:

- *Pneumatic PTO – Turbine Transfer*: The flow of the fluid (air or seawater) rotates a turbine directly coupled with a generator. Issues relevant to the variable speed of these devices are similar to the wind energy technology. The main advantage is the non-environmental danger in case of leakages. If the working fluid is air, popularly through a Wells turbine, then slow velocities can be exploited. Poor efficiency, hard-starting and high noise levels are some major disadvantages. If seawater is used, then behavioral fluid complexity, particles contamination, corrosion and cavitation are serious drawbacks.
- *Hydraulic PTO – Turbine/Motor Transfer*: The implementation and installation of accumulators and check valves in a hydraulic circuit for power production is another idea. The oscillation of a moving part of the WECs body, such as a piston, which is called as actuator, can force the flow of a fluid in the circuit and finally drive a hydraulic motor or a turbine, coupled with the generator. High pressures, size and weight dimensioning, acting forces, seawater containment, sealing, end-stop constraints and maintenance are subjects of strenuous study. Another critical issue is the energy storage. Batteries are still costly to be developed for this applications while the other alternative of high efficiency, the storage as hydraulic potential in a reservoir, is accompanied with environmental issues and additional costs.
- *Electrical linear generator*: At first these technologies were proven too heavy, too expensive and inefficient. With the progress in modern materials may now be a feasible suggestion. The direct conversion of mechanical energy into electrical power is much simpler than hydraulic and other PTOs. This system is constituted with a translator with permanent magnets, the equivalent of the rotor, and a fixed or large-inertia stator with windings. The main obstacle is the signal processing and transformation into a compatible with the electrical grid waveform.

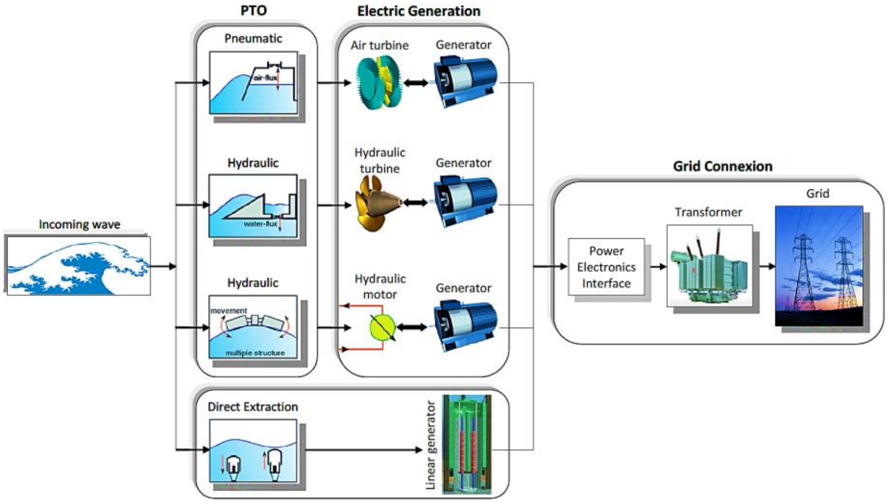

Figure 30: PTOs for wave energy extraction [42]

1.2.2.5 5th Categorization criterion: Control

The behavior of every device and therefore the energy capture depends on the damping. Devices with high damping are restricted to move within limits and therefore little power is absorbed, while soft dampers cannot take off sufficient amount of power. The optimal adjustment is crucial for WECs operation in irregular seas and active control systems of dynamic response are implemented, tuning the function for improved year-round efficiency. The suggested controls can be categorized in:

- Hydrodynamic control
- PTO control
- Grid/Load side control

There are many suggested ways of controlling the operation of a WEC such as latching control, reactive loading control, declutching, phase and amplitude control, feedback linearization control, hydraulic PTO control, turbine PTO and all-electric PTO control [43]. Among this wide range of different control strategies two of them have captured the interest of the industry and scientific society [14]:

- *Latching control*: The aim of this strategy is stalling the device at extremes of its oscillation and releases it when acting forces enables the energy capture maximization. The latching control is highly non-linear, discrete and naturally sub-optimal. The optimization of its implementation is the determination of the right-to-release moment. The opposite of latching control, the declutching or dubbed unlatching allows the device to move freely for a part of the whole cycle and the PTO is engaged with the moving body at the desired velocities, showing an improvement factor of two for some sea states.
- *Reactive loading control*: This control is used to improve the efficiency range near the resonance frequency of a WEC by adjusting dynamic parameters of the system. The main principal for its optimization is the minimization of the reactive force on moving part of the WEC.

Simulation and Design of Experiments (DOE) are essential for optimizing and validating the operation of this controllers, especially in irregular seas, where spectrum analysis must be accurately evaluated. In addition, in many cases more controllers and sensors are applied in order to overcome the uncertainty of predicting waves, and they are called causal, aiming to gain this incoming wave information at a distance before the device by evaluating developed algorithms. Furthermore, the idea of developing multi-DOFs PTOs and WECs, referred as Multiple Input-Multiple Output systems (MIMO), has gained attention, and therefore the development of sufficient controllers and strategies is another interesting research subject [44].

1.2.2.6 6th Categorization criterion: Mooring

The mooring on WECs industry is of great interest and special treatment. This is because, unlike any other typical mooring installation, this time the mooring system has to deal with two main objects: ensuring survivability in extreme conditions and allowing the WEC to operate effectively and absorb as much energy as possible from the waves. Different arrangements and different materials have been proposed and studied. The most common systems are [42]:

- *Spread type*
    - Catenary mooring
    - Taut mooring
    - Turret mooring

- *Single point*
    - Catenary Anchor Leg Mooring (CALM)
    - Single Anchor Leg Mooring (SALM)
    - Articulated Loading Column (ALC)
    - Single Point Mooring & Reservoir (SPAR)

In the following **Fig. 31** are illustrated the main types of spread type mooring configurations and in **Fig. 32** is shown an example of SALM type.

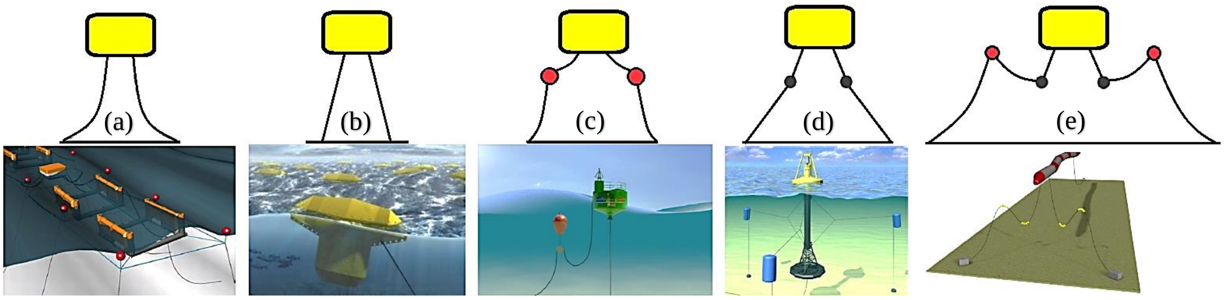

Figure 31: Mooring configurations examples and applications [42]:
(a) Catenary line (Langlee), (b) Taut line (Searev), (c) Taut line with floats (Flansea),
(d) Taut line with weights (PowerBuoy) and (e) Taut line with floats and weights (Pelamis)

Figure 32: CorPower WEC with its PTO and the single point mooring [45]

1.2.3 Capturing the wave power

Every structure placed in a liquid environment underlies to the interaction with this fluid and is able to move along the six degrees of freedom, described in **Fig. 33**:

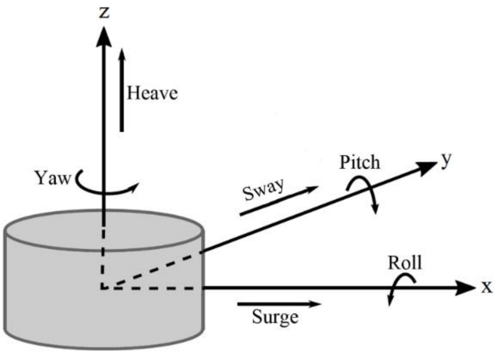

Figure 33: Degrees of freedom of a rigid body

The main principal for wave energy extraction proposes that the device must generate a wave field to interfere destructively the sea waves. An efficient WEC is an efficient wave generator. A critical design aspect, which defines this radiating wave field, is the submerged volume of the system, which though its oscillation displaces equal volume of fluid, a function easily comprehensible especially for heave oscillation. However, due to structural reasons, most of the WEC devices have a large percentage of "dead" volume not participating in this fluid displacement.

For each of these motions, with the appropriate PTO, energy from the wave can be captured by the device. Among these modes of oscillation and rotation the heave and surge modes are the most power concentrating oscillations, but there is no clear superiority for one of them upon the other.

In theory an array of infinite number of point absorbers or alternatively an attenuator with infinite length, operating simultaneously, can harvest the 100% of the incident sinusoidal wave power. However, this is limited by the radiating waves and therefore the maximum power capture is calculated as:

$$P_{max_{rad}} = \alpha \frac{J}{k} = \alpha \frac{\lambda}{2\pi} J \tag{1.1}$$

where J is the wave powerflux per unit of wavefront, k is the wavenumber, λ is the wavelength and α is a constant defined as $\alpha=1$ for heave and $\alpha=2$ for surge or pitch modes [44]. The efficiency of a WEC is maximized when all these three modes of operation are included and then:

$$P_{max_{rad,(surge,\, heave,\, pitch)}} = \frac{3\lambda}{2\pi} J \tag{1.2}$$

In deep water, where $\lambda = \frac{g}{2\pi} T^2$ and $J = \frac{\rho g^2 T H^2}{32\pi}$, for a heaving point absorber the upper limit of power capture is:

$$P_{max_{rad,heave}} = \frac{\rho (g/\pi)^3}{128} T^3 H^2 \tag{1.3}$$

Another limitation is implemented from the finite-volume constraint of the submerged part of the WEC:

$$P_{max_{struct,heave}} = \frac{\pi}{4}\rho g \frac{V_s H}{T} \tag{1.4}$$

where ρ is the fluid density, g is the gravitational acceleration, V_s is the wave-generating volume, H is the amplitude of the sinusoidal wave and T is the wave period [44,46].

These limitations can be illustrated from the known Budal’s Diagram, which follows in **Fig. 34**. The absorbed power and thus the power production by a heaving WEC are bounded in the area below the two limit-lines described by the **Eqs (1.3)** and **(1.4)**.

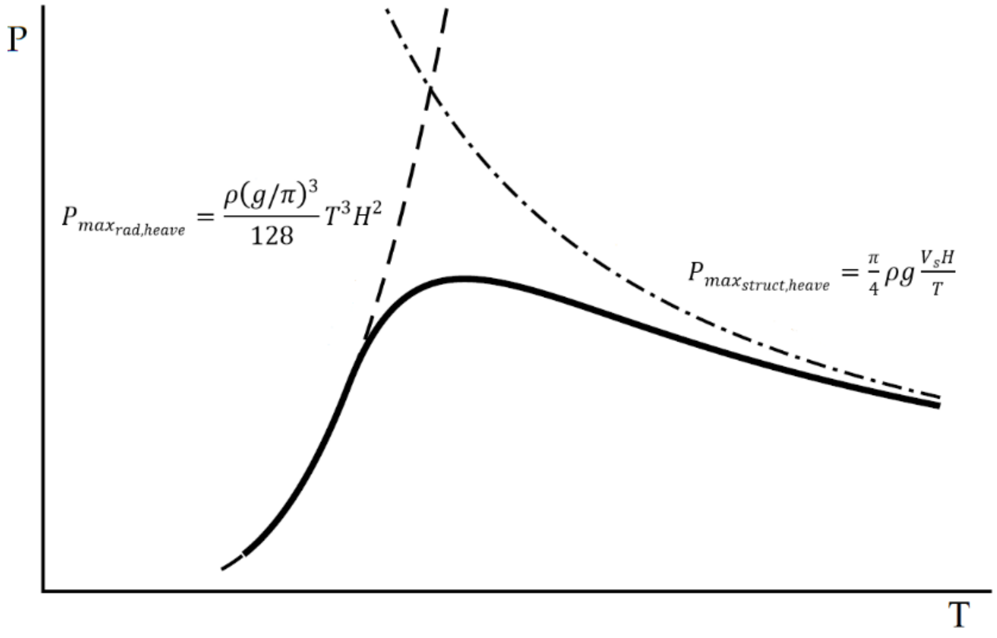

Figure 34: Heaving WEC power capture limits
(Budal's Diagram: Power capture-P vs Wave Period-T).

The main advantage of heaving point absorbers are their independence from the directional spectrum of the incident wave field due to their axisymmetric body design and their relatively small dimensions. There almost seventy four different companies operating in this specific field, with strong deviations in the efficiency and advantages of their WEC proposals.

The investigation of the behavior of a heaving point absorber and its power capture is the subject of many researches all over the world. In this thesis project a novel method, formulated and validated, able to treat shape examination and 3D variable topography interactions, is used for the estimation of its response.

As stated previously, a device combining multi-modes of operation is another key feature of future design. The multi-DOF WEC is also the subject of a subsequent chapter of this thesis. In the following analysis the water density and the reference water depth, in case of flat bottom examination, are considered equal to unit however, this value, along with the incident wave height, has no significant impact, because the results are calculated by the solver and presented in non-dimensional form, permitting the comprehensible expansion to any other case of conditions and design.

2

The BEM: Implementation and validation

2.1 BEM introduction

The Boundary Element Method (BEM) have been developed as an alternative, however with high prospects, method, to treat problems usually evaluated with Finite Element Method (FEA), due to the last ones inefficiency in many engineering problems and their subsequent Computer Aided Engineering (CAE) implementation. A brief presentation of engineering problems analysis and available solution approaches follows in **Fig. 35** [47].

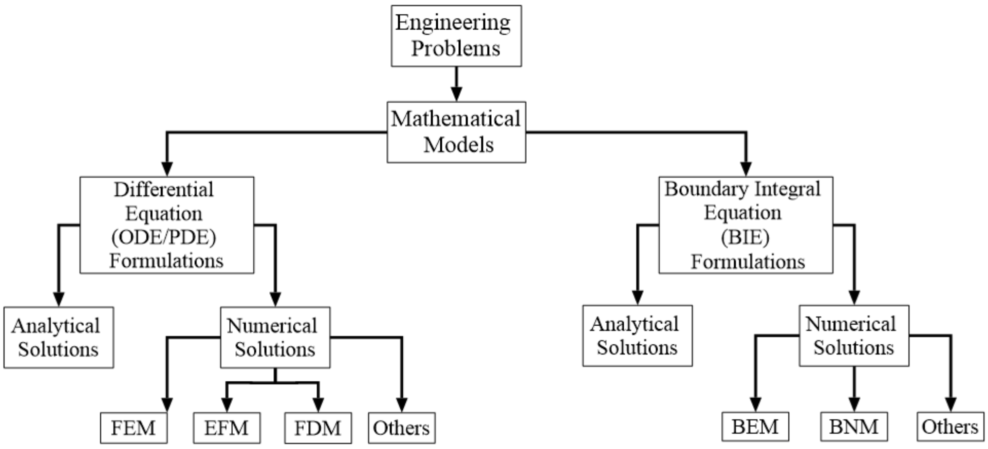

Figure 35: Solution approaches for engineering problems

Both of these theories are different philosophies of the same main problems, the Boundary Values Problems or BVPs. Theoretically, every physical problem can be modelled and solved as a BVP with appropriate boundary conditions (BCs) and its differential physical-governing equation. The evaluation process aims to the satisfaction both of the BCs and the governing equation. This is feasible only in very simple a not so interesting for an engineer problems. Most of the times the solution is utopian to satisfy exactly both the differential equation and the boundary conditions.

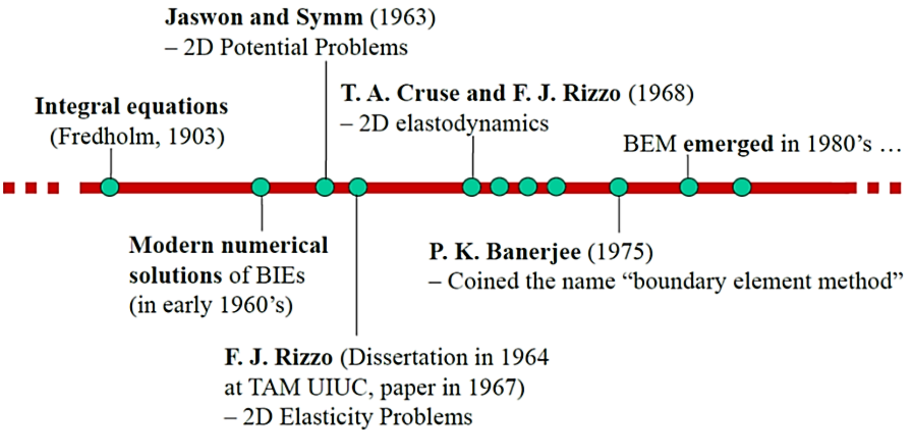

Figure 36: Description of evolution history of BEM [47]

Upon this compromise, two different mathematical theories were developed: The Finite Element Method based on the theory of Ritz (1909) and the Boundary Element Method based on Trefftz's (1926) theory. A compendious flashback to the history of evolution of BEM is presented in **Fig. 36** with the nascence of the theory dating back to 1980s.

The FEM’s target is the absolute satisfaction of the BCs and the optimal approximation of the governing equation in the whole domain mesh. On the other hand, the BEM’s objective is the best approximation of the BC’s while the physical equation is exactly and globally satisfied in the domain. More specifically, BEM is proven to be far more efficient and computational cost-saving in cases of infinite or semi-infinite domains, also described as exterior domain problems, initially mentioned in aerodynamics science field, and also in case of stress concentration during structural modelling and analysis. As its name declare the main difference between BEM and FEM is that in the first method only the surface-boundary of the domain has to be discretized and meshed, while in the second case the whole volume of the domain has to be assigned with the appropriate mesh (**Figs 37**, **38**).

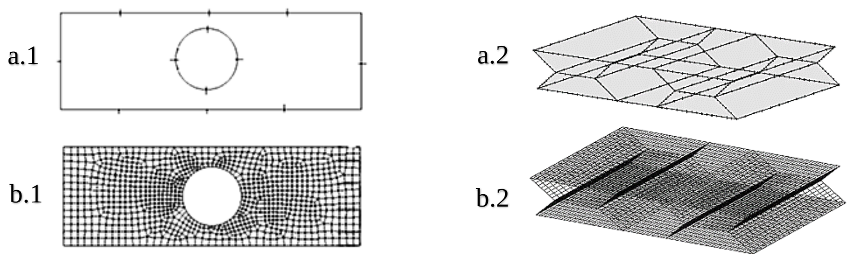

Figure 37: Mesh representation: (a.1, a.2)-BEM, (b.1, b.2)-FEM [48]

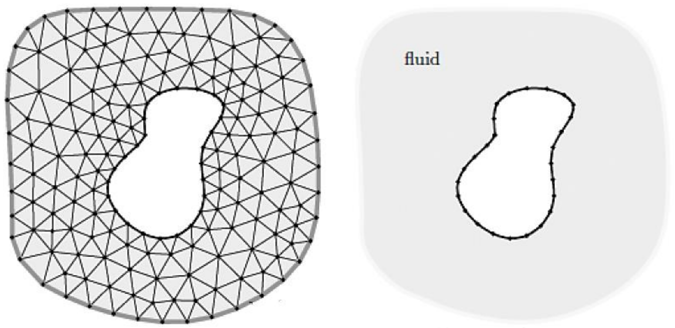

a.1) Exterior-FEM a.2) Exterior-BEM

b.1) Interior-FEM b.2) Interior-BEM

Figure 38: Exterior (a) and Interior (b) problem treatment: FEM (1) vs BEM (2) [49]

In more details, the FEM domain has to be discretized in elementary domains, known as subdomains, and the whole process aims to the minimization of the difference of the governing equation values at the intersection points, known as nodes. Obviously, two main problems automatically emerge: the need of an approach for the solution at the nodes and an increased computational power, especially in problems of engineering interest. However, even under these conditions, there are nodes where the governing equation is violated. Speaking now in terms of the BEM, the final formulation of the solution is a composition of fundamental solutions, the Green Functions, which satisfy the governing equation individually and as a result, the composed solution does the same too [50]. These singularities are distributed in the boundary and the demand for BCs satisfaction leads to the formulation and as a consequence the solution-approximation of a Boundary Integral Equation (BIE).Comparing the BE Method, with its main competitor, the FE Method, many conclusions arise [51,52], which can be categorized as:

BEM Advantages

- *Less data preparation time*. This comes as a result of the surface-only modeling and their subsequent easier changes and re-meshes.
- *Application to infinite domain problems*. The solution satisfies a priory the governing equations and is able to treat problems which FEM is impossible to.
- *Higher solution resolution*. More accurate solution due to the insignificance of interior points where the governing equation is fully continuous and exact.
- *Less computational cost*. Significantly reduced computation time and storage space because BEM uses less number of nodes and elements.
- *Minimum unwanted information*. In most of the engineering problems, especially structural, the "worst" situation or the under study interaction occurs only on the surface and "garbage in – garbage out" effect may cost a big amount of CPU and memory.
- *No need for spatial subdivision*. This task is often a serious numerical problem.
- *Ability for analytical integration*. In many cases, the integration can be evaluated analytically, pointing out BEM as ideal for 3D strongly unsteady problems.

BEM Disadvantages

- *Lack of essential mathematic background*. In BEM formulation the applied mathematics may seem unfamiliar for many engineers.
- *In non-linear problems the interior modelling in unavoidable*. However, for simplification can be restricted in selected areas of interest.
- *Fully populated and unsymmetric solution matrix*. The solution matrix in which a BEM results, is fully populated with non-zero elements, unsymmetric and even it is smaller than the FEM solution matrix, because of its non-sparse form, binds more computer memory, which counterbalances the memory savings due to the modest number of nodes and elements.
- *Inefficiency in thin-shell three dimensional structures*. Inaccuracies are implemented by the large surface to volume ratio and the proximity of each element on both of the sides.
- *Requirement for fundamental solution*. This is the main disadvantage of BEM. If the fundamental solution is not simple then the computation cost is highly increased. In addition, the evaluation of singular integrals may also present difficulties.

In order to overcome problems arising from the frailty of the BEM many studies concentrate on the fundamental functions formulation [53–55]. Present research focuses on the implementation of high order BEM [56,57], while others attempt to combine BEM with FEM along with CFD tools and create hybrid and more effective methods, taking advantage of each numerical "component" to the region in which is more efficient [58–60].

The final selection among BE and FE method is up to the engineer and is mainly related to the following aspects of each problem:

- Type of the problem (linear, non-linear, shell-like analysis, etc.)
- Requirement or accuracy
- Amount of time for data pre-processing

In conclusion, BEM appears to be more efficient in 3D linear problems with variables changing rapidly. It can be used as a preliminary design analysis, when time has to be shortened and the effort minimal. It is also a little immature in comparison with FEM and in many studies scientists prefer a well-established FEA computer software than new methods and source code development. Finally, it should be mentioned the relation between those two methods which allows the direct applicability of FE in BE problems and conversely, with a not so difficult "translation".

The following computational processes are handled by a personal computer with the following specifications: 64bit Intel® Core™ i7-5500U CPU @ 2.40GHz, 8GB RAM. The source code is combining scripts developed in Mathworks MATLAB and FORTRAN programming languages.

2.2 2D validation: The Wavemaker case

2.2.1 Boundaries treatment

The Boundary Element Method (BEM) is ideal for treating problems with infinite or semi-infinite domains. In additions, it is the most commonly used numerical method for solving physical hydrodynamic problems of irrotational flows, ruled by the Laplace Equation along with relevant to each problem boundary conditions, which can be a Dirichlet, a Neumann or a mixed-Robin type BC, based on the participant functions and their derivatives [60,61]:

- $\Phi = g_1$ (Dirichlet BC) (2.1)
- $\frac{\partial \Phi}{\partial n} = g_2$ (Neumann BC) (2.2)
- $\frac{\partial \Phi}{\partial n} + \alpha\,\Phi = g_3$ (Robin BC) (2.3)

In problems with unbounded boundaries the main arising problem for numerical evaluations is the Radiation Condition, which expresses the energy losses and the physical deadening behavior of an outgoing signal away from its source. Scientist can overcome this obstacle by the implementation of mathematical tools in the theories, i.e. the adoption of the Perfectly Matched Layer (PML) technique. However, in the 2D wavemaker problem, which is evaluated in this section, the radiation condition has the analytic Sommerfeld expression and its implementation is effortless.

2.2.2 Mathematical formulation for the 2D semi-infinite strip problem

Assuming, the assignment of the appropriate Cartesian coordinate system at a point of Standard Water Level (SWL) and the computational domain as the 2D semi-infinite strip area expanding from the boundary of the free water surface to the boundary of the plain seabottom of constant depth-*h* along *z*-axis, and from the wavemaker position towards infinity along *x*-axis, as shown in **Fig. 39**, the problem of potential evaluation of small amplitude and slope waves is linearized and ruled by the Laplace Equation and thence can be formulated as follows:

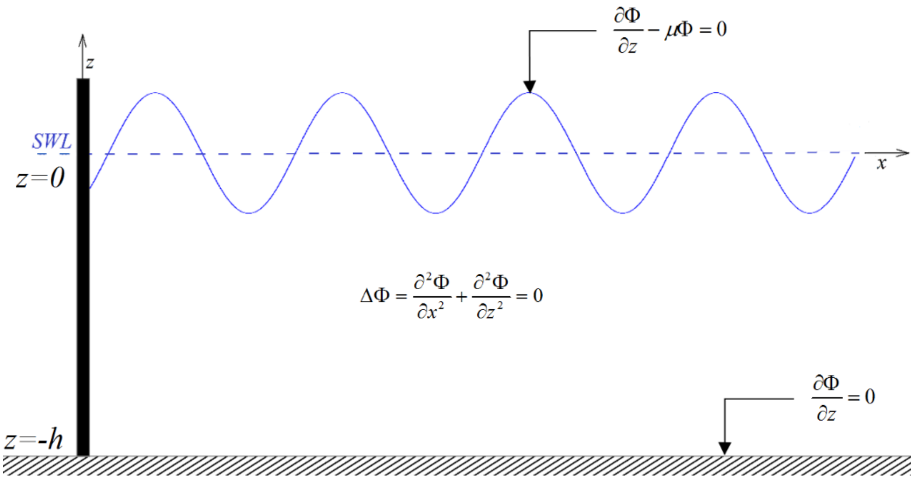

Figure 39: The 2D wavemaker problem formulation

- *Laplace Equation*

$$\Delta\Phi = \frac{\partial^2\Phi}{\partial x^2} + \frac{\partial^2\Phi}{\partial z^2} = 0\,, \text{ for } -h < z < 0,\ \ a < x < \infty \tag{2.4}$$

- *Free Surface Boundary Condition (FS-BC)*

$$\frac{\partial\Phi}{\partial z} - \mu\Phi = 0\,,\ \ z = 0 \tag{2.5}$$

where $\mu=\omega^2/g$ is the frequency parameter, ω is the angular frequency of the waves, g the acceleration of gravity and $i=\sqrt{-1}$. The free surface is a dynamic boundary described by two separate conditions: The Kinematic BC and the Dynamic BC, which in case of natural waves of small slopes (H/λ=7÷10 %) can be combined and lead to the formulation of the Generalized BC, described in **Eq. (2.5)**.

- *Bottom Boundary Condition (B-BC)*

$$\frac{\partial\Phi}{\partial n} \equiv \frac{\partial\Phi}{\partial z} = 0\,,\quad z = -h \tag{2.6}$$

The solutions of the above system, described by the **Eqs (2.4-2.6)**, can be obtained with the variables separation method and appropriate algebra handling with the complex representation of the Φ-potential as: $\Phi(x,z;t)=\mathrm{Re}\{\varphi(x,z)\ e^{-i\omega t}\}$ and then the problem reformulates to an Ordinary Differential Equations Problem (ODE problem) in conjunction with its BCs. The variables separation is based on solutions pursuit for the **Eq. (2.7)** with the presentation of the hypothetic solution $\varphi(x,z)$ as a complex number:

$$\varphi(x,z) = \varphi_R(x,z) + i\varphi_i(x,z) = X(x)\cdot Z(z) \tag{2.7}$$

The solution $\varphi(x,z)$ can be then substituted is the Laplace Equation:

$$X(x)\cdot Z(z)\cdot\left[\frac{\ddot{X}(x)}{X(x)} + \frac{\ddot{Z}(z)}{Z(z)}\right] = 0 \Rightarrow \ddot{X}(x) + k_n^2 X(x) = 0 \ \ \&\ \ \ddot{Z}(z) - k_n^2 Z(z) = 0 \tag{2.8}$$

The BCs for the Free Surface (FS-BC) (**Eq. (2.5)**) and the Bottom (B-BC) (**Eq. (2.6)**) are related and can be satisfied only by the $Z(z)$ function, and then a vertical Sturm-Liouville (St-L) eigenvalues problem is formulated with expressions for the solutions $Z_0(z)$ and $Z_n(z)$:

$$St-L:\left\{\begin{array}{c}\ddot{Z}(z)-k_n^2Z(z)=0\\ \dot{Z}(z)-\mu Z(z)=0,z=0\\ \dot{Z}(z)=0,z=-h\end{array}\right\}\Rightarrow$$

$$Z_0(z)=\frac{\cosh\left[k_0(z+h)\right]}{\cosh(k_0h)},\ n=0 \qquad \text{and} \qquad Z_n(z)=\frac{\cos\left[k_n(z+h)\right]}{\cos(k_nh)},\ n\geq 1 \tag{2.9}$$

along with an equation which connects the angular frequency-ω with the wavenumber-k_n as a function of the strip depth-h:

$$\omega^2=k_0g\tanh(k_0h),\ n=0 \qquad \text{and} \qquad \omega^2=-k_ng\tan(k_nh),\ n\geq 1 \tag{2.10}$$

It is also obtained:

$$X_0(x)=\exp(\pm ik_0x),\ n=0 \qquad \text{and} \qquad X_n(x)=\exp(\pm k_nx),\ n\geq 0 \tag{2.11}$$

The **Eq. (2.10)** is known as the Generalized Dispersion Relation, which obviously has an infinite set of solutions due to the fact that Laplace Equation is solved in two dimensions, admitting oscillating and exponential solutions. For $n=0$, this relation expresses a one-way connection between ω and k, which in this case is a real number and expresses the oscillating component of the solution. For $n\neq 0$, among the exponential roots only the decaying ones can be accepted because in any other case the condition of the bounded physical problem is violated. The roots of the Generalized Dispersion Relation are plotted in **Fig. 41**, while a reference case is also graphically solved in **Fig. 42**. From the graphic results it is ratiocinated that: $k_n\rightarrow n\pi/h$ for $n\rightarrow\infty$ (practically for $n\geq 5$), due to the approximation of the asymptotic limit.

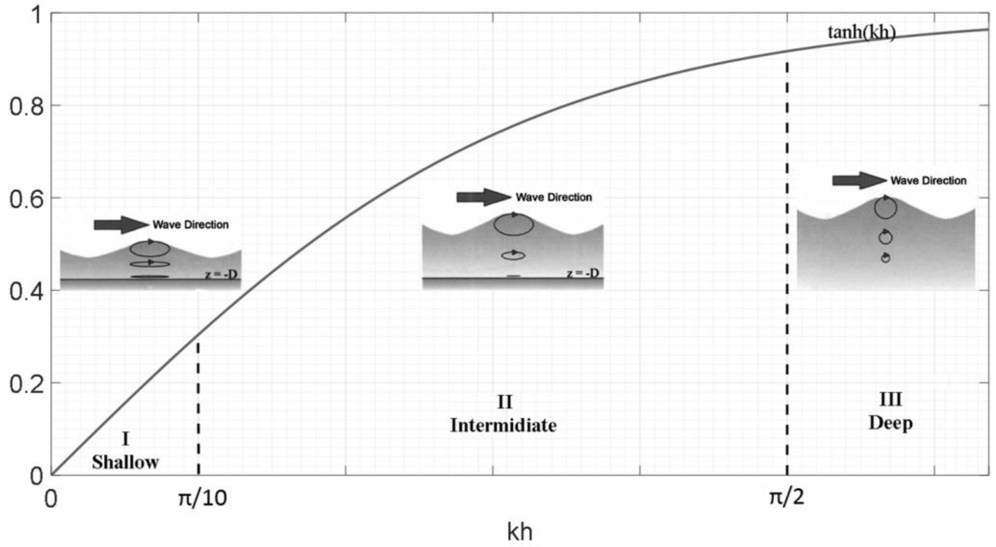

Figure 40: Depth conditions in regard with tanh(*kh*) and particles orbits

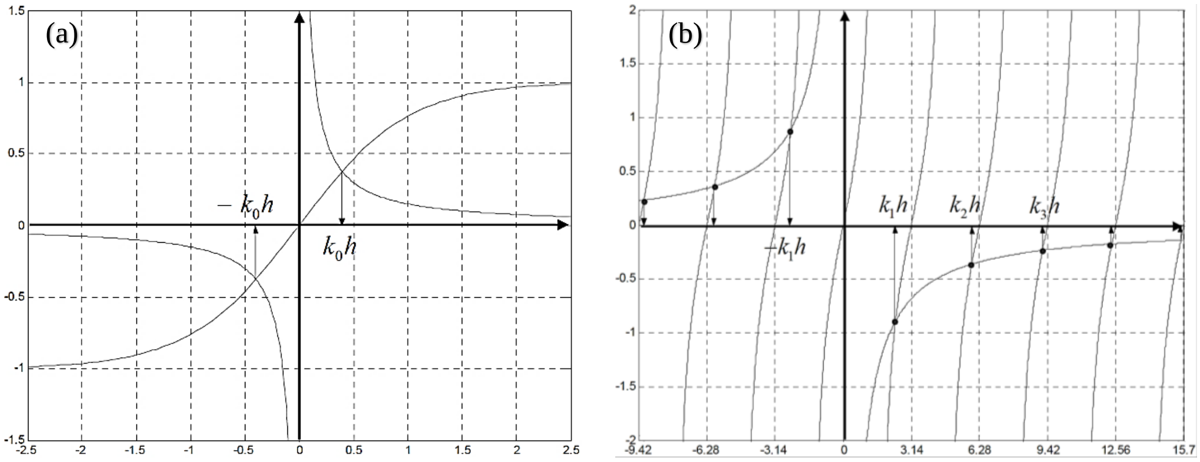

Figure 41: Graphical solution of the Dispersion Relation [62]:
(a) $\omega^2 = k_0\, g \tanh(k_0 h)$,
(b) $\omega^2 = -k_n\, g \tan(k_n h)$

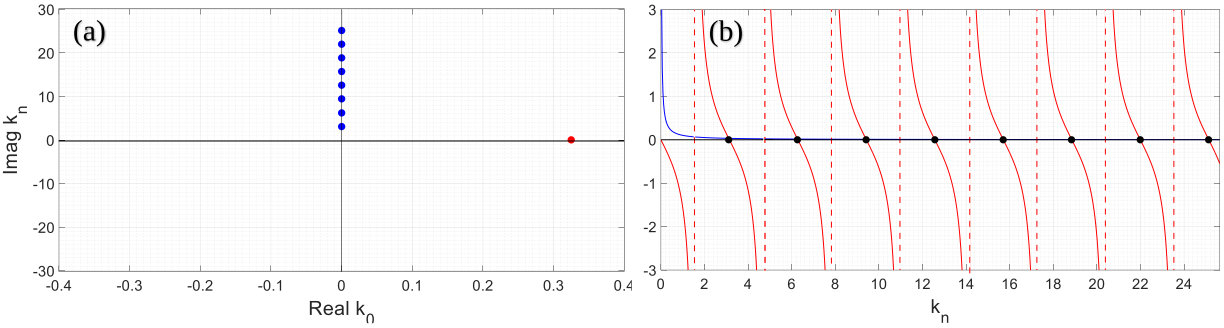

Figure 42: Graphical solution of the Dispersion Relation for ω=1 rad/s and h=1 m:
(a) $\omega^2 = k_0\, g \tanh(k_0 h)$ (red marker) and $\omega^2 = -k_n\, g \tan(k_n h)$ (blue marker)
(b) $\omega^2 = -k_n\, g \tan(k_n h)$

The k_n are the eigenvalues of the formulated regular Sturm-Liouville problem [63] and its solution presents the following interesting features:

1. $k_n \in \mathbb{R}$ and $n \in \mathbb{N}$
2. In every k_n corresponds only one linearly independent eigenfunction $Z_n(z)$
3. Mutually orthogonal eigenfunctions:

$$\langle Z_n, Z_m \rangle := \int_{z=-h}^{z=0} Z_n(z) \cdot Z_m(z)\, dz = \delta_{nm} \|Z_n\|^2, \quad \delta_{nm} = \begin{cases} 0, \text{ if } n \neq m \\ 1, \text{ if } n = m \end{cases} \tag{2.12}$$

4. An orthonormal system is formulated by the eigenfunctions:

$$\tilde{Z}_n(z) = \frac{z_n(z)}{\|z_n\|} \Rightarrow \langle \tilde{Z}_n, \tilde{Z}_m \rangle = \delta_{nm} \tag{2.13}$$

   where δ_{nm} denotes Kroneckers delta.

5. The eigenfunctions constitute a base on the space L_2 $(-h,0)$ and is a generalization of the Fourier Systems, and accordingly every function in the interval $-h< z< 0$ can be represented by the generalized Fourier series:

$$f(z) = \sum_{n=0}^{\infty} \frac{\langle f, Z_n \rangle}{\|Z_n\|^2} Z_n(z) = \sum_{n=0}^{\infty} \langle f, \tilde{Z}_n \rangle \tilde{Z}_n(z) \tag{2.14}$$

6. The completeness of the Sturm-Liouville systems permits the representation of Dirac's delta function in the following form:

$$\delta(z - z_0) = \sum_{n=0}^{\infty} \tilde{Z}_n(z) \tilde{Z}_n(z_0) \tag{2.15}$$

Deriving from **Eqs (2.9)** and **(2.11)** a general representation of the solutions for the potential-φ and the free surface elevation-η are:

$$\varphi(x,z) = \left(A_0^+ e^{ik_0 x} + A_0^- e^{-ik_0 x}\right) Z_0(z) + \sum_{n=1}^{\infty} A_n e^{-k_n x} Z_n(z) \tag{2.16}$$

$$\eta(x) = -\frac{i\omega}{g} \varphi(x, z=0) = -\frac{i\omega}{g} \left(A_0^+ e^{ik_0 x} + A_0^- e^{-ik_0 x}\right) + \sum_{n=1}^{\infty} A_n e^{-k_n x} \tag{2.17}$$

In the above expression for the potential, the first right part indicates the right-propagating mode, the second the reflected mode and the rest ($n>0$) the evanescent modes exponentially decaying towards infinity ($x\to\infty$). These equations are general representations of solutions in the right semi-infinite strip for every value of coefficients (A_n, $n=0,1,2,\ldots$). The series on **Eqs (2.16)**, **(2.17)** are converging fast, practically for $n \geq 5$, the exponential components are nullified and only the oscillating component remains. This convergence limit, expressed in length units, is equal to 2λ. The analytical evaluation of these coefficients in the wavemaker problem are totally related with its type: flap-type or piston-type wavemaker, positioned at $x=0$ (without loss of generality). The formulation of these expressions are the subject of the following section.

2.2.3 Analytical Treatment

Basically there are two main types of wavemakers: the flap type and the piston type, shown in the representative **Fig. 43**. For these types, their function is described in **Fig. 44**. Hybrid types of wavemakers, or more sophisticated designs, i.e. the one shown in **Fig. 45**, can also be found in the relevant fields of research and applications, in relation to the aspects of the studied phenomenon.

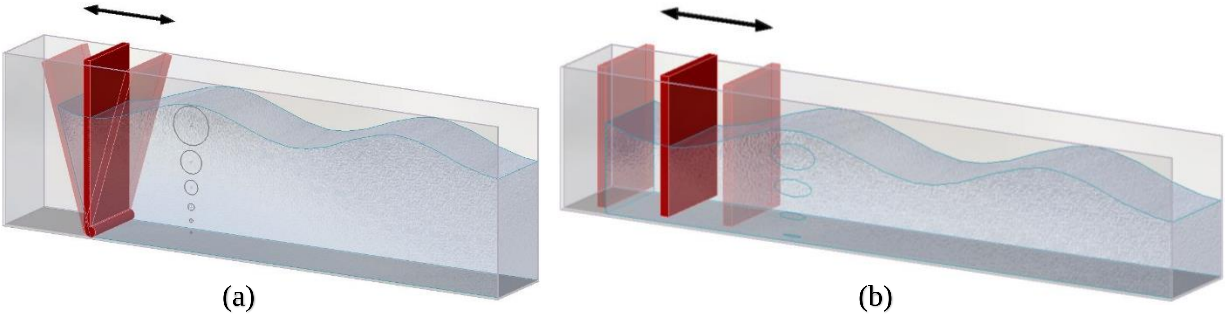

Figure 43: Main types of wavemakers: (a) Flap type, (b) Piston type [64]

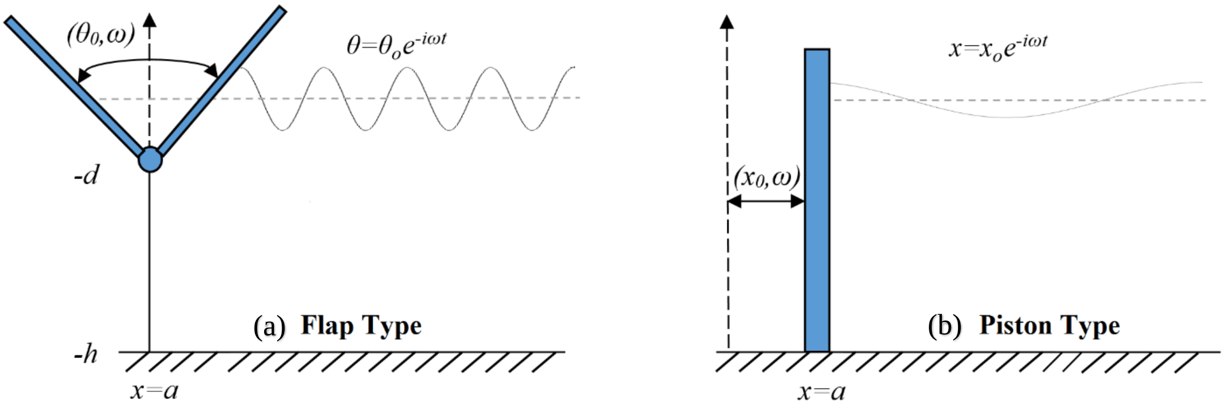

Figure 44: Wavemakers function: (a) Flap type, (b) Piston type

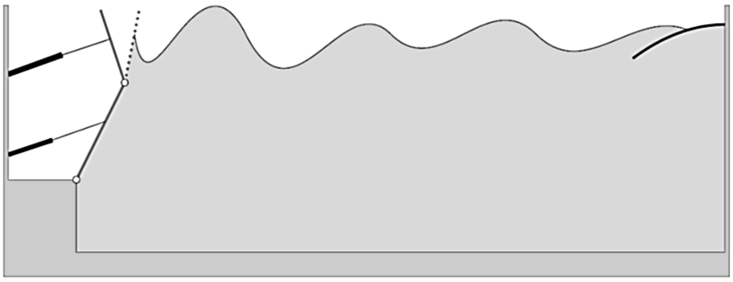

Figure 45: Double flap wavemaker [65]

For the flap type wavemaker, a harmonically rotating flap around a pivot point in depth-*d* and with an angle amplitude-θ_0 produces harmonic waves of the same angular frequency-ω, equal to its rotation frequency. At this point it should be mentioned that, the flap movement induces flow velocities both horizontally and vertically, but for small amplitudes of its rotation due to the linearity satisfaction, only horizontal velocities are considered. On the other hand, the piston type wavemaker oscillates horizontally with an angular frequency-ω and with a stroke-x_0 and therefore generates harmonic waves of the same frequency.

Due to the particles orbits, described in **Fig. 46**, the flap type wavemaker approximates better the intermediate and deep water depth conditions, while the piston type models the conditions of shallow water.

Deep Water: The wave motion is basically confined to the surface layers

Shallow Water: The horizzontal component of the motion of each particle is almost constant at every depth

Figure 46: Particles motion in case of the two types of wavemakers: (a) Flap type, (b) Piston type

In regard with the velocities developing field, the flap type for small amplitudes-θ_0 generates horizontal flow above the pivot-joint point equal to $\omega(z+d)$, for $z > -d$, while under the pivot point the body is assumed as rigid wall and consequently the velocity is zero for $z < -d$. The piston type causes a horizontal flow velocity constant in every depth of the water column.

Based on the above theory for the boundary condition at the positon of the wavemaker and the St-L problem properties, the following formulation of the analytical solution can be developed, aiming to the evaluation of the coefficients A_n and in compliance with the satisfaction of the boundary conditions:

For $x=a$:

<u>Flap Type Wavemaker</u>

$$\frac{\partial\varphi}{\partial x}=-\frac{\partial\varphi}{\partial n}=-i\omega\left(z+d\right),\quad -d<z<0 \tag{2.18}$$

$$\frac{\partial\varphi}{\partial x}=0,\quad -h<z<-d \tag{2.19}$$

$$\varphi_{,x}\left(x=0,z\right)=A_0ik_0e^{ik_0x}Z_0\left(z\right)-\sum_{n=1}^{\infty}A_nk_ne^{-k_nx}Z_n\left(z\right)=f\left(z\right)=\sum_{n=0}^{\infty}\frac{\langle f,Z_n\rangle}{\left\|Z_n\right\|^2}Z_n\left(z\right) \tag{2.20}$$

$$A_0ik_0=\frac{\langle f,Z_0\rangle}{\left\|Z_0\right\|^2}\Rightarrow A_0=-\frac{i\omega}{ik_0}\frac{G_0}{\cosh k_0h}\frac{1}{N_0},\quad N_0=\left\|Z_0\right\|^2=\frac{1}{2}\frac{\cosh\left(k_0h\right)\sinh\left(k_0h\right)+k_0h}{k_0\cosh^2\left(k_0h\right)} \tag{2.21}$$

$$-A_nk_n=\frac{\langle f,Z_n\rangle}{\left\|Z_n\right\|^2}\Rightarrow A_n=-\frac{i\omega}{k_n}\frac{G_n}{\cos\left(k_nh\right)}\frac{1}{N_n},\quad N_n=\left\|Z_n\right\|^2=\frac{1}{2}\frac{\cos\left(k_nh\right)\sin\left(k_nh\right)+k_nh}{k_n\cos^2\left(k_nh\right)} \tag{2.22}$$

where,

$$G_0 = \int_{z=-d}^{z=0} (z+d)\cosh\left[k_0\left(z+h\right)\right]dz \Rightarrow$$

$$G_0 = \int_{u=-d+h}^{u=h} \left(u+d-h\right)\cosh\left(k_0 u\right)du = \frac{\left(d-h\right)}{k_0}\left[\sinh\left(k_0 h\right)-\sinh\left[k_0\left(h-d\right)\right]\right]+$$
$$+\frac{1}{k_0}\left(h\sinh\left(k_0 h\right)-\left(h-d\right)\sinh\left[k_0\left(h-d\right)\right]\right)-\frac{1}{k_0^2}\left(\cosh\left(k_0 h\right)-\cosh\left[k_0\left(h-d\right)\right]\right) \tag{2.23}$$

and,

$$G_n = \int_{z=-d}^{z=0} (z+d)\cos\left[k_n\left(z+h\right)\right]dz \Rightarrow$$

$$G_n = \frac{\left(d-h\right)}{k_n}\left(\sin\left(k_n h\right)-\sin\left[k_n\left(h-d\right)\right]\right)+\frac{1}{k_n}\left(h\sin\left(k_n h\right)-\left(h-d\right)\sin\left(k_n\left(h-d\right)\right)\right)$$
$$+\frac{1}{k_n^2}\left(\cos\left(k_n h\right)-\cos\left[k_n\left(h-d\right)\right]\right) \tag{2.24}$$

<u>Piston Type Wavemaker</u>

$$\frac{\partial\varphi}{\partial x} = -i\omega, \quad -h<z<0 \tag{2.25}$$

$$\varphi_{,x}\left(x=0,z\right) = A_0 i k_0 e^{ik_0 x} Z_0\left(z\right)-\sum_{n=1}^{\infty} A_n k_n e^{-k_n x} Z_n\left(z\right) = f\left(z\right) = \sum_{n=0}^{\infty}\frac{\langle f,Z_n\rangle}{\left\|Z_n\right\|^2}Z_n\left(z\right) \tag{2.26}$$

$$A_0 i k_0 = \frac{\langle f,Z_0\rangle}{\left\|Z_0\right\|^2} \Rightarrow A_0 = -\frac{i\omega}{ik_0}\frac{G_0}{\cosh k_0 h}\frac{1}{N_0}, \ N_0 = \left\|Z_0\right\|^2 = \frac{1}{2}\frac{\cosh\left(k_0 h\right)\sinh\left(k_0 h\right)+k_0 h}{k_0\cosh^2\left(k_0 h\right)} \tag{2.27}$$

$$-A_n k_n = \frac{\langle f,Z_n\rangle}{\left\|Z_n\right\|^2} \Rightarrow A_n = -\frac{i\omega}{k_n}\frac{G_n}{\cos\left(k_n h\right)}\frac{1}{N_n}, \ N_n = \left\|Z_n\right\|^2 = \frac{1}{2}\frac{\cos\left(k_n h\right)\sin\left(k_n h\right)+k_n h}{k_n\cos^2\left(k_n h\right)} \tag{2.28}$$

where,

$$G_0 = \int_{z=-h}^{z=0}\cosh[k_0\left(z+h\right)dz = \int_{u=0}^{u=h}\cosh\left(k_0 u\right)du = \frac{1}{k_0}\left[\sinh\left(k_0 h\right)\right], \ u=z+h \tag{2.29}$$

and,

$$G_n = \int_{z=-h}^{z=0}\cos\left[k_n\left(z+h\right)\right]dz = \frac{1}{k_n}\left[\sin\left(k_n h\right)\right] \tag{2.30}$$

An example of the analytical solution of this problem both for the two types of wavemakers follows in the next **Figs 47**, **48**. The conditions are ω=1 rad/sec and h=1 m, and as a result h/λ=0.1285, corresponding to intermediate depth conditions, conditions which both of the wavemakers can model effectively. The flap type wavemaker is bottom hinged (d=h).

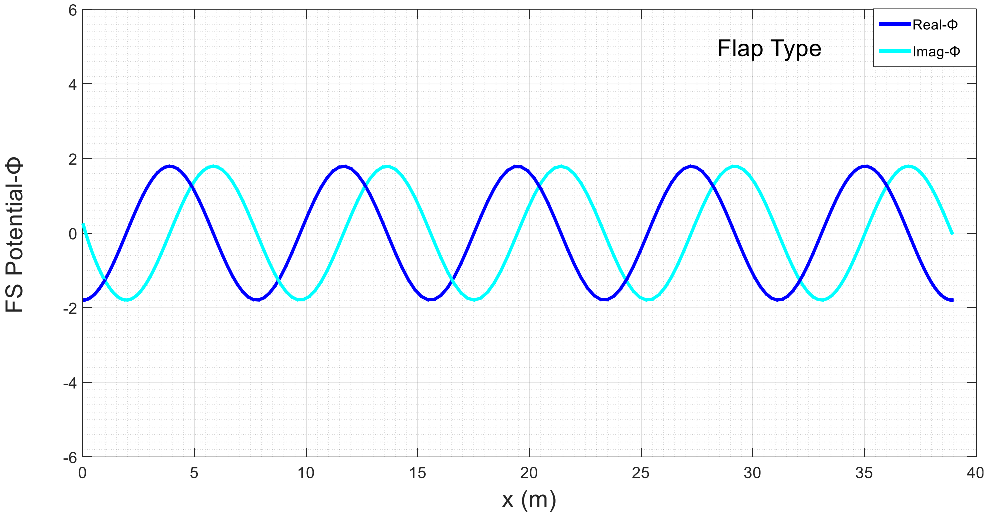

Figure 47: Free surface potential for flap type wavemaker (bottom hinged) (ω=1 rad/sec, h=1 m)

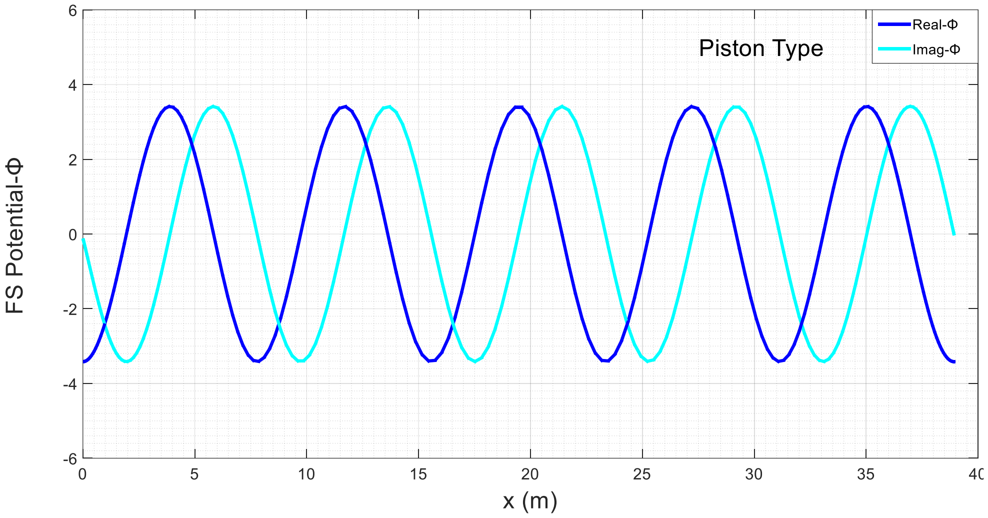

Figure 48: Free surface potential for piston type wavemaker (ω=1 rad/sec, h=1 m)

From the above plots it is obvious that, for these depth conditions, the piston type wavemaker achieves greater values of potential at the free surface in comparison to the flap type, a fact that is justified by the way of operation, the relative stroke of each wavemaker and the water displacement volume.

According to the water volume displaced by each type of wavemaker, a simplified theory was proposed is 1964 by Galvin [66]. The basic idea behind this theory is that the water volume displaced by the wavemaker in one stroke is equal to the generated propagating wave crest volume and is graphically described in **Fig. 49**:

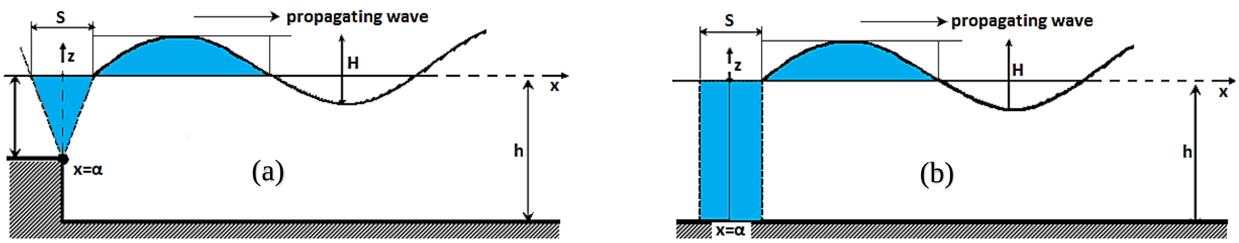

Figure 49: Galvin Theory for wavemakers: (a) Flap type, (b) Piston Type

For a piston type wavemaker for example, with a stroke-*S*, the volume equilibrium is:

$$\int_0^{L/2} (H/2)\sin kx\,dx = H/k \tag{2.31}$$

Assuming a unitary stroke for both wavemakers: $S_f = S_p = 1$, the non-dimensional equations of wave height to stroke ratio can then formulate as:

Flap Type Wavemaker

For *d*=*h* (Bottom hinged)

$$\frac{H}{S} = \frac{H}{2h\theta_0} = \frac{\omega^2}{kgh}\frac{\dfrac{1-\cosh(kh)+kh\sinh(kh)}{k^2}}{\dfrac{kh+\cosh(kh)\sinh(kh)}{2k\cosh(kh)}} = 2\frac{\tanh(kh)}{kh}\frac{\left(1-\cosh(kh)+kh\sinh(kh)\right)}{\dfrac{kh}{\cosh(kh)}+\sinh(kh)} =$$

$$4\frac{\tanh(kh)}{kh}\frac{\left(1-\cosh(kh)+kh\sinh(kh)\right)\cosh(kh)}{2kh+\sinh(2kh)} = 4\frac{\sinh(kh)}{kh}\frac{\left(1-\cosh(kh)+kh\sinh(kh)\right)}{2kh+\sinh(2kh)} \tag{2.32}$$

Shallow water: $kh \to 0, \quad \dfrac{H}{S} = 2\dfrac{-0.5(kh)^2+(kh)^2}{kh+kh} = \dfrac{kh}{2}$ (2.33)

Deep water: $kh \to \infty, \quad \dfrac{H}{S} = \dfrac{H}{2\mathrm{X}_0} = 2\dfrac{1}{0+1} = 2$ (2.34)

Piston Type Wavemaker

$$\frac{H}{S} = \frac{H}{2\mathrm{X}_0} = 2\frac{\sinh^2(kh)}{kh+\cosh(kh)\sinh(kh)} = 2\frac{\tanh^2(kh)}{\dfrac{kh}{\cosh^2(kh)}+\tanh(kh)} = 2\frac{\cosh(2kh)-1}{2kh+\sinh(2kh)} \tag{2.35}$$

Shallow water: $kh \to 0, \quad \dfrac{H}{S} = \dfrac{H}{2\mathrm{X}_0} = 2\dfrac{(kh)^2}{kh+kh} = kh$ (2.36)

Deep water: $kh \to \infty, \quad \dfrac{H}{S} = \dfrac{H}{2\mathrm{X}_0} = 2\dfrac{1}{0+1} = 2$ (2.37)

In shallow water conditions, where: $kh < \frac{\pi}{10}$, the above height-to-stroke ratios of **Eqs (2.33)**, **(2.36)**, which are:

$$\underline{\text{Shallow water}}:\ kh \to 0, \quad \left(\frac{H}{S}\right)_{piston} = kh = 2\left(\frac{H}{S}\right)_{flap} \tag{2.38}$$

are also proving that the piston type presents dominant efficiency in comparison to the flap type at shallow waters. The relevant curves of H/S ratio and the non-dimensional power for these wavemakers, for ω=2.3 rad/sec and: $S_f = S_p$=1, are plotted in **Figs 50** and **51**:

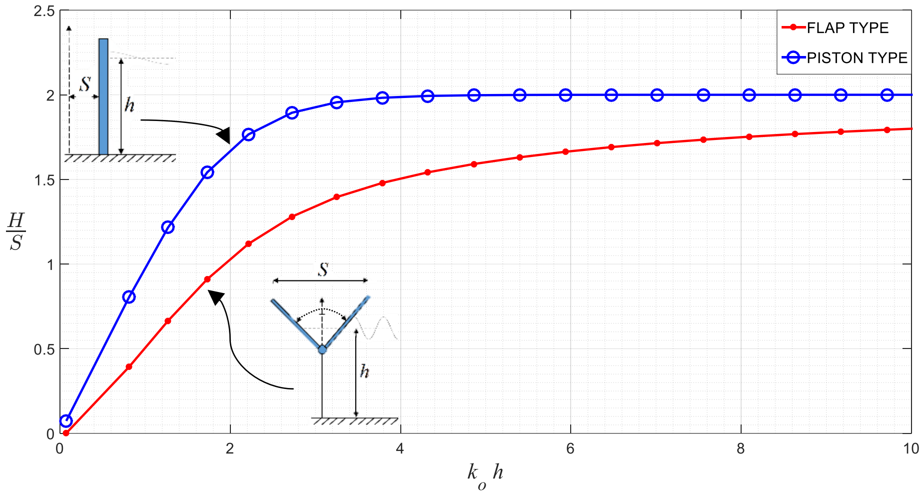

Figure 50: HS ratio curves for wavemakers ([67])

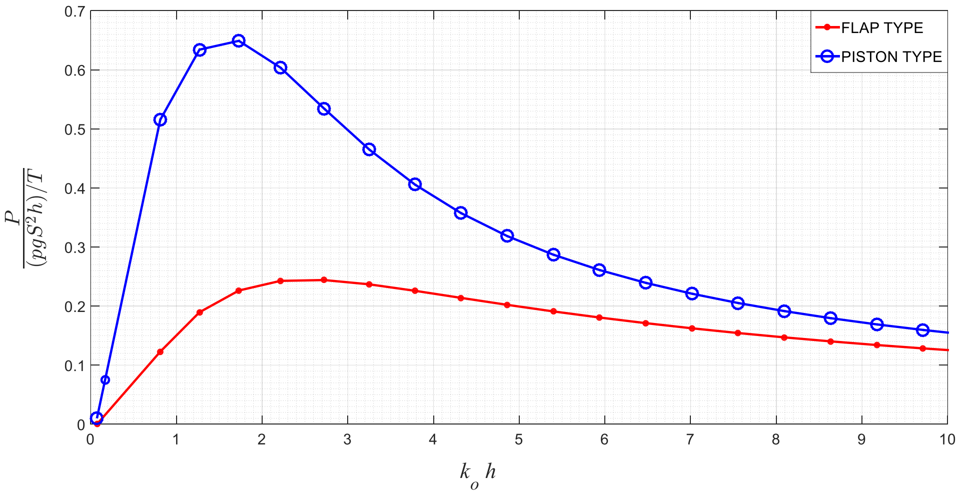

Figure 51: Non-dimensional power curves for wavemakers ([67])

2.2.4 *BEM-2D treatment*

As the problem of semi-infinite stripe is already solved analytically, during the preceding section, it is now time to step on the numerical approximation of the same problem. The implementation of a validated numerical method, able to treat problems, not so simple like the one described previously, is of high significance because, in more complicated problems, analytical solutions are infeasible. One of the most common methods is, as stated previously, the Boundary Element Method (BEM). One form of this method is the low-order, or panels BEM, also known as *1st* order BEM. In this theory, the boundary geometry is approximated with an amount of linear elements, the panels with distributed fundamental solutions of the Laplace Equation, located at the center of each panel. As a result, the problem reformulates to a BIE, which can be solved numerically.

Focusing on the 2D-problem, the fundamental solution of the Laplace Equations, known as Green 2D Function and also referred as source function, is:

$$G(\mathrm{x} \mid \mathrm{y}) = \frac{1}{2\pi} \ln |x-y|^{-1} \tag{2.39}$$

With its substitution in Laplace Equation it is further ratiocinated that:

$$\Delta_x G(\mathrm{x} \mid \mathrm{y}) = \frac{\partial^2 G(\mathrm{x} \mid \mathrm{y})}{\partial x_1^2} + \frac{\partial^2 G(\mathrm{x} \mid \mathrm{y})}{\partial x_2^2} = -\delta(x-y), \quad x \in \mathbb{R}^2 \tag{2.40}$$

where,

$y=(y_1,y_2) \in D$ is a fixed point in the D-domain

$x=(x_1,x_2) \in D$ is the general field point in the D-domain

$\delta(x\text{-}y)=\delta(x_1\text{-}y_1)\ \delta(x_2\text{-}y_2)$ is the Dirac Function, defined by:

$$\int_{\Omega} \sigma(x)\delta(x-y)\,dx = \sigma(y), \quad \forall\ \sigma \in C_0^{\infty}(\Omega) \tag{2.41}$$

Among the different variations of this method, one is reliant on Green's 2nd Theorem:

$$\iiint_D (\Phi \cdot \Delta G - G \cdot \Delta \Phi)\,dV = \iint_{\partial D} \left(\Phi \cdot \frac{\partial G}{\partial n} - G \cdot \frac{\partial \Phi}{\partial n} \right) dS \tag{2.42}$$

where with n is indicated the unit normal vector of the boundary geometry ∂D directing to the exterior of the D.

The potential in any point of the interior domain, based on Green's Theorem, can then be represented by the surface distribution of sources or sinks of constant strength-$\sigma(y)$ from the following **Eq. (2.43)**:

$$\varphi(x) = \int_{\partial D} \sigma(y) G(\mathrm{x} \mid \mathrm{y})\,ds(y) \tag{2.43}$$

and therefore the velocity potential for any point in the interior domain is:

$$u = \nabla \varphi = \nabla_x \left(\int_{\partial D} \sigma(y) G(\mathrm{x} \mid \mathrm{y})\,ds(y) \right) = \int_{\partial D} \sigma(y) \nabla_x G(\mathrm{x} \mid \mathrm{y})\,ds(y) \tag{2.44}$$

The gradient ∇_x appeared in the above equation is applied on $G(x|y)$ inside the integral, because $\sigma(y)$ is constant in each panel, independent from the space variable.

As the approximation is formulated for the interior problem, another expression must be found for the boundary. In this case the velocity expression includes one more term:

$$u = \frac{\sigma(y)n(x)}{2} + \int_{\partial D} \sigma(y)\nabla_x G(\mathrm{x}\,|\,\mathrm{y})\,ds(y) \tag{2.45}$$

where $n(x)$ is the unit normal vector to the ∂D towards the exterior of D. Hence, the normal component of the velocity can be calculated by the inner product of (u,n):

$$\mathrm{u},\mathrm{n}(x):\mathrm{u}(x)n(x) \equiv \frac{\partial\varphi}{\partial n} = \frac{\sigma(x)}{2} + n(x)\int_{\partial D} \sigma(y)\nabla_x G(\mathrm{x}\,|\,\mathrm{y})\,ds(y), \quad x \in \partial D \tag{2.46}$$

The BCs can be either Dirichlet type: $g_0(x)$ or Neumann type: $g_n(x)$, $x \in \partial D$, hence the **Eq. (2.46)** is now:

$$\int_{\partial D} \sigma(y)\, G(\mathrm{x}\,|\,\mathrm{y})\,ds(y) = g_0(x), \quad x \in D \tag{2.47}$$

or,

$$\frac{\sigma(x)}{2} + n(x)\int_{\partial D} \sigma(y)\nabla_x G(\mathrm{x}\,|\,\mathrm{y})\,ds(y) = g_n(x), \quad x \in \partial D \tag{2.48}$$

The numerical evaluation of these integrals requires the approximation of the boundary of the domain with a simpler, easier to handle, geometry. In *1st* order BEM, 1D elements are used for this approximation. However, due to its simplicity, this method requires a large number of elements in order to achieve the needed accuracy in the solution, while higher order BEM deploys panels with more degrees of freedom able to bend and approximate more easily the geometry of the domain with a lower number of panels. With this approach, any boundary can be approximated by a polygon composed by linear elements, each one bringing a constant σ_i source, sink or doublet distribution in its center, as shown in **Fig. 52**:

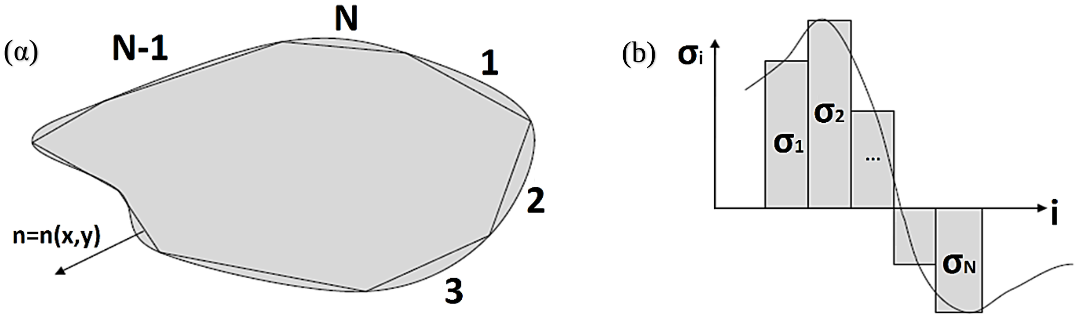

Figure 52: *1st* order BEM: (a) Approximation of the boundary in the case of low-order BEM by a polygon, (b) Source, sink and doublet distribution on each element.

As long as the panels number increases the polygon approaches the real geometry of the boundary and theoretically when *N→∞* then *Polygon→ ∂D* and *Numerical Solution → Real Solution*. The first step is the evaluation of the normal vector in each panel. The basic idea is the assumption of constant strength source distribution in each panel, described by the histogram of **Fig. 52(b)**, on the verge of actual sources form. Except from sources, sinks and doublets distribution, used in this study, vortex distribution is also used in problem with vorticity in a similar way. The strength of each source (general term including both source, sink and doublet) are unknown and will be evaluated by the solution of a linear system. The calculation of the integrals above may be a hard task, even for simple sources form and straight lines boundaries. The boundary is discretized with a certain number of points N, known as nodes and the nodes are connected with straight lines, forming the method's panels.

Inserting now a coordinate system for each panel (**Fig. 53**) the aim is to find the induced potential and velocity to a hypothetic point $P(x_2,x_3)$ from each panel, defined by the nodes A, B with general coordinates $(x^A{}_2,x^A{}_3)$ and $(x^B{}_2,x^B{}_3)$ respectively. The local coordinates are consisted of the axis-ζ parallel to (AB) and axis-η perpendicular to ζ. In this system the coordinates of A, B points are exhibiting simpler expressions: A $(\zeta_A,0)$ and B $(\zeta_B,0)$.

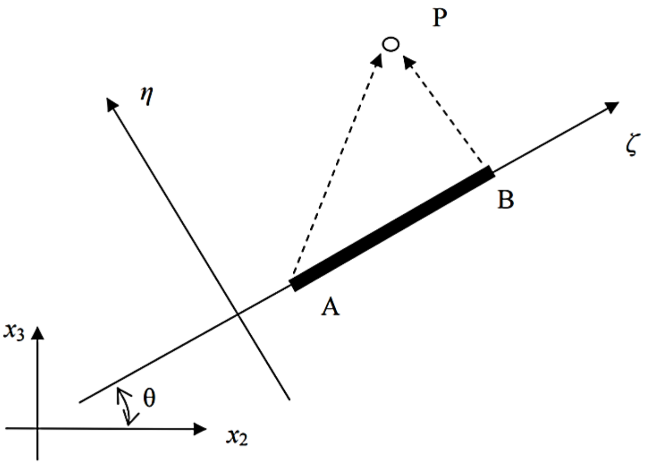

Figure 53: Local coordinate system on the panel

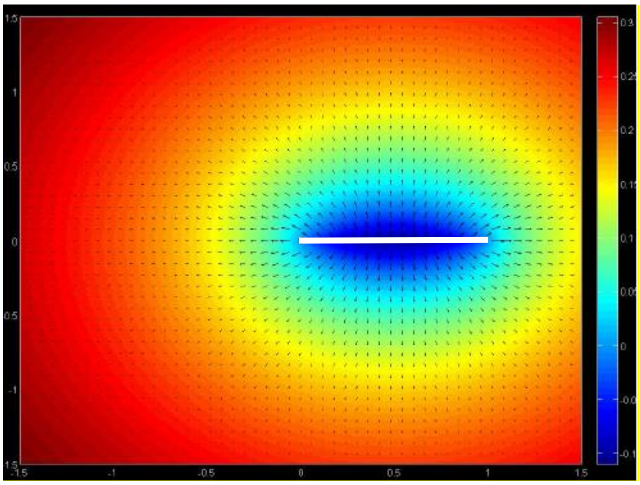

Figure 54: Induced field (potential, velocities) from a linear element ($A(\zeta_A=0, \eta_A=0)$, $B(\zeta_B=1, \eta_B=0)$) [62]

The midpoint of (*AB*)-panel induces a potential and a velocity to the point *P* expressed by the **Eqs (2.50)-(2.55)** while the total induced potential from all *N*-panels is expressed in **Eq. (2.49)**:

$$\varphi = \sum_{n=1}^{N} \int_{panel\ j} \frac{\sigma(s)\ln r}{2\pi} ds \tag{2.49}$$

$$\varphi(\zeta,\eta) = -\frac{\sigma}{2\pi}\left\{\begin{array}{l}(\zeta-\zeta_{\mathrm{A}})\ln\left[(\zeta-\zeta_{\mathrm{A}})^2+\eta^2\right]-(\zeta-\zeta_{\mathrm{B}})\ln\left[(\zeta-\zeta_{\mathrm{B}})^2+\eta^2\right]\\ +2\eta\left(\tan^{-1}\left(\dfrac{\eta}{\zeta-\zeta_{\mathrm{B}}}\right)-\tan^{-1}\left(\dfrac{\eta}{\zeta-\zeta_{\mathrm{A}}}\right)\right)\end{array}\right\} \tag{2.50}$$

$$u_\zeta(\zeta,\eta) = -\frac{\sigma}{2\pi}\ln\left(\frac{(\zeta-\zeta_{\mathrm{A}})^2+\eta^2}{(\zeta-\zeta_{\mathrm{B}})^2+\eta^2}\right) \tag{2.51}$$

$$u_\eta(\zeta,\eta) = -\frac{\sigma}{2\pi}\left(\tan^{-1}\left(\frac{\eta}{\zeta-\zeta_{\mathrm{B}}}\right)-\tan^{-1}\left(\frac{\eta}{\zeta-\zeta_{\mathrm{A}}}\right)\right) \tag{2.52}$$

Through the coordinates transformation it can be finally assumed that:

$$u_{x2}(x_2,x_3) = u_\zeta(\zeta,\eta)\cos(\theta) - u_\eta(\zeta,\eta)\sin(\theta) \tag{2.53}$$

$$u_{x3}(x_2,x_3) = u_\zeta(\zeta,\eta)\sin(\theta) + u_\eta(\zeta,\eta)\cos(\theta) \tag{2.54}$$

where,

$$\theta = \tan^{-1}\left(\frac{x_3^B - x_3^A}{x_2^B - x_2^A}\right) \tag{2.55}$$

An example of this induced field is represented in **Fig. 54**. Furthermore, a linear system can be formulated (**Eq. (2.56)**) for the solution of the unknown strengths of the sources, which implicates the matrix of influence A_{jk}, the unknowns σ_k and the boundary conditions g_j. Specifically, the matrices of influence express the induced potential from the midpoint of *k*-panel to the midpoint of *j*-panel.

$$\sum_{k=1}^{N} A_{jk}\sigma_k = g_j, \quad j = 1,\ldots,N \tag{2.56}$$

where,

$$g(P_j) = \varphi(P_j): \text{ Dirichlet BC} \tag{2.57}$$

$$g(P_j) = \frac{\partial\varphi(P_j)}{\partial n}: \text{ Neumann BC} \tag{2.58}$$

The system can be easily solved in a mathematical software with the inverse of matrix A_{jk} of the **Eq. (2.56)**.

2.2.4.1 *Wavemaker problem BEM-2D implementation*

In this section a comparison between the analytical results, discussed previously, and the BE Method results for the semi-infinite strip problem is attempted. For the implementation of the numerical method a computational algorithm is developed in Mathworks MATLAB environment.

The first step is to define the computational domain, consisted of three main regions (**Fig. 55**):

- The Free Surface (FS) – (**M**1)
- The Wavemaker: Two subregions, one for the moving flap and one for the fixed rest of the body of the device or single region for the piston type wavemaker – (**M**2)
- The rigid bottom – (**M**3)

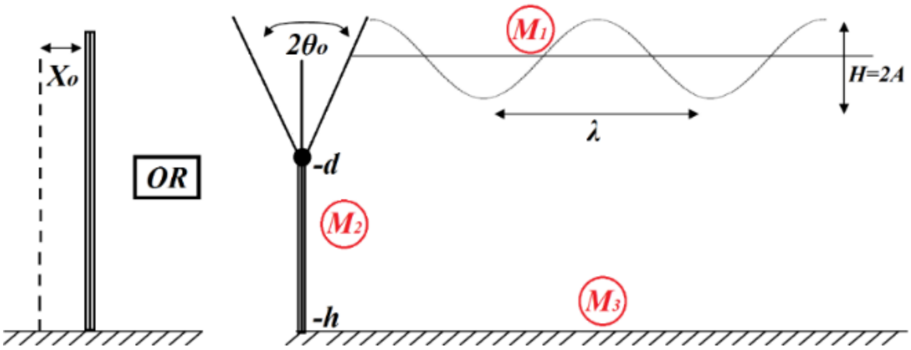

Figure 55: Semi-infinite strip computational domain and regions M_i *(i*=1,..,3*)*

A technique for a more dense mesh near the position of the wavemaker, where the phenomenon is more intense due to the movement and thus requires higher detail, is used. The next steps of algorithm's development is the finding of the panels' midpoint and the angle between each local coordinates system and the general one and the calculations of the unit normal vector with its two components, vertical and horizontal. Then, the matrix of BCs in the right hand of the **Eq. (2.56)** can be formulated. The induced potential and velocities to the *j*-collocation point, which is the center of the *j*-element, from all the *i*-center points is calculated by a short subroutine. Finally, the linear system can be easily solved for the source strength σ_k.

Free Surface:

$$\frac{\sigma_k}{2}+\sum_{m=1}^{M}\sigma_m\left(n_k U_{km}-\mu\varphi_{km}\right)=0,\quad k=1,M_1 \tag{2.59}$$

where μ: is the frequency parameter defined as:

$$\mu(\omega)=\frac{\omega^2}{g} \tag{2.60}$$

Wavemaker Position:

$$\frac{\sigma_k}{2}+\sum_{m=1}^{M}\sigma_m\left(n_k U_{km}\right)=f(y),\quad k=M_1+1,\ \sum_{i=1}^{2}M_i \tag{2.61}$$

where,

$$\text{Flap type:}\quad f(y)=\left\{\begin{array}{ll} 0, & y<-d \\ i\omega(y+d), & y\geq -d \end{array}\right\} \tag{2.62}$$

indicates the velocity of the flap and therefore the velocity of the water column in touch with the wavemaker, or:

$$\text{Piston type:}\quad f(y)=i\omega \tag{2.63}$$

Rigid Bottom:

$$\frac{\sigma_k}{2}+\sum_{m=1}^{M}\sigma_m\left(n_k U_{km}\right)=0,\quad k=\sum_{i=1}^{2}M_i+1,\ \sum_{i=1}^{3}M_i \tag{2.64}$$

Now, it is essential to model the behavior of the outgoing wave towards infinity. This is the aim of the appliance of the radiation condition which is responsible for the formulation of the final solution. As governed and determined by the physics of the problem, the wave, as a disturbance, far from the stimulation field is weakening and finally disappears. In many cases this condition cannot be formed a priory because of the lack of analytical or even semi-analytical solutions of the problem and as a result preliminary mathematical analysis is the key to overcome this obstacle. A case of this need is going to be examined in the subsequent chapters. However, in this problem the radiation condition takes the well-known Sommerfeld expression (**Eq. (2.65)**).

$$\frac{\partial\Phi}{\partial r}+jk_o\Phi=\mathrm{O}\left(\left(k_o r\right)^{-3/2}\right)\Rightarrow\lim_{r\to\infty}\left(\frac{\partial\Phi}{\partial r}+jk_o\Phi\right)=0 \tag{2.65}$$

The Sommerfeld Condition:

- It is not applied in a specific border of the domain
- It is not the result of simple assumptions
- It is not general but depends on each problem individually

Practically, the deadening of the waves is achieved by the construction of a wave breaking beach.

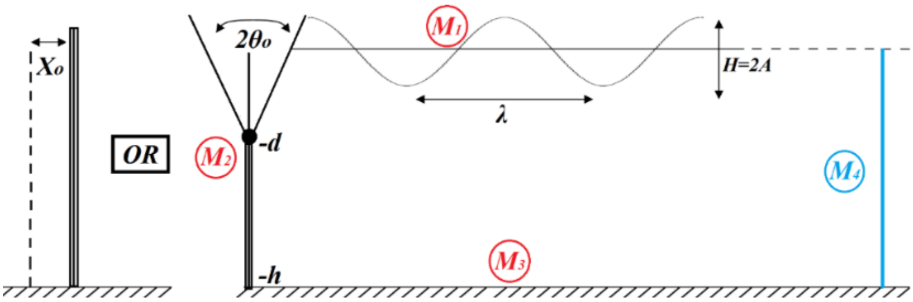

Figure 56: Semi-infinite strip computational domain and regions M_i $(i=1,..,4)$ with the radiation boundary

Radiation Condition:

$$\frac{\sigma_k}{2}+\sum_{m=1}^{M}\sigma_m\left(n_k U_{km}-jk_o\varphi_{km}\right)=0,\quad k=\sum_{i=1}^{3}M_i+1,\ \sum_{i=1}^{4}M_i \tag{2.66}$$

2.2.4.2 Wavemaker problem BEM-2D validation

The BEM approach of this problem can be further validated by the comparison with the results deriving from the analytical description and solution of this specific problem, which is described in advance. Some examples are plotted in the following **Figs 57**, **58**.

As stated before, as long as the number of nodes-N on the boundary increases, the BEM results tend to the analytic solution. In order to visualize this convergence, the error of the approximation is calculated as:

$$error = \int \left| \mathrm{Re}\left\{ \Phi_{FS(BEM)} \right\} - \mathrm{Re}\left\{ \Phi_{FS(An)} \right\} \right| \tag{2.67}$$

Therefore the exponential convergence of the approximation is indicated in **Fig. 59**.

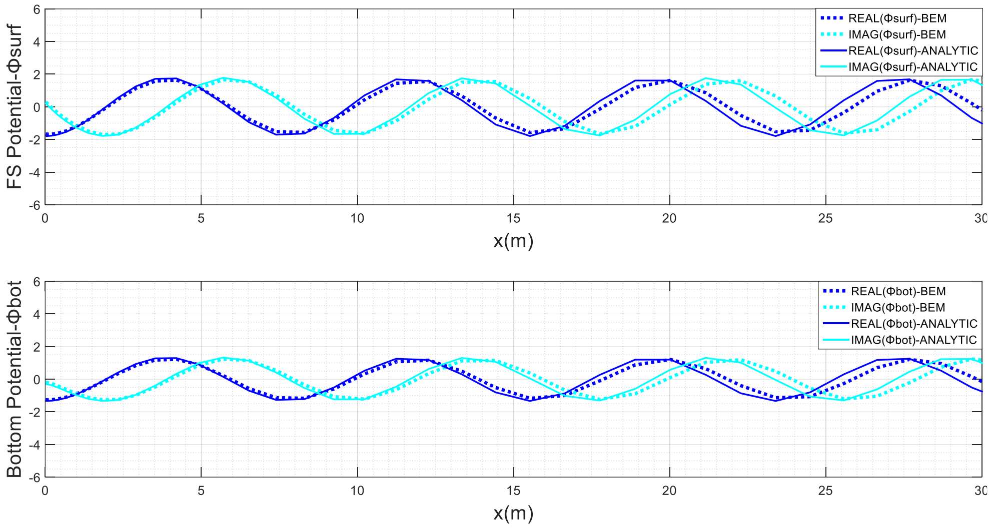

Figure 57: BEM vs Analytic-Flap type wavemaker (ω=2.3 rad/sec, h=1 m, Bottom hinged d=h, N=11)

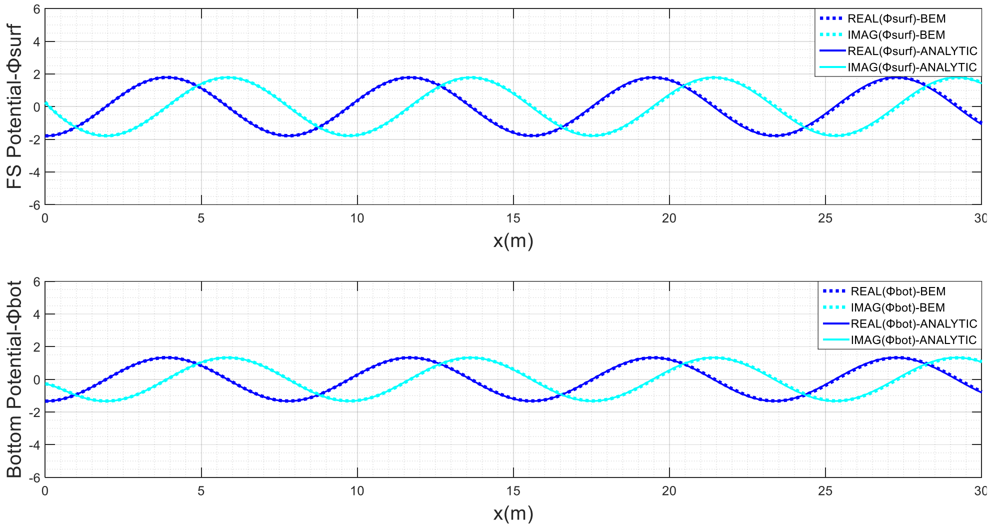

Figure 58: BEM vs Analytic-Flap type wavemaker (ω=2.3 rad/sec, h=1 m, Bottom hinged d=h, N=41)

From the convergence plot (**Fig. 59**) arises the meaning of the compromise between accuracy and computational cost. The number of nodes defines the mesh resolution and therefore the time consumption and the CPU usage cost. However, in this case the time for evaluating the solution even with 61 nodes is insignificant, with the evaluation process lasting for almost 213 sec.

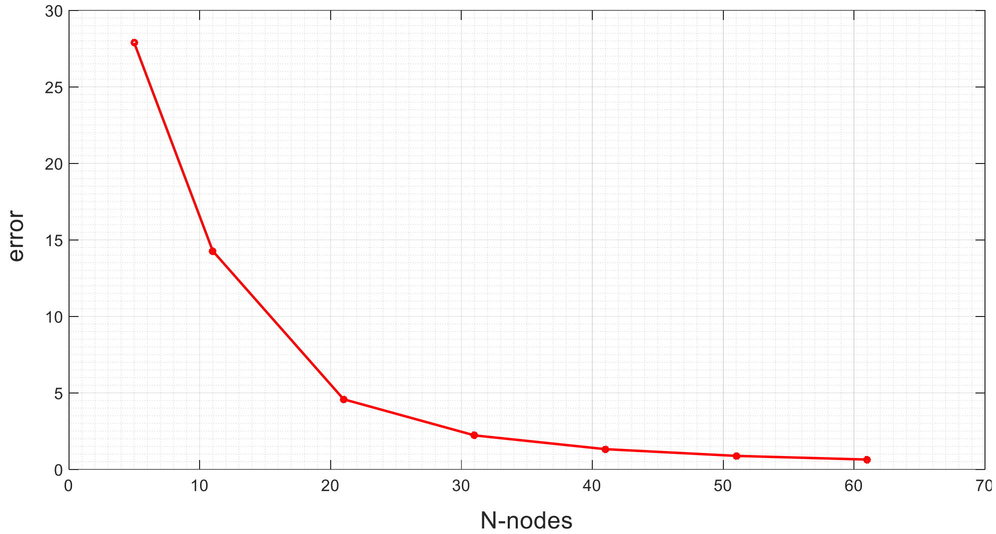

Figure 59: Convergence plot for number of nodes-*N* in flap type wavemaker BEM.

In the same way, analysis and validation process can also be evaluated for the piston type wavemaker (**Fig. 60**), with only one difference: the usage of **Eq. (2.63)** instead of **Eq. (2.62)**.

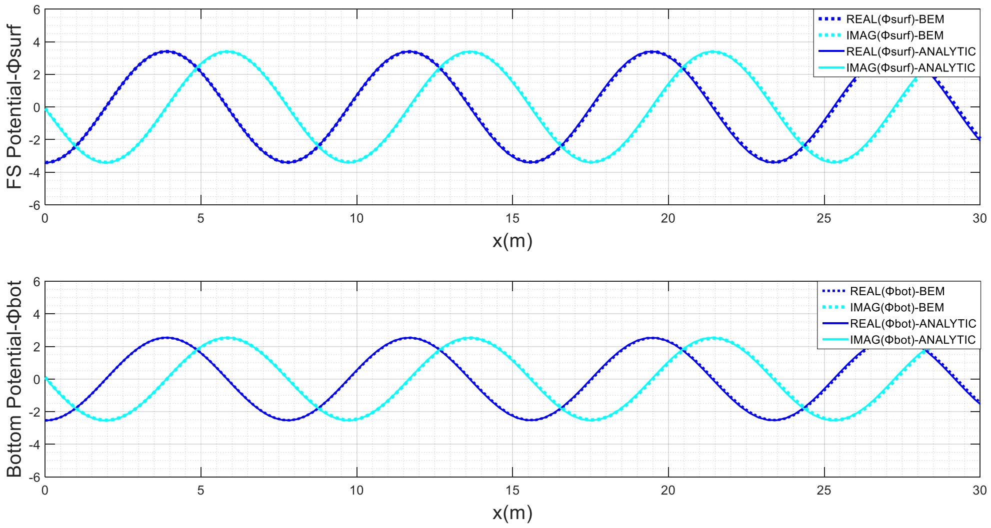

Figure 60: BEM vs Analytic-Piston type wavemaker (ω=2.3 rad/sec, h=1 m, N=41)

2.3 3D validation: The heaving cylinder

2.3.1 Analytical treatment

The capability of having at the same time a numerical-BEM solution and an analytical one is very useful in order to prove the BEM reliability. Moreover, it will provide the researcher with an essential asset for comparing these two results and optimizing the BEM-PML scheme performance. One problem which combine all these leverages about the numerical method optimization is the heaving cylinder 3D problem, following in the subsequent section. The cylinder operates over a constant-depth bathymetric profile where analytical and numerical solutions can be accomplished. In the second step, those solutions will be compared and the implemented PML model will be optimized in order to achieve convergence between the numerical and the analytical solution and then, with small modifications, will be applied in the forthcoming analysis of 3D problems, this time even with different body shapes and over a varying sea bottom, a case where the formulation is far more complicated and an analytical treatment is impracticable.

A cylindrical body is subjected to the excitation of the propagating wave field over a flat bottom. Cylindrical bodies are very common in offshore installations and extensive studies for the formulation of the analytical expressions of the dynamic equations and responses for this problem has been carried through during the past century [68,69]. Furthermore, cylindrical bodies are nowadays used in many WEC concepts capturing the energy form the waves, pointing out the great interest on the investigation of cylinder's hydrodynamic behavior.

Considering a heaving vertical cylinder with radius-*a* and draft-*T* in water of depth-*h* and consequently of bottom clearance equal to $d=h-T$, the symmetry of the problem defines that the response is independent from the attack angle of the incident waves and it is possible to assume without loss of generality that the waves propagate parallel to the x_1-axis (**Fig. 61**). Evaluating the hydrostatic balance equation for the cylinder, the mass is equal to $M=\rho\pi\alpha^2 T$ and the cylinder is considered upright with the center of mass vertically coincident to the center of buoyancy.

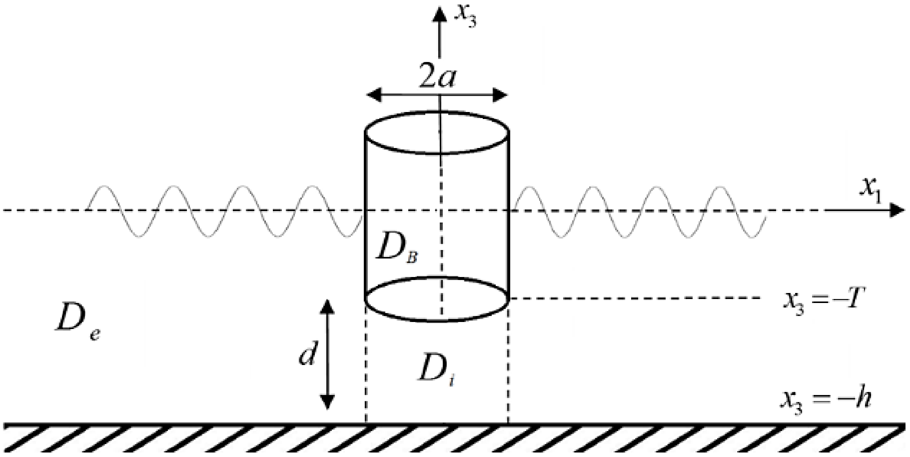

Figure 61: Heaving oscillation of a vertical cylinder

For the heave mode (ξ_3 motion), the symmetry also imposes that the hydrostatic coefficients are: $C_{33}=\rho g\pi\alpha^2$ and $C_{34}=C_{35}=0$ and the added mass are $M_{33}=M$ and $M_{35}=0$. For the same reason, the radiation potentials, related with the surge, sway, roll and pitch motions (ξ_1, ξ_2, ξ_4 and ξ_5), namely the $\Phi_1(x)$, $\Phi_2(x)$, $\Phi_4(x)$ and $\Phi_5(x)$ are antisymmetric and their multiplication with the symmetric generalized normal vector n_k $(k=1,\ldots,6)$ to the body surface results is their total nullification:

$$\Pi_{l3}=\rho\iint_{\partial D_B}\Phi_l n_3 dS_B=0,\quad l=1,2,4,5 \tag{2.68}$$

In addition, the $\Phi_6(x)$ radiation potential of yaw-ξ_6 motion is equal to zero ($\Phi_6(x)=0$) because the $n_6=0$, as the generalized normal vector resets at the submerged body part.

As a result, the equation expressing the dynamic equilibrium in this case is simplified, taking the form of **Eq. (2.69)**, where only the coefficients of added mass and damping matrix, connected with the heave-ξ_3 motion exclusively (i.e. indicators $(\ldots)_{33}$), and participating in vertical oscillation, are non-zero, simplifying severely the equation of motion and de-complexing it from the other equations:

$$\left(-\omega^2\left(\mathrm{M}+\mathrm{A}_{33}(\omega)\right)+i\omega\mathrm{B}_{33}(\omega)+C_{33}\right)\xi_3(\omega)=X_{03}(\omega)+X_{d3}(\omega) \tag{2.69}$$

where $X_{03}(\omega)$ and $X_{d3}(\omega)$ are the complex amplitudes of the Froude-Krylov and Diffraction forces respectively, while their summation is the Total heave excitation forces. Any other outer forces should be included in the right part of the above equation.

Stepping on the appliance of the Coupled Mode Method (CMS) the potential $\Phi_3(x)$ can be defined and the corresponding hydrodynamic coefficients of added mass and damping can be evaluated as the real and the imaginary part of a complex number, as a function of Φ_3-potential:

$$A_{33}+\frac{1}{i\omega}B_{33}=\rho\iint_{\partial D_B}\Phi_3 n_3 dS_B=\rho\int_{\theta=0}^{2\pi}d\theta\int_{r=0}^{r=a}r\,\Phi_3\left(r,x_3=-T\right)dr \tag{2.70}$$

The right part of the above equation is evaluated by taking account that the Φ_3-potential is axisymmetric, independent from the azimuthal angle $\theta=\tan^{-1}(x_2/x_1)$ and thus: $\Phi_3=\Phi_3(r,x_3)$ where $r=\sqrt{(x_1)^2+(x_2)^2}$ is the distance between the horizontal plane and the centerline of the cylinder.

The FK forces can be easily calculated through direct integration of the incident wave field (**Eq. (2.71)**) over the submerged cylindrical wetted surface ∂D_B:

$$\Phi_0(x)=\frac{gA}{\omega^2}\cdot\frac{\cosh\left[k_0\left(x_3+h\right)\right]}{\cosh k_0 h}\exp\left[ik_0x_1\right] \tag{2.71}$$

where A is the free surface elevation amplitude and angular frequency-ω is calculated by the Dispersion Relation: $\omega^2=gk_0\tanh(k_0h)$. Considering now that the generalized normal vector equals to: $n_3=0$ on the vertical wetted surface of the cylinder and $n_3=1$ on the cylinder's bottom ($x_3=-T$), the FK forces are given analytically by the following **Eq. (2.72)**:

$$X_{03} = \rho\omega^2 A \iint_{\partial D_B} \Phi_0 n_3 dS_B = \rho\omega^2 A \int_{\theta=0}^{2\pi} d\theta \int_{r=0}^{r=a} r\,\Phi_0\left(r, x_3 = -T\right) dr \tag{2.72}$$

However, the evaluation of the diffraction potential $\Phi_d(x)$ and the corresponding X_{d3} forces:

$$X_{d3} = \rho\omega^2 A \iint_{\partial D_B} \Phi_d \, n_3 dS_B \tag{2.73}$$

presents difficulties because the field in this case is not axisymmetric and is depending on all three dimensions. The CMS can also be applied in this case to provide the solution [70,71].

Furthermore, the hydrodynamic forces can also be derived by the well-known Haskind-Newmann Equations according only to $\Phi_3(r,x_3)$, or also their amplitude can be calculated through B_{33}, which is evaluated again according only to $\Phi_3(r,x_3)$, making possible at both cases the avoidance of the tough evaluation of the diffraction potential.

2.3.1.1 Radiation potential evaluation

The Coupled Mode Model (CMS) for the determination of the propagating field, is an alternative novel method for determining also the potential of the radiation problem for the heave motion of a cylindrical body. The CMS is a very common approach not only in hydrodynamics, but also in many wave propagation problems i.e. acoustic waves, free surface waves and vibrations and it is based on the coupling of analytical general representations of the field in subareas of the domain and the requirement for continuity of potential and their vertical derivative at the matching surfaces. As shown in **Fig. 61**, the domain $D=D_e \cup D_i$ is separated in this two subdomains: D_e exterior domain and D_i the interior domain, below the cylinder, while the matching of these domains is obviously the vertical cylindrical surface ∂D_B, where: $r=\sqrt{(x_1)^2+(x_2)^2}=a$, $-h<x_3<-T$. These two domains will be treated separately in the subsequent paragraphs.

Exterior Domain Problem

The physical far-field wave behavior with the outgoing and decaying wave propagation towards infinity, explained by the energy equilibrium between cylindrical surfaces of constant growth as they stray from the cylinder body, is the reason providing the representation of the solution for the radiation problem in the exterior domain along with the General Representation Theorem [72]. The field is axisymmetric and therefore all terms depending trigonometrically on the azimuthal angle are nullified, except the first one:

$$\Phi_3^{(e)}\left(r, x_3\right) = a_0 H_0^{(1)}\left(k_0 r\right) Z_0^{(e)}\left(x_3\right) + \sum_{n=1}^{\infty} a_n K_0\left(k_n r\right) Z_n^{(e)}\left(x_3\right)$$
$$\text{for} \quad r \geq a \ , \ -h < x_3 < -T \tag{2.74}$$

where $H_0^{(1)}$, K_0 and I_0 correspond to the Hankel and Bessel functions respectively, and

$$Z_0^{(e)}\left(x_3\right) = \cosh\left[k_0\left(x_3+h\right)\right] / N_0^{1/2} \quad \text{and} \quad Z_n^{(e)}\left(x_3\right) = \cos\left[k_n\left(x_3+h\right)\right] / N_n^{1/2}, \quad n=1,2\ldots \tag{2.75}$$

$$N_0 = \frac{1}{2}\left(1 + \frac{\sinh k_0 h}{2k_0 h}\right) \quad \text{and} \quad N_n = \frac{1}{2}\left(1 + \frac{\sinh k_n h}{2k_n h}\right), \quad n = 1, 2, ... \tag{2.76}$$

and k_0, k_n, n=1,2,… are the local wavenumber, deriving from the Dispersion Relation:

$$\mu h = k_0 h \tanh(k_0 h) \quad \text{and} \quad \mu h = -k_n h \tanh(k_n h), \quad n = 1, 2 \ldots \tag{2.77}$$

where $\mu = \omega^2 / g$ is the frequency parameter. In the above formulation the coefficients $\{\alpha_n, n=0,1,2,\ldots\}$ are the only unknowns.

Interior Domain Problem

For the subdomain D_i beneath the cylinder the following equations and BCs are satisfied:

Laplace Equation: $$\Delta\Phi_3 \equiv \frac{1}{r} \cdot \frac{\partial}{\partial r}\left(r \frac{\partial \Phi_3}{\partial r}\right) + \frac{\partial^2 \Phi}{\partial x_3^2} = 0 \tag{2.78}$$

Axisymmetry: $$\frac{\partial \Phi_3}{\partial \theta} = 0 \tag{2.79}$$

Bottom BC: $$\frac{\partial \Phi_3}{\partial n} = -\Phi_{,x_3} = 0, \quad x_3 = -h \tag{2.80}$$

Cylinder Bottom BC: $$\frac{\partial \Phi}{\partial n} \equiv \Phi_{,x_3} = n_3 = 1, \quad x_3 = -T \tag{2.81}$$

The general solution of the above system of equations can be composed by a solution referring to the homogenous problem of **Eq. (2.80)** and a solution for the inhomogeneous problem of **Eq. (2.81)** as it is presented in **Eq. (2.82)**:

$$\Phi_3(r, x_3) = \Phi_3^{NH}(r, x_3) + \Phi_3^{H}(r, x_3) \tag{2.82}$$

where, an easily obtained solution for the inhomogeneous problem $\Phi_3^{NH}(r, x_3)$ is:

$$\Phi_3^{NH}(r, x_3) = \frac{1}{2d}\left((x_3 + h)^2 - \frac{r^2}{2}\right) \tag{2.83}$$

The general representation of the solution for the homogenous problem $\Phi_3^{H}(r,x_3)$ can be achieved with variables separation in D_i :

$$\Phi_3^{H}(r, x_3) = \sum_{n=0}^{\infty} b_n I_0(\lambda_n r)\cos(\lambda_n x_3), \quad \lambda_n = \frac{n\pi}{d}, \quad n = 0, 1, 2, ... \tag{2.84}$$

Combining those two expression it can be written that:

$$\Phi_3^{(i)}(r,x_3)=\frac{1}{2d}\left((x_3+h)^2-\frac{r^2}{2}\right)+\sum_{n=0}^{\infty}b_n I_0(\lambda_n r)Z_n^{(i)}(\lambda_n x_3),\quad Z_n^{(i)}(x_3)=\cos(\lambda_n x_3) \tag{2.85}$$

For the interior problem the coefficients $\{b_n\,,\,n=0,1,2,\ldots\}$ are the unknowns. At this point, the representation of the solution described above meets all the requirements except two conditions:

(A) The BC at the vertical wetted part of the cylinder:

$$\frac{\partial\Phi}{\partial n}\equiv-\Phi_{,r}^{(e)}=0,\quad \text{for}\quad r=a,\quad -T<x_3<0 \tag{2.86}$$

(B) The matching conditions on the common interface of the domains D_i and D_e, requiring continuity of the potential and its first derivative:

$$\Phi^{(i)}=\Phi^{(e)}\quad\text{and}\quad \Phi_{,r}^{(i)}=\Phi_{,r}^{(e)}\quad\text{for}\quad r=a,\quad -h<x_3<-T \tag{2.87}$$

After applying the CMS, the property of normalized orthogonal basis constitution by the eigenfunctions $\left\{Z_n^{(e)}(x_3),\ n=0,1,2,\ldots\right\}$ and $\left\{Z_n^{(i)}(x_3),\ n=0,1,2,\ldots\right\}$ can be utilized, constituting finally a complete set of functions in the field of squared integrable functions in the intervals $-d<x_3<0$ and $-h<x_3<-T$, respectively. Therefore, the **Eqs (2.86)**, **(2.87)** can be projected to the vertical basis $\left\{Z_k^{(e)}(x_3),\ k=0,1,2,\ldots\right\}$ and $\left\{Z_k^{(i)}(x_3),\ k=0,1,2,\ldots\right\}$for the relevant subdomains:

$$\int_{x_3=-h}^{x_3=-T}\left(\Phi_{,r}^{(i)}\left(r=a,x_3;\{a_n\}\right)-\Phi_{,r}^{(e)}\left(r=a,x_3;\{b_n\}\right)\right)Z_k^{(e)}(x_3)\,dx_3$$
$$-\int_{x_3=-T}^{x_3=0}\Phi_{,r}^{(e)}\left(r=a,x_3;\{b_n\}\right)Z_k^{(e)}(x_3)\,dx_3=0\quad\text{for}\quad k=0,1,2,\ldots \tag{2.88}$$

and,

$$\int_{x_3=-h}^{x_3=-T}\left(\Phi^{(i)}\left(r=a,x_3;\{a_n\}\right)-\Phi^{(e)}\left(r=a,x_3;\{b_n\}\right)\right)Z_k^{(i)}(x_3)\,dx_3=0\quad\text{for}\quad k=0,1,2,\ldots \tag{2.89}$$

The substitution of the representation of potential for the exterior domain D_e (**Eq. (2.74)**) and for the exterior domain D_i (**Eq. (2.85)**) in the **Eqs (2.88)**, **(2.89)** and their analytical integration in respect to x_3 leads to the final solution of the system for the unknown coefficients $\{a_n\,,\,b_n\,,\,n=0,1,2,\ldots\}$ [73]:

$$b_n-\sum_{j=0}^{\infty}e_{nj}b_j=g_n,\quad\text{for}\quad n=0,1,\ldots \tag{2.90}$$

$$e_{nj}=\left[\sum_{k=0}^{\infty}\frac{C_{nk}C_{jk}}{m_k}\left(\frac{R_k}{R_k^{'}}\right)\right]S_j \tag{2.91}$$

$$g_n = \sum_{k=0}^{\infty} \frac{C_{nk}}{m_k} \left(\frac{R_k}{R_k^{'}} \right) A_k^{*} - b_n^{*} \tag{2.92}$$

where m_k are solutions of the equation: $m\tanh(m)=v$, $(m=m_0$ or $m=im_k$ $k=1,2,\ldots)$

$$A_k^{*} = \int_0^d \frac{\partial}{\partial r} \Phi_3^{NH}\left(r, x_3\right) Z_k^{(i)}\left(x_3\right) dx_3 \tag{2.93}$$

$$b_n^{*} = \frac{2}{d} \int_0^d \Phi_3^{NH}\left(r, x_3\right) \cos\left(\lambda_n x_3\right) dx_3 \tag{2.94}$$

$$b_n = \sum_{k=0}^{\infty} R_k C_{nk} A_k + b_n^{*} \quad \text{for} \quad n = 0,1,2,... \tag{2.95}$$

$$A_k = \left(\sum_{n=0}^{\infty} S_n C_{nk} b_n + A_k^{*} \right) / \, m_k R_k^{'} \tag{2.96}$$

$$R_k\left(m_k r\right) = \begin{cases} H_0^{(1)}\left(m_0 r\right) & \text{for} \quad k=0 \\ K_0\left(m_k r\right) & \text{for} \quad k \geq 1 \end{cases} \tag{2.97}$$

where the value-S_n is:

$$S_n = \frac{n\pi}{2} I_0^{'}\left(\lambda_n a\right) / \, I_0\left(\lambda_n a\right) \tag{2.98}$$

The coupling integrals C_{nk} are:

$$C_{nk} = \frac{2}{d} \int_0^d \cos\left(\lambda_n x_3\right) Z_k\left(m_k x_3\right) dx_3 \qquad \begin{matrix} n = 0,1,... \\ k = 0,1,... \end{matrix}$$

$$= \begin{cases} \dfrac{2(-)^n \sinh\left(m_0 d\right) / \left(m_0 d\right)}{\left[1 + \left(\dfrac{\lambda_n}{m_0}\right)^2\right] N_0^{1/2}} & \text{for } k=0 \\[3ex] \dfrac{2\sin\left(m_k d - n\pi\right)}{\left(m_k d - n\pi\right)} - \dfrac{m_k d}{\left(m_k d + n\pi\right)} & \text{for } k = 1,2,... \end{cases} \tag{2.99}$$

The infinite representation series of **Eqs (2.74)**, **(2.85)** are practically converged after first *K*-terms, formulating a system of 2*K*-equations and 2*K*-unknowns, ready for numerical solution. The presented simplified method, which is nothing else but an application of Galerkin's Method [74], is characterized by fast convergence and progressive error minimization as *K* increases.

2.3.1.2 Hydrodynamic coefficients evaluation

Applying for the radiation potential that:

$$\Phi_3\left(r, x_3=-T\right)=\Phi_3^{(i)}\left(r, x_3=-T;\left\{b_n\right\}\right) \tag{2.100}$$

the hydrodynamic coefficients for the cylinder can now be evaluated. Using the indefinite integral property: $\int x\,\mathrm{I}_0(x)dx = x\mathrm{I}_1(x)$ the final non-dimensional expression for the hydrodynamic coefficients is:

$$\hat{A}_{33}-i\hat{B}_{33}=\frac{A_{33}-\left(i/\omega\right)B_{33}}{\rho\pi a^3}=2\left(\frac{1}{4}\frac{d}{a}-\frac{1}{16}\frac{a}{d}+\frac{\Lambda}{a}\right) \tag{2.101}$$

where,

$$\Lambda=\frac{b_0}{2}+\frac{d}{a}\sum_{n=1}^{\infty}\left(-1\right)^2 b_n\frac{I_1\left(\lambda_n a\right)}{n\pi}, \quad n=1,2,... \tag{2.102}$$

The present method is able to treat problems and estimate the response in various water depth conditions. In the following **Figs 62-66** the added mass and damping coefficients are calculated and plotted in regard to the non-dimensional wavenumber $k\,a=2\pi\alpha/\lambda$ or to the non-dimensional angular frequency $\omega\sqrt{\alpha/g}$ for a reference case of a cylinder $(\alpha/h=1/3.5,\ T/\alpha=3/2)$, which is also used in the forthcoming study, while a complete investigation of these coefficients can be found in [68,69]. Another type of normalization is also applied in regard to the cylinder mass-M, which is one of great importance design variable, totally related with the hydrodynamic behavior of the body. These coefficients are evaluated in the following figures for the reference case (**Fig. 64**) and for various ratios of bottom clearance-d over depth-h (**Figs 65**, **66**).

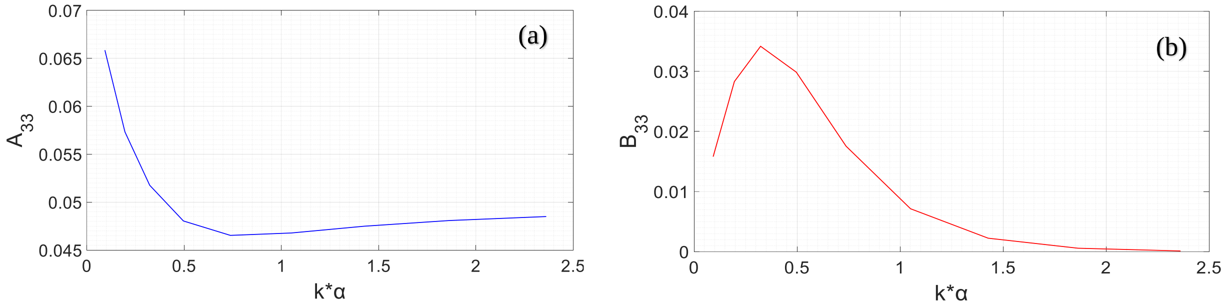

Figure 62: Hydrodynamic coefficients for a cylinder (α/h=1/3.5, T/α=3/2, d/h=4/7): (a) A_{33}-added mass, (b) B_{33}-damping

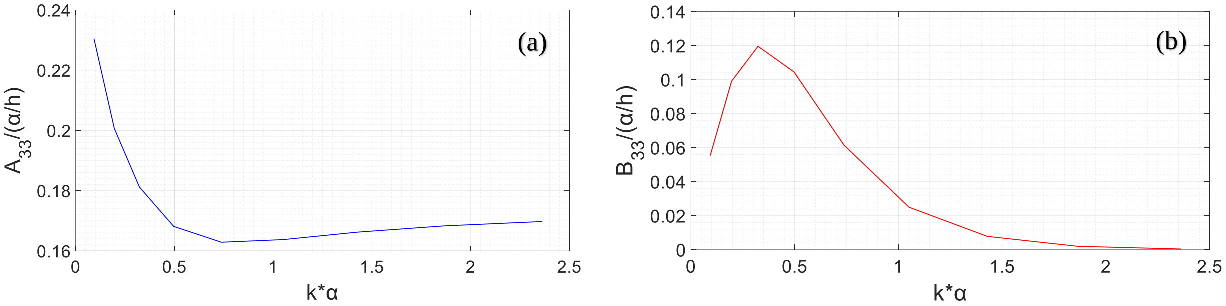

Figure 63: Non-dimensional hydrodynamic coefficients for a cylinder (α/h=1/3.5, T/α=3/2, d/h=4/7): (a) $A_{33}/(\alpha/h)$-added mass, (b) $B_{33}/(\alpha/h)$-damping

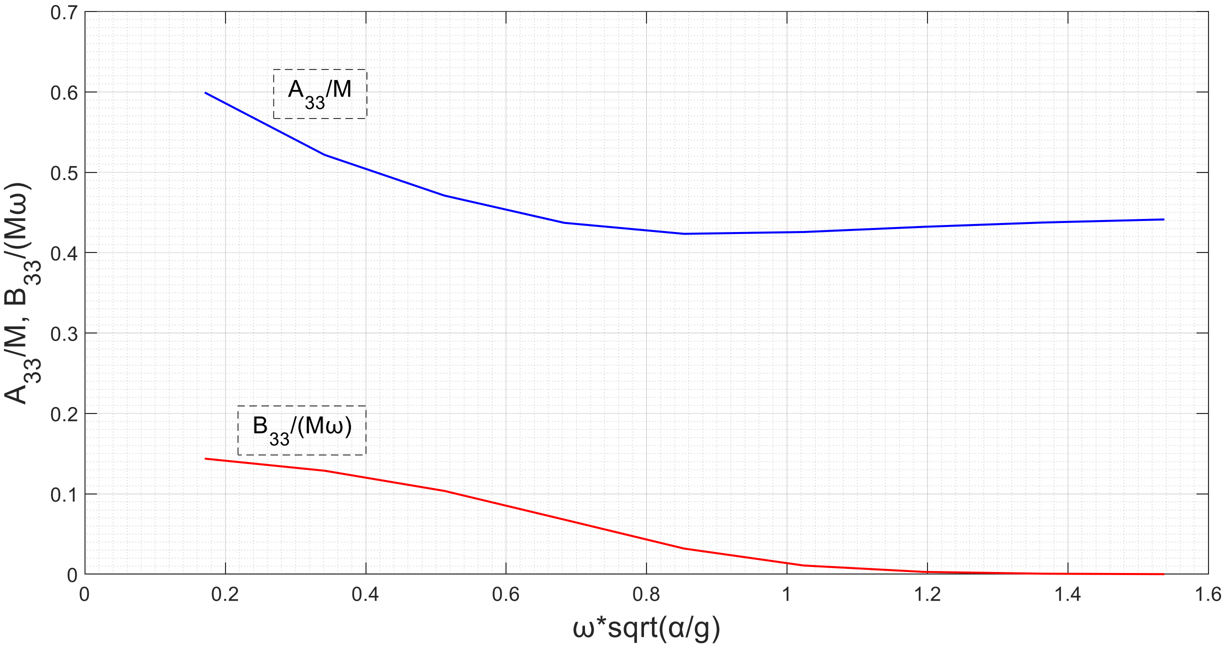

Figure 64: Non-dimensional hydrodynamic coefficients A_{33}/M-added mass $B_{33}/M\omega$-damping for a cylinder (α/h=1/3.5, T/α=3/2, d/h=4/7)

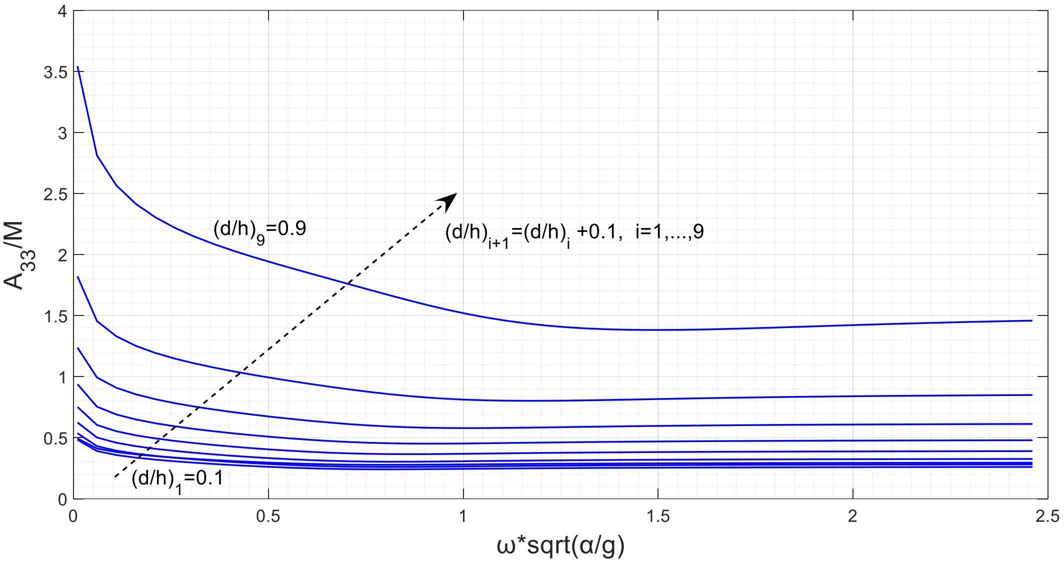

Figure 65: Non-dimensional hydrodynamic coefficient A_{33}/M-added mass for a cylinder (α/h=1/3.5) and for various progressive d/h ratios

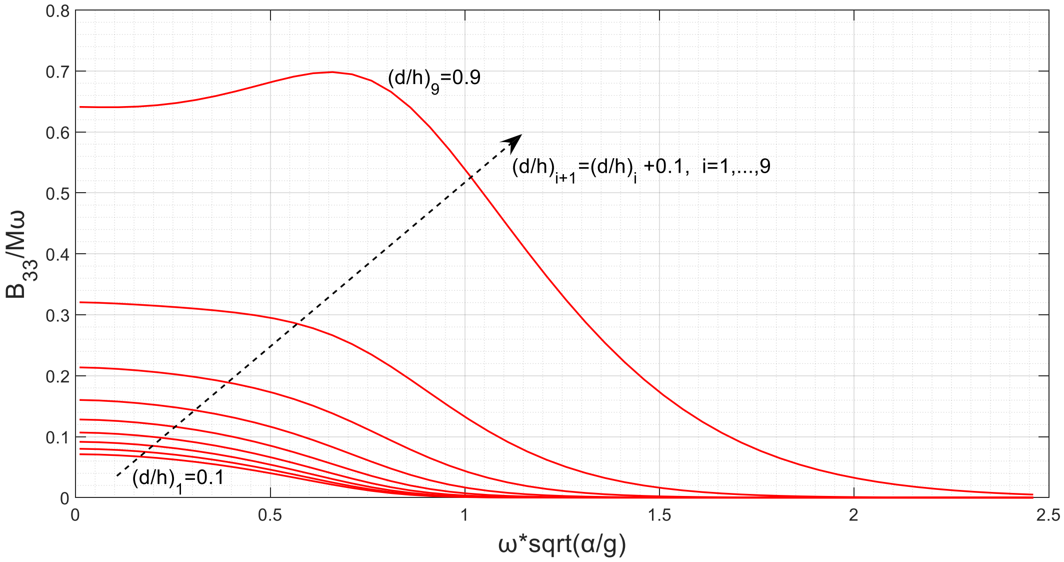

Figure 66: Non-dimensional hydrodynamic coefficient $B_{33}/M\omega$-damping for a cylinder (α/h=1/3.5) and for various progressive d/h ratios

2.3.1.3 Froude-Krylov forces evaluation

If the **Eq. (2.71)** is substituted in **Eq. (2.72)**, under the consideration of the analytic expression for the exp($-ikx_1$):

$$\exp\left(-ikx_1\right)=\sum_{m=0}^{\infty} e_m\left(-i\right)^m J_m\left(k_0 r\right)\cos m\theta \tag{2.103}$$

with e_m=1 for m=1 and e_m=2 for m=2,3,…, then it can be obtained that:

$$X_{03}=\rho\omega^2 A\frac{g}{\omega^2}\cdot\frac{\cosh k_0 d}{\cosh k_0 h}\int_{\theta=0}^{2\pi} d\theta \int_{r=0}^{r=a} r\sum_{m=0}^{\infty} e_m\left(-i\right)^m J_m\left(k_0 r\right)\cos m\theta \, dr \tag{2.104}$$

where J_m corresponds to the real part of the Hankel-H_m. From the terms appearing in the sum of **Eq. (2.104)**, due to the integration of θ-angle, only the m=0 term has non-zero contribution:

$$X_{03} = 2\pi\rho g A \frac{\cosh k_0 d}{\cosh k_0 h} \int_{r=0}^{r=a} r\, J_0\left(k_0 r\right) dr = 2\pi\rho g A \frac{\cosh k_0 d}{\cosh k_0 h} \frac{k_0 a}{k_0^2} J_1\left(k_0 a\right) \tag{2.105}$$

where obviously: $\int x\, \mathrm{J}_0(x)dx = x\mathrm{J}_1(x)$, and in non-dimensional form is:

$$\widehat{X}_{03} = \frac{X_{03}}{\rho g \pi a^2 A} = \frac{2}{k_0 a} \frac{\cosh k_0 d}{\cosh k_0 h} J_1\left(k_0 a\right) \tag{2.106}$$

According to the above equation for very slow motion (ω, $k_0 a \to 0$), as is naturally expected, the Diffraction forces are negligible and so the FK-forces tend to the hydrostatic added force with wave elevation $\widehat{X}_{03} \to 1$. On the opposite case, when (ω, $k_0 a \to \infty$) the FK-forces and the Total-forces tend to zero. The last behavior can be explained by the fact that whenever the frequency increases the wavelength tends to zero and the pressure-induced forces by the big number of wavelengths on the cylinder bottom are mutually reversed. Furthermore, it can be concluded that FK-forces for the vertical oscillation of a cylinder present zero phase difference from the incident wave's free surface elevation at the center r=0 of the cylinder for every frequency and this is a physical consequence of the axisymmetric oscillating body, while the Total-forces present non-zero phase difference, being equal to zero for low frequencies and showing asymptotic behavior: $\arg\{X_3\} \to ka - \pi/4$ for high frequencies. A typical example is plotted in the following **Figs 67**, **68** for a cylinder (a/h=0.11667, d/h=0.79), compliant to the above predictions of asymptotic natural behavior.

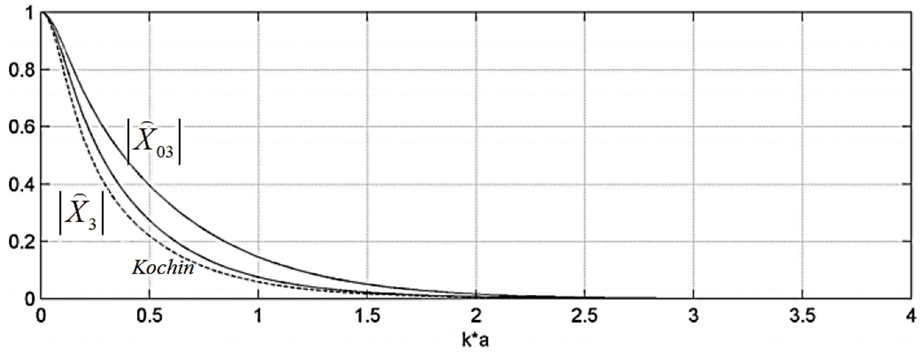

Figure 67: Normalized Total forces (FK+Diffr) on a cylinder (a/h=0.11667, d/h=0.79) [75]

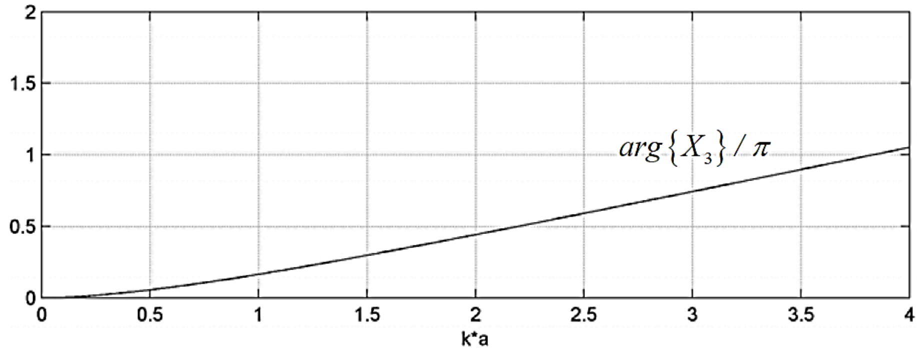

Figure 68: Phase of Total forces (FK+Diffr) on a cylinder (a/h=0.11667, d/h=0.79) [75]

2.3.1.4 Total hydrodynamic forces evaluation

The Total forces, acting on the body, are the summation of FK and Diffraction forces:

$$X_3(\omega) = X_{03}(\omega) + X_{d3}(\omega) \tag{2.107}$$

And can be evaluated by integrating the incident wave and radiation potential on the cylinder's collateral surface ∂D_R^* for $R \to \infty$:

$$X_3 = -\rho\omega^2 A \iint_{\partial D_R^*} \left(\Phi_0 \frac{\partial \Phi_3}{\partial R} - \Phi_3 \frac{\partial \Phi_0}{\partial R} \right) dS_B = -\rho\omega^2 A \int_{x_3=-h}^{x_3=0} dx_3 \int_{\theta=0}^{\theta=2\pi} d\theta\, R\mathrm{E}(R,\theta,x_3) \tag{2.108}$$

where: $E(r=R,\theta,x_3) = \left(\Phi_0 \frac{\partial \Phi_3}{\partial R} - \Phi_3 \frac{\partial \Phi_0}{\partial R} \right)_{\partial D_R^*}$ and the incident wave potential can be written as:

$$\Phi_0(r=R,\theta,x_3) = \frac{g}{\omega^2} \frac{\cosh\left[k_0(x_3+h)\right]}{\cosh k_0 h} \sum_{m=0}^{\infty} e_m (-i)^m J_m(k_0 R)\cos m\theta \tag{2.109}$$

Stepping on the substitution of radiation potential $\Phi_3^{(e)}(r,x_3)$ in the exterior domain D_e and keeping in mind that:

- The functions $K_0(k_n r)$ are exponentially decaying far from the source and thus can $K_0(k_n r) \to 0$ for $R \to \infty$.
- The m-terms which include $\cos(m\theta)$, $m = 1, 2, 3\ldots$ are nullified during the θ-integration.

the expression of the Total hydrodynamic forces is:

$$X_3 = \int_{x_3=-h}^{x_3=0} \frac{\cosh^2\left[k_0(x_3+h)\right]}{N_0^{1/2}\cosh k_0 h} dx_3 \int_{\theta=0}^{\theta=2\pi} r d\theta \left(J_0(k_0 R) \frac{\partial H_0^{(2)}(k_0 R)}{\partial R} - H_0^{(2)}(k_0 R) \frac{\partial J_0(k_0 R)}{\partial R} \right) \tag{2.110}$$

The x_3-integral in the above equation is calculated analytically:

$$\int_{x_3=-h}^{x_3=0} \frac{\cosh^2\left[k_0(x_3+h)\right]}{N_0^{1/2}\cosh k_0 h} dx_3 = \frac{hN_0^{1/2}}{\cosh k_0 h} \tag{2.111}$$

For the r-integration, the expression inside the bracket can be simplified, using the Wronski-determinant of the functions $J_0(k_0R)$ and $Y_0(k_0R)$ of the real-J_0 and the imaginary-Y_0 part of the Hankel-H_0, it is obtained that:

$$jk_0\left(Y_0(k_0R)J_1(k_0R) - J_0(k_0R)Y_1(k_0R)\right) = \frac{2i}{\pi R} \tag{2.112}$$

After making all the above evaluations and their substitution in **Eq. (2.110)**, the final expression for the normalized Total hydrodynamic forces is:

$$\widehat{X}_3 = \frac{X_3}{\rho g \pi a^2 A} = \frac{4i}{\pi} \frac{a_0}{(a/h)^2} \frac{N_0^{1/2}}{\cosh k_0 h} \tag{2.113}$$

where a_0 is the first frequency-depended coefficient in series of $\Phi_3^{(e)}(r,x_3)$ (**Eq. (2.74)**) and the divider $\rho g\pi\alpha^2 A$ corresponds to the added hydrostatic forces induced by the incident wave of A-amplitude.

Additionally, it is referred that the amplitude of Total hydrodynamic forces can be alternatively calculated by the Kochin function, which is also connected with the damping coefficient B_{33}:

$$|H_3|^2 = \frac{2k_0 B_{33}}{\rho\omega D(k_0 h)} \tag{2.114}$$

and due to axisymmetry, the Kochin function can be exploited regardless the azimuth θ-angle, resulting in the following expression:

$$\left|\widehat{\mathrm{X}}_3\right| = \frac{|\mathrm{X}_3|}{\rho g \pi a^2 A} = \sqrt{\frac{2\left[\tanh(k_0 h) + k_0 h\left(1-\tanh^2(k_0 h)\right)\right] B_{33}}{\pi k_0 a}} \tag{2.115}$$

In **Fig. 67** the Total hydrodynamic forces are also evaluated by the above Kochin-based formulation and they are indicated with the dashed line, showing good approximation, while the error is caused by the usage of only K=5 terms and tends to be eliminated as the K increases.

2.3.1.5 Heave response evaluation

The calculation of the transfer function of heave response in regard to the incident wave amplitude-A, known as Response Amplitude Operator (RAO)-ξ_3, can now be achieved:

$$\frac{\xi_3(\omega)}{A} = RAO_{heave}(\omega) = \frac{1}{A} \frac{X_{03}(\omega) + X_{d3}(\omega)}{\left(-\omega^2\left(M + A_{33}(\omega)\right) + i\omega B_{33}(\omega) + C_{33}\right)} \tag{2.116}$$

with all the participating quantities already evaluated analytically.

The continuation of the evaluation for the example presented in **Figs 67**, **68** is completed here with the following plots (**Figs 69**, **70**). The resonance frequency, where theoretically $\mathrm{RAO}_{heave} \to \infty$ is drawn with dashed line. For low frequencies the cylinder oscillates hydrostatically in phase with the wave and behaves like a floating cork $\left(\xi_3(\omega)/A \to 1,\ \omega \to 0\right)$ while in high frequencies the oscillation is declining towards zero and the phase difference increases continually. These conclusions are naturally expected, within the regime of the linear theory of small amplitude and slope waves.

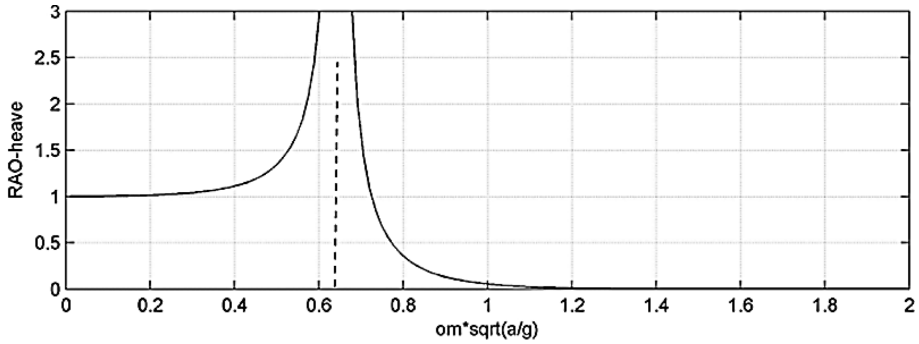

Figure 69: Heave RAO for a cylinder (*a/h*=0.11667, *d/h*=0.79) [75]

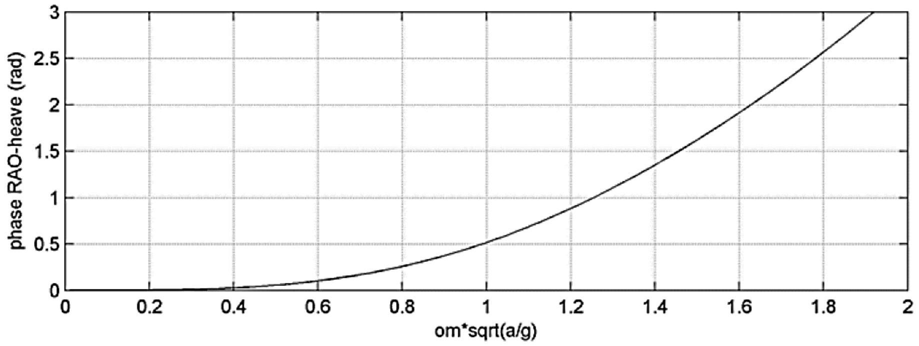

Figure 70: Phase RAO for a cylinder (*a/h*=0.11667, *d/h*=0.79) [75]

2.3.2 BEM-3D treatment

In this section a BEM will be set up to treat the diffraction-$\Phi_D(x,z)$ and radiation-$\Phi_k(x,z)$ potential problems of a heaving cylinder now in a 3D domain, which were examined previously analytically, under the assumption of constant-depth seabed profile.

The present BEM will be a low-order method with piecewise constant normal-dipole singularity distribution on 4-node quadrilateral elements, which will approximate continuously the various boundaries. The evaluation of potential and velocity field for these quadrilateral panels is presented in **Appendix A**.

The main purpose is to finally formulate a method applicable in 3D problems and validated by comparison with the analytic solution of a heaving cylinder over a flat bottom, which is already described. A crucial aspect of this research is the absorbing layer implementation. In this problem radiation condition cannot be formed by default and further numerical treatment is needed for its appliance. The Perfectly Matched Layer (PML) technique is one of these techniques and now it is time to be implemented, processed and optimized.

2.3.2.1 BEM-PML 3D implementation

Based on the **Fig. 71**, the diffraction and radiation potentials have to be evaluated on the wetted surface of the cylinder-∂D_c, on the flat-bottom-∂D_{Π} and on the free surface-∂D_F.

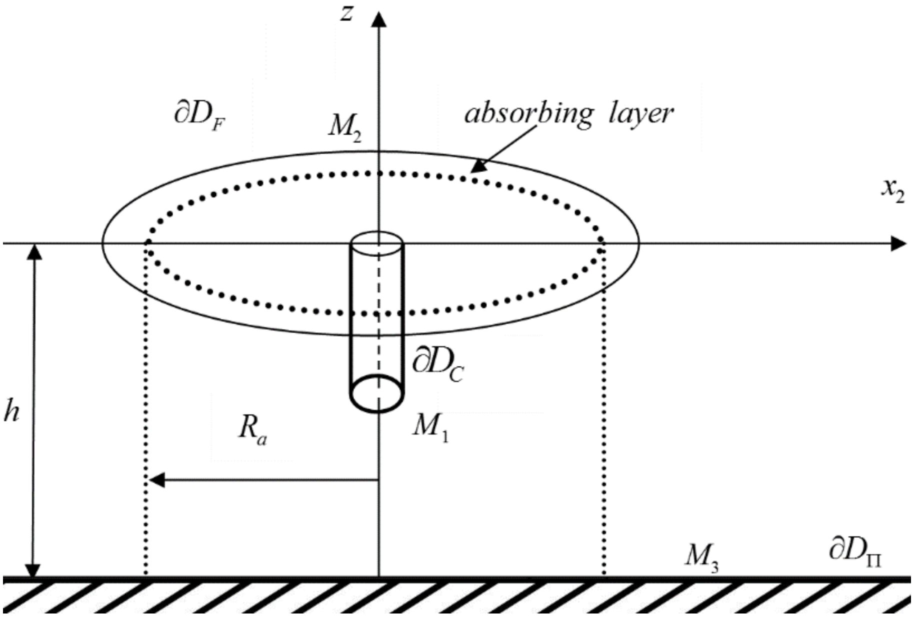

Figure 71: 3D-Computational domain of a heaving cylinder over a flat bottom

For this latter BEM, the BC on the free surface will be modified as to include the satisfaction of the radiation condition through the effect of the PML, as follows:

$$\frac{\partial \Phi}{\partial n} - \mu(\omega)\Phi = 0, \quad r \in \partial D_F \tag{2.117}$$

where now the expression for the frequency parameter-μ is extended in:

$$\mu(\omega) = \begin{cases} \dfrac{\omega^2}{g}, & R = \sqrt{x_1^2 + x_2^2} < R_a \\ \dfrac{\omega^2}{g}\left(1 + i\tilde{c}\dfrac{(R - R_a)^n}{\lambda^n}\right)^2, & R = \sqrt{x_1^2 + x_2^2} \geq R_a \end{cases} \tag{2.118}$$

in order to include the activation of the absorbing layer at radial distances larger than the activation length-R_α. In other words, R_α denotes the radius where the PML is initially activated and starts to filter negatively the outgoing waves, applying the physical radiation property of the deadening behavior of a straying signal far from its source.

As evaluated in **Appendix A**, the induced potential and velocities by a piecewise constant singularity distribution on 2-node boundary elements is approximately:

$$\varphi(r) = \sum_p F_p \Phi_p(r), \quad \nabla\varphi(r) = \sum_p F_p U_p(r) \tag{2.119}$$

where the summation refers to all the elements in every sub-boundary and $\Phi_p(r)$, $U_p(r)$ are respectively the induced potential and induced velocity from the p^{th} element with strength F_p to a field point-r.

The BC for the bottom is, as known $\partial\Phi/\partial n = 0$, $r \in \partial D_\Pi$ and it can be expressed also as:

$$\frac{F_p}{2} + \sum_{m=1}^{M} F_p\left(n_p U_{pm}\right) = 0, \quad p = \sum_{i=1}^{2} M_i + 1, \ \sum_{i=1}^{3} M_i \tag{2.120}$$

and the BCs on the body can be expressed discretely as:

$$\sum_{m=1}^{M} F_p\left(n_p U_{pm}\right) = n_{d,p} \text{ (diffraction) or } n_{l,p} \ (l-\text{radiation problem}), \quad p = 1, M_1 \tag{2.121}$$

where for the diffraction problem:

$$n_d = -\Phi_{0,1}n_1 - \Phi_{0,2}n_2 - \Phi_{0,3}n_3 \tag{2.122}$$

or for radiation problems (l=1,2,…,6):

$$n_l = \begin{cases} n_1 = n_x, & \text{Surge} \\ n_2 = n_y, & \text{Sway} \\ n_3 = n_z, & \text{Heave} \\ n_4 = zn_2 - yn_3, & \text{Roll} \\ n_5 = xn_3 - zn_1, & \text{Pitch} \\ n_6 = xn_2 - yn_1, & \text{Yaw} \end{cases} \tag{2.123}$$

Finally, the free surface BC is:

$$\frac{F_p}{2} + \sum_{p=1}^{P} F_p\left(n_p U_{pm} - \mu\Phi_{pm}\right) = 0, \quad p = M_1 + 1, \ \sum_{i=1}^{2} M_i \tag{2.124}$$

2.3.2.2 Mesh generation

In computational hydrodynamic problems mesh generation is one parameter of great importance. With the correct and consistent discretization of the boundaries, the numerical solution can converge and approximate the analytical solutions, whenever they are feasible. In the present problem, every boundary, namely the body surface, the free surface and the seabottom, is discretized with a cylindrical distribution of panels, which, along with continuous junction of these various sub-meshes and the quadrilateral elements, ensures global continuity of the boundary. The cylindrical arrangement is ideal for the representation of the radiating behavior of the solution in diffraction and multi scattering problems. A typical representation of the meshes follows in the next **Fig. 72**.

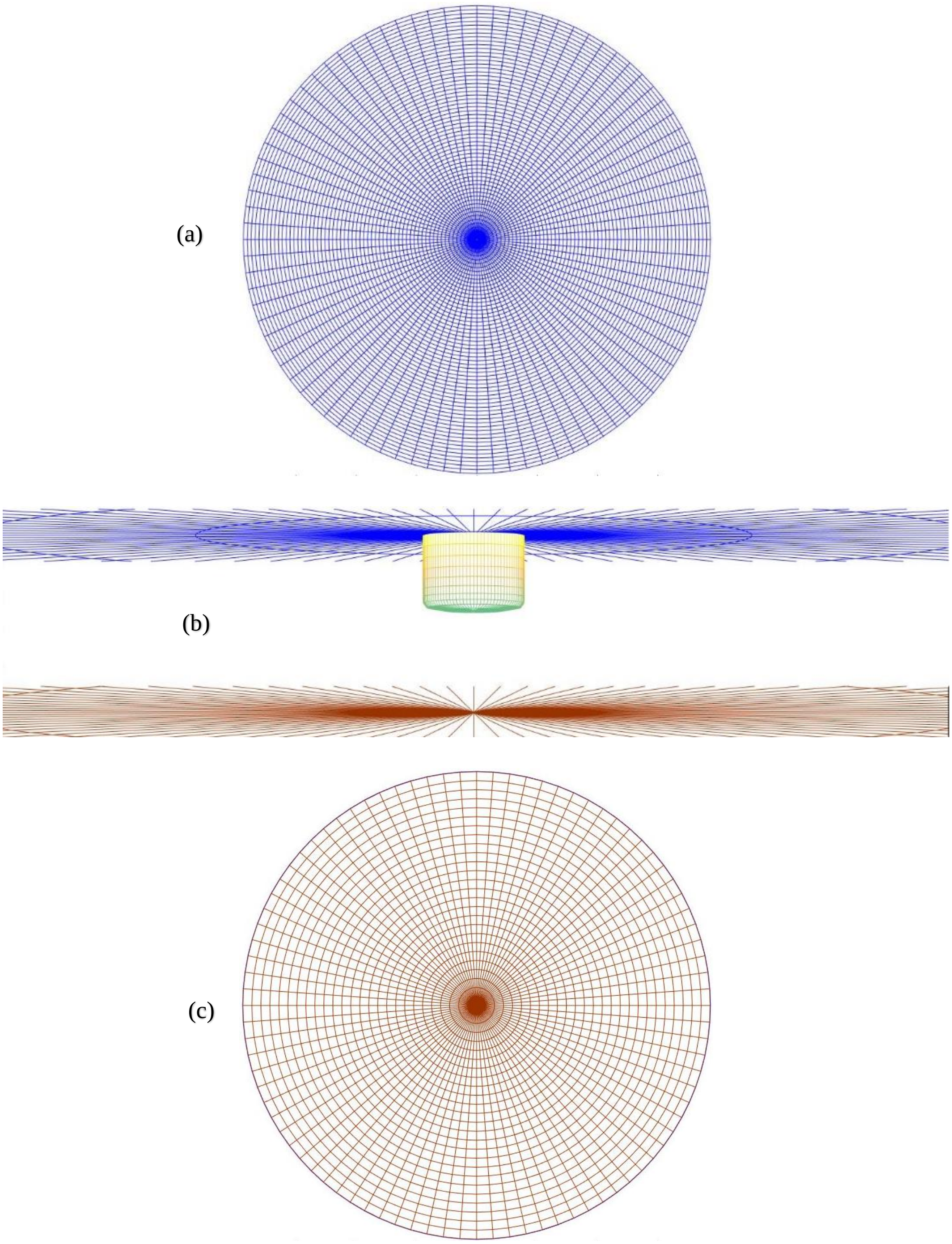

Figure 72: Computational cylindrical meshes: (a) Free Surface, (b) 3D side view near the cylinder, (c) Bottom

However, the researcher has to consider that a very fine mesh is not always ideal for every problem and in many cases convergences differs from analytical solution’s approximation. A mesh-element size consistency among the different sub-boundaries is the key to achieve reliable solutions. Choosing a very fine mesh on the body surface requires exponentially larger amount of same sized elements on the free surface and on the bottom and, due to the dimension of the problem, is unavoidably bounded by the computational cost. Further details on this and its impact, specifically in this problem, will follow in a subsequent paragraph.

2.3.2.3 PML optimization

In many areas of interest for a scientist and an engineer, radiation conditions, which expresses the weakening behavior of the outgoing waves at the far field, and which formulates the final solution, cannot be formed a priori, demanding smart techniques and further tuning of them. The inheritance of the absorbing layer technique from a specific length of activation and with defined characteristics, based on the Perfectly Matched Layer (PML) model, is applied in this specific study [76,77]. In this approach, the deadening of the waves is induced by a hypothetic part of frequency (**Eqs (2.117)**, **(2.118)**), operating as a damping filter for the waves without significant reflections. The evaluation and optimization of the PML is a multi-parametric problem, based mainly on five crucial parameters. The main objective function of the PML's optimization procedure is the minimization of any influence of the PML in the region before its appliance, due to reflections, ensuring at the same time the progressive nullification of the wave field in the region after its activation length. Its effectiveness can be tested by comparing the numerical and the analytical solution in case of a cylindrical body over a steady depth seabed. The requirement for PML efficiency is quantified with the usage of the relative error based on L_2 norm for the FS potential.

The main PML tuning parameters, discussed above, are:

- Dimensionless frequency $\omega\sqrt{h/g}$
- Coefficient $\hat{c}=c\lambda^n/\omega$
- The activation length R/λ
- The exponent n
- The number of panels per wave length (N/λ)

For the numerical evaluation is used as reference case a cylinder of α/h=1/3.5, T/α=3/2 and d/h=4/7. The meshes, with the first number corresponding to spatial and the second number corresponding to azimuthal discretization, are: 10x88 on Cylinder Body-∂D_c, (4*N/λ)x88 on the free surface-∂D_F for 4-wavelengths spatial distribution and 26x88 on the bottom-∂D_Π. Logically, the azimuthal discretization must be the same for all boundaries for reasons of consistency. Targeting to the minimization of the relative error based on L_2 norm, 64 different PMLs, corresponding to different sets of these parameters, are put under investigation resulting in the optimum set of **Table 5**, where the frequency takes values corresponding to all depth conditions, from deep to shallow. As a result the mesh resolution varies from 6688 to 10208.

Table 5
Optimum PML parameters

$\omega < 2$	$\hat{c}$ =1	R/λ=2	N/λ=15	n=5
$2 \leq \omega < 7$	$\hat{c}$ =1	R/λ =3	N/λ=20	n=3
$7 \leq \omega < 8$	$\hat{c}$ =1	R/λ =3	N/λ=15	n=3
$8 \leq \omega \leq 9$	$\hat{c}$ =1	R/λ =3	N/λ=10	n=3

2.3.2.4 BEM-PML 3D validation

For the PML-optimum set of **Table 5**, numerical results for the potential are plotted in comparison with the relevant analytical results in the subsequent **Fig. 73**. It can be obtained that as the frequency approaches very low or very high values the approximation presents slightly bigger errors, however if we consider a WEC operating in this location, which its performance estimation is the final purpose of this study, the efficient frequency bandwidth is among these extreme limits, where good approximation is achieved as the **Fig. 73** proves. Finally, the corresponding Froude-Krylov and Total forces, as well as the hydrodynamic coefficients, calculated both from the analytical and the numerical method are plotted in **Figs 74**, **75**.

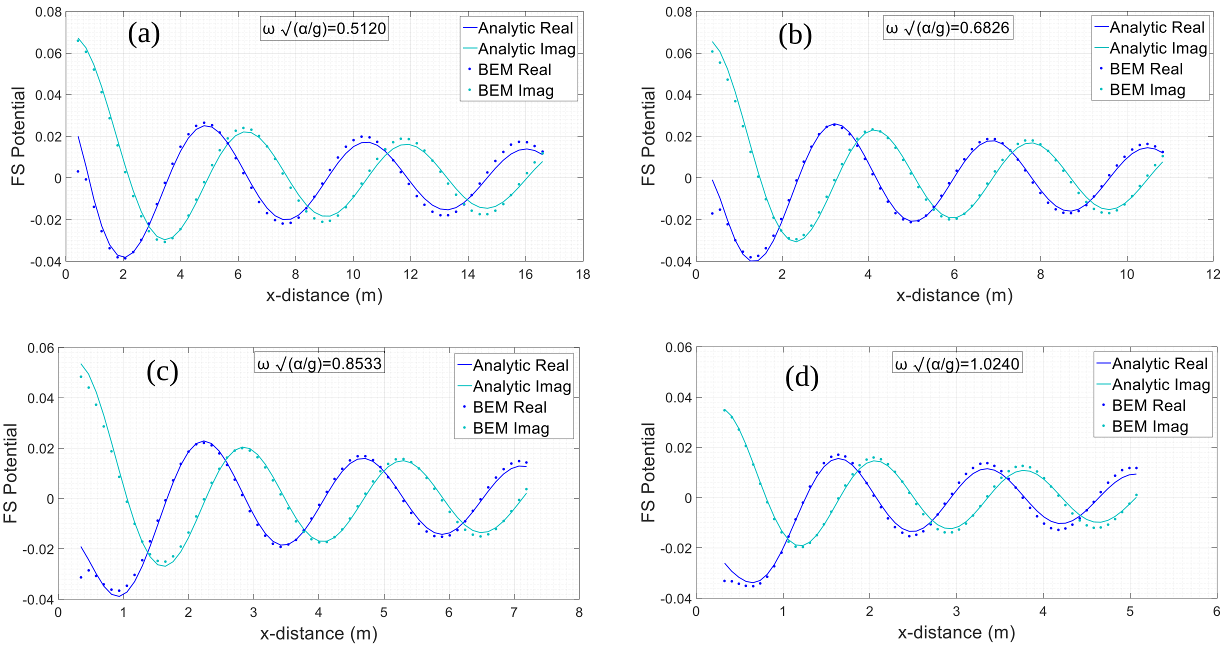

Figure 73: BEM approximation of the analytic solution for the free surface potential for various frequencies in case of cylindrical body (*α/h*=1/3.5, *T/α*=3/2, *d/h*=4/7)

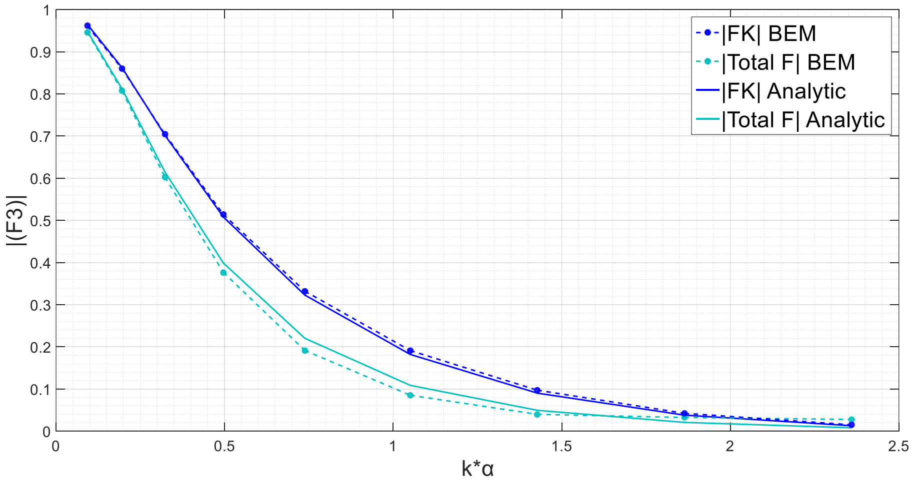

Figure 74: BEM approximation of the analytic solution for the normalized hydrodynamic forces in case of cylindrical body (*α/h*=1/3.5, *T/α*=3/2, *d/h*=4/7)

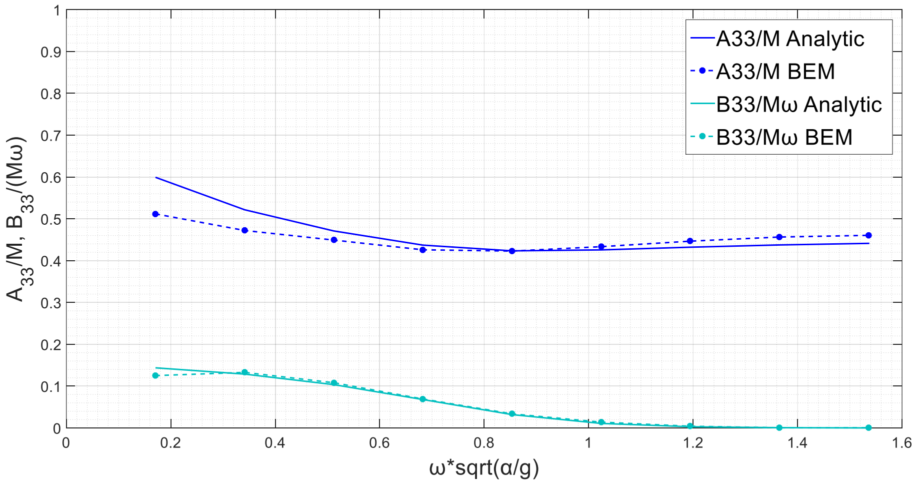

Figure 75: BEM approximation of the analytic solution for the hydrodynamic coefficients in case of cylindrical body (α/h=1/3.5, T/α=3/2, d/h=4/7)

Remembering now, that very fine partial mesh resolution, for example only on WEC surface, is not recommended if it is not vindicated with analogous increase of mesh resolution in all boundaries, which binds most of the memory and demands added computational cost, because in any other case discontinuities and errors may arise in the matching positions of the boundaries. For example, the evaluation of the hydrodynamic coefficients for two different meshes on the cylinder body, specifically 10x88 and 20x88, keeping the meshes identical on the free surface and on the bottom, approximates differently the analytical expressions, as shown in **Fig. 76**, with the finer mesh on the body showing worse approximation indeed.

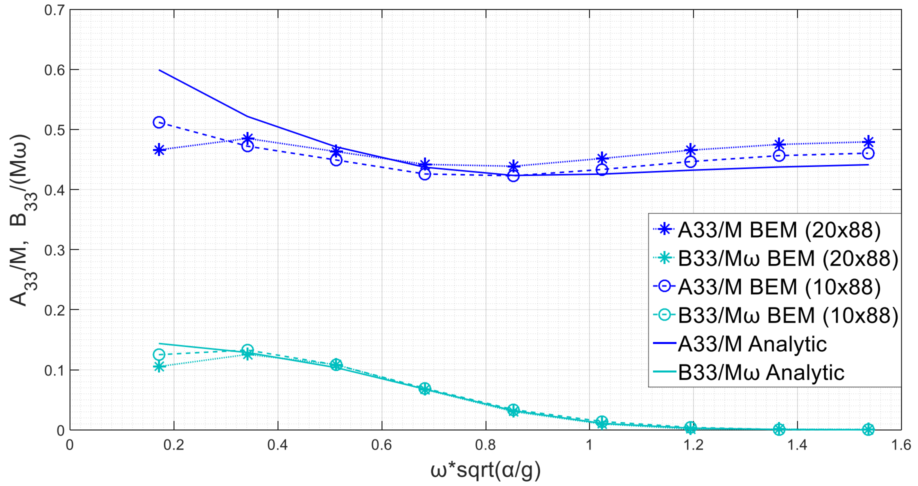

Figure 76: BEM approximation of the analytic solution for the hydrodynamic coefficients in case of cylindrical body (α/h=1/3.5, T/α=3/2, d/h=4/7) for two different meshes on the cylinder's surface.

2.3.2.5 BEM – Heave response evaluation

For the evaluation of heave RAO, phase RAO as well as for the power output of a typical WEC of this geometry, estimations about the PTO are upon consideration. For this reason is assumed a typical PTO damping coefficient B_s with indicative values considered as 5,10 and 20 times a mean value of hydrodynamic damping b_m over frequency, which is estimated as $2\pi b_m/m\omega_R$ =0.12, where the resonance frequency is $\omega_R\sqrt{a/g}$=0.7:

$$B_{PTO}=B_s=[5,10,20]\quad b_m=\frac{0.084}{2\pi\sqrt{\alpha/g}} \qquad (2.125)$$

Very low values of PTO damping ($C_{PTO} \ll 1$) may lead to unconstrained resonance effect for the device and higher values of RAOs, however a very "soft" PTO has to comply both with industrial feasibility and power performance. The averaged power output from the combination of *k*-oscillation modes with *m*-parameters each (**Eq. (2.126)**) is normalized with respect to the incident wave power, defined as $P/(0.25\rho C_g H^2 \alpha)$, for $\eta_{eff}=1$.

$$P(N;\omega,\theta)=\frac{1}{2}\omega^2\left|\sum_{k=1}^{N}\eta_{eff}^{m}B_s^{m}\left(\xi_k\right)^2\right| \qquad (2.126)$$

The Heave-RAO is logically decreases as the PTO damping increases. Starting from the unit, where the WEC follows the wave in low frequencies, hitting a peak in the resonance frequency and then asymptotically approaching to zero.

For the phase, it should be noticed that is converges to π-value for high frequencies and to zero for low frequencies, where RAO equals to unit and therefore the WEC behaves like a cork. In the resonance frequency the phase is $\pi/2$.

The maximization of power output seems to occur at the resonance frequency and is more intense for the lower values of PTO damping. In addition, higher values of PTO-damping cause decrease of peak values of RAO and of powerlevels however, with wider frequency spreads of efficient energy capture by the device (**Fig. 77**).

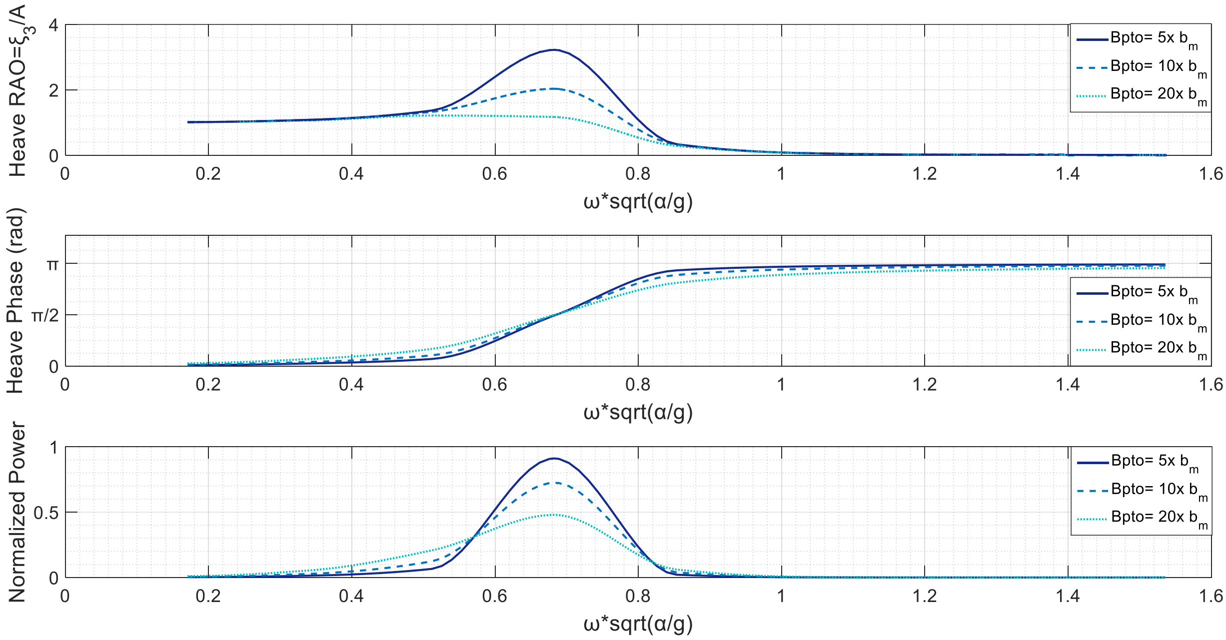

Figure 77: Heave RAO, Phase RAO and Normalized Power Output for Cylindrical WEC (*α/h*=1/3.5, *T/α*=3/2, *d/h*=4/7)

3

Heaving cylinder and varying seabed: The BEM-PML model

3.1 Hydrodynamic problem formulation

Considering all the study so far, the main purpose was the development of a numerical method, able to treat more complex, however far more interesting, problems in the field of floating bodies. The proposed method, combining multiple techniques, namely the Boundary Element Method, the Coupled Mode Model and the Perfectly Matched Layer (BEM-CMS-PML), is now fully developed and more importantly step by step validated in 2D and 3D problems by the analytical solution. Therefore, the research will proceed with the implementation of this method in problems where analytic solutions are unfeasible.

One problem of this type, is the interaction of the floating body and a varying seafloor. The problem of the evaluation of its response is studied from the past century [78,79], however modern techniques and far more efficient computational tools are now available to the scientists [56,80]. Floating bodies are essential components of floating structures, and recently are gathering more and more scientific interest through their applications as wave energy harnessers, applications which are constantly evolving and becoming step by step commercialized.

Despite the fact that the pertinent industry is growing fast, most of the researches focus only on body-wave interaction, omitting possible impacts of a varying seabed. These interactions may be critical for the response and power output of a WEC operating over a terrain of non-negative slopes, due to trapping modes and localized disturbances, and therefore this is the aim of the present section through the investigation at this time of body-wave-seabed hydrodynamic coupling [81,82] by implementing the optimized BEM-PML method, as a good compromise between error minimization and low computational cost.

The formulation of the present problem is illustrated in **Fig. 78** for a generally shaped floating body over a seabed with a variable profile:

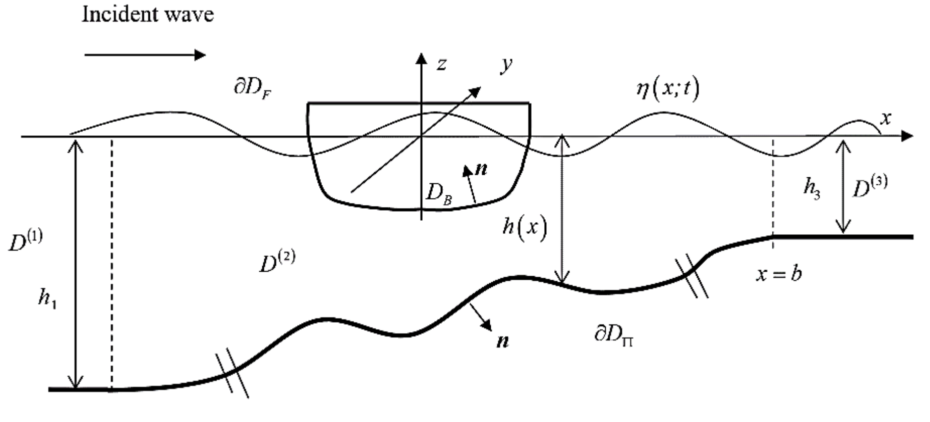

Figure 78: Formulation of the 3D hydrodynamic problem with a variable bathymetry

The first component of this problem has to deal with the evaluation of the propagating incident wave potential over this region, coming from a far constant depth region and with the absence of the floating body.

For reasons of simplicity, and without violation of generality, the bathymetry profile function is considered as a typical transition from a deeper subregion of constant depth-h_3 to a shallower region of constant depth-h_1, while in the middle subregion the $h(x)$ follows an arbitrary variation. The wave potential, with the assumptions of small free surface elevations and wave velocities, can be expressed for an incident wave of amplitude-A and frequency-ω as:

$$\Phi(x,z;t)=\operatorname{Re}\left\{-\frac{igH}{2\omega}\varphi(x,z;\mu)\cdot\exp(-i\omega t)\right\} \tag{3.1}$$

and free surface elevation is:

$$\eta(x;t)=-\frac{1}{g}\frac{\partial\Phi(x,z=0)}{\partial t} \tag{3.2}$$

where $x=(x_1,x_2)$ satisfies the linearized water wave equations. In regard to the hydrodynamic theory for floating bodies [79] the complex potential can be decomposed on eight components, namely the normalized incident propagating wave potential $\varphi_P(x,z)$, without the presence of the body, the diffraction potential $\varphi_D(x,z)$, due to the presence of the rigid motionless body and the total radiation potential $\varphi_R(x,z)$, related with the six degrees of freedom for the body motion:

$$\varphi(x,z)=\varphi_P(x,z)+\varphi_D(x,z)+\frac{2\omega^2}{gH}\varphi_R(x,z) \tag{3.3}$$

where the radiation potential $\varphi_R(x,z)$ can be synthesized as the summation of the six radiation potentials in the non-uniform domain $\varphi_\ell(x,z)$, $l=1,2,\ldots6$, associated with the six l-oscillation modes of amplitude ξ_l:

$$\varphi_R(x,z)=\sum_{\ell=1}^{6}\xi_\ell\varphi_\ell(x,z) \tag{3.4}$$

The BCs, which should be satisfied on the body's wetted surface, are:

$$\partial\varphi_D(x,z)/\partial n=-\partial\varphi_P(x,z)/\partial n \tag{3.5}$$

where $n=(n_1,n_2,n_3)$ denotes the normal vector on the wetted surface of the body with direction outwards the fluid domain, and thence inwards the body, and:

$$\partial\varphi_\ell(x,z)/\partial n=n_\ell \tag{3.6}$$

where n_l is the l-component of the generalized normal vector on the wetted surface of the body ($n_\ell=(r\times n)_{\ell-3}$, $l=4,5,6$) **(Eq. (2.123))**.

For the evaluation of the propagating wave potential $\varphi_P(x,z)$, it will be used the CMS [83], which is described in more detail in **Appendix B**.

Considering now a heaving WEC, only the vertical oscillation ξ_3 is evaluated, which also consists one of the most power intensive modes, and this explains why a very large number of WEC-concepts is taking advantage of the heave-motion of the device. The response then can be formulated as:

$$\xi_3 = \left(A\right)^{-1}\left(X_P + X_D\right) \tag{3.7}$$

where, X_P+X_D are the heaving exciting vertical forces due to propagation and diffraction and can be individually evaluated as functions of the corresponding potentials:

$$X_P = \frac{\rho g H}{2} \iint_{\partial D_B} \varphi_P n_3 \, dS \tag{3.8}$$

$$X_D = \frac{\rho g H}{2} \iint_{\partial D_B} \varphi_D n_3 \, dS \tag{3.9}$$

The hydrodynamic coefficients complex matrix A can now be evaluated as:

$$A = -\omega^2\left(M + a_{33}\right) - i\omega\left(B_S + b_{33}\right) + \left(C_S + c\right) \tag{3.10}$$

where α_{33} and b_{33} are the added mass and damping coefficients of the body, calculated by integrating the relevant heaving radiation potential φ_3 on the submerged part of the WEC:

$$a_{33} - \frac{1}{i\omega} b_{33} = \rho \iint_{\partial D_B} \varphi_3 n_3 \, dS \tag{3.11}$$

The coefficient $c=\rho g A_{WL}$ is the hydrostatic coefficient in heave motion, where A_{WL} is the waterline surface. The coefficients B_s, C_s are characteristics parameters for the PTO system.

The average power output from the WEC, considering only the ξ_3-heave mode and assuming η_{eff} efficiency of the PTO is:

$$P\left(\omega,\theta\right) = \frac{1}{2}\eta_{eff}\,\omega^2 \left|B_S\left(\xi_3\right)^2\right| \tag{3.12}$$

The power output obviously relies on the frequency, the direction and the wave height of the incident wave, as well as on the PTO used in this installation and the natural environment. In general, the operation of the device is characterized by multichromatic wave conditions determined by a directional wave spectrum, which needs to be modelled with spectral analysis.

3.1.1 Propagation problem evaluation

The Coupled Mode Model is an alternative technique to solve wave propagation problems over a varying seabottom, even with steep topography, where analytic solutions cannot be accomplished. The wave potential $\varphi_P(x,z)$ of the propagating filed over a variable bathymetry, with absence of the floating body-scaterrer, can be evaluated by means of a consistent CMS method developed in [83] end extended to 3D regions in [84]. The method is described in detail in **Appendix B**.

Briefly, this model is based on the local-mode representation of the potential:

$$\varphi_P(x,z) = \varphi_{-1}(x) Z_{-1}(z;x) + \sum_{n=0}^{\infty} \varphi_n(x) Z_n(z;x) \tag{3.13}$$

Where the $\varphi_0(x)\, Z_0(z;x)$ refers to the propagating mode of the generalized incident field and the $\varphi_n(x)\, Z_n(z;x)$, $n=1,2,\ldots$ correspond to the evanescent modes of the field. The additional term $\varphi_{-1}(x)\, Z_{-1}(z;x)$ is the sloping-bottom mode, a correction tuning-term ensuring the satisfaction of the Neumann BC at the seabed on every part of its profile, including the non-horizontal parts and the non-mildly sloped parts, and effecting on the fast convergence of the local-mode series. The $Z_{-1}(z;x)$ is the vertical structure of this mode. The mode vanishes in constant-depth subregions. Finally, the Coupled Mode System of the horizontal equations for the amplitudes of the incident propagating wave field over the variable bathymetric terrain takes the following form:

$$\sum_{n=-1} A_{mn}(x) \nabla^2 \varphi_n(x) + B_{mn}(x) \nabla \varphi_n(x) + C_{mn}(x) \varphi_n(x) = 0, \quad m = -1, 0, 1, \ldots. \tag{3.14}$$

where the coefficients A_{mn}, B_{mn}, C_{mn} are defined in terms of the vertical modes $Z_n(z;x)$ and depend on x-variable. Supplemented also by the essential BCs for reflection, transmission and radiation of the wave, the CMS formulation is discussed in **Appendix B** along with characteristic examples.

3.1.2 Diffraction-Radiation problems evaluation

The evaluation for the diffraction and radiation potentials will be based on the already developed and validated 3D BEM method, described in the previous chapter, where the expressions for the total induced potential and velocity from all the 4-node quadrilateral elements allocated on the boundaries are:

$$\varphi(r) = \sum_p F_p \Phi_p(r) \tag{3.15}$$

$$\nabla\varphi(r) = \sum_p F_p U_p(r) \tag{3.16}$$

The optimized BEM-PML method will be implemented in order to treat the diffraction and radiation problems, with the PML’s same formulation and activation length-R_α as in the previous chapter and described in **Table 5**.

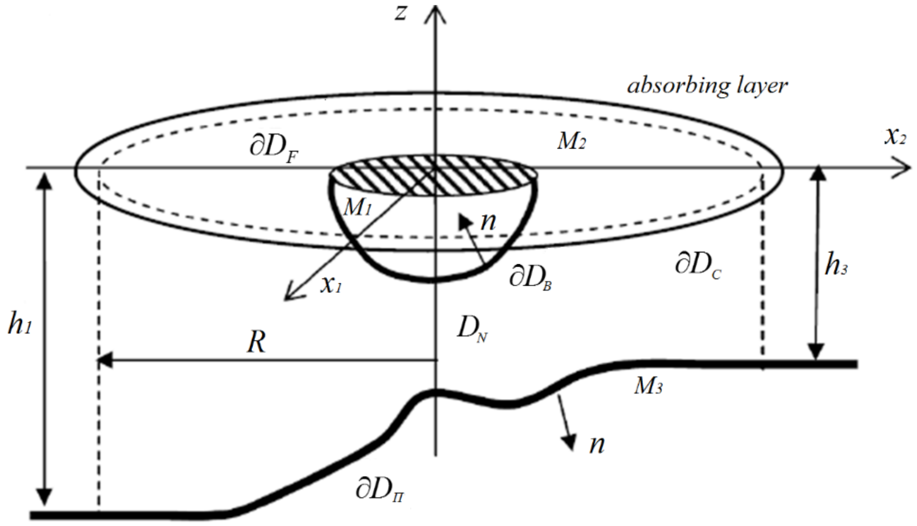

Figure 79: Formulation of the 3D hydrodynamic problem with a variable bathymetry and PML

Therefore, the BC on free surface of **Eq. (3.17)** reformulates again as previously, with the implementation of a hypothetic part of frequency, expressed by the second formula in the bracket of **Eq. (3.18)**:

$$\frac{\partial \Phi}{\partial n} - \mu(\omega)\Phi = 0, \quad r \in \partial D_F \tag{3.17}$$

$$\mu(\omega) = \left\{ \begin{array}{ll} \dfrac{\omega^2}{g}, & R < R_a \\ \dfrac{\omega^2}{g}\left(1 + i\tilde{c}\dfrac{(R-R_a)^n}{\lambda^n}\right)^2, & R \geq R_a \end{array} \right\} \tag{3.18}$$

The discrete solution is achieved with the usage of collocation method, through the satisfaction of BCs at the centroid of each quadrilateral panel, distributed on all boundaries with mesh generation. By treating the self-induced quantities semi-analytically, as it is described in **Appendix A**, the induced potential and velocities from the p^{th}-element at any collocation point can be calculated by numerical quadratures. These BCs, along with the free-surface BC of **Eq. (3.18)**, are:

$$\text{Bottom BC: } \frac{\partial \Phi}{\partial n} = 0, \quad r \in \partial D_\Pi \tag{3.19}$$

$$\text{Body BC: } \frac{\partial \Phi}{\partial n} = n_d \ (\text{diffraction}) \ \text{ or } \ n_l \ (l - \text{radiation problem}), \quad r \in \partial D_B \tag{3.20}$$

It is finally obtained the following linear system for the body's boundary:

$$\sum_{m=1}^{M} F_p\left(n_p U_{pm}\right) = n_{d,p} \text{ (diffraction) or } n_{l,p} \text{ } (l-\text{radiation problem}), \quad p = 1, M_1 \tag{3.21}$$

where for the diffraction problem:

$$n_d = -\Phi_{0,1} n_1 - \Phi_{0,2} n_2 - \Phi_{0,3} n_3 \tag{3.22}$$

and for the radiation problem:

$$n_l = \begin{cases} n_1 = n_x, & \text{Surge} \\ n_2 = n_y, & \text{Sway} \\ n_3 = n_z, & \text{Heave} \\ n_4 = z n_2 - y n_3, & \text{Roll} \\ n_5 = x n_3 - z n_1, & \text{Pitch} \\ n_6 = x n_2 - y n_1, & \text{Yaw} \end{cases} \tag{3.23}$$

The rest discrete BCs (free surface and bottom) are now expressed as:

$$\text{Free Surface BC: } \frac{F_p}{2} + \sum_{p=1}^{P} F_p\left(n_p U_{pm} - \mu \Phi_{pm}\right) = 0, \quad p = M_1 + 1, \sum_{i=1}^{2} M_i \tag{3.24}$$

$$\text{Bottom BC: } \frac{F_p}{2} + \sum_{m=1}^{M} F_p\left(n_p U_{pm}\right) = 0, \quad p = \sum_{i=1}^{2} M_i + 1, \sum_{i=1}^{3} M_i \tag{3.25}$$

3.1.3 Mesh generation

The mesh will be the same as previously and through the sufficient resolution on the bottom with 26x88 elements cylindrically arranged, in a way similar to the body and free-surface meshing, and with consistency in azimuthal discretization, which is equal to 88 elements for all three boundaries, will model reliably the hydrodynamic phenomena and varying seabed effects. This meshing technique also ensures the continuous transition from one boundary to another and therefore global continuity of the geometry. The resolution on the free surface will be again higher, because the interaction with the body is located near the free surface and causes more intense variations of the potential and of the velocities.

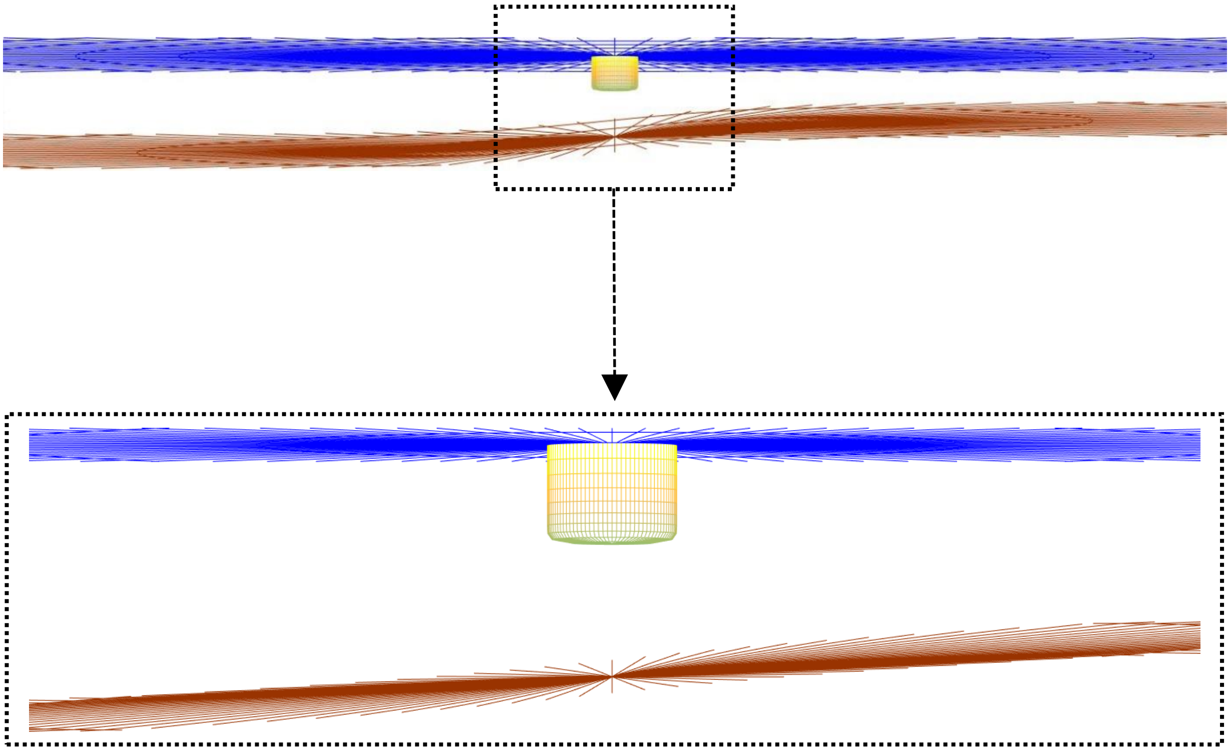

Figure 80: Computational cylindrical meshes: 3D side view far and near the cylinder over a variable monotonic bathymetric variation with constant depths at infinity.

3.2 Numerical results

The formulation of the numerical method has now be completed. The total process of the algorithm is depicted in the flowchart of **Fig. 81**. It is now possible to proceed with numerical examples, following in the next section.

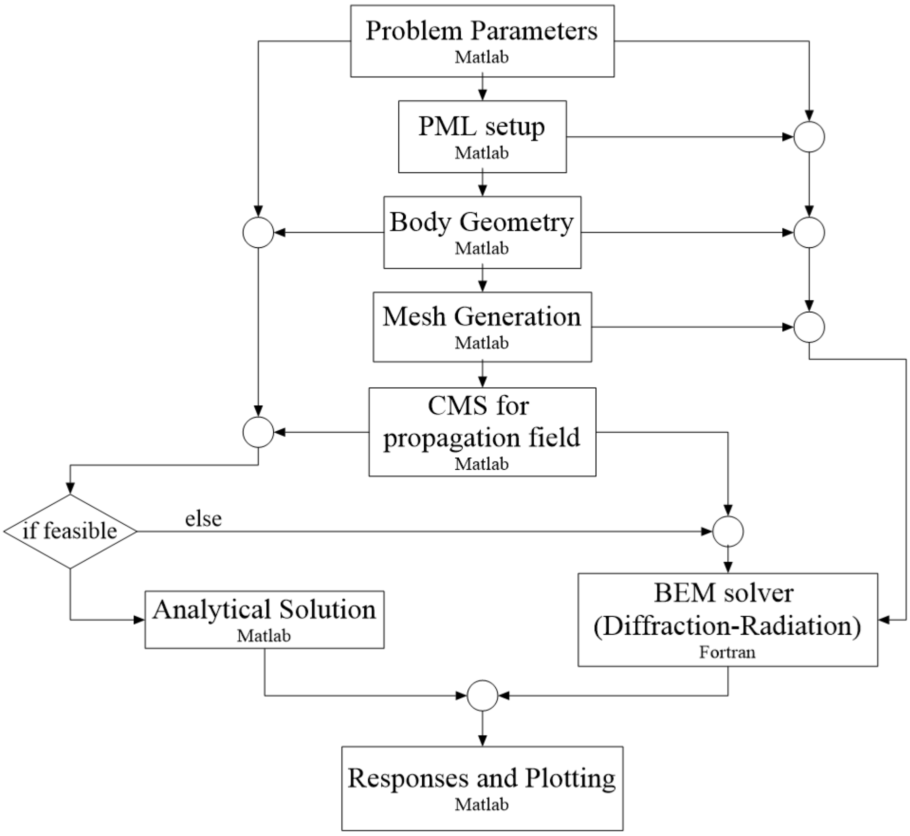

Figure 81: Flowchart of the method for the solution of 3D problems of floating bodies over variable seabed

A reference case for a cylinder over a region of monotonic depth decrease has been evaluated and the results are visualized in the following figures.

The design parameters of the cylinder body are: α/h=1/3.5, T/α=3/2 and d/h=4/7. The non-dimensional frequency is $\omega\sqrt{\alpha/g}$=0.5461. The mesh generation is using 10x88 elements on the body-∂D_B, 80x88 on the free surface-∂D_F and 26x88 on the bottom skin-∂D_Π with a total of 10208 elements. The seabed profile exhibits a simplified monotonic function of the relevant position along x_1-axis:

$$h(x) = h_m - 0.5(h_1 - h_3)\tanh\left(\alpha_{bot}\pi\left(x - x_{mean}\right)\right) \tag{3.26}$$

where the mean depth is: h_m=0.5 (h_1+h_3). The coefficient-α_{bot} defines the bottom slope and for this example is set α_{bot}=0.5, while h_1=3 m and h_2=1 m. The region is characterized by constant depths at infinity. The propagating field is calculated by the CMS with 2nd order finite differences scheme using 201 elements for discretization and keeping only 5 modes, which is enough for numerical convergence. The incident wave angle is set to 0deg. In the following figures are plotted the propagating field using contours, where is obvious the satisfaction of the bottom Neumann BC with the equipotential lines becoming perpendicular to the seabed profile. In these contour plots is included also the illustration of the free surface’s elevation by using the dashed black line. Finally, scatter plot for the diffraction and heave radiation potentials and 3D plots for some indicating of the seven potentials (diffraction potential and 1÷6 for the radiation potentials) are evaluated in the near field (namely for surge, heave, roll and pitch), proving the potential’s reformulation between to different depth-regions with the field in the shallower side being increased and "suppressed". The effectiveness of the absorbing layer is clear in these plots by the deadening behavior of the outgoing waves after the PML-activation at a radius of three wavelengths towards the end of the free surface domain, without significant contamination of the field before its application due to reflections, contaminations which can be generated in case of applying typical Sommerfeld-type radiation conditions.

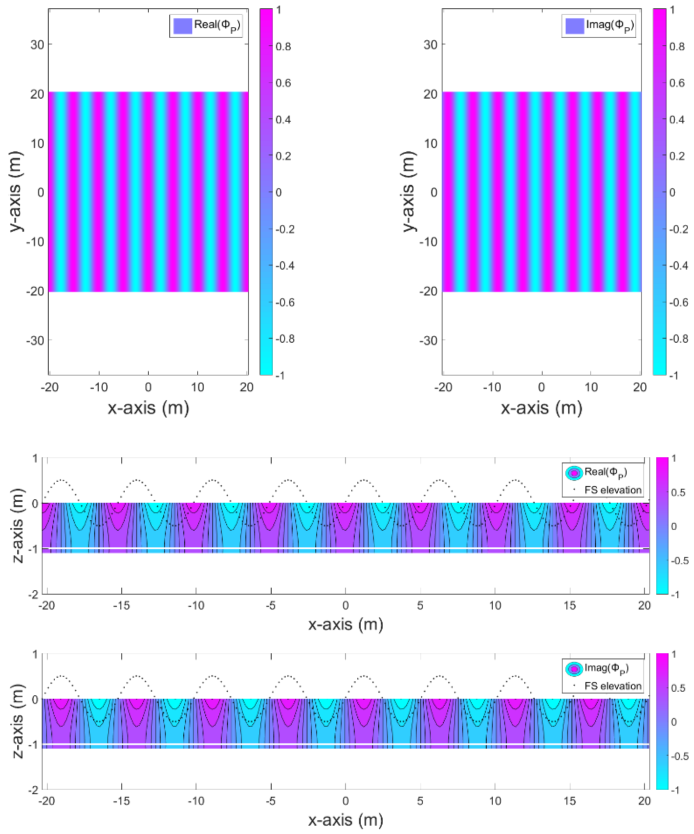

Figure 82: Propagating field (Real and Imag) by CMS (top and side view) for $\omega\sqrt{\alpha/g}$=0.5461, 0deg Flat bottom

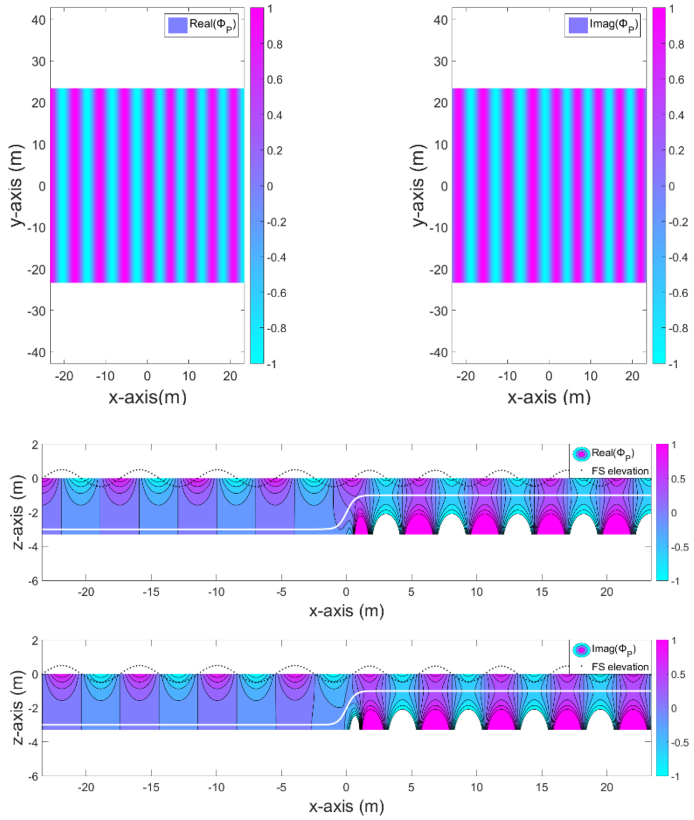

Figure 83: Propagating field (Real and Imag) by CMS (top and side view) for $\omega\sqrt{\alpha/g}$=0.5461, 0deg Variable bottom (h_1=3 m, h_3=1 m, α_{bot}=0.5)

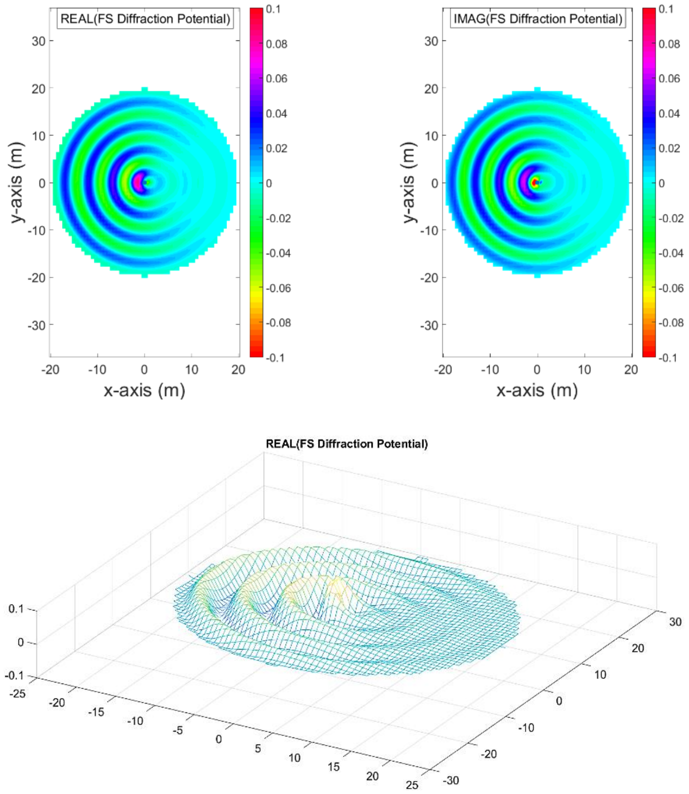

Figure 84: Diffraction field (Real and Imag) (top and 3D view) for $\omega\sqrt{\alpha/g}$=0.5461, 0deg
Flat bottom

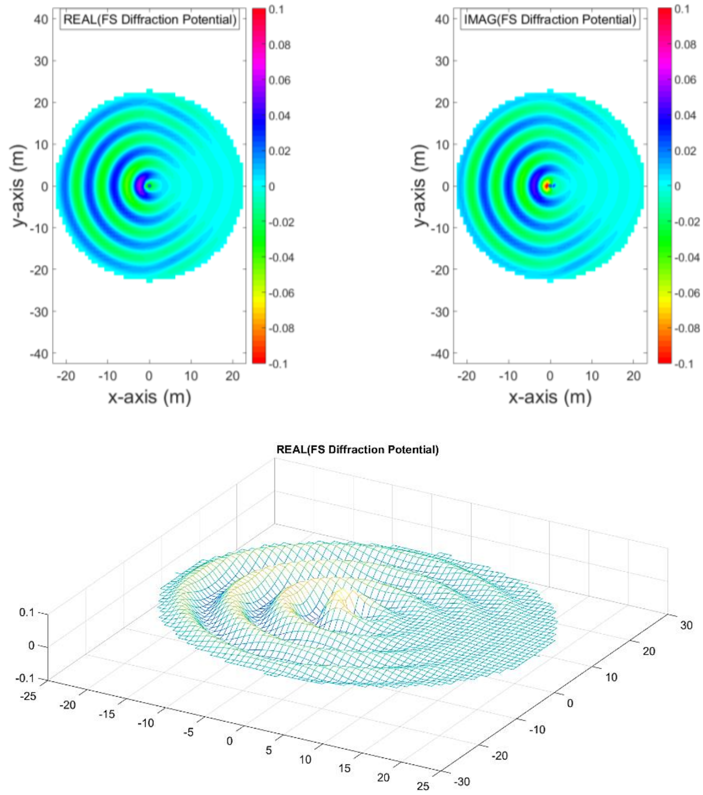

Figure 85: Diffraction field (Real and Imag) (top and 3D view) for $\omega\sqrt{\alpha/g}$=0.5461, 0deg
Variable bottom (h_1=3 m, h_3=1 m, α_{bot}=0.5)

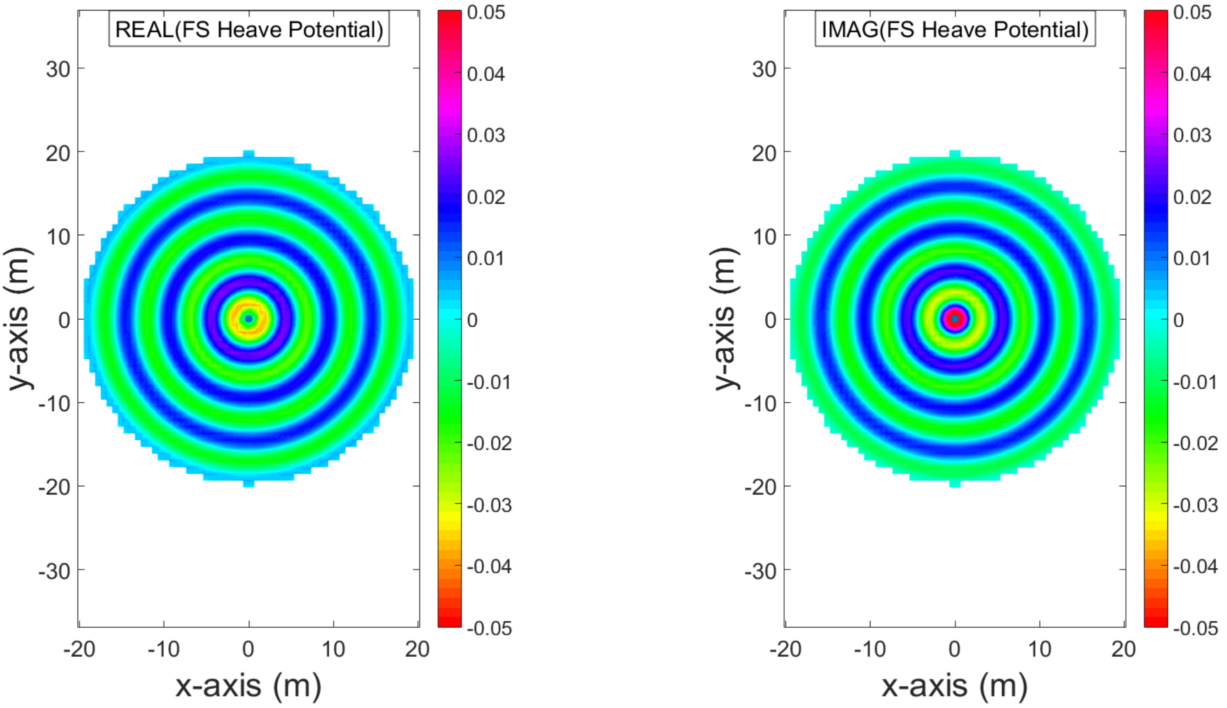

Figure 86: Heave field (Real and Imag) (top view) for $\omega\sqrt{a/g}$=0.5461, 0deg
Flat bottom

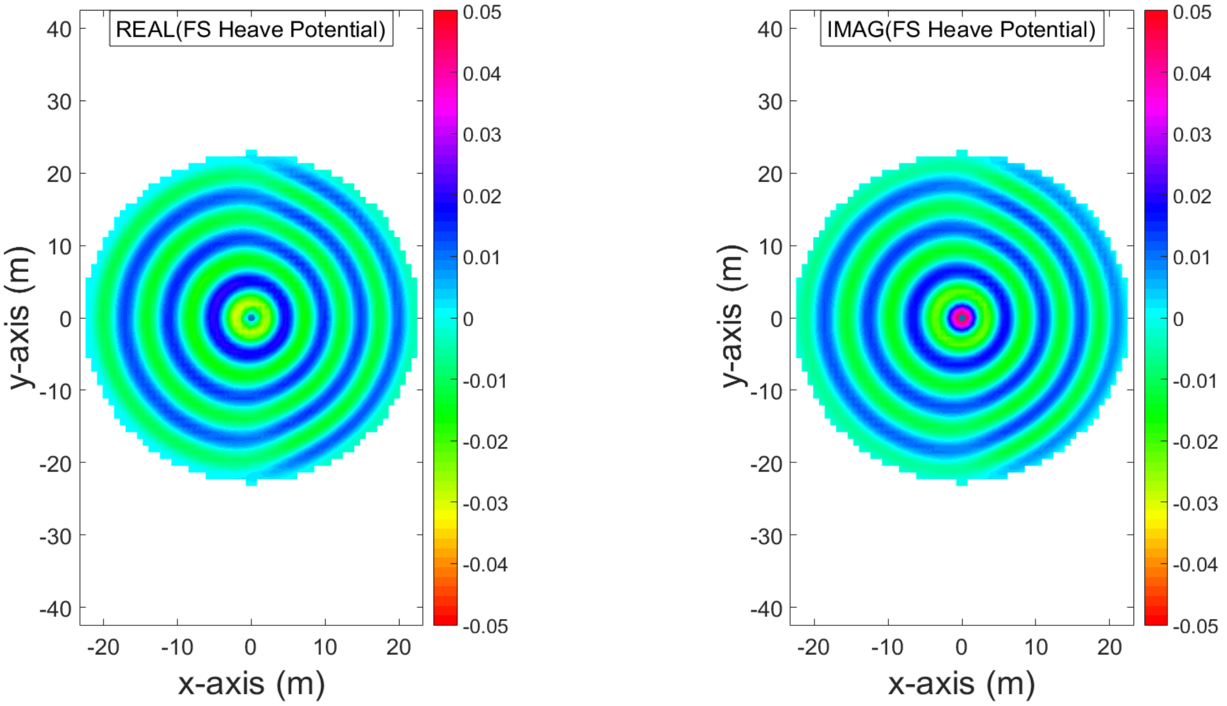

Figure 87: Heave field (Real and Imag) (top view) for $\omega\sqrt{a/g}$=0.5461, 0deg
Variable bottom (h_1=3 m, h_3=1 m, α_{bot}=0.5)

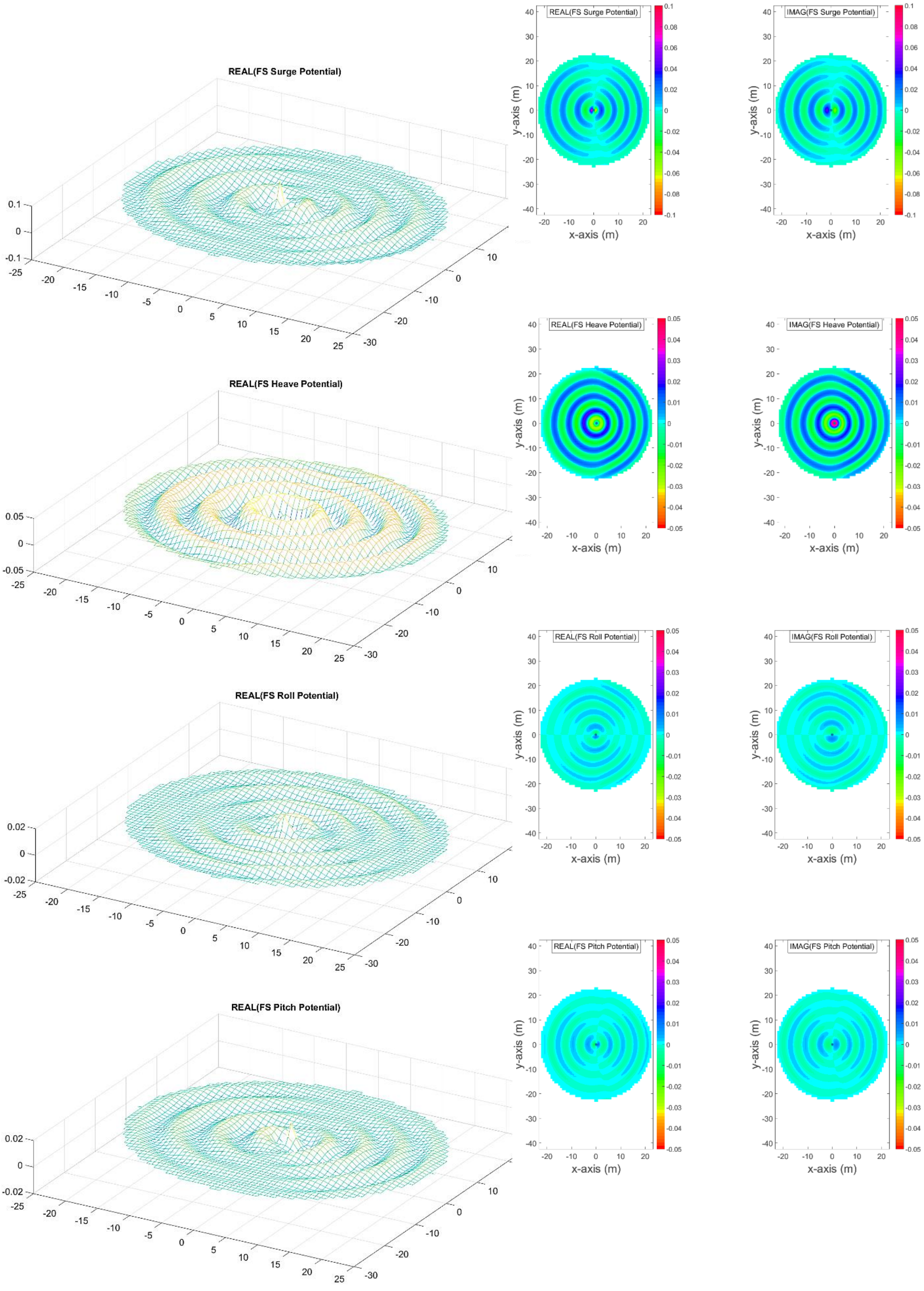

Figure 88: Radiation potentials (surge, heave, roll, pitch) (3D and top view) for $\omega\sqrt{\alpha/g}$=0.5461, 0deg
Variable bottom (h_1=3 m, h_3=1 m, α_{bot}=0.5)

4

On WECs shape investigation: Flat and variable bathymetry

4.1 Commercial WEC shapes

An essential feature of studying wave-body interactions is the shape of the floating, or submerged device. With the optimization of the wetted surface, further improvements in efficiency can be accomplished, resulting to an optimized WEC performance. In regard with the heaving WECs, which has also the type of the already studied cylindrical device, the relevant industry directs the efforts towards axisymmetric floating bodies, with their operation independent from the heading angle of the waves. Typical examples of WEC devices in a commercialize level are presented in **Fig. 89**.

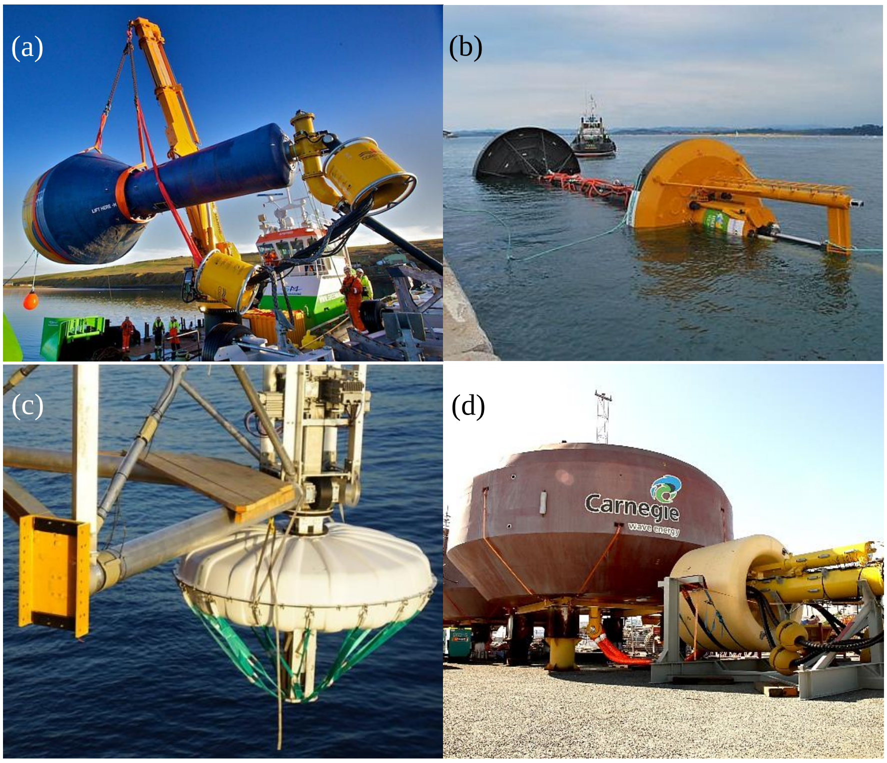

Figure 89: Deployment phase of different commercial WECs:
(a) CorPower Buoy [45,85], (b) PowerBuoy OPT [29,86], (c) Sinn Power [87], (d) CETO Carnegie [31,86]

The investigation of the impact of the WEC shape in its performance is also one of the main subject in research projects. Shapes like the conical, the semi-spherical, the elliptical and many others are examined in [88–90].

4.2 Investigated geometries

4.2.1 Geometries generation

In the present research eight different geometries are investigated. These shapes are chosen with an impartial view of the relevant industry trends and research activity [81] and they are the:

- Cylindrical
- Disk-shaped
- Egg-shaped
- Floater-shaped
- Nailhead-shaped
- Elliptical
- Conical
- Semi-spherical

In particular, the nailhead-shaped design presents further interest, due to its unconventional geometry, for performing with higher efficiency as a multi-DOF WEC, combining heave and an extra rotational degree of freedom. The generation of these geometries is carried out in a Mathworks MATLAB code with the implementation of a spline interpolating over some determined nodes. The formation of the nailhead-shaped wetted surface is indicated in the following **Fig. 90**, with the 360°-rotation of the generating spline.

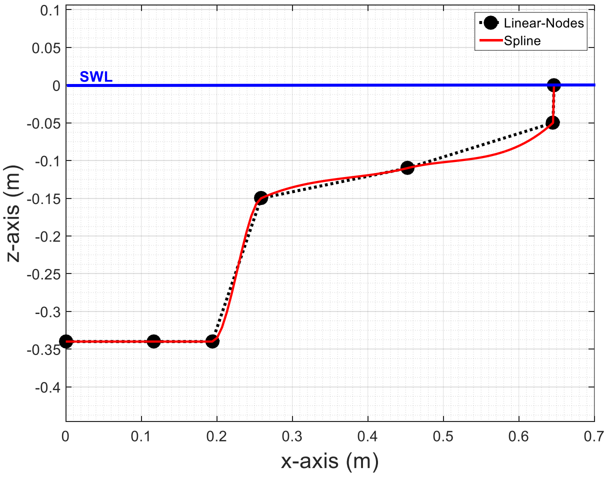

Figure 90: Generating spline of the Nailhead-shaped WEC wetted surface

All of these shapes are axisymmetric and thus only 0deg of incident wave will be considered without loss of generality. One significant feature of this shape investigation process is the determination of the geometries in compliance with constant-mass constraint. If the same material is considered for the construction of these point absorbers with the same mass distribution, then the radius and the draft of each shape can be calculated so as to keep the submerged vertical cross section area equal to the submerged vertical cross section area of the reference cylindrical design of α/h=1/3.5, T/α=3/2 and d/h=4/7. This assumption of constant-mass is adopted as a basic reference feature for all the geometries, permitting this way a more unbiased comparison. The dimensions can be read in the **Fig. 91** and in the **Table 6**.

The mesh generation follows the same principals of the relevant process in case of the cylinder, with one modification. The mesh on the WEC body is now finer for approaching more effectively the abrupt geometry changes of the proposed shapes without discontinuities. As a consequence, a mesh of 18x88 is considered in each WEC body, except the cylindrical WEC with the unchangeable 10x88 discretization. For all these cases, except cylinder, there are no analytic solutions for their response. The developed and validated BEM method is used for the estimation of their performance. The geometries are illustrated in **Fig. 91**, along with the meshes on the WEC, on the free-surface and on the bottom, in the near field.

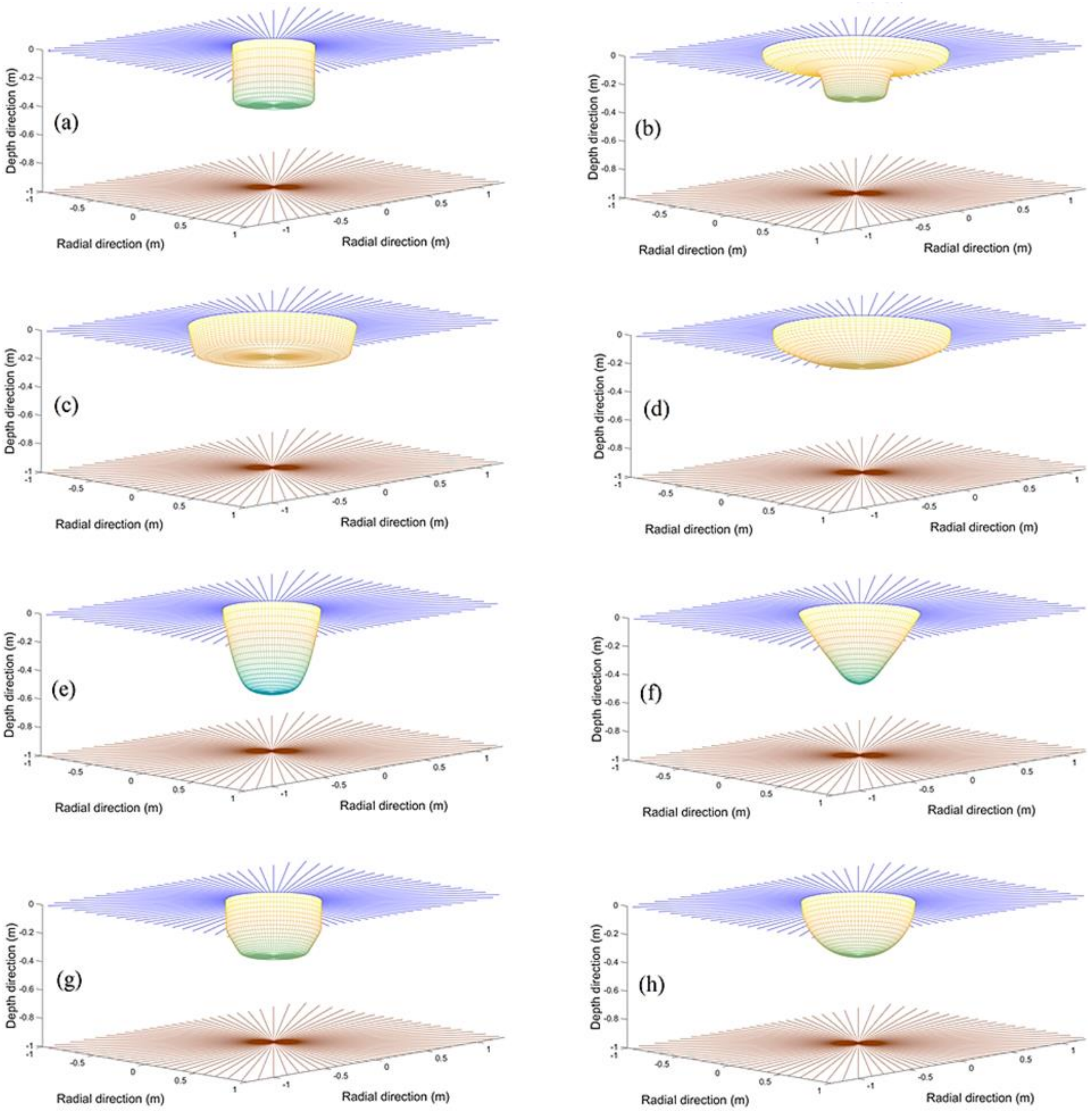

Figure 91: WEC shapes and near field computational mesh over flat bottom:
(a) Cylindrical, (b) Nailhead-shaped, (c) Disk-shaped, (d) Elliptical,
(e) Egg-shaped, (f) Conical, (g) Floater-shaped, (h) Semi-spherical

The generation of geometries can also be handled by an optimizer. The algorithm will run the computational code as many times as needed for convergence, or until he reaches the limit of maximum iterations, and will evaluate the most efficient geometry by determining the position of the spline-nodes. However, the computational cost and the memory demands at this scenario are exponentially larger. The above geometries will supply the researcher with a very useful estimation on which is the most efficient general shape of a WEC. Very sophisticated designs are normally rejected due to high R&D and manufacturing costs. This subject, for implementing an optimizer, is let for future work.

4.3 Numerical results

4.3.1 *Steady-depth bathymetry*

4.3.1.1 Response evaluation

Stepping on the assessment of these geometries and their power output, RAOs of heave motion and heave phase, along with the non-dimensional power output are evaluated in the present section. The PTO damping is considered the same for each device and equal to a reference PTO of the cylindrical WEC, described as: B_{PTO}=B_s=[1, 5, 25, 50, 100, 200, 400, 600] b_m. This procedure will allow further appraisal of these shapes and their efficiency and as a result determination of the most effective designs for a wide spread of PTO damping values.

Firstly are plotted the responses and power outputs by a Cylindrical WEC for eight PTO damping values. As proven by the **Figs 92-94** there are significant differences as these damping values change. Resonance effect is intense for the two lower PTO damping values. Furthermore, in these figures is obvious the effect of PTO induced constraints, describing why this range of damping values is taken under consideration and especially why lower values of PTO damping are neglected as industrial unfeasible, or as unpropitious for survival and smooth operation or as power inadequate.

Then, for each of the shapes the RAO of heave mode, its phase and the normalized power output is evaluated. Despite the fact that the evaluation refers to all these PTO cases, in the following figures, in order to visualize part of these results, will be plotted the responses for all eight geometries, but for reasons of simplicity, only three representative values of PTO damping will be considered, i.e. for B_{PTO}=B_s=[1, 10, 100] b_m.

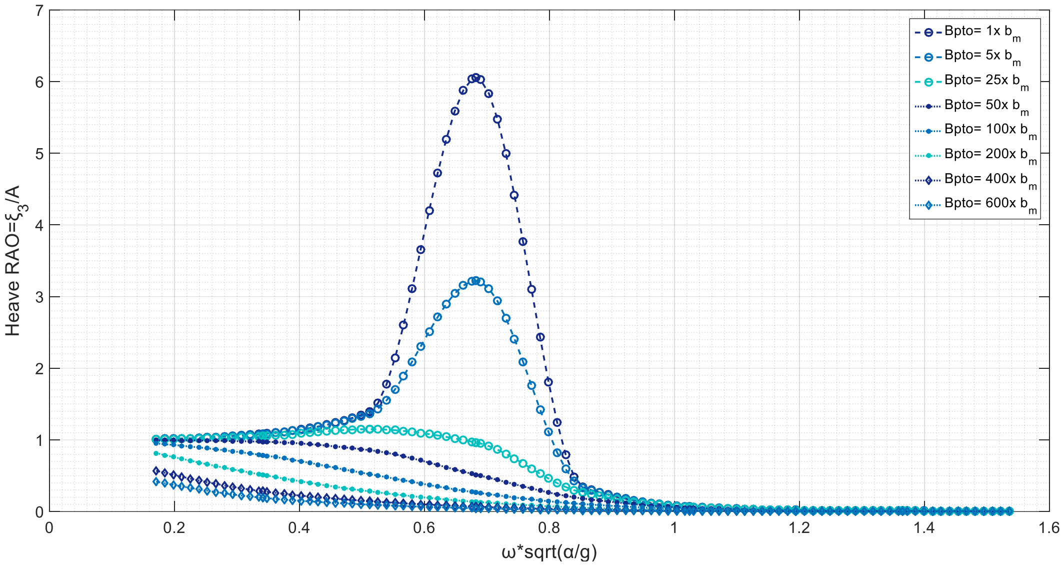

Figure 92: Heave RAO for various PTOs for Cylindrical WEC over a flat bottom

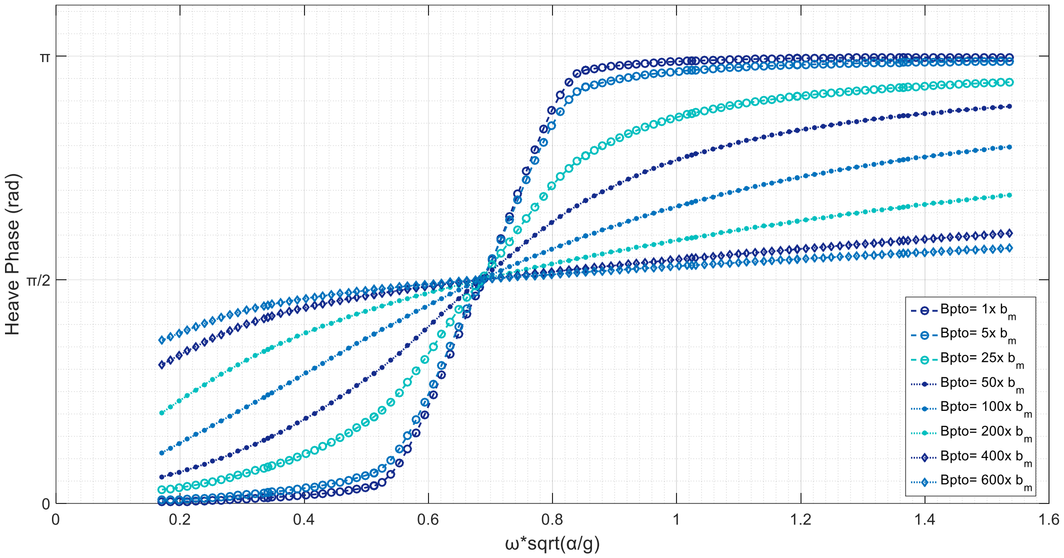

Figure 93: Heave Phase for various PTOs for Cylindrical WEC over a flat bottom

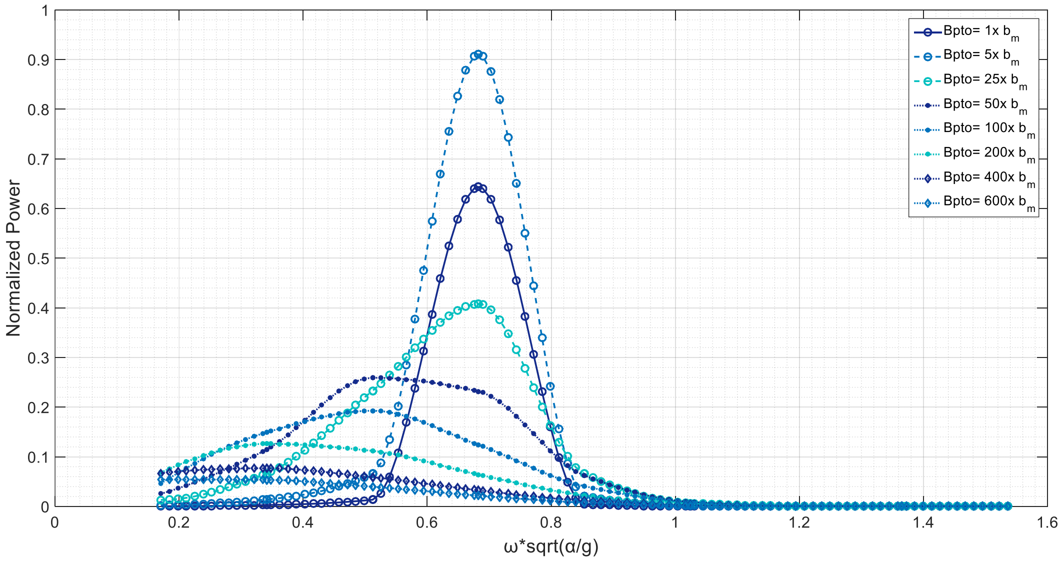

Figure 94: Normalized Power Output for various PTOs for Cylindrical WEC over a flat bottom

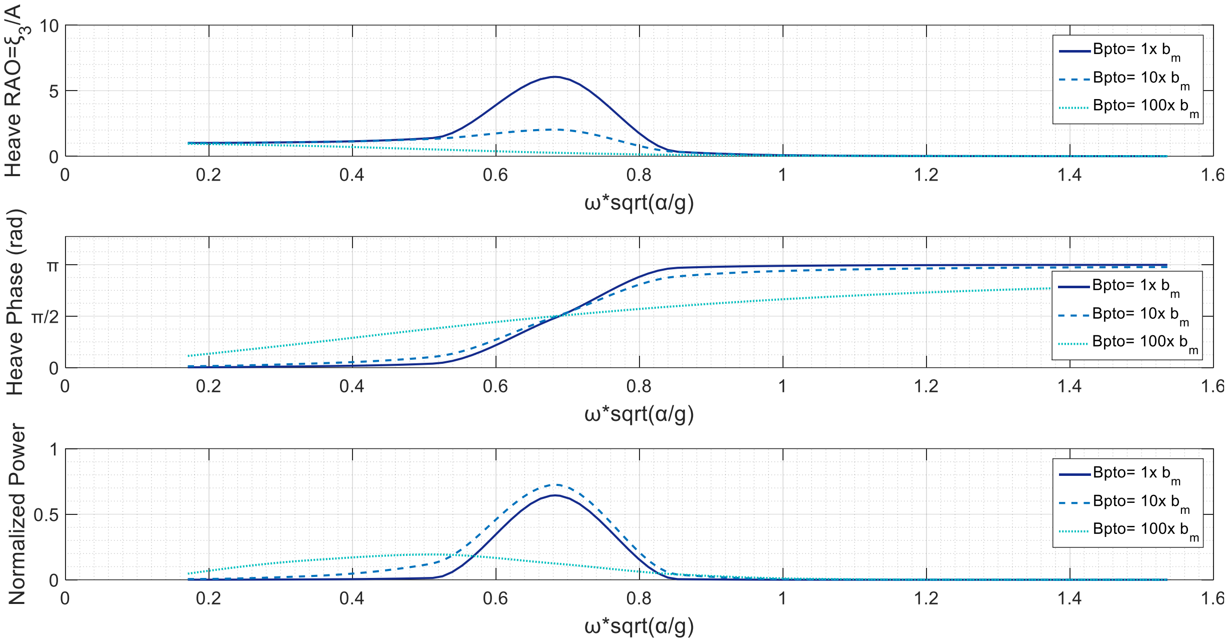

Figure 95: Heave RAO, Phase RAO and Normalized Power Output – Cylindrical WEC – Flat bottom

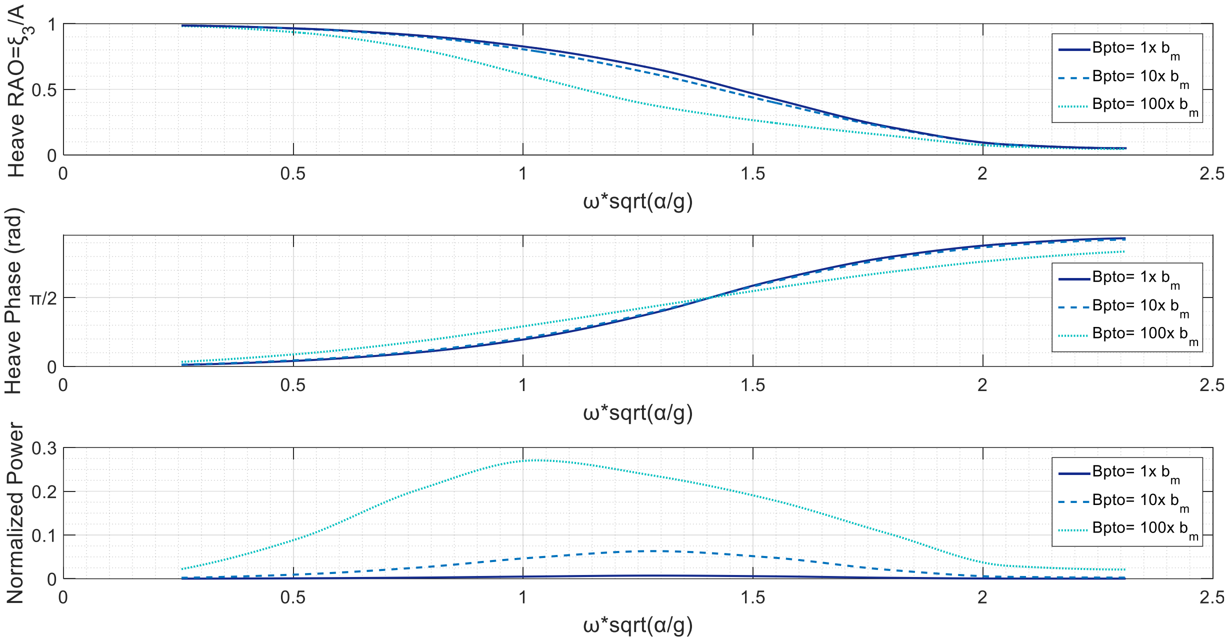

Figure 96: Heave RAO, Phase RAO and Normalized Power Output – Nailhead-shaped WEC – Flat bottom

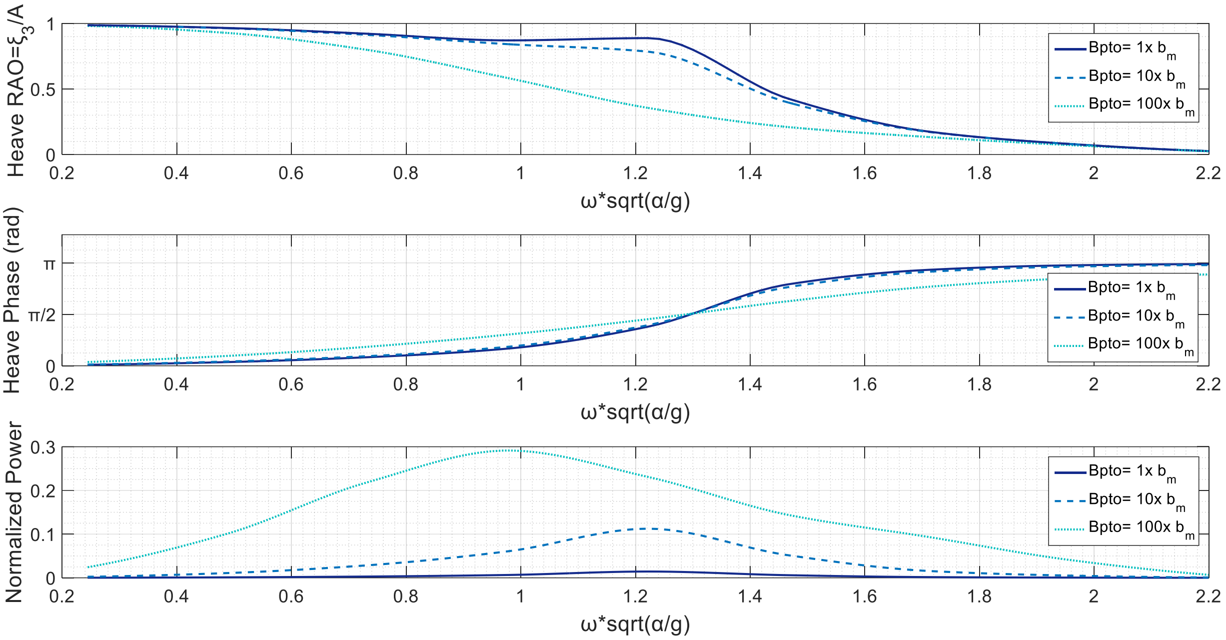

Figure 97: Heave RAO, Phase RAO and Normalized Power Output – Disk-shaped WEC – Flat bottom

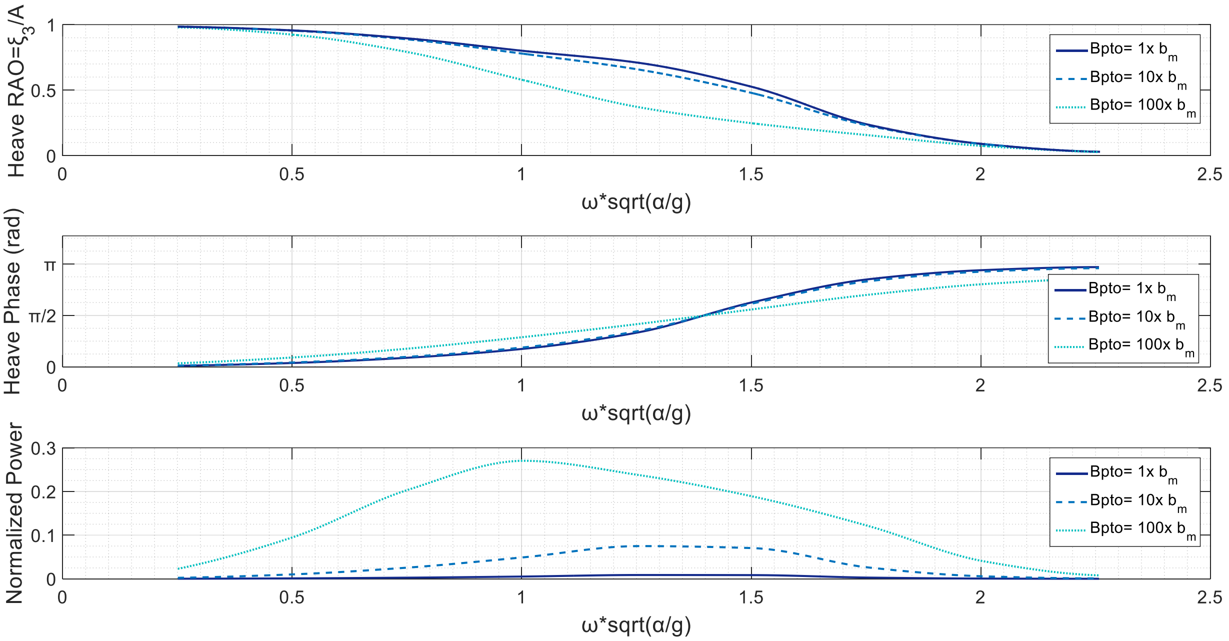

Figure 98: Heave RAO, Phase RAO and Normalized Power Output – Elliptical WEC – Flat bottom

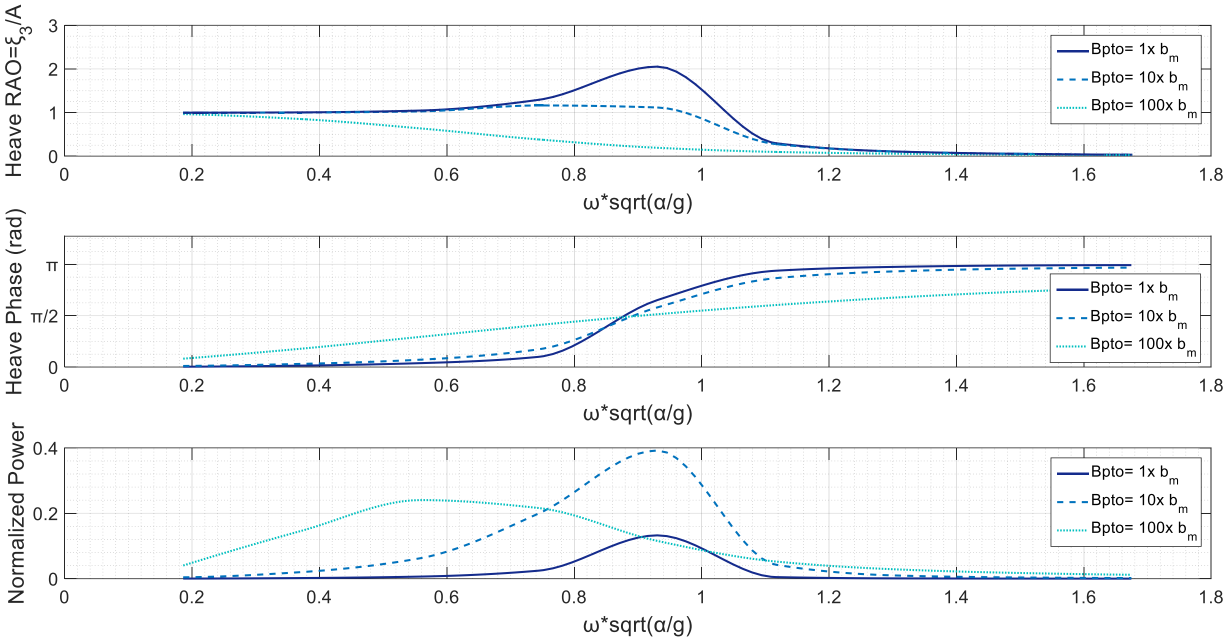

Figure 99: Heave RAO, Phase RAO and Normalized Power Output – Egg-shaped WEC – Flat bottom

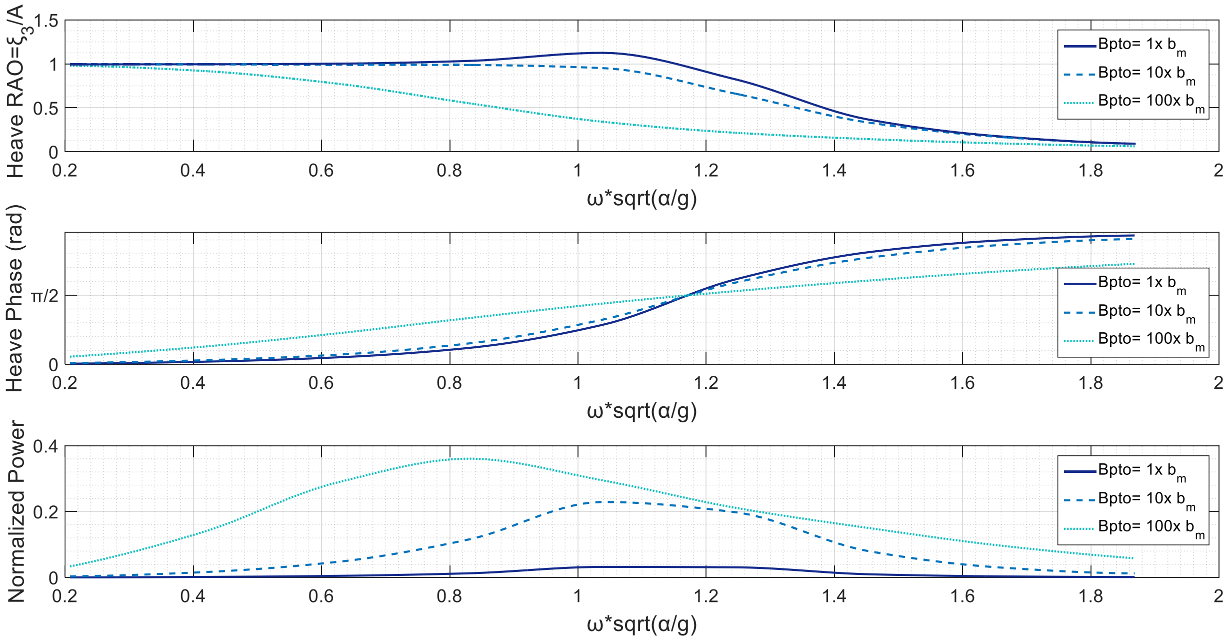

Figure 100: Heave RAO, Phase RAO and Normalized Power Output – Conical WEC – Flat bottom

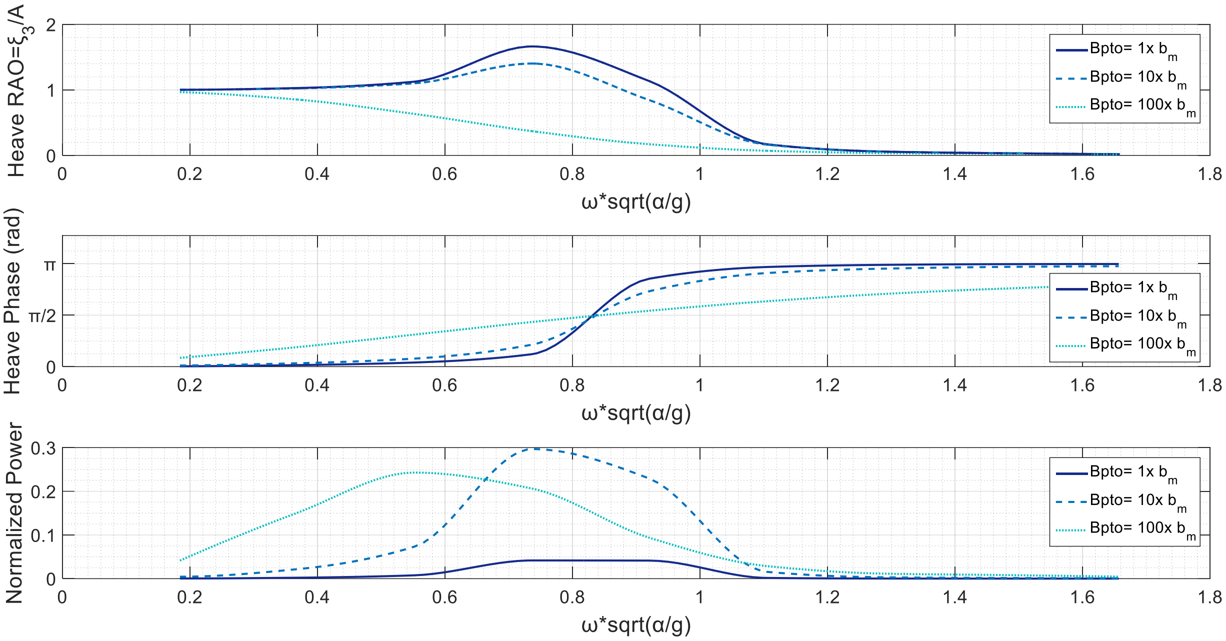

Figure 101: Heave RAO, Phase RAO and Normalized Power Output – Floater-shaped WEC – Flat bottom

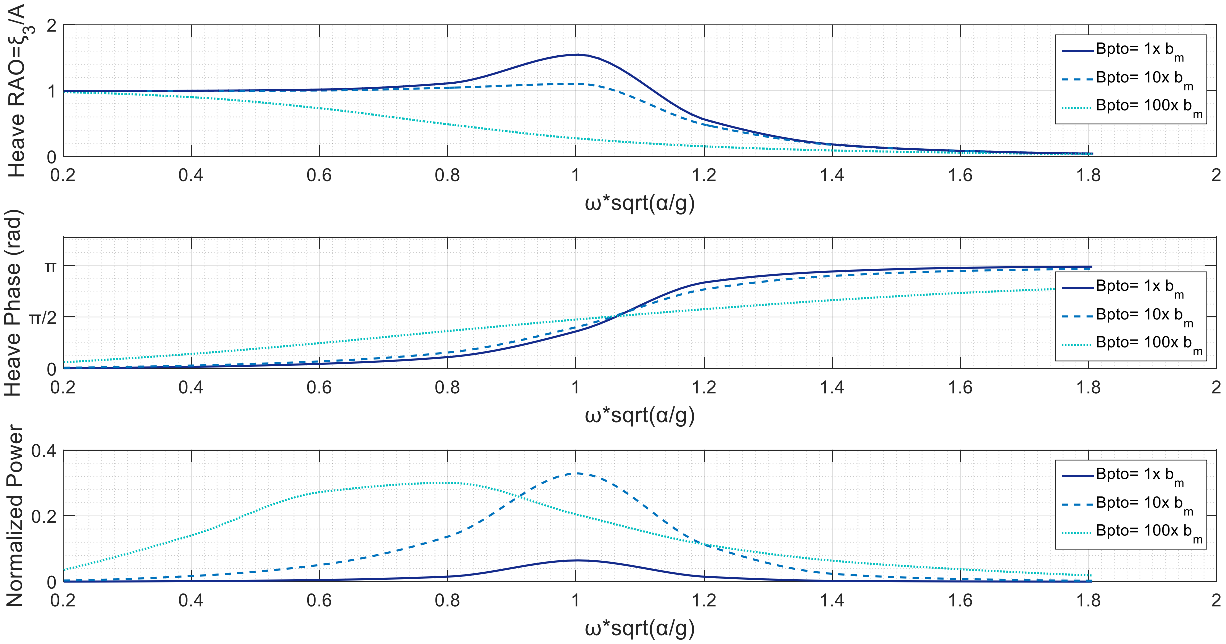

Figure 102: Heave RAO, Phase RAO and Normalized Power Output – Semi-spherical WEC – Flat bottom

The crucial value for estimating the WEC performance is obviously the power output. As illustrated in the previous evaluation, each wave energy device exploits in a different way the wave spectrum. There are concentrated power absorption cases, in a small effective frequency bandwidth, with the most indicating example the Cylindrical WEC, which reaches its maximum efficiency in the resonant frequency and in its neighbor presents appreciable power absorption levels (**Fig. 95**). On the other hand, most of the devices achieve lower power-levels but for a larger frequency bandwidth (**Figs 96-102**). In addition, resonance in some cases is too constrained and no peaks are obtained in the relevant curves, for example in case of the nailhead-shaped design (**Fig. 97**).

By the above figures, the researcher can assert that each WEC can operate most efficiently for a specific value of PTO damping. The idea of optimizing the PTO damping will be evaluated in the next section.

Coming to an induction, there is no possibility for pre-defining the optimum shape for a WEC or its PTO variables, unless the details of topography and the sea state are known. The researcher has to come along with a compromise depending on the application, on what is more preferable: exploiting the waves with high efficiency but only in near-resonance frequencies or absorbing the offered power in a larger band of frequencies but with lower performance levels. The final selection is inseparable linked with the site of installation and the local wave spectrum, while control strategies on WECs attempt to model and apply mathematically this compromise.

4.3.1.2 Performance assessment

The evaluation of the performance of these proposed WECs will be based in the area below the "most-efficient-curve" of normalized power. In more detail, the area above the power curve with the most effective PTO will be calculated, and then divided by the area of the surrounding rectangle. The area above the WEC power curve represents the absorbed normalized energy by the device, while the area of the rectangle represents the normalized energy offered by the waves. The result will be a ratio, quantifying the performance of the WEC and will be called as performance index. For this procedure, PTO damping takes different values, in order to include each geometry's optimal area: $B_{PTO}=B_s=[1, 5, 10, 50, 100, 250, 500, 750, 1000]\ b_m$, securing this way that the following comparison will be consistent and reliable. Taking this into account, the results are presented in **Table 6**, along with the WEC waterline radius and draft:

Table 6
WEC shapes, main dimensions and performance index over flat bottom

WEC design	FS radius (m)	Draft (m)	max {Performance index}
Cylindrical	0.28571	0.42857	11.29 %
Nailhead-shaped	0.64654	0.34000	15.38 %
Disk-shaped	0.58588	0.22000	13.66 %
Elliptical	0.61724	0.25000	14.73 %
Egg-shaped	0.33963	0.60000	10.63 %
Conical	0.42273	0.50000	17.70 %
Floater-shaped	0.33238	0.40000	9.87 %
Semi-spherical	0.39485	0.39485	13.30 %

From the results of **Table 6** there are qualified two designs as the most efficient: the Nailhead-shaped and the Conical WECs. The first of them, the Nailhead-shaped WEC presents special interest for combining more than one modes of power absorption, but this will be examined in a subsequent chapter. After an overall evaluation, the Conical WEC is selected as the most efficient wave energy converter, among all the investigated alternative designs for a 1-DOF device. Comparisons for different WEC shapes are also evaluated in [89], comparing indeed two of the most efficient designs of the present analysis: the cone and the semi-spherical and concluding again in slight superiority of the conical shape over the semi-spherical.

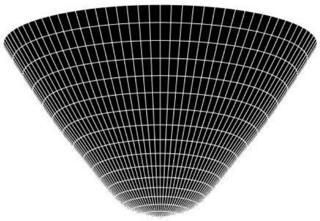

Figure 103: The conical WEC

4.3.1.3 PTO damping optimization

The damping coefficient of the Power Take Off system is a decisive parameter for the performance of the device. It is also, a tuning parameter, chosen by the manufacturer of the PTO, and thus is a design variable for maximizing the energy output. With the right selection of its value the performance index of the previous section will be significantly improved.

The ten PTO damping values, selected in the previous analysis, are typical and they are used for comparing the different shapes, regardless the PTO. After this evaluation, the conical shape was found as the most efficient design. Then, for this shape, the second step is to decide the relevant ideal PTO damping value. For this purpose, different PTO values, inside a utilized range for the Conical WEC, will be tested. This values are:

$$B_{PTO}=B_s= C_{PTO}\, b_m = [1{:}1{:}200]\ \ b_m \tag{4.1}$$

The corresponding power curves are depicted in **Fig. 104**.

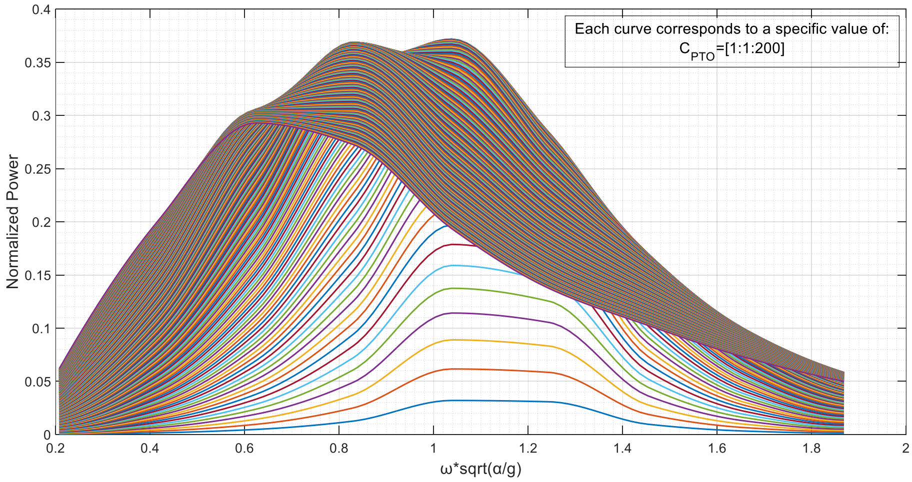

Figure 104: Normalized Power Output for various PTO damping values – Conical WEC over flat bottom

By evaluating the area below the curves, the performance index can now be calculated and the results are presented in **Fig. 105**. As shown, the optimal PTO damping for the conical WEC is almost $B_{PTO}=C_{PTO}\,b_m=77\,b_m$, resulting in a performance index of 17.95%. It can be also obtained that for a high damped system, the resonance frequency has no meaning because the hard PTO does affect strongly in the operation of the device and restricts its resonance response, and optically the peak of the power curve is smaller and shifted left (**Fig. 104**).

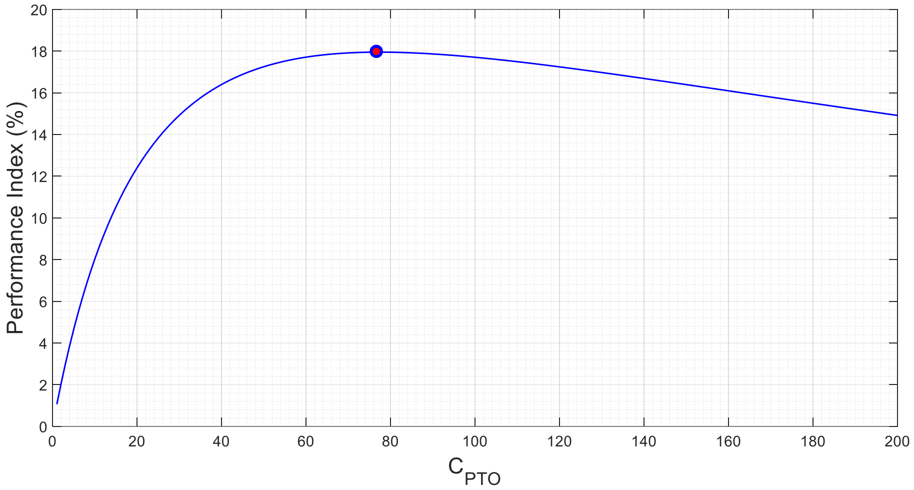

Figure 105: Performance index for PTO values – Conical WEC over flat bottom

4.3.2 Variable-depth bathymetry

4.3.2.1 Geometries and depth-profile

A seabed with varying depth conditions can affect the performance of floating WECs. The numerical estimation of this effect is the aim of the present section.

The investigated geometries are the eight different shapes, presented previously. After the evaluation of their response, the optimal shape will be re-selected and compared with the Conical WEC results, which found to be the superior design in case of a flat bottom. The processes of geometries generation and meshing are totally unchangeable.

The bottom profile is described by an arbitrary function. In here, it takes the form of a smooth shoal, common in nearshore and coastal environments. The function which describes the seabed profile is:

$$h(x)=h_m-0.5(h_1-h_3)\tanh\left(\alpha_{bot}\pi\left(x-x_{mean}\right)\right) \qquad (4.2)$$

where the mean depth is: $h_m=0.5\ (h_1+h_3)$. The coefficient-α_{bot} defines the bottom slope and for this example is set $\alpha_{bot}=0.5$, while $h_1=1.2$ m and $h_2=0.8$ m. The region is characterized by constant depths at infinity. The resulting mean depth $h_m=1$ m, is equal to the depth of the flat-bottom case, for reasons of consistency during the comparison. This is not a significant depth-step and so the effects of the seabed on the response of the WEC will be slightly alternated.

For supervisory reasons, the depth profile will be shown in **Fig. 106**, with the Cylindrical WEC on the free-surface, along with the flat bottom equivalent illustration. The rest of shapes are omitted for brevity.

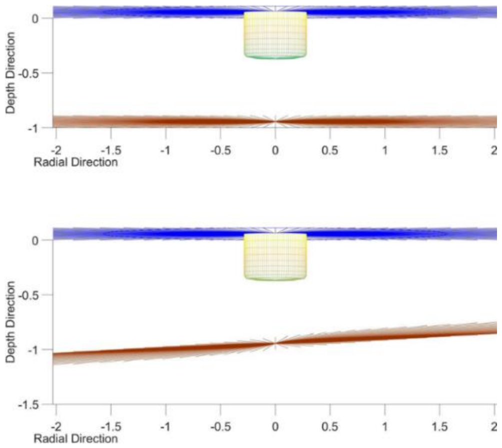

Figure 106: Flat and varying seabed below the Cylindrical WEC

4.3.2.2 *Performance assessment*

The evaluation of the results for the different shapes, operating over the varying seabottom, led to the estimation of their performance index, presented in **Table 7**:

Table 7
WEC shapes and performance index for flat and variable bottom

WEC design	**max {performance index} Flat Bottom**	**max {performance index} Variable Bottom**
Cylindrical	11.29 %	11.41 %
Nailhead-shaped	15.38 %	15.74 %
Disk-shaped	13.66 %	14.11 %
Elliptical	14.73 %	15.11 %
Egg-shaped	10.63 %	10.82 %
Conical	17.70 %	17.92 %
Floater-shaped	9.87 %	10.10 %
Semi-spherical	13.30 %	13.39 %

As proven by the above table, a varying seabottom is affecting the performance of a WEC and actually causes an increase of the device's ability for harnessing wave energy, with the highest improvement detected for the Disk-shaped WEC and being equal to almost 3.3%. These results are very promising and may be a first indication of installations of WECs over a deliberately varying seabed, in order to improve their performance. This proposal is vacated for future work.

The optimal design is again the Conical WEC, with an increase (1.24%) to its performance index due to the varying seabed profile. If a steeper step of depth is considered, then the above variations in results might be more intense.

4.3.2.3 *PTO damping optimization*

The damping coefficient of the PTO will now be optimized again, for the optimum Conical WEC, but now for the case of the variable seafloor. The curve of the performance index as a function of the PTO values will be re-plotted. The PTO damping values are similar to those evaluated in **(4.3.1.3)**. The optimal PTO damping value is now $B_{PTO}=C_{PTO}\,b_m=80\,b_m$, corresponding to a performance index of 18.10% (**Fig. 107**).

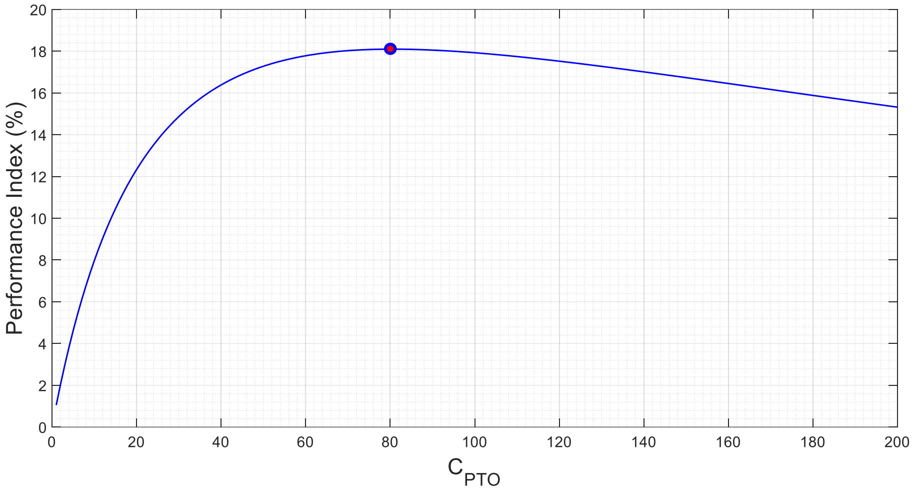

Figure 107: Performance index for PTO values – Conical WEC over variable bottom (h_1=1.2 m, h_3=0.8 m, α_{bot}=0.5)

4.3.3 *Design comparison*

One of the main purposes of the study is the comparison of an optimal WEC shape operating over a flat or a varying seabed. The optimum shape is now found to be the Conical WEC. The ideal value of PTO damping is $B_{PTO}=C_{PTO}\,b_m=77\,b_m$ for flat bottom and $B_{PTO}=C_{PTO}\,b_m=80\,b_m$ for variable bottom, and for this PTOs are illustrated the normalized power curves in **Fig. 108**. The superiority of the variable-bottom results are mainly obtained in lower frequencies, while in the mid-frequencies the WEC presents more efficient operation over the flat bottom end finally, in high frequencies the power output is similar despite the change of the bathymetric profile.

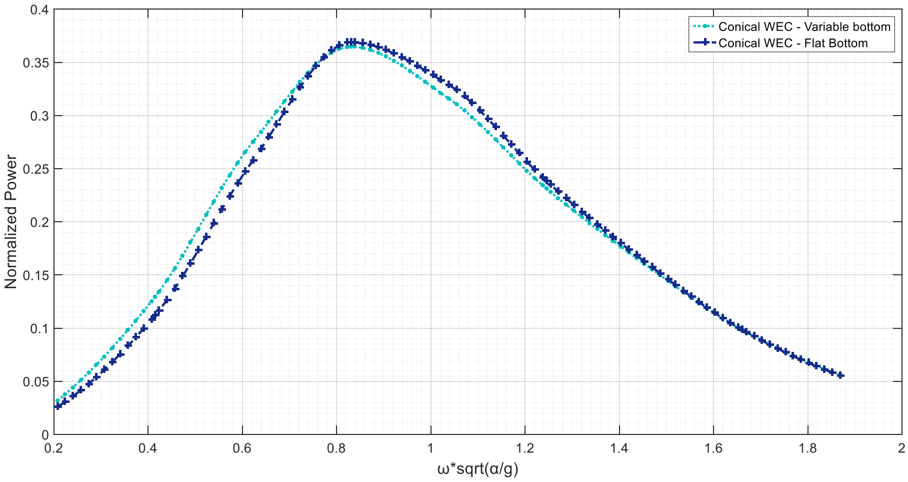

Figure 108: Normalized Power Output for optimum PTO damping value. Conical WEC over flat and variable bottom (h_1=1.2 m, h_3=0.8 m, α_{bot}=0.5)

5

Arrays treatment: On WECs interaction

5.1 Arrays layout

Most of the devices, deployed in the renewable energy sector, are installed in an array layout for maximizing the energy capture levels. Wave energy harnessers, especially heaving WECs, which are investigated in the present study, are normally considered in farm configurations in order to obtain an appreciable utilizable amount of power absorption.

One issue of great interest, arising from this farm layout, is the hydrodynamic interaction between the devices and the wave field alteration by each device. Design and optimization of this layout is a critical task for the total efficiency of the wave park. Furthermore, the effects of a variable seafloor on the propagating field and on the WECs performance is upon further notice.

The WEC transforms the whole fluid domain and thus affects all the nearby devices, in contrast with the wind or tidal turbines, which have their highest impact in their wake (**Fig. 109**). There are two main design concerns regarding arrays of wave energy converters. These are the positioning issues and the coupling issue.

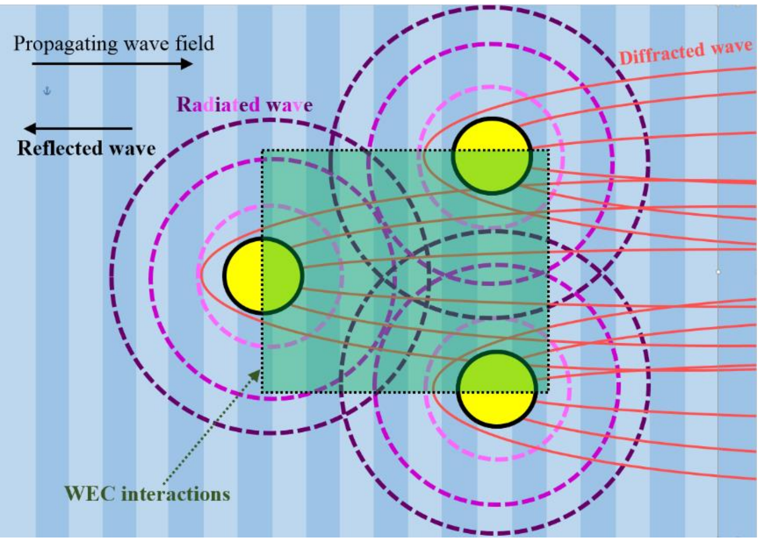

Figure 109: Interactions and wave field analysis in an array of three WECs

The optimization of WECs operating in arrays is different than the optimum design of a single WEC. An appropriate design and arrangement may cause higher excitation forces and accordingly higher output, known as constructive interaction phenomenon.

The problem of wave-seabed-multiple body interactions will be treated by means of the developed and presented 3D BEM-PML, a method ideal for modeling in detail the near-body potential field and estimating the WEC responses. Analytical methods for flat-bottom regions ([91]) and phase-averaging spectral wave methods ([92]) have been used, however higher accuracy on evaluating the field near the WEC body and modelling the interaction effects and then proceeding on array layout optimization and design demands Computational Fluid Dynamics tools (CFD) implementation ([93]).

More complex effects relate with the operation of WECs in an array layout. Hydrodynamic coupling, entrapped modes around periodic arrays, the park-effect, chaotic resonance and radiation admittances are only few of the problems need to be solved and numerically approached, if a large scale array of active WECs is upon design and performance estimation [94].

5.2 Mathematical formulation

5.2.1 The hydrodynamic problem of WEC arrays

The proposed numerical method is the BEM-CMS-PML method, discussed in **(2.3.2)**, for treating problems of floating bodies over a 3D varying sea-bottom. The propagating field is calculated by the CMS model, presented in **Appendix B**. The evaluation of the radiation and diffraction field is handled by the BEM computational code, where the radiation condition in forced by the previously optimized PML model, in order to avoid reflections contamination of the field induced by a typical Sommerfeld expression of radiation condition.

In the former case, only one floating body was considered and its responses were finally obtained using this method. The only alteration herein, is that *k*-bodies are installed and thus the code has to deal with the evaluation of the 6*k*-radiation potentials and the relevant hydrodynamic coefficients and responses.

Based on [79] the complex potential $\varphi(x,z)$ can be decomposed on the propagating potential, on the diffraction potential and on the radiation potentials:

$$\varphi(x,z)=\varphi_P(x,z)+\varphi_D(x,z)+\frac{2\omega^2}{gH}\varphi_R(x,z) \tag{5.1}$$

$$\varphi_R(x,z)=\sum_{k=1}^{N}\sum_{\ell=1}^{6}\xi_{k\ell}\varphi_{k\ell}(x,z) \tag{5.2}$$

where $\varphi_P(x,z)$ is the normalized propagation wave field without the presence of the bodies, $\varphi_D(x,z)$ is the diffraction field due to the insertion of the motionless bodies D_B^k , $k=1,N$, satisfying the BC: $\partial\varphi_D(x,z)/\partial n_k= -\partial\varphi_P(x,z)/\partial n_k$ on the *k*-body where $n_k=(n_1,n_2,n_3)_k$ is the normal vector on the wetted surface of the *k*-body, directing outwards of the fluid domain and so inwards the body. Moreover, φ_{kl} is the radiation potential due to the *l*-motion of the *k*-body, satisfying the BC: $\partial\varphi_{kl}(x,z)/\partial n=n_{kl}$, where n_{kl} is the *l*-component of the generalized normal vector on the wetted surface of the *k*-body and thus $n_{kl}=(r \times n_k)_{l\text{-}3}$, $l=4,5,6$.

Considering now only simple heaving *N*-WECs, the response ξ_{k3} can be evaluated for each device as well as the hydrodynamic coefficients of added mass and damping of each *k*-WEC. The heave response of the *k*-WEC is:

$$\xi_{k3}=(A_{km})^{-1}(X_{Pm}+X_{Dm})\ ,\ \ k,\, m=1,\ldots,N \tag{5.3}$$

where the matrix A_{km} can be calculated as:

$$A_{km}=-\omega^2\ (M+a_{km})-i\omega(B_S\,\delta_{km}+b_{km})+(C_S+c)\delta_{km} \tag{5.4}$$

In the **Eq. (5.4)** the δ_{km} denotes the Kronecker's delta, *M* is the body mass, which is assumed similar for all the devices, while a_{km} and b_{km} are the added mass and damping coefficients respectively, calculated as:

$$a_{km}-\frac{1}{i\omega}b_{km}=\rho\iint\limits_{\partial D_{Bm}}\varphi_{k3}n_{m3}\,dS\ ,\ \ k,\,m=1,\ldots,N \tag{5.5}$$

In addition, $c=\rho g A_{WL}$ is the hydrostatic coefficient in heaving oscillation, where A_{WL} is the waterline surface. The coefficients B_s and C_s are characteristic of the PTO, which is also assumed the same for each device.

The exciting forces, FK and Diffraction, are evaluated by the following integrals of the corresponding potentials on the wetted surface-∂D_{Bm} of the m-WEC, respectively:

$$X_{Pm}=\frac{\rho g H}{2}\iint\limits_{\partial D_{Bm}}\varphi_P n_m\,dS\ ,\ \ m=1,\ldots,N \tag{5.6}$$

$$X_{Dm}=\frac{\rho g H}{2}\iint\limits_{\partial D_{Bm}}\varphi_D n_m\,dS\ ,\ \ m=1,\ldots,N \tag{5.7}$$

As a result, the total average power output of the heaving WEC-array is:

$$P\left(N;\omega,\theta\right)=\frac{1}{2}\eta_{eff}\,\omega^{2}\left|B_S\sum_{k=1}^{N}\left(\xi_{k3}\right)^2\right| \tag{5.8}$$

Finally, q-index is used to indicate how the interaction between the WECs affects the power output. Assuming the same efficiency for each WEC η_{eff}, the q-index is the ratio of the mean power output by the array, divided by the power output of a single device operating in the same region and sea-state conditions:

$$q_N(\omega,\theta)=N^{-1}P\left(N;\omega,\theta,H\right)/\,P_1(\omega,\theta,H) \tag{5.9}$$

5.2.2 Mesh generation

The mesh on the various boundaries is now composed by several subparts. The near-WEC mesh is cylindrically developed around the WEC's waterline. This cylindrical mesh is gradually reformed into a rectangular mesh, ensuring the matching between the cylindrical meshes around the WECs. The rectangular mesh finally deforms again into cylindrical mesh on the far-field, which is ideal for representing the radiating solution. Meshes are also used for the discretization of the WECs and of the variable bottom, based again on cylindrical distribution of elements. The usage of this technique along with the quadrilateral elements ensures continuity of the geometric approximation of the (N+N+1+1)-boundaries: N-WECS, N-near fields, 1-FS far field and 1-bottom.

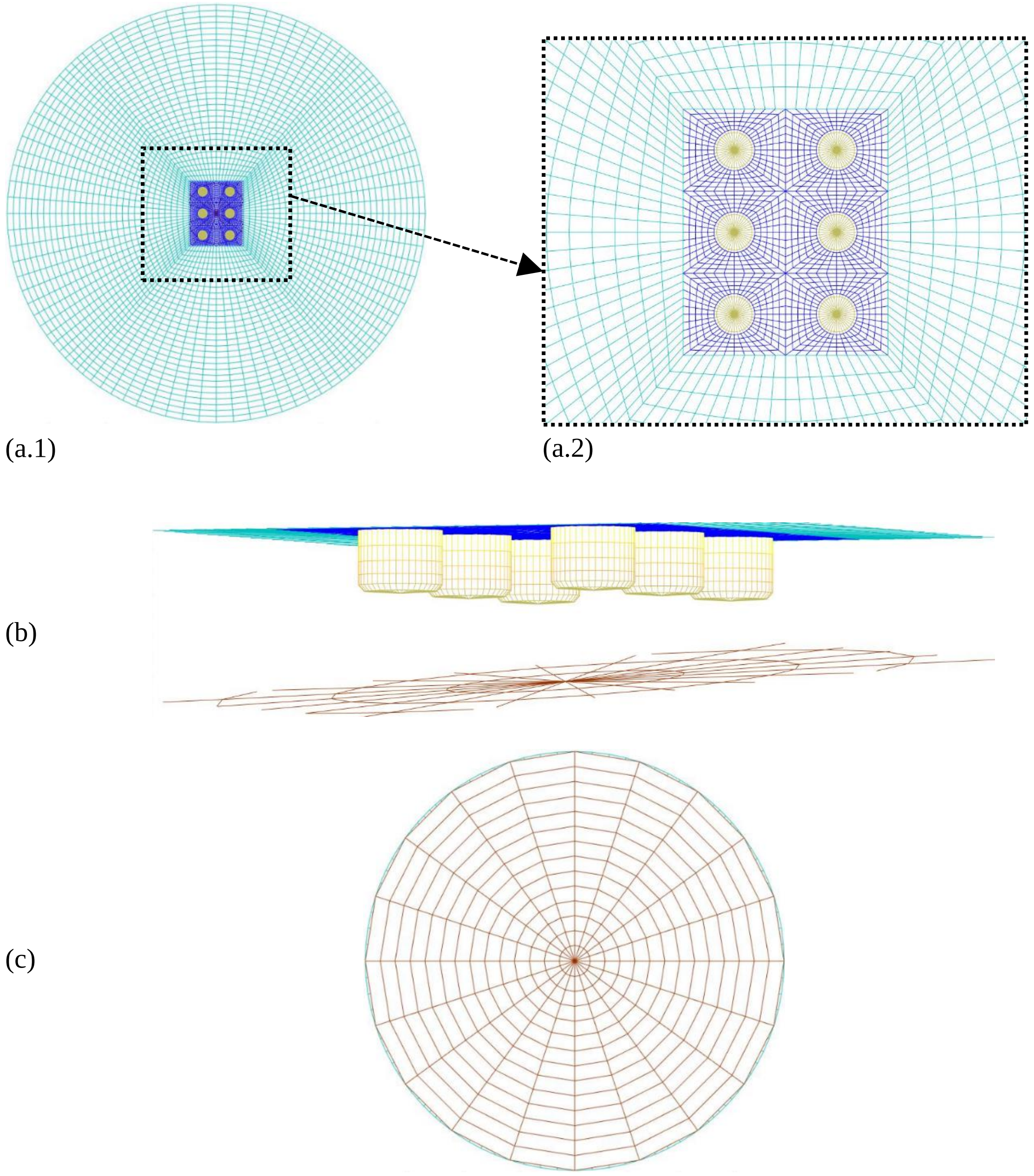

Figure 110: Computational meshes: (a) Free surface far (a.1) and near the WECs (a.2), (b) Side 3D view of the near field and WECs, (c): Variable bottom

The corresponding meshes for the following example of **(5.3)** are: 6x40 on each WEC, 5x40 for each of the near-fields, 30x100 on the far field and 14x20 on the bottom skin. The total elements used for the discretization are then 5920. The total number of subparts are 14. They are depicted in **Fig. 110**, where all the sub-meshes are plotted with different colors.

5.3 Numerical results

A typical example of a WEC array is considered hereupon. An array of 3x2 cylindrical WECs of radius $a=1$ m and of draft to radius ratio of $d/a=1.5$ are installed over a variable depth region.

The depth profile is described by the **Eq. (5.10)**:

$$h(x) = h_m(x) = \begin{cases} h_1 = 5a \text{ m}, \\ \dfrac{h_1 + h_3}{2} - \dfrac{h_1 - h_3}{2} \tanh\left(\alpha_{bot}\pi\left(x - x_{mean}\right)\right) \\ h_3 = 2a \text{ m} \end{cases} \tag{5.10}$$

The non-dimensional frequency is $\omega\sqrt{h_m/g}=1.5$, or equivalently $\omega\sqrt{a/g}=0.8$ is also considered. The horizontal spacing of WECs is $s_1/a=5$ along x-axis and $s_2/a=4$ along y-axis. This spacing in regard to the wavelength is small and thus the interaction of the WECs is strong.

In **Fig. 111** is illustrated the propagating field for 0deg of incident waves, while in **Figs 112**, **113** is shown the diffraction pattern, where is obvious the backscattered wave by the array, the main reflection as well as the scattering effect in the downwave area of the array. The WECs are indicated with white solid lines.

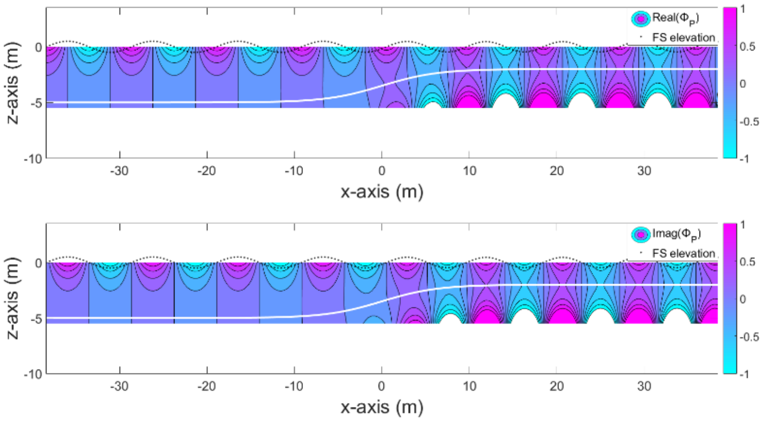

Figure 111: Propagating field (Real and Imag) by CMS (top and side view) for $\omega\sqrt{\alpha/g}$=0.8, 0deg Variable bottom (h_1=5 m, h_3=2 m, α_{bot}=0.05)

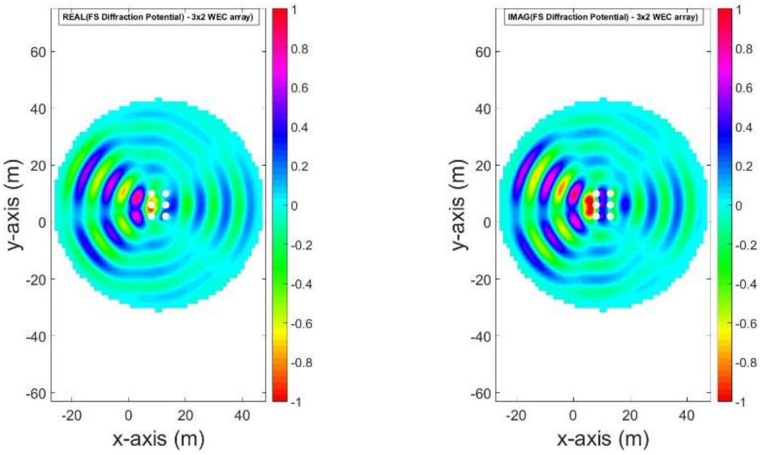

Figure 112: Diffraction field (Real and Imag) (top view) for $\omega\sqrt{\alpha/g}$=0.8, 0deg Variable bottom (h_1=5 m, h_3=2 m, α_{bot}=0.05)

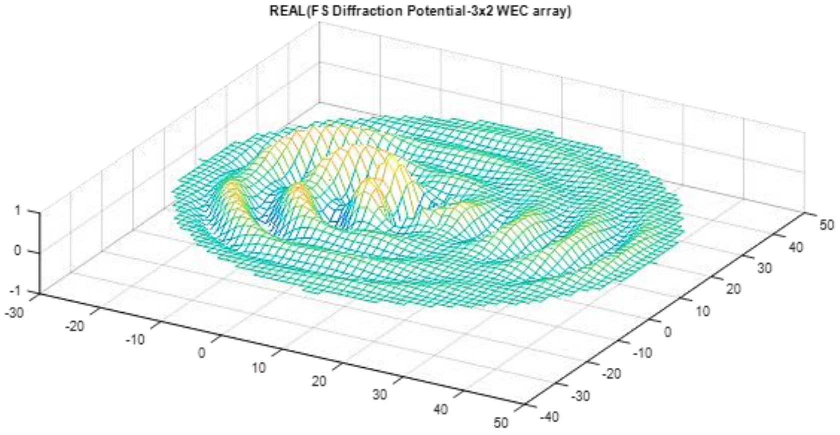

Figure 113: Diffraction field (Real and Imag) (3D view) for $\omega\sqrt{\alpha/g}$=0.8, 0deg Variable bottom (h_1=5 m, h_3=2 m, α_{bot}=0.05)

Same results are also obtained for the 45deg oblique waves (**Figs 114**, **115**, **116**). In this case special comments are added on the diffraction pattern plot, indicating the backscattered wave, the reflected wave as well as the downwave scattering effect (**Fig. 117**).

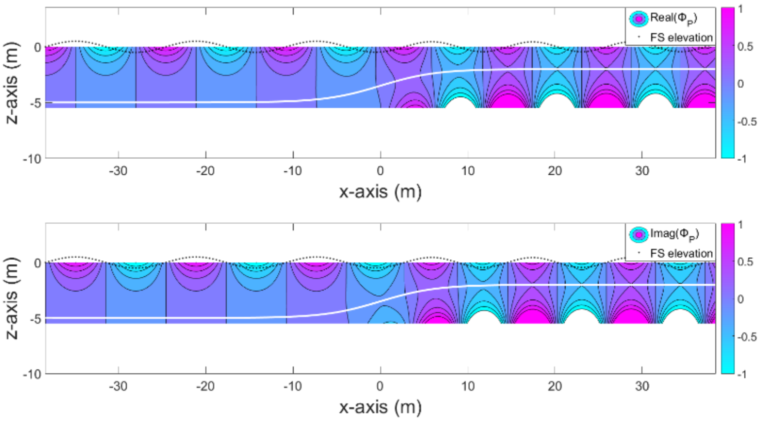

Figure 114: Propagating field (Real and Imag) by CMS (top and side view) for $\omega\sqrt{\alpha/g}=0.8$, 45deg Variable bottom ($h_1=5$ m, $h_3=2$ m, $\alpha_{bot}=0.05$)

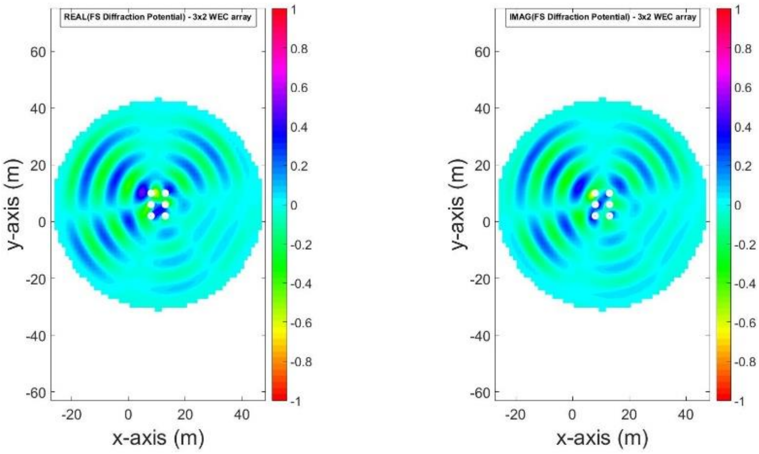

Figure 115: Diffraction field (Real and Imag) (top view) for $\omega\sqrt{\alpha/g}=0.8$, 45deg Variable bottom ($h_1=5$ m, $h_3=2$ m, $\alpha_{bot}=0.05$)

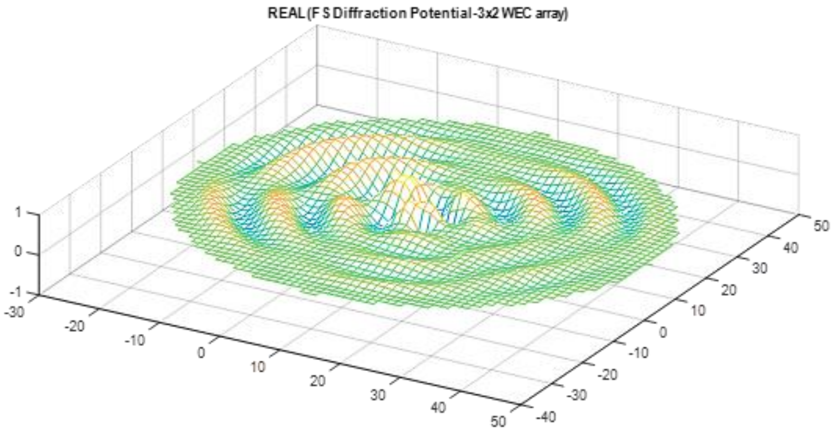

Figure 116: Diffraction field (Real and Imag) (3D view) for $\omega\sqrt{\alpha/g}=0.8$, 45deg Variable bottom ($h_1=5$ m, $h_3=2$ m, $\alpha_{bot}=0.05$)

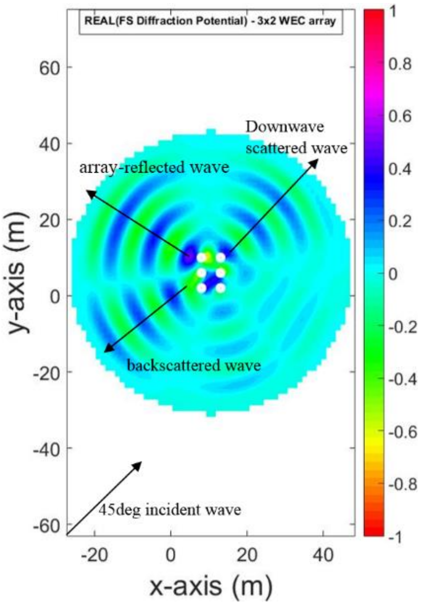

Figure 117: Diffraction field (Real) for the 45deg oblique waves by the 3x2 WEC array for $\omega\sqrt{\alpha/g}$=0.8, 45deg Variable bottom (h_1=5 m, h_3=2 m, α_{bot}=0.05)

The illustration of the heave-radiation potential is based on the assumption of one active WEC. Each time only one active WEC radiates potential by its heave motion, while the other five remain motionless. For better understanding, in **Fig. 118** is depicted a numbering assignment for the WECs of the array.

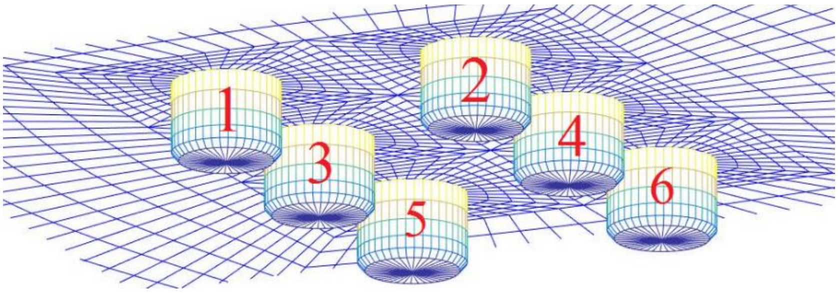

Figure 118: Numbering of the WECs in the 3x2 array configuration

Hereupon, will be presented the radiation potential plots for two cases of different active WECs, namely the WEC No.1 and No.4 and for 45deg of incident waves.

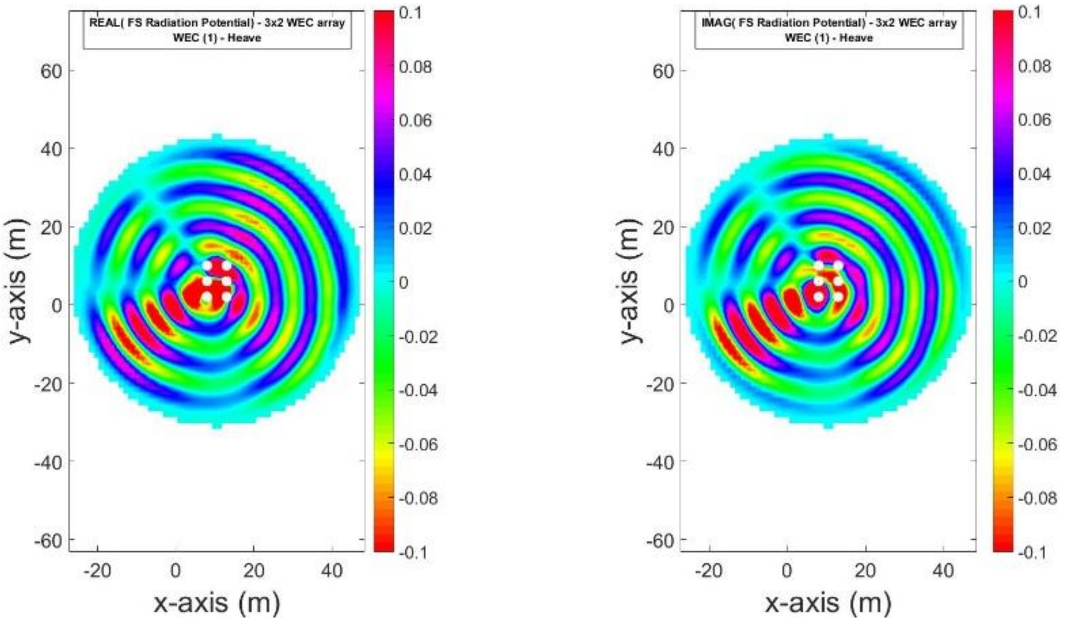

Figure 119: Heave-Radiation field (Real and Imag) (top view) for $\omega\sqrt{\alpha/g}$=0.8, 45deg Variable bottom (h_1=5 m, h_3=2 m, α_{bot}=0.05) – WEC No.1 active

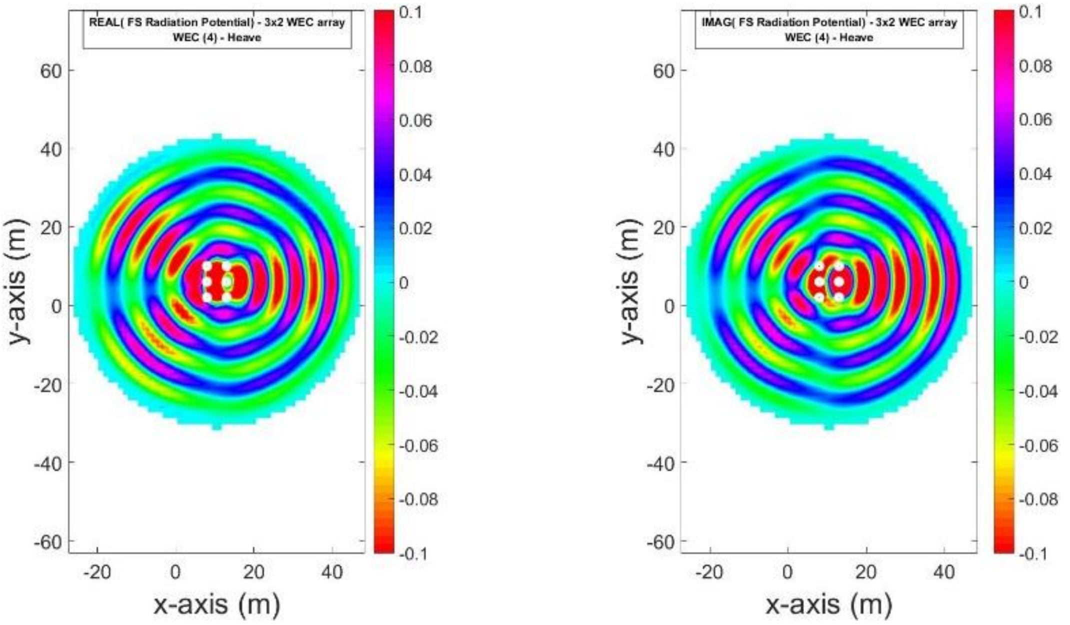

Figure 120: Heave-Radiation field (Real and Imag) (top view) for $\omega\sqrt{\alpha/g}$=0.8, 45deg Variable bottom (h_1=5 m, h_3=2 m, α_{bot} =0.05) – WEC No.4 active

The minimization of the shadowing effect in the downwave region is the main reason behind the layout optimization. The quantification of this wake effect is accomplished through the q-index. Assuming a PTO similar to this of **(4.3.1.1)**, the non-dimensional heave amplitude, in respect to the incident wave amplitude, and the q-index are calculated for the three typical PTO damping values and for 0deg and 45deg wave incident angles. The maximum q-index is 92% for the case of 0deg incident waves and C_{PTO}=5, while it decreases to 65% for the "hardest" PTO of C_{PTO}=20. The relevant q-index for the 45deg wave heading angle are 77% for C_{PTO}=5 and 53% C_{PTO}=20. The results are tabulated in **Table 8**.

Table 8
Array *q*-index for various PTO values and for 0deg and 45deg incident angle over variable bottom

C_{PTO}		5	10	20
$\lvert\xi_3\rvert/(H/2)$		0.86	0.76	0.58
q-index	0deg	0.92	0.80	0.65
	45deg	0.77	0.66	0.53

Finally, in the subsequent **Figs 121** and **122** , the total potential and its absolute value are illustrated in the case of activated WEC No.1 for the above presented sea state of $\omega\sqrt{\alpha/g}$=0.8 and 45deg incident waves, over a variable seafloor.

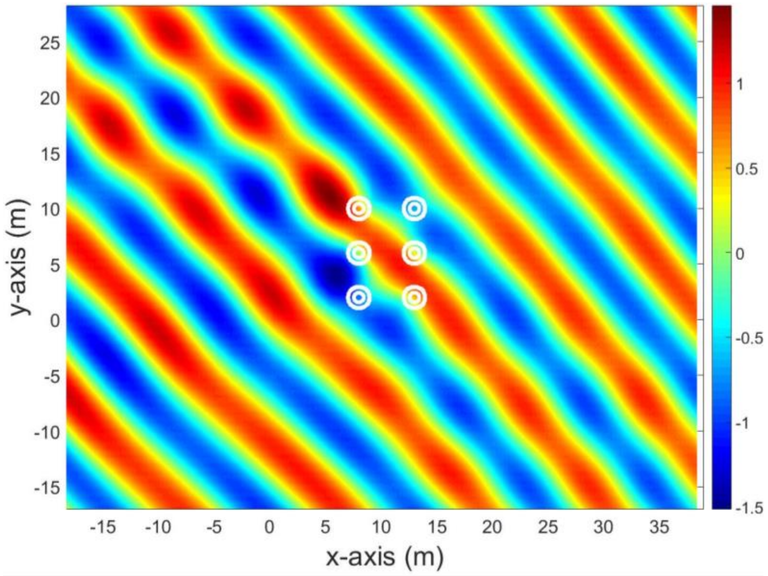

Figure 121: Total field (Real) (top view) for $\omega\sqrt{\alpha/g}$=0.8, 45deg Variable bottom (h_1=5 m, h_3=2 m, α_{bot} =0.05) – WEC No.1 active

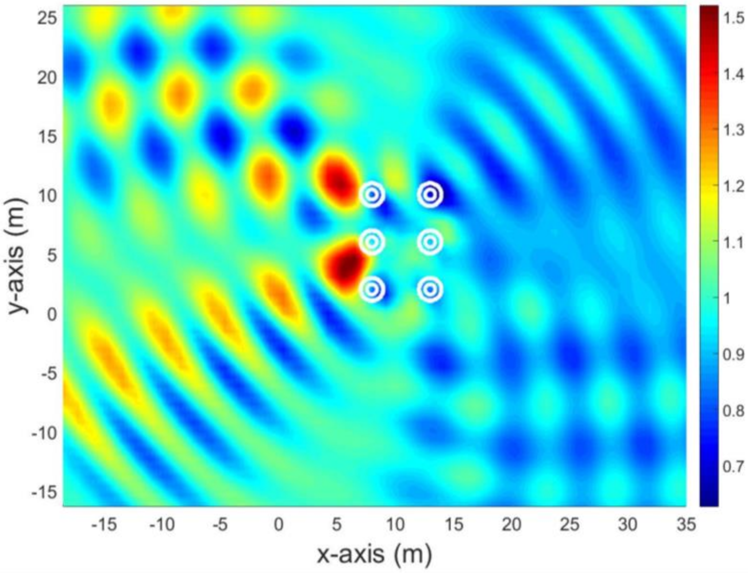

Figure 122: Absolute value of total field (Real) (top view) for $\omega\sqrt{\alpha/g}$=0.8, 45deg Variable bottom (h_1=5 m, h_3=2 m, α_{bot} =0.05) – WEC No.1 active

6

The 2-DOF WEC: Performance evaluation

6.1 The conceptual idea

The analysis of a WEC in heave motion have shown the prospects and the significance of research in this field of eco-friendly power production, regarding computational process coding, design decisions, bathymetry effects and interactions in arrays configuration.

At the same time, the idea of combining more than one degrees of freedom for harnessing the available power by the wave is another perspective on how these systems will be more efficient. Many studies have been carried through upon this subject and pertain to the concept of a WEC with two or more DOFs ([44,95–98]), and therefore able to absorb higher amount of the wave power and achieve more stable power supply to the grid. A typical review of PTOs with more than one power capture mode is presented in **Fig. 123**.

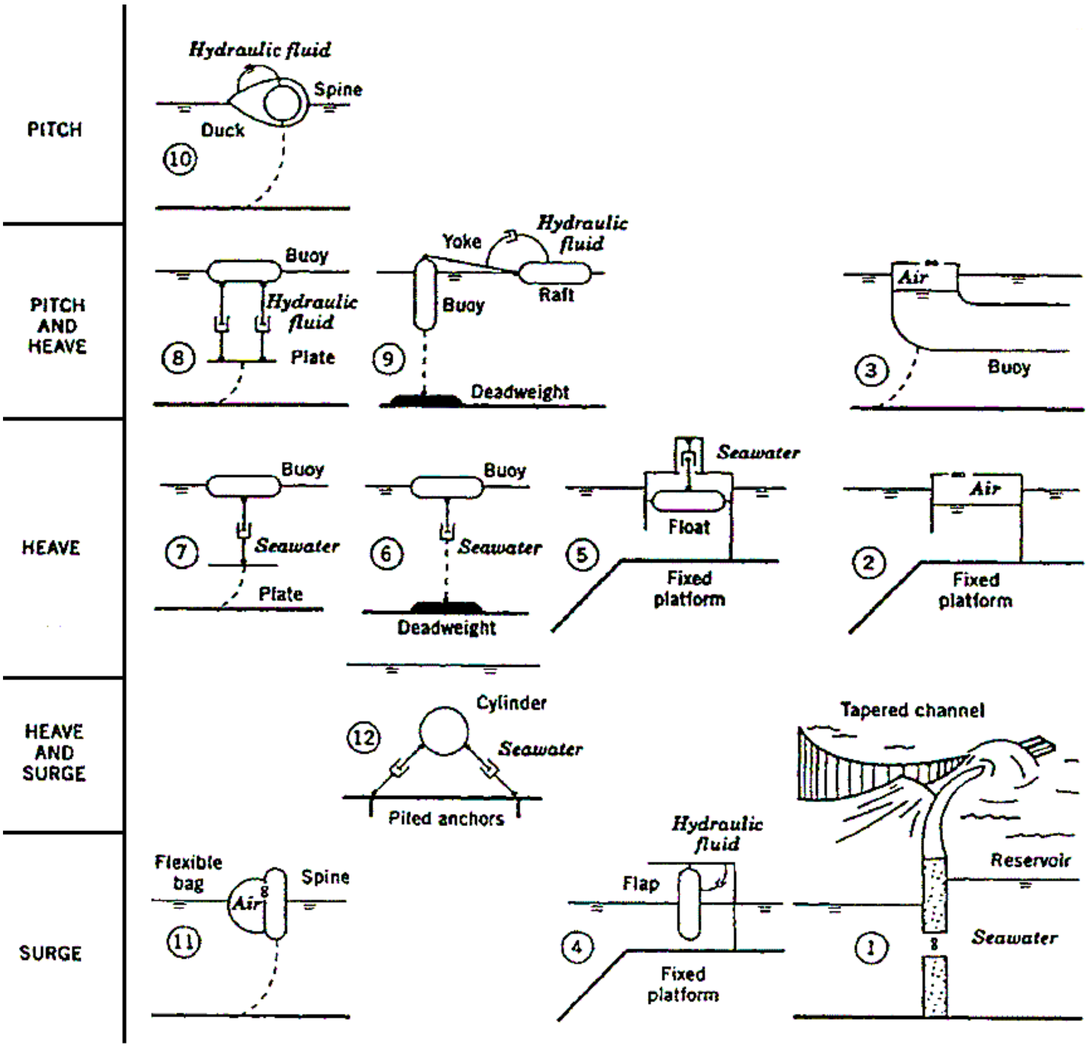

Figure 123: Classification of wave energy PTOs based on the power capture mode [95]

In this specific study the idea of a device in heave-pitch mode will be examined. A typical PTO for these two modes of operation is the No.8 in **Fig.123** and also illustrated in **Fig. 124** where power capture from pitch mode come as a result of differential heave between the two sides of the WEC, which in this case should have probably a large ratio of radius to draft. Otherwise, the PTO for pitch may be totally different than the PTO for heave and this is the general case which will be examined in the following study where damping values for PTO are independent.

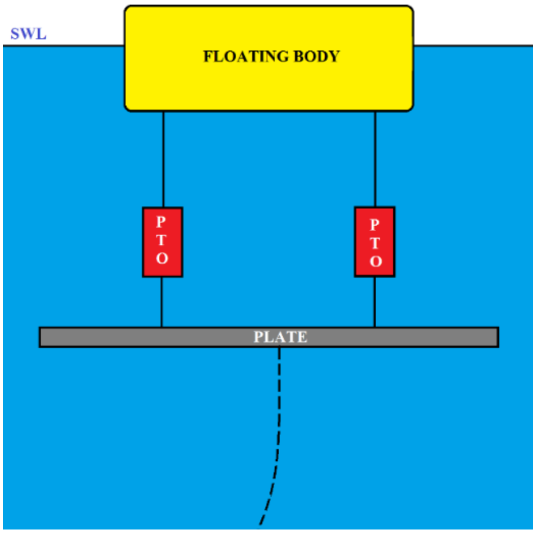

Figure 124: Heave-Pitch PTO configuration for a WEC

6.2 Mathematical formulation

At this time the solution for the responses of heave and pitch will be obtained by the formulation and evaluation of the system of coupled equations. The coupled system of heave-pitch equations is expressed as [99]:

$$D_{33}\xi_3+D_{35}\xi_5=X_{P3}+X_{D3} \tag{6.1}$$

$$D_{53}\xi_3+D_{55}\xi_5=X_{P5}+X_{D5} \tag{6.2}$$

where,

$$D_{33}=-\omega^2(M+A_{33})+i\omega(B_{33}+B_{S3})+C_{33} \tag{6.3}$$

$$D_{35}=-\omega^2(I_{35}+A_{35})+i\omega B_{35}+C_{35} \tag{6.4}$$

$$D_{53}=-\omega^2(I_{53}+A_{53})+i\omega B_{53}+C_{53} \tag{6.5}$$

$$D_{55}=-\omega^2(I_{55}+A_{55})+i\omega(B_{55}+B_{S5})+C_{55} \tag{6.6}$$

The hydrodynamic coefficients of added mass and damping, A_{ij}, B_{ij}, for i, j=3, 5, respectively, as well as the excitation FK and Diffraction heave-forces and pitch-moments, X_{Pi}, X_{Di} for i=3, 5 are calculated by the BEM solver. For the evaluation of the rest of the included coefficients in the above expressions, it should be taken under consideration that the center of gravity is coincident to the center of waterline, so $X_G=0$ and $\overline{GB}=0$, where X_G is the long-center of gravity and $\overline{GB}$ is the vertical distance of the center of gravity from the center of waterline, positively signed when the center of waterline is above the center of mass. The waterline for every investigated geometry is circular and the first and second moments of the waterline , which are: $A_k=\int_A x_k\, dA$ and $A_{km}=\int_A x_k\, x_m\, dA=\pi\frac{D_{wl}^4}{64}$, $k, m=1,2$ where $D_{wl}=2a$ is the diameter of the circular waterline and a is the waterline radius., introduce the following simplifications on the hydrostatic coefficients: $C_{33}=\rho g\pi\alpha^2$, $C_{35}=C_{53}=\rho gA_1=0$, $C_{55}=\rho gA_{22}+Mg\,\overline{GB}=0$. The inertia coefficients are: $I_{35}=I_{53}=-MX_G=0$ and $I_{55}=M\,R_{yy}^2$, where R_{yy} denotes the gyration radius with respect to the transverse axis and , assuming a typical mass distribution near the surface of the WEC, this radius is set to: $R_{yy}=0.7a$.

After the calculation of the involved variables, the response of the WEC can now be obtained. For the evaluation of the normalized power output by the device typical PTO damping values are examined. The Heave-PTO is defined as: [1, 5, 10, 20:10:340] times a mean value of hydrodynamic damping b_{m3} over frequency, which is estimated as $2\pi b_{m3}/m\omega_{R3}=0.12$, where the resonance frequency $\omega_{R3}\sqrt{a/g}=0.7$, thus $B_{PTO3}=B_{s3}=C_{PTO3}\, b_{m3}$. Same PTO assumption is considered for the pitch motion, where the PTO damping is evaluated in regard with a mean value of damping of the system as: [50:10:400] times a mean value of hydrodynamic damping b_{m5} over frequency, which is estimated as $2\pi b_{m5}/m\omega_{R5}=0.01$, where the resonance frequency $\omega_{R5}\sqrt{a/g}=0.45$ and consequently $B_{PTO5}=B_{s5}=C_{PTO5}\, b_{m5}$. Lower values for PTO coefficients, both for heave and pitch mode, are not considered because either are unfeasible by the industry, or allow high resonance amplitudes of RAO and may cause survivability issues, or at last they are not power effective.

The coefficients of D_{35} and D_{53} are, for every geometry, too small, compared with the relevant D_{33} and D_{55}, therefore the coupling is weak for this motion study and the RAOs obtained by the solution of the coupled system are slightly different than the results of the uncoupled heave or pitch equations solution. The evaluation of response and power output will be examined for the eight geometries and both for flat and variable bottom regions of installation.

6.3 Numerical results

6.3.1 *Steady-depth bathymetry*

6.3.1.1 Response evaluation

The coupled system of equations of motion is solved for different combination of PTO damping coefficients for heave and pitch mode. The relevant RAOs and their phases are firstly calculated. An indicative example will be presented in the following figures for the Cylindrical WEC and for three different PTOs for heave and pitch, i.e.: B_{PTO3}=B_{s3}=[1, 10, 100] b_{m3} and B_{PTO5}=B_{s5}=[50, 100, 200] b_{m5}.

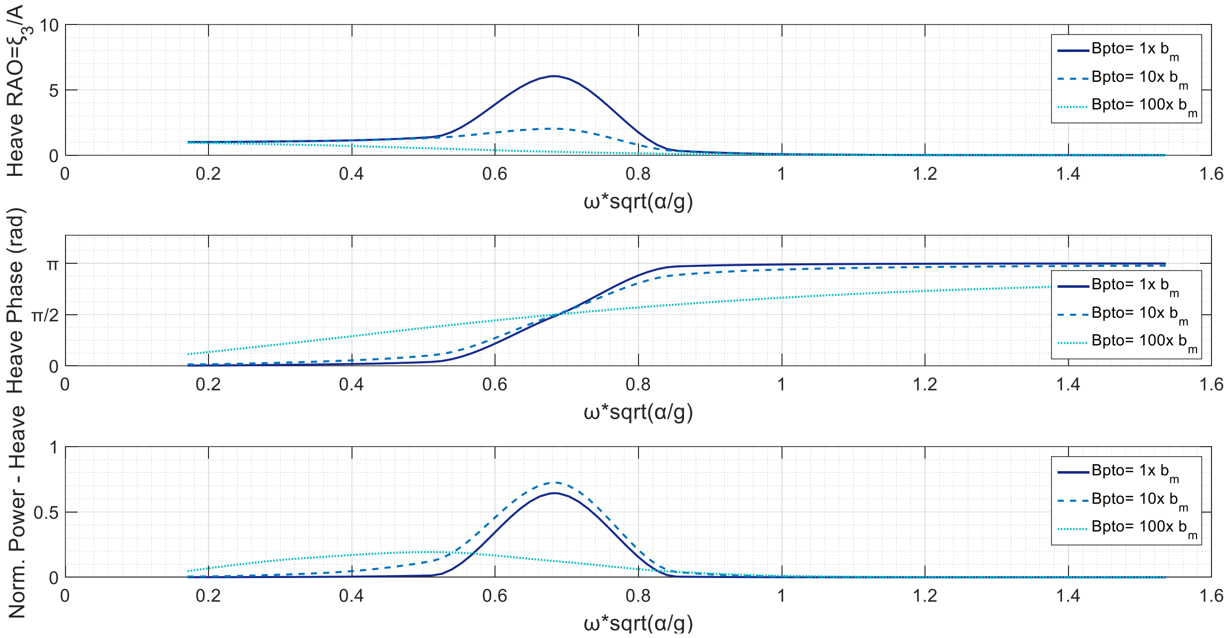

Figure 125: Heave RAO, Phase RAO and Normalized Power Output – Cylindrical WEC – Flat bottom

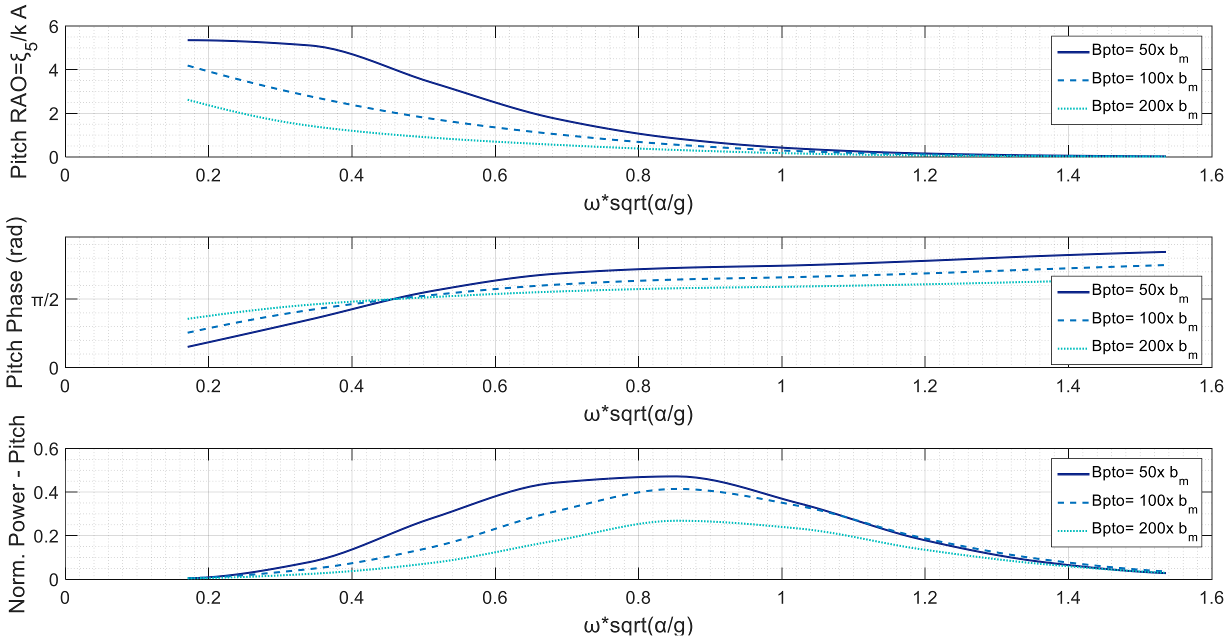

Figure 126: Pitch RAO, Phase RAO and Normalized Power Output – Cylindrical WEC – Flat bottom

Comparing the results of heave-response by the coupled motion (**Fig. 125**) with them of the heaving alone (**Fig. 95**), they are slightly alternated and affected by the pitch mode, due to the very weak coupling. The RAO of pitch is presented in non-dimensional form: (ξ_5/kA) (**Fig. 126**). As illustrated by the normalized power curve of pitch mode this WEC-PTO combination exploits a large bandwidth of wave frequencies with almost 50% performance, resulting in great amounts of absorbed power by this mode and being a testament for the significance of this 2-DOF proposal. In the same way these curves are evaluated for all the 36x36 PTOs combinations and for the eight different shapes of WECs.

6.3.1.2 Performance assessment

The gross power output from each WEC, calculated as the summation of the power output by each mode individually, will be divided by the area of the rectangle and lead to the calculation of the total performance index, which is the main variable for estimating and comparing the performance of the devices. The results are tabulated in **Table 9**.

Table 9
WEC shapes and 2-DOF performance index over flat bottom

WEC design	max {Performance index (Heave+Pitch)} Flat Bottom
Cylindrical	32.43 %
Nailhead-shaped	29.00 %
Disk-shaped	22.04 %
Elliptical	27.12 %
Egg-shaped	26.25 %
Conical	21.99 %
Floater-shaped	19.65 %
Semi-spherical	13.44 %

From the assessment of the above results many interesting conclusions arise. First of all, the Cylindrical WEC is the most efficient design, with the Nailhead-shape being the second most qualified. The optimal design for heave power mode, the Conical WEC, is now withdrawn in the fifth place. Another very interesting comment, has to do with the semi-spherical design. The performance index is almost unchangeable for the 2-DOF scenario, proving the fact that the submerged semi-spherical wetted surface experiences very low pitch excitation, and so absorbs incapable amount of energy, with only 0.4% improvement of the performance index.

The performance index is determined by the PTO coefficients. For every geometry particularly, there are different optimum values for the damping of the two power extracting modes. Therefore, curves of iso-performance lines can be plotted for every geometry, evaluating the performance index as a function of the PTO values. Similar approach to the evaluation of a 3-DOF WEC with a 6-PSS (prismatic pair–spherical pair–spherical pair mechanism have been studied in [97] resulting in an optimum output of normalized power of 46% (126KW for incident wave of $H_{1/3}$=2 m, T_e=6.98 sec and a WEC radius of 5 m), while in the present study, considering only 2 degrees of freedom the relevant values is equal to 32.4%, obtained for the cylindrical shape.

Probably, the optimum PTOs for heave and pitch will be only one couple of values for each geometry, however in the following contour plots the effective values lay inside a wide range, represented by the red area. The evaluation for the exact values of PTOs for the most efficient designs will follow in the next section.

6.3.1.3 PTO damping optimization

The qualified design for the 2-DOF scenario, are the Cylindrical WEC and the Nailhead-shaped WEC. The benefits of the second conceptual design in case of a 2-DOF power absorption has been mentioned previously and is explained by the benefits of combining two cylindrical bodies with a smooth transition from a small-radius high-draught cylinder to a big-radius small-draught cylinder in the free surface, experiencing strong excitation in both of these modes. For the estimation of the exact optimal PTO values, the considered damping coefficients are: $B_{PTO3}=B_{s3}$=[1:1:340] b_{m3} and $B_{PTO5}=B_{s5}$=[50:1:389] b_{m5}. The two optimal shapes and the results are presented in **Fig. 127** and in **Table 10**:

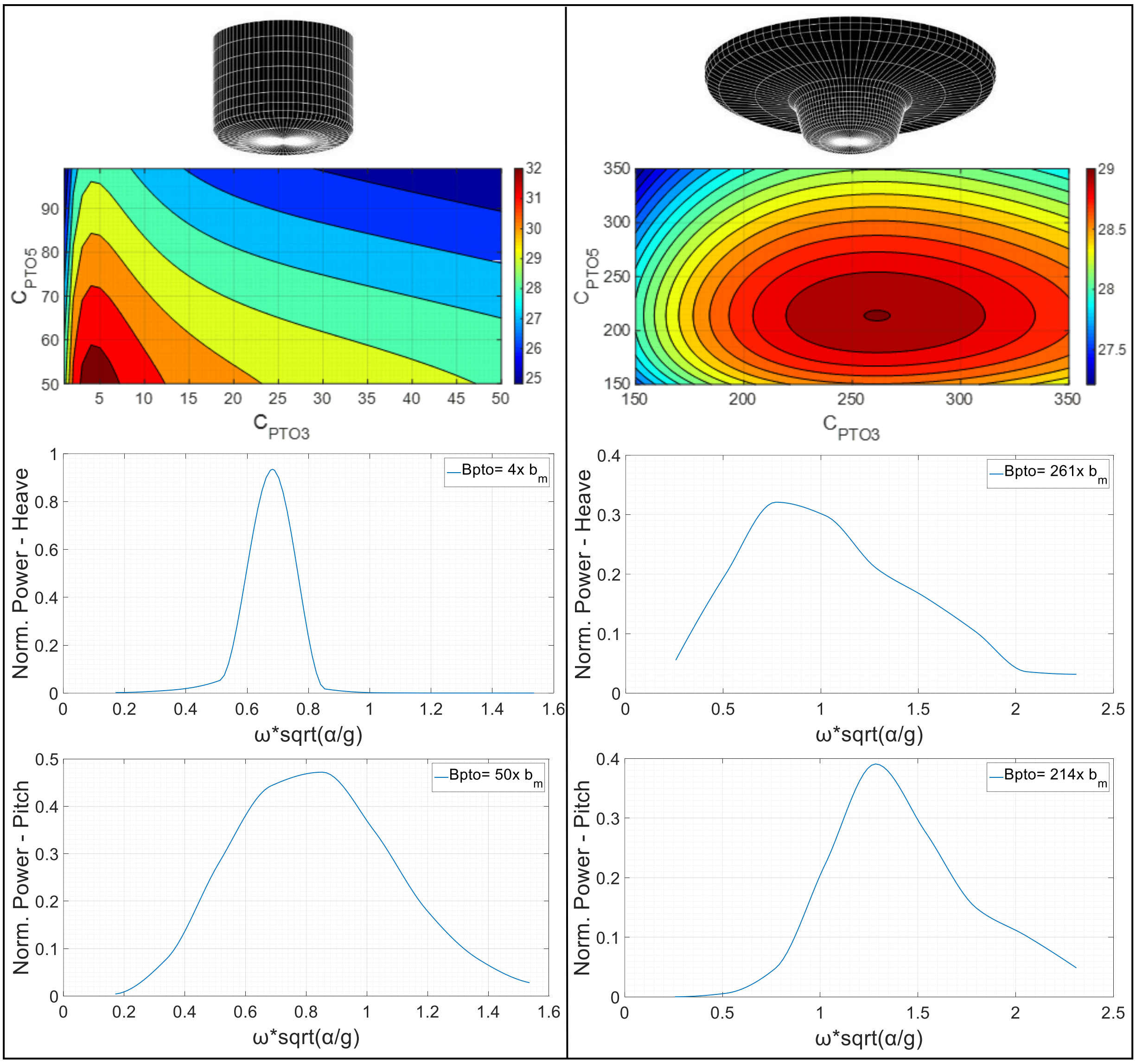

Figure 127: The 2-DOF scenario: optimum WEC shapes, iso-performance curves and normalized power output by each mode over a flat bottom

Table 10
Optimum WEC designs, performance index and PTO couple over flat bottom

Design & Performance	Cylindrical WEC	Nailhead-shaped WEC
Radius (m)	0.28571	0.64654
Draft (m)	0.42857	0.34
Max{Performance index (Heave+Pitch)}	32.47 %	29.00 %
Optimum PTO damping: [C_{PTO3}, C_{PTO5}]	[4, 50]	[261, 214]

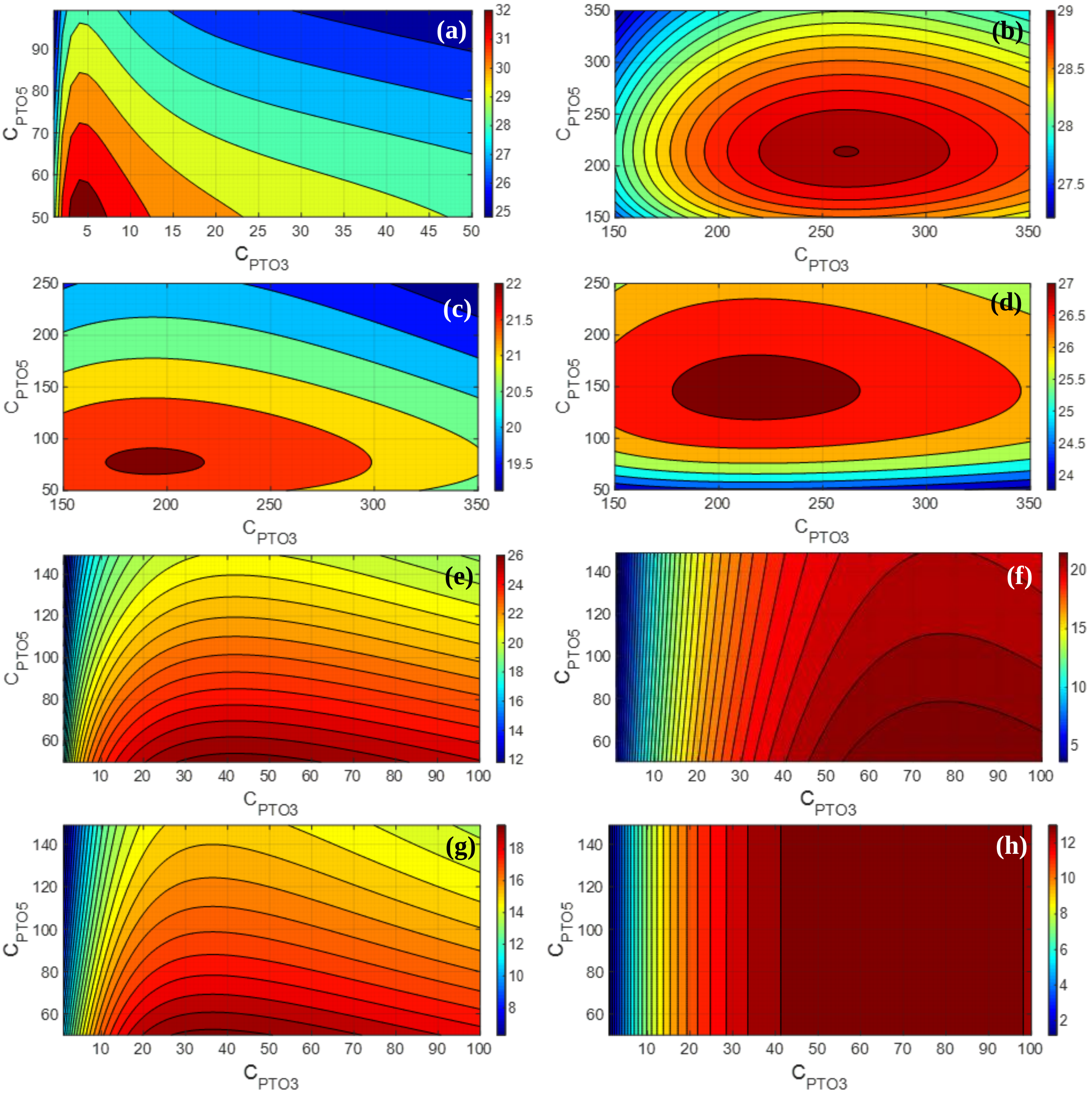

Figure 128: Iso-performance curves for each WEC over flat bottom:
(a) Cylindrical, (b) Nailhead-shaped, (c) Disk-shaped, (d) Elliptical,
(e) Egg-shaped, (f) Conical, (g) Floater-shaped, (h) Semi-spherical

The optimal values for the PTOs in case of the cylindrical WEC are approaching the lower limits of these coefficients, set by the requirements of industry, survival conditions operation and power efficiency, thus despite its superiority over the other candidate, the attainment of such low values of PTO damping may be challenging. The iso-performance contours are depicted, for a utilized for each shape range, in **Fig. 128**, to show the optimum area of PTOs coefficients for every shape, allowing both the direct comparison between the designs and the determination of optimum PTO values.

6.3.2 Variable-depth bathymetry

6.3.2.1 Performance assessment

The investigation of the performance of the above shapes with two power modes over an arbitrary bathymetry is now considered. The bathymetric profile is described by the same equation with the heaving WECs of the **Chapter 4** (**Eq. 4.2**) with h_1=1.2 m, h_2=0.8 m and a_{bot}=0.5:

$$h(x) = h_m - 0.5(h_1 - h_3)\tanh\left(\alpha_{bot}\pi\left(x - x_{mean}\right)\right) \tag{6.7}$$

The PTO damping is described in **(6.2)** and the relevant coefficients are: C_{PTO3} = [1, 5, 10, 20:10:340] and C_{PTO5} = [50:10:400]. For these values the results for the varying seabed scenario are gathered in **Table 11**, along with the results over the flat bottom:

Table 11
WEC shapes and 2-DOF performance index over flat and variable bottom

WEC design	max {Performance index (Heave+Pitch)} Flat Bottom	max {Performance index (Heave+Pitch)} Variable Bottom
Cylindrical	32.43 %	32.00 %
Nailhead-shaped	29.00 %	29.08 %
Disk-shaped	22.04 %	22.31 %
Elliptical	27.12 %	27.26 %
Egg-shaped	26.25 %	25.84 %
Conical	21.99 %	22.07 %
Floater-shaped	19.65 %	19.59 %
Semi-spherical	13.44 %	13.60 %

As proven by comparing the results of the above table, the effects of the variable depth region are not easily predictable on the WECs performance. If only heave-mode is considered then, as concluded in **Chapter 4**, the performance is slightly improved over the varying floor. However, in this case, where both heave and pitch modes contribute to the power output of the device, there are examples of performance improvements and examples of performance pejoration. The highest rated increase of performance index is obtained for the disk shape (+0.27%) and the most intense decrease is espied for the cylindrical shape (-0.43%).

6.3.2.2 PTO damping optimization

Focusing on the most efficient designs, the Cylindrical WEC and the Nailhead-shaped WEC, the optimal values of the PTO damping, will now be recalculated, considering the PTOs range of (**6.3.1.3**) for the varying seabed case and compared with the relevant values for the flat seabed case. The results are presented in **Table 12**, from where it can be deduced that the optimal PTO values are changed for the nailhead shape resulting in almost same performance ratings and remain unchangeable for the cylindrical shape along with an appreciable decrease of performance index.

Table 12
Optimum WEC designs, performance index and PTO couples for flat and variable bottom case

Design & Performance		Cylindrical WEC	Nailhead-shaped WEC
Max{Performance index (Heave+Pitch)}	Flat	32.47 %	29.00 %
	Variable	32.04 %	29.08 %
Optimum PTO damping: [C_{PTO3}, C_{PTO5}]	Flat	[4, 50]	[261, 214]
	Variable	[4, 50]	[276, 213]

6.3.3 Design comparison

The performance of each shape over both bathymetric profiles will be illustrated, through the normalized power output curves, in the following figures, showing that the strongest effect on the performance, induced by the varying seafloor, is detected for the pitch oscillation of the Cylindrical WEC (**Fig. 129**) and for the heave oscillation of the Nailhead-shaped WEC (**Fig. 130**). The total impact on the WECs performance is quantified though the estimation of the performance index, which is found significantly decreased for the cylindrical shape and almost identical (slight increase) for the nailhead-shape.

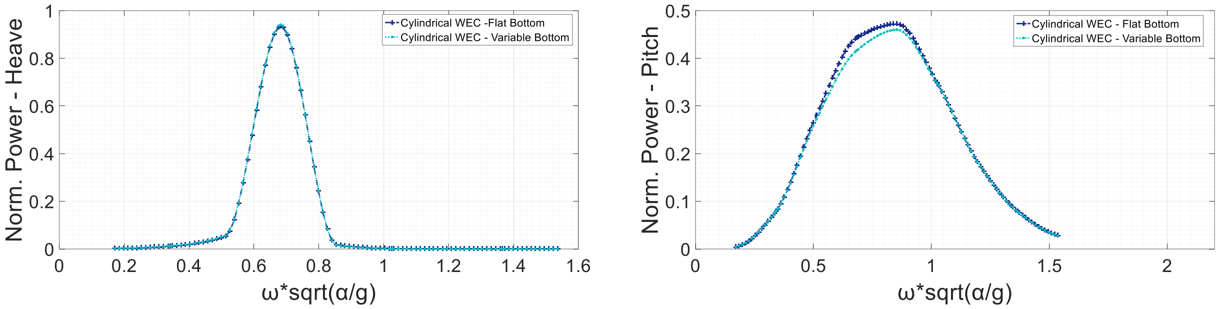

Figure 129: Normalized power output for each power mode (Heave, Pitch) for the Cylindrical WEC over flat and variable bottom (h_1=1.2 m, h_3=0.8 m, α_{bot}=0.5) with optimized PTO.

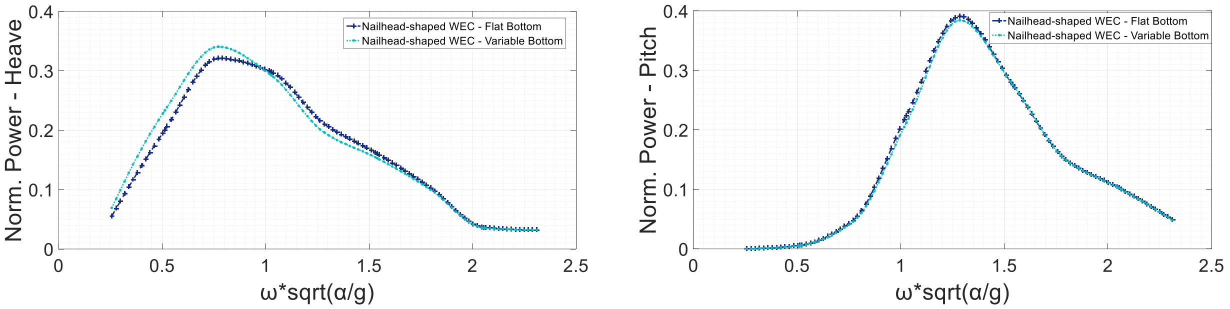

Figure 130: Normalized power output for each power mode (Heave, Pitch) for the Nailhead-shaped WEC over flat and variable bottom (h_1=1.2 m, h_3=0.8 m, α_{bot}=0.5) with optimized PTO.

7
Conclusions and future research

7.1 Discussion and conclusion

In the present thesis several aspects of point absorbers have been investigated, accompanied with the development and implementation of a numerical method for approaching and solving the general hydrodynamic problem.

The proposed computational code is synthesized by Mathworks MATLAB and FORTRAN scripts, developed to evaluate the total potential flow field by means of a utilized BEM for diffraction and radiation problems, combined with the CMS for the propagation field and an optimized PML for the enforcement of the radiation condition. The conceptual method is able to treat the 3D hydrodynamic boundary problem over an arbitrary bathymetry and calculate the response of any number of floating bodies over this region. The method is developed and validated step by step, starting from the 2D wavemaker problem, stepping on the 3D problem of a heaving cylinder over a flat seabed and finally numerically approaching the heave oscillation of a cylinder over a region of general topography.

Afterwards, the range of the examined body geometry is expanded to eight different and common shapes of wave energy converters, pertained to the category of point absorbers. The WECs are capturing the wave energy only through their heaving mode of oscillation. Flat and variable depth, with the form of a smooth coastal shallowing, conditions are examined. The damping of PTO is found one of the most significant tuning parameters and design variables for performance maximization. The Conical WEC is the most efficient design both for the two depth conditions, with a performance index of 17.95% for a PTO coefficient equal to C_{PTO}=77 for flat bottom, and gently improved for operation over a variable bottom with a performance index of 18.10% and C_{PTO}=80, proving that the arbitrary bathymetry will affect the performance of a device and actually may cause a performance upgrade for all of the considered shapes.

The interaction among devices in an array configuration is then upon further research. A farm of 3x2 cylindrical heaving WECs is examined and the potential flow total field is evaluated, resulting in a q-index maximized for 0deg of incident waves and C_{PTO}=5 and being equal to 92% and minimized to 53% for 45deg of incident wave angle and C_{PTO}=20.

Finally, the conceptual idea of combining more than one power modes resulted during the final section in that the cylindrical shape and the nailhead shape are the most efficient for operating both above a flat or a varying seabed, with the Cylindrical WEC being almost 3^{+} % more power effective than the Nailhead-shaped WEC, reaching a performance index of 32.43% over a flat bottom and 32.00% over a smooth shallowing depth profile. The impact of the topographic profile in now not so simple and affects the performance in a non-easily predictable way, causing improvements or worsening of the performance of the devices depending on their shape. The PTOs used now for harnessing power form the sea environment are obtaining two with different damping values, thus the optimization of PTO coefficients has now three design parameters: the geometry of the WEC, the heave-PTO damping and the pitch-PTO damping, and one objective function: the performance index, resulting in 2D contour plots illustrating the iso-performance lines for each WEC and for every couple of PTOs. The bathymetry does also affect the optimal values of PTO damping for each device, and can be accounted as another design constraint.

The main conclusions arising from this research can be presented in brief as:

- The BEM-PML-CMS method is able to treat the general 3D hydrodynamic problem in frequency domain with great reliability, justified by the validation process and upon further utilization for every problem after fine tuning, independently from the geometry of the body, the bathymetry, the number of the floating bodies or the modes of their power capture.
- The PTO damping values are exhibiting constrained lower limits, due to feasibility, survivability and power efficiency issues.
- The ratio of the area below the normalized power curve divided with the area of the surrounding rectangle, defines the performance index and it is a very useful comparing value.
- The Conical WEC is the most efficient design for a heaving point absorber, irrespective to the seabed profile.
- The Cylindrical and the Nailhead-shaped WECs are the ones with the highest performance ratings for the concept of a 2-DOF device, capturing power from heave and pitch modes, regardless the seafloor topography and achieving promising power output levels.
- A varying seafloor can affect appreciably the performance of a floating device, and in many cases may cause increased performance levels indeed.
- Wake effects in arrays configuration might be crucial for the performance of the heaving WECs, and thus in the power output from the whole wave park.
- The optimization of the PTO damping is one of the greatest aspects upon research in the quest of the most efficient design, taking values utilized and specific for each shape and each bathymetric profile case. With the usage of the iso-performance contours the determination of the optimal PTO couple for each shape is effortless.

7.2 Future research proposals

During this research, in the pursuit of the master diploma, side by side with notable results and conclusions many other prospects for future research have emerged and might be a first impetus for the forthcoming activities in this field.

First of all, the examination of the effects by a more steep depth profile will be another area of study with, possibly, many promising results. The idea of a man-made seafloor, like a platform, in order to intentionally disturb the potential field in a desirable way and achieve better performance levels is another novelty opportunity.

Secondly, the shape optimization has many other prospects of research. For example, the conical shape, one of the most efficient for heaving point absorbers, is a general shape with numerous design variables, such as waterline radius, draft and deadrise angle, which can be optimized, resulting in an even better performance. More sophisticated designs is definitely on hand for future studies and their aspects can be objectives of an algorithmic optimizer scheme.

Treating the problem in terms of the presented method, the consideration of *n*-power modes is now the next step to obtain maximized power output by devices of this type, reaching ideally all the six modes of oscillation as contributors to the total power output of a concept design with a more sophisticated PTO. In addition, the investigation of different control strategies and their evaluation will be certainly part of the recent trend in the wave energy industry. Engagement of the mechanical engineering sector is essential for determining crucial parameters, such as survivability limits, PTO coefficient ranges, manufacturing processes and operation & maintenance issues.

The optimization of an array layout is another design variable which affects in a very serious way the performance. The minimization of wake effects and a strategic design taking advantage of the constructive interaction effect will be the aim of future research for establishing an effective way for capturing great amount of energy from the oceans.

Examination of techno-economical parameters and environmental impacts of WECs are unquestionably one already marching area of research and development activities in companies and organizations around the world and of course a required part of study for every well-rounded proposal.

Finally, the generalization of the computational code in a format to treat any geometry over any bathymetry, through simple commands, will be an, at least, practical asset. The implementation of coding optimization techniques and of a user friendly interface will finally assist the total research and development work. Simply by controlling some nodes, the researcher will provide the code with the desirable geometry of the device and the relevant bathymetric profile of this specific region of installation. This task will also be expanded to treat arrays of WECs. The scale up in computational terms, accompanied with state of the art CFD tools and hybrid methods will provide higher accuracy and more detail-oriented design. The interconnection between a computational code for wave energy converters, a mapping tool providing the bathymetric profile in every region of interest and of a wave forecasting model introducing the wave spectrum will be a cutting-edge evolution in the modelling of wave energy technologies and will be the first step for a real-time time-domain model for observing, assessing and controlling the devices.

8

References

[1] Renewables in Electricity Production - Statistics Map by Region | Enerdata https://yearbook.enerdata.net/renewables/renewable-in-electricity-production-share.html (accessed October 16, 2018).

[2] BP Statistical Review of World Energy. 67th Edition. 2018:56.

[3] European Environmental Agency. Renewable energy in Europe — Recent growth and knock-on effects. 2016. doi:10.2800/123258.

[4] NASA: Global Climate Change Facts https://climate.nasa.gov/vital-signs/ (accessed October 16, 2018).

[5] The EU 2020 Schedule https://askjaenergy.com/2013/03/25/10-twh-of-icelandic-green-energy-available/ (accessed October 16, 2018).

[6] Eurostat - Energy from renewable sources https://ec.europa.eu/eurostat/statistics-explained/index.php/Energy_from_renewable_sources (accessed October 16, 2018).

[7] Healy S, Li L. Requested by the ENVI committee: China ’ s climate policies with an emphasis on carbon trading markets. 2018. ISBN: 978-92-846-3998-4

[8] Hales D. Renewables 2018 - Global Status Report. REN21. 2018. ISBN: 9783981891133

[9] European Commission - Ocean Energy https://ec.europa.eu/jrc/en/news/new-technologies-ocean-energy-sector (accessed October 31, 2018).

[10] Ocean Energy Systems (OES). Annual Report 2016. 2016:188.

[11] López I, Andreu J, Ceballos S, Martínez De Alegría I, Kortabarria I. Review of wave energy technologies and the necessary power-equipment. Renew Sustain Energy Rev 2013;27:413–34. doi:10.1016/j.rser.2013.07.009.

[12] Mørk G, Barstow S, Kabuth A, Pontes MT. Assessing the Global Wave Energy Potential. 29th Int Conf Ocean Offshore Arct Eng Vol 3 2010:447–54. doi:10.1115/OMAE2010-20473.

[13] Soukissian TH, Denaxa D, Karathanasi F, Prospathopoulos A, Sarantakos K, Iona A, et al. Marine renewable energy in the Mediterranean Sea: Status and perspectives. Energies 2017;10:1–56. doi:10.3390/en10101512.

[14] Drew B, Plummer AR, Sahinkaya MN. A review of wave energy converter technology. Proc Inst Mech Eng Part A J Power Energy 2009;223:887–902. doi:10.1243/09576509JPE782.

[15] World Energy Council. World Energy Resources: Marine Energy 2016. 2016:79. doi:http://www.worldenergy.org/wp-content/uploads/2013/09/Complete_WER_2013_Survey.pdf.

[16] Orbital Marine Power https://orbitalmarine.com/news (accessed October 18, 2018).

[17] Raventos A, Sarmento A, Neumann F, Matos N. Projected Deployment and Costs of Wave Energy in Europe. 3rd Int Conf Ocean Energy 2010:12–7. doi:10.1016/j.electacta.2004.11.040.

[18] Rusu E, Onea F. A review of the technologies for wave energy extraction. Clean Energy 2018;2:10–9. doi:10.1093/ce/zky003.

[19] Vosough A. Wave Energy. Int J Multidiscip Sci Eng 2011;2:60–3.

[20] Bonovas M. Modeling of operation and optimum design of a wave power take-off system with energy storage. National Technical University of Athens. 2017.

[21] Falnes J, Hals J. Heaving buoys, point absorbers and arrays. Philos Trans R Soc A Math Phys Eng Sci 2012;370:246–77. doi:10.1098/rsta.2011.0249.

[22] Falcão AF d. O. Wave energy utilization: A review of the technologies. Renew Sustain Energy Rev 2010;14:899–918. doi:10.1016/j.rser.2009.11.003.

[23] Catch the wave | MIT News http://news.mit.edu/2008/waves-portugal-tt1217 (accessed October 20, 2018).

[24] Tapered Channel Wave Energy https://taperedchannelwaveenergy.weebly.c

om/how-does-it-work.html (accessed October 20, 2018).

[25] Oscillating Water Column Devices http://coastalenergyandenvironment.web.unc.edu/ocean-energy-generating-technologies/wave-energy/oscillating-water-column-devices/ (accessed October 20, 2018).

[26] Chatzigiannakou M, Dolguntseva I, Leijon M. Offshore Deployments of Wave Energy Converters by Seabased Industry AB. J Mar Sci Eng 2017;5:15. doi:10.3390/jmse5020015.

[27] Seabased-Invesdor https://www.invesdor.com/en/pitches/899 (accessed October 20, 2018).

[28] OPT - Offshore Technology https://www.offshore-technology.com/features/feature-bringing-wave-power-offshore-industry/ (accessed October 20, 2018).

[29] Ocean Power Technologies https://www.oceanpowertechnologies.com/ (accessed May 4, 2018).

[30] AWS Ocean Energy http://www.awsocean.com/ (accessed October 19, 2018).

[31] CETO - Carnegie Clean Energy https://www.carnegiece.com/wave/what-is-ceto/ (accessed October 20, 2018).

[32] Li Y, Yu Y-H. A synthesis of numerical methods for modeling wave energy converter-point absorbers. vol. 16. 2012. doi:10.1016/j.rser.2011.11.008.

[33] EMEC - Pelamis Wave Power http://www.emec.org.uk/about-us/wave-clients/pelamis-wave-power/ (accessed October 20, 2018).

[34] Youssef J, Matar J, Rahme P, Bou-Mosleh C. A Nearshore Heaving-Buoy Sea Wave Energy Converter for Power Production. Procedia Eng 2016;145:136–43. doi:10.1016/j.proeng.2016.04.032.

[35] Aquamarine Power http://www.aquamarinepower.com/ (accessed October 20, 2018).

[36] SEEWEC http://www.seewec.org/wp6.html (accessed October 20, 2018).

[37] Kofoed JP, Frigaard P, Kramer M. Recent Developments of Wave Energy Utilization in Denmark. Proc Work Renew Ocean Energy Util 20th Annu Conf 2006:8.

[38] Wavestarenergy http://wavestarenergy.com/ (accessed October 20, 2018).

[39] Bevilacqua.G, Zanuttigh.B. Overtopping Wave Energy Converters : general aspects and stage of development. Int Coast Eng Proc 2011:21. doi:10.6092/unibo/amsacta/3062.

[40] Wavedragon http://www.wavedragon.net/ (accessed October 20, 2018).

[41] EMEC - Wave devices http://www.emec.org.uk/marine-energy/wave-devices/ (accessed October 20, 2018).

[42] Titah-Benbouzid H., Benbouzid M. , An Up-to-Date Technologies Review and Evaluation of Wave Energy Converters. Int. Rev. Elec. Eng.-IREE, 2015; 10 (1):pp.52-61. doi:<10.15866/iree.v10i1.5159>. <hal-01153767>

[43] Wang L, Isberg J, Tedeschi E. Review of control strategies for wave energy conversion systems and their validation: the wave-to-wire approach. Renew Sustain Energy Rev 2018;81:366–79. doi:10.1016/j.rser.2017.06.074.

[44] Sergiienko NY. Three-Tether Wave Energy Converter : Hydrodynamic Modelling , Performance Assessment and Control. 2018.

[45] The CorPower Wave Energy Converter http://www.corpowerocean.com/corpower-technology/corpower-wave-energy-converter/ (accessed October 18, 2018).

[46] Falnes J. A review of wave-energy extraction. Mar Struct 2007;20:185–201. doi:https://doi.org/10.1016/j.marstruc.2007.09.001.

[47] Liu Y, An Introduction to the Boundary Element Method (BEM) and Its Applications in Engineering. 2013:1–43.

[48] Wrobel LC. The boundary element method. Vol.2: Applications in solids and structures 2002;2:598. ISBN: 0470842989.

[49] Humpherys CM. Application of an Isogeometric Boundary Element Method to the Calculation of Acoustic Radiation Modes and Their Efficiencies. 2014.

[50] Prössdorf S. Kress, R., Linear Integral Equations. Berlin etc., Springer-Verlag 1989. XI, 299 pp., DM 78,00. ISBN 3-540-50616-0 (Applied Mathematical Sciences 82). ZAMM - J Appl Math Mech / Zeitschrift Für Angew Math Und Mech;71:504. doi:10.1002/zamm.19910711207.

[51] Belibassakis KA. Engineering Analysis with Boundary Elements A boundary element method for the hydrodynamic analysis of

floating bodies in variable bathymetry regions 2008;32:796–810. doi:10.1016/j.enganabound.2008.02.003.

[52] Antes H. A Short Course on Boundary Element Methods. Inst Fur Angew Mech 2010:1–118.

[53] Muskhelishvili NI. Some Basic Problems of the Mathematical Theory of Elasticity: Fundamental Equations, Plane Theory of Elasticity, Torsion, and Bending. P. Noordhoff; 1953.

[54] Heinrich H. S. G. Mikhlin, Variational Methods in Mathematical Physics. (International Series of Monographs in Pure and Applied Mathematics, Volume 50) Oxford, Edinburgh, London, New York, Paris, Frankfurt 1964. Pergamon Press. - J Appl Math Mech;45:270. doi:10.1002/zamm.19650450439.

[55] Polyanin A, Manzhirov A. Handbook of Integral Equations. 1998. ISBN: 978-0849328763

[56] Belibassakis KA, Gerostathis TP, Kostas K V, Politis CG, Kaklis PD, Ginnis AI, et al. A BEM-isogeometric method for the ship wave-resistance problem. Ocean Eng 2013;60:53–67. doi:https://doi.org/10.1016/j.oceaneng.2012.12.030.

[57] Gao Z, Zou Z. A NURBS-based high-order panel method for three-dimensional radiation and diffraction problems with forward speed. Ocean Eng 2008;35:1271–82.

[58] Shirkol AI, Nasar T. Coupled Boundary Element Method and Finite Element Method for Hydroelastic Analysis of Floating Plate. J Ocean Eng Sci 2017;3:19–37. doi:10.1016/j.joes.2017.11.003.

[59] Ghassabzadeh M, Ghassemi H, Saryazdi MG. Determination of hydrodynamics characteristics of marine propeller using hydro-elastic analysis. Brodogradnja 2013;64:40–5.

[60] Beer G, Smith I, Duenser C. The Boundary Element Method with Programming: For Engineers and Scientists. Bound Elem Method with Program Eng Sci. 2008. ISBN: 978-3211715765

[61] Katz J, Plotkin A. Low Speed Aerodynamics. 2001. ISBN: 978-0521665520

[62] L. Thermos. A boundary element method for the hydrodynamic analysis of floating bodies in variable bathymetry regions. National Technical University of Athens. 2018.

[63] Coddington E a., Levinson N. Theory of ordinary differential equations. 1984. ISBN: 978-0898747553

[64] Wave Generators - Edinburgh Designs http://www4.edesign.co.uk/waves/some-wave-1/ (accessed October 9, 2018).

[65] Kusumawinahyu WM, Karjanto N, Klopman G. Linear theory for single and double flap wavemakers. J. Indones. Math. Soc. (MIHMI) Vol. 12, No. 1 (2006), pp. 41–57.

[66] Galvin CJ, (U.S.) CERC. Wave-height prediction for wave generators in shallow water. 1964

[67] Voss S, Martello S, Osman IH, Roucairol C, Taylor RE, Dean RG, et al. Water Wave Mechanics for Engineers and Scientists. vol. 7. 1999. doi:10.1017/CBO9781107415324.004.

[68] Yeung RW. Added mass and damping of a vertical cylinder in finite-depth waters. Appl Ocean Res 1981;3:119–33. doi:10.1016/0141-1187(81)90101-2.

[69] Academy USN. Hydrodynamic coefficients for vertical circular cylinders at finite depth 1981;8:25–63.

[70] Garrett C JR. Wave forces on a circular dock. J Fluid Mech 1971;46:129–39. doi:10.1017/S0022112071000430.

[71] Black JL, Mei CC, Bray MCG. Radiation and scattering of water waves by rigid bodies. J Fluid Mech 1971;46:151–164. doi:10.1017/S0022112071000454.

[72] Belibassakis KA, Athanassoulis GA. A coupled-mode system with application to nonlinear water waves propagating in finite water depth and in variable bathymetry regions. Coast Eng 2011;58:337–50. doi:10.1016/j.coastaleng.2010.11.007.

[73] Yeung RW. Numerical Methods in Free-Surface Flows. Annu Rev Fluid Mech 1982;14:395–442. doi:10.1146/annurev.fl.14.010182.002143.

[74] Davies AM, Stephens C V. Comparison of the finite difference and Galerkin methods as applied to the solution of the hydrodynamic equations. Appl Math Model 1983;7:226–40. doi:10.1016/0307-904X(83)90076-8.

[75] Belibassakis KA, Athanassoulis GA. Ship Dynamics. National Technical University of Athens. 2012.

[76] Turkel E, Yefet A. Absorbing PML boundary layers for wave-like equations. Appl Numer Math 1998;27:533–57. doi:10.1016/S0168-9274(98)00026-9.

[77] Filippas ES, Belibassakis KA. Hydrodynamic analysis of flapping-foil thrusters operating beneath the free surface and in waves. Eng Anal Bound Elem 2014;41:47–59. doi:10.1016/j.enganabound.2014.01.008.

[78] Mei CC. The Applied Dynamics of Ocean Surface Waves. World Scientific; 1989. ISBN: 9789971507893

[79] Wehausen J V. The Motion of Floating Bodies. Ann. Rev. Fluid Mech. 1971;3:237–268.

[80] Sjökvist L, Wu J, Ransley E, Engström J, Eriksson M, Göteman M. Numerical models for the motion and forces of point-absorbing wave energy converters in extreme waves. Ocean Eng 2017;145:1–14. doi:10.1016/j.oceaneng.2017.08.061.

[81] Belibassakis K, Bonovas M, Rusu E. A Novel Method for Estimating Wave Energy Converter Performance in Variable Bathymetry Regions and Applications. Energies 2018;11:2092. doi:10.3390/en11082092.

[82] Belibassakis KA, Gerostathis Th.P, Athanassoulis G.A. A 3D-BEM coupled-mode method for WEC arrays in variable. 2014.

[83] Athanassoulis G.A, Belibassakis KA. A consistent coupled-mode theory for the propagation of small-amplitude water waves over variable bathymetry regions 1999;389:275–301. doi:https://doi.org/10.1017/S0022112099004978

[84] Belibassakis KA, Athanassoulis GA, Gerostathis TP. A coupled-mode model for the refraction-diffraction of linear waves over steep three-dimensional bathymetry. Appl Ocean Res 2001;23:319–36. doi:10.1016/S0141-1187(02)00004-4.

[85] EMEC - CorPower Ocean http://www.emec.org.uk/about-us/wave-clients/corpower-ocean/ (accessed November 24, 2018).

[86] Pinterest https://gr.pinterest.com/ (accessed November 24, 2018).

[87] SINN Power https://www.sinnpower.com/ (accessed November 24, 2018).

[88] Blommaert C. Composite Floating ’ Point Absorbers ’ for Wave Energy Converters : Survivability Design , Production Method and Large-Scale Testing. 2010.

[89] Backer G. Hydrodynamic design optimization of wave energy converters consisting of heaving point absorbers. 2009. doi:10.1017/CBO9781107415324.004.

[90] Dölerud E. Automated optimisation of a heaving point absorber. 2012.

[91] Mavrakos SA, McIver P. Comparison of methods for computing hydrodynamic characteristics of arrays of wave power devices. Appl Ocean Res 1997;19:283–91. doi:10.1016/S0141-1187(97)00029-1.

[92] Charrayre F, Peyrard C, Benoit M, Babarit A. A Coupled Methodology for Wave-Body Interactions at the Scale of a Farm of Wave Energy Converters Including Irregular Bathymetry 2014:V08AT06A043.

[93] Devolder B, Stratigaki V, Troch P, Rauwoens P. CFD Simulations of Floating Point Absorber Wave Energy Converter Arrays Subjected to Regular Waves. Energies 2018;11:641. doi:10.3390/en11030641.

[94] De Chowdhury S, Nader J-R, Sanchez AM, Fleming A, Winship B, Illesinghe S, et al. A review of hydrodynamic investigations into arrays of ocean wave energy converters. Fluid Dyn 2015. doi: arXiv.org > physics >arXiv:1508.00866

[95] Brooke J. Wave Energy Conversion. Elsevier Science; 2003. ISBN: 9780080543703

[96] Zhang Z, Nielsen SRK, Basu B. Dynamics and Control of the GyroPTO Wave Energy Point Absorber under Sea Waves. Procedia Eng 2017;199:1828–33. doi:10.1016/j.proeng.2017.09.098.

[97] Ye Y, Chen W. Frequency- and time-domain analysis of a multi-degree-of-freedom point absorber wave energy converter. Adv Mech Eng 2017;9:1–10. doi:10.1177/1687814017722081.

[98] Davis AF, Thomson J, Mundon TR, Fabien BC. Modeling and Analysis of a Multi Degree of Freedom Point Absorber Wave Energy Converter. Vol 8A Ocean Eng 2014:V08AT06A046. doi:10.1115/OMAE2014-23475.

[99] Belibassakis KA, Filippas ES. Ship propulsion in waves by actively controlled flapping foils. Appl Ocean Res 2015;52:1–11. doi:10.1016/j.apor.2015.04.009.

[100] Ergatoudis I, Irons BM, Zienkiewicz OC. Curved, isoparametric, “quadrilateral”

elements for finite element analysis. Int J Solids Struct 1968;4:31–42. doi:https://doi.org/10.1016/0020-7683(68)90031-0.

[101] Hess JL, Smith AMO. Calculation of potential flow about arbitrary bodies. Prog Aerosp Sci 1967;8:1–138. doi:https://doi.org/10.1016/0376-0421(67)90003-6.

[102] Stanford University - Modeling in geotechnical engineering https://web.stanford.edu/class/cee296/ (accessed November 16, 2018).

[103] Hess JL, Company DA, Corporation MD. Calculation of Potential Flow about Arbitrary Three-dimensional Lifting Bodies: Final Technical Report. NTIS; 1972.

[104] Newman JN. Distributions of sources and normal dipoles over a quadrilateral panel. J Eng Math 1986;20:113–26. doi:10.1007/BF00042771.

[105] Massel SR. Extended refraction-diffraction equation for surface waves. 1992;19:97-126. doi:https://doi.org/10.1016/0378-3839(93)90020-9

[106] Crowley SH, Porter R, Evans D V. A submerged cylinder wave energy converter with internal sloshing power take off. Eur J Mech B/Fluids 2014;47:108–23. doi:10.1016/j.euromechflu.2014.03.008.

[107] Kapsoulis D, Tsiakas K, Trompoukis X, Asouti V, Giannakoglou K. Evolutionary multi-objective optimization assisted by metamodels, kernel PCA and multi-criteria decision making techniques with applications in aerodynamics. Appl Soft Comput J 2018. doi:10.1016/j.asoc.2017.11.046.

[108] Cretel JAM, Lightbody G, Thomas GP, Lewis AW. Maximisation of energy capture by a wave-energy point absorber using model predictive control. vol. 18. IFAC; 2011. doi:10.3182/20110828-6-IT-1002.03255.

[109] CDIP: Station-185 Data https://bit.ly/2E3lkC8 (accessed June 27, 2018).

Appendix A

The quadrilateral elements on BEM

A.1 Quad-elements on BVPs

In the presented formulation of this low order Boundary Element Method, one key feature is the discretization of the boundary geometry with the assignment of elements. These elements can be 1D in case of a 2D problem, or 2D panels in 3D problems. On these elements a singularity distribution is considered and the induced potential and velocities at any specific location of the domain can be evaluated with the summation of effects by each one element.

Stepping on the investigation of the geometry of these elements and focusing on 3D problems, the panels may take different shapes, such as triangular or rectangular, which are the most common and the simplest of shapes. The triangular elements are becoming more popular lately, due to the easier approximation of the boundary and their relevant efficiency on this task, even on complicated geometries of boundaries. However, the quadrilateral elements, which have more limited freedom on modelling the boundary shape with high accuracy, have the advantage of modelling at first order curvature effects, exhibiting this extra degree of freedom and they are very useful in BVPs due to this curving ability. Both these techniques present first order accuracy. The usage of curved quadrilateral elements are a way to approximate shapes and ensure the continuity of the geometry. Additionally, characterized by four nodes they give more accuracy, however accompanied with further complication on solving the problem [100]. If higher accuracy is required, then added nodal points can be allocated along the sides or on the surface of each quadrilateral element, adding extra parameters for each element and permitting the usage of only few of them for the solution of the whole problem (**Fig. 131**).

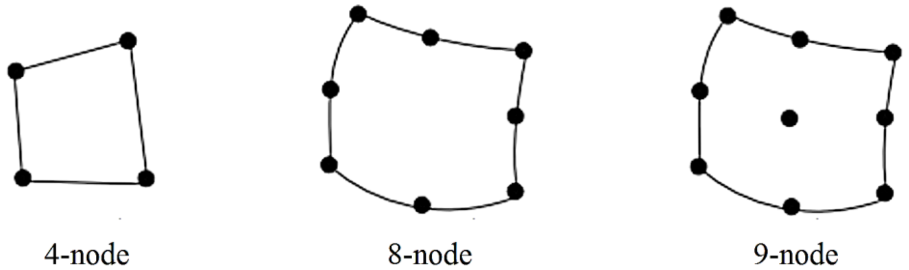

Figure 131: Quadrilateral elements with four nodes and with added nodal points

In this specific case of BVP, considered in this study, the 4-node curved quadrilateral element is applied for the approximation of boundaries, securing the continuity of the approximation of the geometry without gaps, in contrast with the constant-strength flat quad-elements, commonly used in potential flow problems [101], which introduce discontinuities on the geometry [61]. The constant-strength 4-node curved quadrilateral element is used in the present work, introducing a low order approximation without any increase of the number of unknowns, which are namely the discrete singularity strengths on each element and ensuring the avoidance of any inter-elemental discontinuities and thus better approximation of the potential.

For the main singularity distribution on the boundary elements is selected the surface dipole, which, in combination with the selected elements, presents some significant properties:

- *Induced potential and velocity of each element can be obtained analytically.* For every not-extremely twisted element on the boundary, which almost refers to any case of interesting applications, the expressions of the induced potential and velocity have analytical forms and thus this method presents very fast calculations even for very large discretization.
- *Self-induced values guarantee the formulation of a diagonal matrix of coefficients.* The induced potential and velocity by each element on its center are very strong and this defines that the matrix of coefficients will be diagonally dominant for every case of BCs of the present 3D free-surface problems.
- *Diagonal matrix of coefficients offers iterative solution methods.* Methods, like Gauss-Seidel, under this matrix-form requirement, are able to solve problems in large domains with variable fine-meshed boundaries.

A.2 Mathematical formulation

A.2.1 Definition of the quadrilateral element

Considering the quadrilateral element of the boundary, an intrinsic coordinates system (ξ,η) is introduced within the element, bounded in [-1,1], as shown in **Fig. 132**. Using coordinates isoparametric transformation, the rectangle $[-1,1]^2 \subset \mathbb{R}^2$ is transformed to the 3D surface element $x \in E$ as follows:

$$x(\xi,\eta)=\sum_{n=1}^{L} x_n N_n(\xi,\eta) \tag{A.1}$$

where $x=(x,y,z)$ are the Cartesian coordinates of a point with intrinsic coordinates (ξ,η) and x_n are the coordinates of the element's corner nodes n=1,…,4, numbered as illustrated in **Fig. 132**.

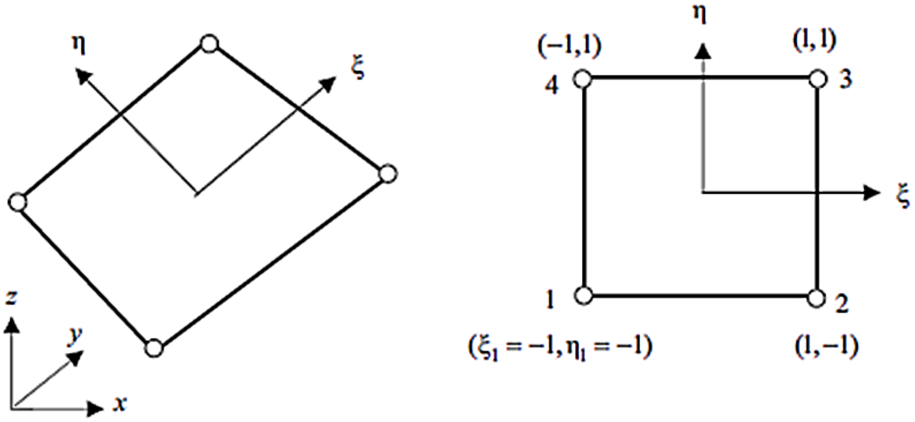

Figure 132: Coordinates systems on a 4-node quadrilateral element: (a): Global CS, (b): Local CS

Therefore, the shape functions can be expressed generally as:

$$N_n=\frac{1}{2}(1+\xi_n\xi)\frac{1}{2}(1+\eta_n\eta) \tag{A.2}$$

and the individual shape function for each node, in respect to the numbering , is:

$$N_1(\xi,\eta)=\frac{1}{4}(1-\xi)(1-\eta) \tag{A.3}$$

$$N_2(\xi,\eta)=\frac{1}{4}(1+\xi)(1-\eta) \tag{A.4}$$

$$N_3(\xi,\eta)=\frac{1}{4}(1+\xi)(1+\eta) \tag{A.5}$$

$$N_4(\xi,\eta)=\frac{1}{4}(1-\xi)(1+\eta) \tag{A.6}$$

Each one of these functions is connected to a single node, describing a curved surface, consisted of straight lines in ξ, η directions and called as hyper-surface. A typical example for the N_1 shape function, as well us for the rest of shape functions are depicted in **Figs 133**, **134**.

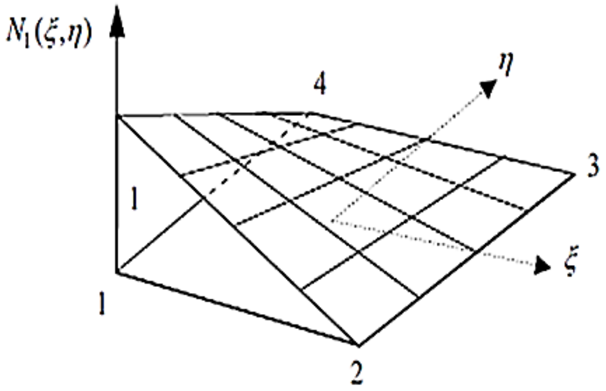

Figure 133: N_1 shape function of the 4-node quad-element

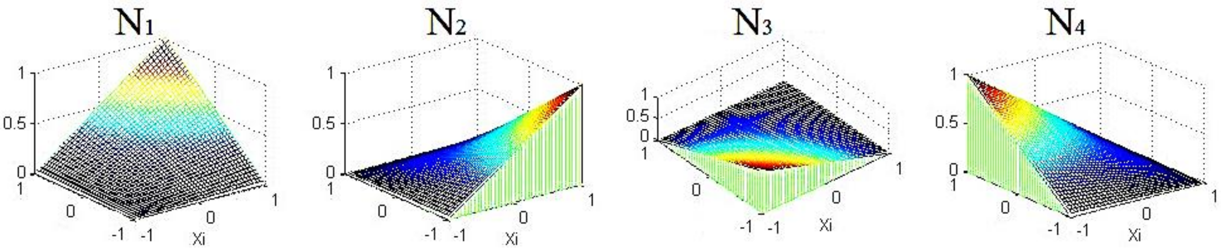

Figure 134: Shape functions of the 4-node quad-element [102]

Secondly, the centroid C_0 and the tangent vectors, parallel to ξ, η directions have now to be evaluated:

$$C_0 = \frac{1}{4}\left(x_1 + x_2 + x_3 + x_4\right) \tag{A.7}$$

$$e_\xi = \frac{\partial x}{\partial \xi} = \sum_{i=1}^{4} \frac{\partial N_i\left(\xi,\eta\right)}{\partial \xi} x_i \tag{A.8}$$

$$e_\eta = \frac{\partial x}{\partial \eta} = \sum_{i=1}^{4} \frac{\partial N_i\left(\xi,\eta\right)}{\partial \eta} x_i \tag{A.9}$$

Any function $f\left(x\left(\xi,\eta\right)\right)$ on the element can now be integrated as follows:

$$\int_{\mathrm{E}} f\, dS = 4 \cdot \int_{\eta=-1}^{\eta=1} \int_{\xi=-1}^{\xi=1} f\left(x\left(\xi,\eta\right)\right)\sqrt{\alpha\left(\xi,\eta\right)}\, d\xi\, d\eta \tag{A.10}$$

where,

$$\sqrt{\alpha} = \left\| e_\xi \times e_\eta \right\| \tag{A.11}$$

is the Jacobian determinant of the transformation and:

$$n = \left(e_\xi \times e_\eta\right) / \left\| e_\xi \times e_\eta \right\| = \left(e_\xi \times e_\eta\right) / \sqrt{\alpha} \tag{A.12}$$

is the unit normal vector on the quad-element.

A.2.2 Evaluation of induced velocity

In problems, like these described in this study, the induced potential and velocities are the values of interest, that need to be evaluated for each element individually and for the whole domain at the end. Assuming a constant doublet distribution of strength-μ for an element pointing towards z-direction, the induced velocity can be obtained through integration:

$$\Phi(x, y, z) = -\mu \int_S n \, \nabla G(x; x_0) \, dS \tag{A.13}$$

where,

$$4\pi G(x; x_0) = \left[(x - x_0)^2 + (y - y_0)^2 + (z - z_0)^2 \right]^{1/2} \tag{A.14}$$

and specifically for the 4-node quad-element with all its nodes laying on the same plane, the velocity potential is expressed as:

$$\Phi(x, y, z) = \frac{-\mu}{4\pi} \int_S \frac{z \, dS}{\left[(x - x_0)^2 + (y - y_0)^2 + z^2 \right]^{1/2}} \tag{A.15}$$

Based on the theory of Katz & Plotkin [61], the 3D constant strength doublet element is equivalent to a constant strength vortex ring, placed on the edges of the element, as shown in **Fig. 135**.

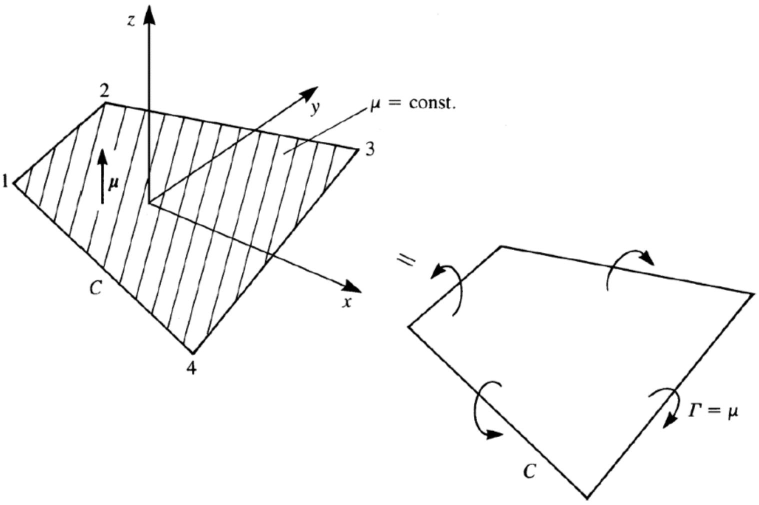

Figure 135: Doublet quad-element and its equivalent vortex ring [61]

Equivalence of constant doublet panel to vortex ring

The induced potential by a constant μ-strength doublet element is expressed as:

$$\Phi = -\frac{\mu}{4\pi}\int_S \frac{z\,dS}{r^3} \tag{A.16}$$

where $r=\sqrt{(x-x_0)^2+(y-y_0)^2+z^2}$.

The corresponding induced velocity is therefore:

$$q=\nabla\Phi=-\frac{\mu}{4\pi}\int_S \nabla\frac{z}{r^3}dS=\frac{\mu}{4\pi}\int_S\left[i\frac{\partial}{\partial x_0}\frac{z}{r^3}+j\frac{\partial}{\partial y_0}\frac{z}{r^3}-k\left(\frac{1}{r^3}-\frac{3z^2}{r^5}\right)\right]dS \tag{A.17}$$

considering for the partial derivatives that: $\frac{\partial}{\partial x}\frac{1}{r^3}=-\frac{\partial}{\partial x_0}\frac{1}{r^3}$ and $\frac{\partial}{\partial y}\frac{1}{r^3}=-\frac{\partial}{\partial y_0}\frac{1}{r^3}$.

If *C* is the closed surrounding perimeter-curve of the element and *Γ* is the circulation, induced by the vortex distribution along *C*, then the velocity due to these vortices is obtained by Biot-Savart Law as follows:

$$q=\frac{\Gamma}{4\pi}\int_C\frac{dl\times r}{r^3} \tag{A.18}$$

where $dl=(dx_0,dy_0)$ and $r=(x-x_0,y-y_0,z)$. For these quantities it is obtained that:

$$q=\oint_C\left\{i\frac{z}{r^3}dy_0-j\frac{z}{r^3}dx_0+k\left[\frac{(y-y_0)dx_0}{r^3}-\frac{(x-x_0)dy_0}{r^3}\right]\right\} \tag{A.19}$$

The Stoke's Theorem for vector $\vec{A}$ and for the length-*S* of curve-*C* is:

$$\oint_C A\cdot dl=\int_S n\cdot\nabla\times A\;dS \tag{A.20}$$

For *n*=*k* the **Eq. (A.20)** becomes:

$$\oint_C A\cdot dl=\int_S\left(\frac{\partial A_y}{\partial x_0}-\frac{\partial A_x}{\partial y_0}\right)dS \tag{A.21}$$

With the appliance of Stoke's Theorem on **Eq. (A.19)**, the expression for the induced velocity finally becomes:

$$q=\frac{\Gamma}{4\pi}\int_S\left[\hat{i}\frac{\partial}{\partial x_0}\frac{z}{r^3}+\hat{j}\frac{\partial}{\partial y_0}\frac{z}{r^3}-\hat{k}\left(\frac{\partial}{\partial x_0}\frac{x-x_0}{r^3}+\frac{\partial}{\partial y_0}\frac{y-y_0}{r^3}\right)\right]dS \tag{A.22}$$

In conclusion, comparing **Eqs (A.17)** and **(A.22)**, it is obvious that the induced velocity by the doublet panel is equal to the induced velocity by the vortex filament for $\Gamma=\mu$. This also is in force in case of the twisted 4-node quad-element [103].

For the calculation of the induced velocity potential, even for twisted elements, is used the above described formula. An additional theorem is also needed, and described hereupon: Considering one segment on one of the edges of the element and a random domain point *P*, as shown in **Fig. 136**:

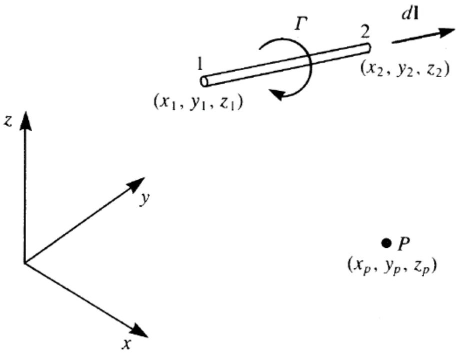

Figure 136: Impact of a straight vortex line segment to a point *P* [61]

The induced velocity by this vortex in this case is:

$$\Delta q=\frac{\Gamma}{4\pi}\frac{dl\times r}{r^3} \tag{A.23}$$

If the direction of the velocity's vector points from 1→2, then the expression for the velocity at the point *P* is:

$$q_{1,2}=\frac{\Gamma}{4\pi}\frac{r_1\times r_2}{\left|r_1\times r_2\right|^2}r_0\cdot\left(\frac{r_1}{r_1}-\frac{r_2}{r_2}\right) \tag{A.24}$$

In general, the coordinates of the points 1, 2 and *P* will be given in the Cartesian system. The steps for evaluating the induced velocity at any point-*P* are:

1) Calculate $\left(r_1\times r_2\right)$:

$$\left(r_1\times r_2\right)_x=\left(y_P-y_1\right)\left(z_P-z_2\right)-\left(z_P-z_1\right)\left(y_P-y_2\right) \tag{A.25}$$

$$\left(r_1\times r_2\right)_y=-\left(x_P-x_1\right)\left(z_P-z_2\right)+\left(z_P-z_1\right)\left(x_P-x_2\right) \tag{A.26}$$

$$\left(r_1\times r_2\right)_z=\left(x_P-x_1\right)\left(y_P-y_2\right)-\left(y_P-y_1\right)\left(x_P-x_2\right) \tag{A.27}$$

and the absolute value of this outer product is:

$$\left|r_1\times r_2\right|^2=\left(r_1\times r_2\right)_x^2+\left(r_1\times r_2\right)_y^2+\left(r_1\times r_2\right)_z^2 \tag{A.28}$$

2) Calculate r_1 and r_2 :

$$r_1 = \sqrt{\left(x_P - x_1\right)^2 + \left(y_P - y_1\right)^2 + \left(z_P - z_1\right)^2} \tag{A.29}$$

$$r_2 = \sqrt{\left(x_P - x_2\right)^2 + \left(y_P - y_2\right)^2 + \left(z_P - z_2\right)^2} \tag{A.30}$$

3) Singular conditions check: The vortex solution will be singular if the *P* lies on the vortex. In this case special handling is essential in the vicinity of the vortex segment and for numerical purposes a very small radius-ϵ of the vortex core size is assumed:

$$\text{if} \quad \left(r_1 \text{ or } r_2 \text{ or } \left|r_1 \times r_2\right|^2 < \in\right) \text{ then } \left(u = \upsilon = w = 0\right) \tag{A.31}$$

where the vortex core size-ϵ can be as small as the truncation error. Otherwise, the velocity components can be calculated by any other vortex core model.

4) Calculate the inner product $\left(r_0\, r_1\right)$ and $\left(r_0\, r_2\right)$:

$$r_0 \cdot r_1 = \left(x_2 - x_1\right)\left(x_P - x_1\right) + \left(y_2 - y_1\right)\left(y_P - y_1\right) + \left(z_2 - z_1\right)\left(z_P - z_1\right) \tag{A.32}$$

$$r_0 \cdot r_2 = \left(x_2 - x_1\right)\left(x_P - x_2\right) + \left(y_2 - y_1\right)\left(y_P - y_2\right) + \left(z_2 - z_1\right)\left(z_P - z_2\right) \tag{A.33}$$

5) The resulting velocity's components are:

$$u = K\left(r_1 \times r_2\right)_x \tag{A.34}$$

$$\upsilon = K\left(r_1 \times r_2\right)_y \tag{A.35}$$

$$w = K\left(r_1 \times r_2\right)_z \tag{A.36}$$

where constant *K* is:

$$K = \frac{\Gamma}{4\pi\left|r_1 \times r_2\right|^2}\left(\frac{r_0 \cdot r_1}{r_1} - \frac{r_0 \cdot r_2}{r_2}\right) \tag{A.37}$$

The above procedure must be accomplished for each vortex segment at the edge of the 4-node element and the induced velocities from each segment have to be summed, in order to evaluate the induced velocity from this boundary element to a point-*P* of the domain.

A.2.3 Evaluation of induced potential

For the evaluation of induced potential by a 4-node quadrilateral element with constant doublet distribution (*μ=const*) at any point *P (x,y,z)* of the domain, based on [104], the following integral should be evaluated:

$$\Phi_{\mu} = \frac{\mu}{4\pi}\int_{\mathrm{E}} \vec{n}_Q \frac{\left(x_P - x_Q\right)}{r^3} dS\left(Q\right) \tag{A.38}$$

where,

E: Quad-element’s area
n_Q: The normal vector at the center of the element
x_P: The position vector of *P*, from the axis origin to the field point *P*
x_Q: The position vector of each point *Q* ϵ *E*, from the axis origin to the element point *Q*

Here is considered μ=1. In case of a sink at the field point *P*, with unit strength σ=-1, it is observed that the sink flow is equal to *U*, with:

$$U_r = -\frac{1}{4\pi r^2} \quad \text{and} \quad U_{\sigma} = -\frac{1}{4\pi}\frac{x_Q - x_P}{r^3} \tag{A.39}$$

With the assumption of a sink at *P*, evaluating the sink flow through *E* leads to the following **Eq. (A.40)**, which proves the equivalence of sink flow and dipole constant distribution:

$$Q\left(U_{\sigma} \mid E\right) = -\frac{1}{4\pi}\int_{\mathrm{E}} n_Q \frac{x_Q - x_P}{r^3} dS_Q \equiv \Phi_{\mu} \tag{A.40}$$

The sink flow rate through the element’s area is also the flow rate through a sphere of radius *r*=1 and center the point-*P*, calculated as:

$$\Phi_{\mu} = \int_{\Sigma\left(x = x_P \mid = r_0\right)} U_{\sigma} d\Sigma = -\frac{1}{4\pi}\int_{\Sigma} r_0^{-2} d\Sigma = -\frac{a}{4\pi} \rightarrow \pm\frac{a}{4\pi} \tag{A.41}$$

where α is the solid angle of the element.

Separating the quad-element on two 3-node elements, as shown in **Fig. 138(α)**, the corresponding angles of each tetrahedral are calculated as well as the potential for each one and finally the total potential is simply the summation of these two quantities.

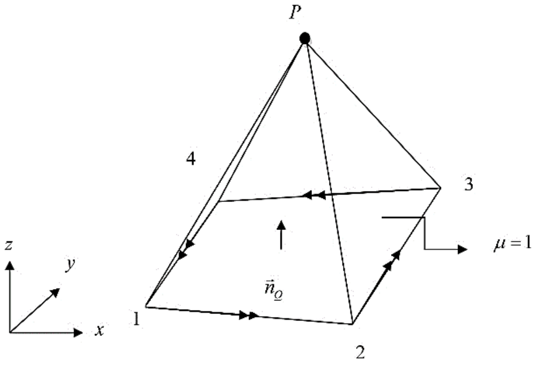

Figure 137: Inducements of a curved quad-element to the field point-*P*

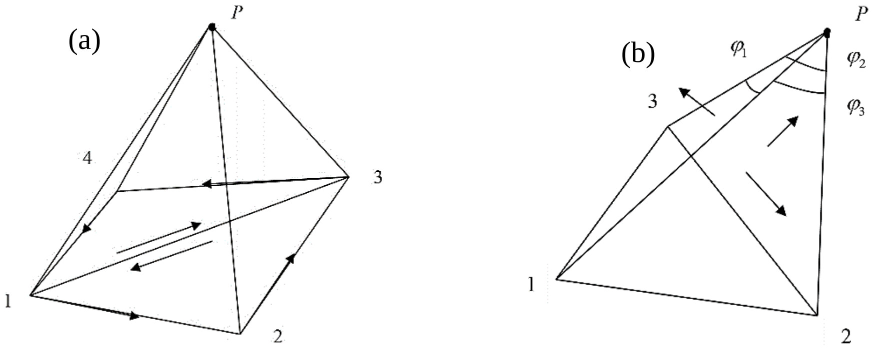

Figure 138: (a) Separation of quad-element to two 3-node elements and (b) Solid angle of a tetrahedron

The solid angle of the tetrahedron, as shown in **Fig. 138(b)** is:

$$a = 2\pi - \varphi_1 - \varphi_2 - \varphi_3 \tag{A.42}$$

Consequently, the induced potential by the quad-element of unit singularity distribution to the field point *P* is:

$$\Phi = \Phi_1 + \Phi_2 = \frac{a_1}{4\pi} + \frac{a_2}{4\pi} \tag{A.43}$$

where α_i corresponds to the solid angle of the i^{th} 3-node element. Validation examples of this method can be found in [62].

Appendix B

The Coupled Mode Model in evaluating the propagation field

B.1 Mathematical formulation

B.1.1 The 3D hydrodynamic problem

The proposed BEM-PML method to treat hydrodynamic problems of floating bodies over a flat or a variable topography in 3D regions requires the evaluation of the relevant potentials. Specifically, the evaluation for the diffraction and radiation potentials demands the calculation of the incident wave propagation field, with the body omitted. The analytic solution for the wave potential is known for the case of a flat seabed [67], however it cannot be extended to a varying-depth region. A numerical method to calculate the wave potential in this problem is the Coupled Mode Model [83].

In **Fig.139** is illustrated the domain, with its decomposition in subdomains:

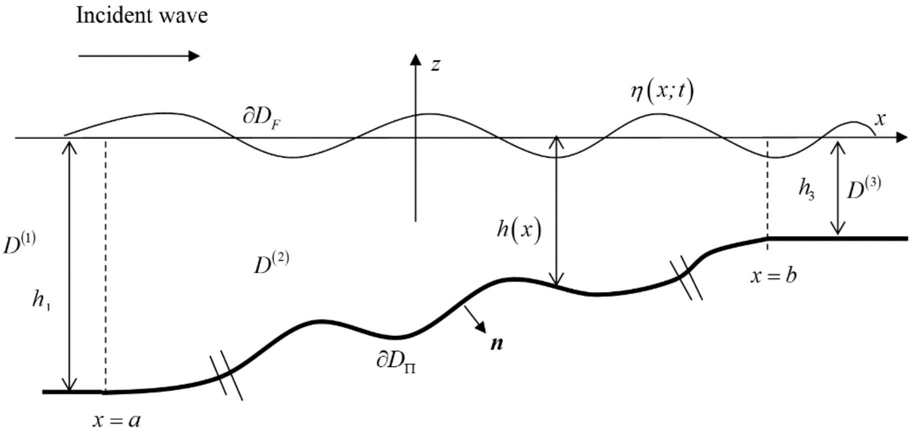

Figure 139: Domain and subdomains of the hydrodynamic problem

The bottom profile, which is described by a one-dimensional arbitrary variation, is a subdomain of finite length and therefore the geometry of the bottom can be described by iso-depth contours. This transitional region is among two others, each one with a constant, but different, depth. Firstly, a Cartesian coordinate system is introduced, with the origin above the variable bathymetry at a point of standard water level (SWL), the z-axis is pointing upwards and the y-axis is parallel to the bottom contours. The domain can then be represented as $D_{3D}=D\times R$, where D is the 2D intersection of D_{3D} with a vertical plane, perpendicular to the bottom contours and $R=(-\infty,+\infty)$ is the real line. This notation can be explicitly defined as:

$$D_{3D}=\{(x,y,z):\ (x,y)\in R^2, -h(x)<z<0\} \tag{B.1}$$

while,

$$D = \{(x,z):\ x \in R, -h(x) < z < 0\} \tag{B.2}$$

The D_{3D} domain is decomposed in three subdomains (**Eq. (B.3)**): $D_{3D}^{(i)}=D^{(i)} \times R,\ i=1,2,3$ where, $D_{3D}^{(1)}$ is the constant-depth subdomain for $x < \alpha$, $D_{3D}^{(3)}$ is the constant-depth subdomain for $x > b$ and $D_{3D}^{(2)}$ is the variable-depth subdomain between $D_{3D}^{(1)}$ and $D_{3D}^{(3)}$.

$$D^{(i)} = \left\{ (x,z): \begin{array}{lll} x < a, & -h_1 < z < 0, & i = 1 \\ a < x < b, & -h(x) < z < 0, & i = 2 \\ x > b, & -h_3 < z < 0, & i = 3 \end{array} \right\} \tag{B.3}$$

The general representation of the wave potential in semi-infinite strips of constant depth is analytically exploited [71,105] and in this specific domain there are two regions of this constant-depth characteristics:

$$\varphi^{(1)}(x,z) = \left(A_0 \exp\left(ik_0^{(1)}x\right) + A_R \exp\left(-ik_0^{(1)}x\right)\right) Z_0^{(1)}(z) + \sum_{n=1}^{\infty} C_n^{(1)} Z_n^{(1)}(z) \exp\left(k_n^{(1)}(x-a)\right), \quad (x,z) \in D^{(1)} \tag{B.4}$$

$$\varphi^{(3)}(x,z) = A_T \exp\left(ik_0^{(3)}x\right) Z_0^{(3)}(z) + \sum_{n=1}^{\infty} C_n^{(3)} Z_n^{(3)}(z) \exp\left(k_n^{(3)}(b-x)\right), \quad (x,z) \in D^{(2)} \tag{B.5}$$

In the above series the terms $\left(A_0 \exp\left(ik_0^{(1)}x\right) + A_R \exp\left(-ik_0^{(1)}x\right)\right) Z_0^{(1)}(z)$ and $A_T \exp\left(ik_0^{(3)}x\right) Z_0^{(3)}(z)$ are the propagating modes, while the others for $n=(1,2,\ldots)$ are the evanescent modes. The variables $\left\{ik_0^{(i)}, k_n^{(i)},\ n=1,2,\ldots\right\}$, $i=1,3$ and $\left\{Z_n^{(i)}(z),\ n=0,1,2,\ldots\right\}$, $i=1,3$ are respectively the eigenvalues and the eigenfunctions of the regular Sturm-Liouville problem evaluated by using the separation of variables in the half-strips $D^{(i)},\ i=1,3$:

$$\mu h_i = -k^{(i)} h_i \tan\left(k^{(i)} h_i\right), \quad i = 1,3 \tag{B.6}$$

$$Z_0^{(i)}(z) = \frac{\cosh\left(k_0^{(i)}\left(z+h_i\right)\right)}{\cosh\left(k_0^{(i)} h_i\right)}, \quad Z_n^{(i)}(z) = \frac{\cos\left(k_n^{(i)}\left(z+h_i\right)\right)}{\cos\left(k_n^{(i)} h_i\right)}, \quad n = 1,2,\ldots, \quad i = 1,3 \tag{B.7}$$

The problem can be reformulated as a transmission BVP in the $D^{(2)}$where the function $\varphi^{(2)}(x,z)$ satisfies the following system of equations, BCs and matching conditions on the vertical boundaries $\partial D_I^{(12)}$ and $\partial D_I^{(23)}$ and on the segments of the FS-line $\partial D_F^{(i)}$ and Bottom-line $\partial D_{II}^{(i)}$:

$$\nabla^2\varphi^{(2)}=0,\quad (x,z)\in D^{(2)} \tag{B.8}$$

$$\frac{\partial\varphi^{(2)}}{\partial n^{(2)}}-\mu\varphi^{(2)}=0,\quad (x,z)\in\partial D_F^{(2)}\quad \text{and}\quad \frac{\partial\varphi^{(2)}}{\partial n^{(2)}}=0,\quad (x,z)\in\partial D_{II}^{(2)} \tag{B.9}$$

$$\varphi^{(2)}=\varphi^{(1)},\quad \frac{\partial\varphi^{(2)}}{\partial n^{(2)}}=-\frac{\partial\varphi^{(1)}}{\partial n^{(1)}},\quad (x,z)\in\partial D_I^{(12)} \tag{B.10}$$

$$\varphi^{(2)}=\varphi^{(3)},\quad \frac{\partial\varphi^{(2)}}{\partial n^{(2)}}=-\frac{\partial\varphi^{(3)}}{\partial n^{(3)}},\quad (x,z)\in\partial D_I^{(23)} \tag{B.11}$$

where $n^{(i)}$ is the unit normal vector to the $\partial D^{(i)}$, i=1,2,3 boundary, directed to the exterior of it.

Afterwards, a variational formulation of the problem follows, as described in [83], and the wave potential expressions is enhanced:

$$\begin{aligned}
&-\int_{D^{(2)}}\left(\nabla^2\phi^{(2)}\right)\delta\phi^{(2)}dV+\int_{\partial D_{\mathrm{II}}^{(2)}}\left(\frac{\partial\phi^{(2)}}{\partial n^{(2)}}\right)\delta\phi^{(2)}dS+\int_{\partial D_F^{(2)}}\left(\frac{\partial\phi^{(2)}}{\partial n^{(2)}}-\mu\phi^{(2)}\right)\delta\phi^{(2)}dS\\
&+\int_{\partial D_{\mathrm{I}}^{(12)}}\left(\frac{\partial\phi^{(2)}}{\partial n^{(2)}}+\frac{\partial\phi^{(1)}}{\partial n^{(1)}}\right)\delta\phi^{(2)}dS\ +\int_{\partial D_{\mathrm{I}}^{(23)}}\left(\frac{\partial\phi^{(2)}}{\partial n^{(2)}}+\frac{\partial\phi^{(3)}}{\partial n^{(3)}}\right)\delta\phi^{(2)}dS\\
&+\int_{\partial D_{\mathrm{I}}^{(12)}}\left(\varphi^{(2)}-\varphi^{(1)}\right)\delta\left(\frac{\partial\varphi^{(1)}}{\partial x}\right)dS-\int_{\partial D_{\mathrm{I}}^{(23)}}\left(\varphi^{(2)}-\varphi^{(3)}\right)\delta\left(\frac{\partial\varphi^{(3)}}{\partial x}\right)dS\ =\ 0
\end{aligned} \tag{B.12}$$

The main usefulness of this variational principle is that it leaves the freedom to choose any among different representations of the unknown $\varphi^{(2)}$ in $D^{(2)}$ and their relevant numerical solution algorithms.

B.1.1 Local Mode representation

The wave potential $\varphi^{(2)}(x,z)$ for the propagation of water gravity waves above variable depth seabed, with the absence of the body, can be calculated conveniently by the CMS, based on the enhanced local mode representation:

$$\varphi^{(2)}(x,z)=\varphi_{-1}(x)Z_{-1}(z;x)+\sum_{n=0}^{\infty}\varphi_n(x)Z_n(z;x) \tag{B.13}$$

In the expression of **Eq. (B.13)**, the term for $n=0$: $\varphi_0(x)\ Z_0(z;x)$correspond to the propagating mode, the terms $\varphi_n(x)\ Z_n(z;x)$, n=1, 2,…, are the evanescent modes and the additional tuning term $\varphi_{-1}(x)\ Z_{-1}(z;x)$, called the sloping-bottom mode, is induced in order to satisfy the Neumann

BC on the non-horizontal parts of the bottom. The functions $Z_n(z;x)$ are the vertical structures of the n^{th}-mode, obtained as eigenfunctions of the local vertical St-L problem and described by **Eqs (B.6)**, **(B.7)** and the functions $\varphi_n(x)$ are the complex amplitude of the n^{th}-mode, describing the horizontal patterns of these eigenfunctions.

$$Local\ St-L: \left\{ \begin{array}{ll} Z_0(z;x) = \dfrac{\cosh\left[k_0(x)\left(z+h(x)\right)\right]}{\cosh\left(k_0(x)\,h(x)\right)} & \\ Z_n(z;x) = \dfrac{\cos\left[k_n(x)\left(z+h(x)\right)\right]}{\cos\left(k_n(x)\,h(x)\right)} & n=1,2,\ldots \\ \mu h(x) = k_0(x)h(x)\tanh\left[k_0(x)h(x)\right] & \\ \mu h(x) = -k_n(x)h(x)\,\tan\left[k_n(x)h(x)\right] & n=1,2,... \end{array} \right\} \tag{B.14}$$

The function $Z_{-1}(z;x)$, defined as the vertical structure of the sloping-bottom mode, is a correction term, assures the satisfaction of the Neumann BC even in the non-horizontal parts of the seabed, making this model consistent and enforces the energy conservation. This term also improves the decay of modal-amplitude functions from the order $O(n^{-2})$ to $O(n^{-4})$, where n is the mode-number and so it accelerates the convergence. In this model, based on the least degree polynomial satisfying conditions, the chosen form of $Z_{-1}(z;x)$ is:

$$Z_{-1}(z;x) = h(x)\left[\left(\frac{z}{h(x)}\right)^3 + \left(\frac{z}{h(x)}\right)^2\right] \tag{B.15}$$

With the substitution of **Eqs (B.13)** and **(B.15)** in the variational **Eq. (B.12)** the final Coupled Mode System of horizontal equations for the amplitudes-φ_n of incident wave propagating field over a variable bathymetry is formulated:

$$\sum_{n=-1}^{\infty} a_{mn}(x)\,\varphi_n''(x) + b_{mn}(x)\,\varphi_n'(x) + c_{mn}(x)\varphi_n(x) = 0, \quad a < x < b, \quad m = -1,0,1,.. \tag{B.16}$$

where the coefficients a_{mn}, b_{mn}, c_{mn} are expressed in terms of the vertical modes $Z_n(z;x)$, as shown in **Table 13**:

Table 13
CMS coefficients

	CASE I	**CASE II**	**CASE III**
	$m=-1$ $n=-1,0,1,2,\dots$	$m=0,1,2,\dots$ $n=-1$	$m=0,1,2,\dots$ $n=0,1,2,\dots$
$a_{mn}(x)$	$\langle Z_{-1}, Z_n\rangle$	$\langle Z_m, Z_{-1}\rangle$	$\delta_{nm}\lVert Z_m\rVert^2$
$b_{mn}(x)$	$2\langle Z_{-1}, \partial Z_n/\partial x\rangle$	$2\langle Z_m, \partial Z_{-1}/\partial x\rangle$	$2\langle Z_m, \partial Z_n/\partial x\rangle +$ $+h'(x)Z_m(-h)Z_n(-h)$
$c_{mn}(x)$	$\langle Z_{-1}, \Delta Z_n\rangle$	$\langle Z_m, \Delta Z_{-1}\rangle +$ $+\left(1+h'(x)\dfrac{\partial Z_{-1}(-h)}{\partial x}\right)Z_m(-h)$	$\langle Z_m, \Delta Z_n\rangle +$ $+h'(x)Z_m(-h)\left(\partial Z_n(-h)/\partial x\right)$

$Z_n = Z_n(z;x)$: parametrically depended on *x* through *h(x)*.

NOTES: $\Delta\,\bullet = \dfrac{\partial^2\bullet}{\partial z^2}+\dfrac{\partial^2\bullet}{\partial x^2}, \quad \langle f,g\rangle = \displaystyle\int_{-h(x)}^{0} f(z)g(z)dz\,, \quad \lVert f\rVert^2 = \langle f,f\rangle\,.$

for $n=0,1,2,\ldots$ $\quad \Delta Z_n = \dfrac{\partial^2 Z_n}{\partial x^2} - (k_n)^2 Z_n\,.$

The above CMS in $\alpha < x < b$ is also supplemented by boundary conditions:

$$\begin{aligned} \varphi_{-1}(a) &= \varphi'_{-1}(a) = 0 \\ \varphi_{-1}(b) &= \varphi'_{-1}(b) = 0 \end{aligned} \tag{B.17}$$

$$\begin{aligned} &\varphi_0(a) + ik_0^{(1)}\varphi_0(a) = 2\,i\,k_0^{(1)}A_0\exp\left(i\,k_0^{(1)}a\right) \\ &\varphi'_n(a) - k_n^{(1)}\varphi_n(a) = 0,\ n = 1,2,\dots \end{aligned} \tag{B.18}$$

$$\begin{aligned} &\varphi'_0(b) - ik_0^{(3)}\varphi_0(b) = 0 \\ &\varphi'_n(b) + k_n^{(3)}\varphi_n(b) = 0, \qquad n = 1,2,3,\dots \end{aligned} \tag{B.19}$$

Finally, due to the equivalence of the variational formulation of the transmission problem of **Eq. (B.12)** and the system of **Eqs (B.16-B.19)**, the coefficients A_R, $C_n^{(1)}$, A_T, $C_n^{(3)}$ (**Eqs (B.4)**, **(B.5)**) can now be calculated as:

$$\begin{aligned} &A_R = \left(\varphi_0(a) - A_0\exp\left(i\,k_0^{(1)}a\right)\right)\exp\left(i\,k_0^{(1)}a\right) \\ &C_n^{(1)} = \varphi_n(a)\,, \quad n = 1,2,3,\dots \end{aligned} \tag{B.20}$$

$$\begin{aligned} &A_T = \varphi_0(b)\exp\left(-i\,k_0^{(3)}b\right) \\ &C_n^{(3)} = \varphi_n(b)\,, \quad n = 1,2,3,\dots \end{aligned} \tag{B.21}$$

By solving the system and substituting the solution in the above equations, the coefficients in semi-infinite strip can be evaluated. The system is supplemented by appropriate BCs for treating reflection, transmission and radiation of waves. Considering only the propagating mode ($n=0$) the above CMS reduces to an one-equation model, which is exactly the modified mild-slope equation derived in [105,106], while neglecting the slopping-bottom mode leads to the extended mild-slope equation derived in [105], equations which are non-conservative with respect to the energy due to the fact that the infinite series of Eq. (B.13) without the slopping-bottom mode cannot converge uniformly in the interval $[-h(x),0]$.

The presented Coupled Mode Model, commensurate with any other linear model, presents some significant advantages:

- *Fast accurate convergence.* Through identifying only the critical couplings, this method treats effectively the nonlocal character of the problem and allows accurate approximation of the wave propagating field in the whole domain with only few modes (3÷5).
- *Easy simplifications.* The CMS can be easily simplified and extended to the mild-slope equation or other modifications, based on the physical conditions of the subareas.
- *High-quality information.* The induced pressure and tangential velocity at the bottom, useful for applications in the field of wave energy, as well in geophysical studies of the bottom, can be calculated with high accuracy.
- *Implementation on Green's Function formulation*. The Green's functions are the main tool for studying wave-body interactions over a varying seabed and the developed CMS offers, through the completeness of representing the velocity field, a method for utilizing the formulation and the numerical efficiency of these functions.

B.2 Numerical results

For reasons of completeness in this section will be evaluated examples of CMS appliance and incident wave propagation field calculations.

The bathymetry is described by a monotonic depth-decrease and constant depths at infinity, common in nearshore and coastal regions, described by the **Eq. (B.22)**:

$$h(x) = h_m(x) = \begin{cases} h_1 = 2 \text{ m}, \\ \dfrac{h_1 + h_3}{2} - \dfrac{h_1 - h_3}{2} \tanh\left(a_{bot}\pi\left(x - x_{mean}\right)\right) \\ h_3 = 1 \text{ m} \end{cases} \tag{B.22}$$

This profile describes a smooth but steep underwater shallowing step from 2 m to 1 m. The following results, correspond to $\omega\sqrt{\alpha/g} = 0.5461$. The ratios h/λ are respectively in these two sub-regions of constant depth are h_3/λ=0.1968 and h_1/λ=0.3421. In addition, another frequency of $\omega\sqrt{\alpha/g} = 0.8532$ is put under investigation, with h_3/λ=0.4111 and h_1/λ=0.8115. These ratios correspond to deep-water ($h/\lambda > 0.25$) and intermediate-depth ($0.05 \leq h/\lambda \leq 0.25$) conditions. The results have been obtained by using 5 nodes, which were found enough for the numerical convergence.

In these figures are plotted the real and imaginary parts of the potential on the free-surface, from two points of view and for different incident wave angles, while in the side view the free-surface elevation is also illustrated with the black dashed line. The bottom surface is shown with white solid line. As shown in these figures, the equipotential lines, in total agreement with the theory, are becoming perpendicular to the bottom when they are intersecting it. The potential, as well as the free-surface elevation, are transforming and they are obliged to be "suppressed", bended and slightly increased in the shallower region, in comparison with their form in the deeper region. This transformation is expressed firstly by the fact that the same amount of potential has now to be fitted in smaller area and secondly by the Snell’s Law which explains the wave diffraction phenomenon during the propagation of the wavefront over a shoaling region, where as the depth decreases the group velocity does the same too and thus the direction is increasing towards 90deg and becomes more near-perpendicular to the shore.

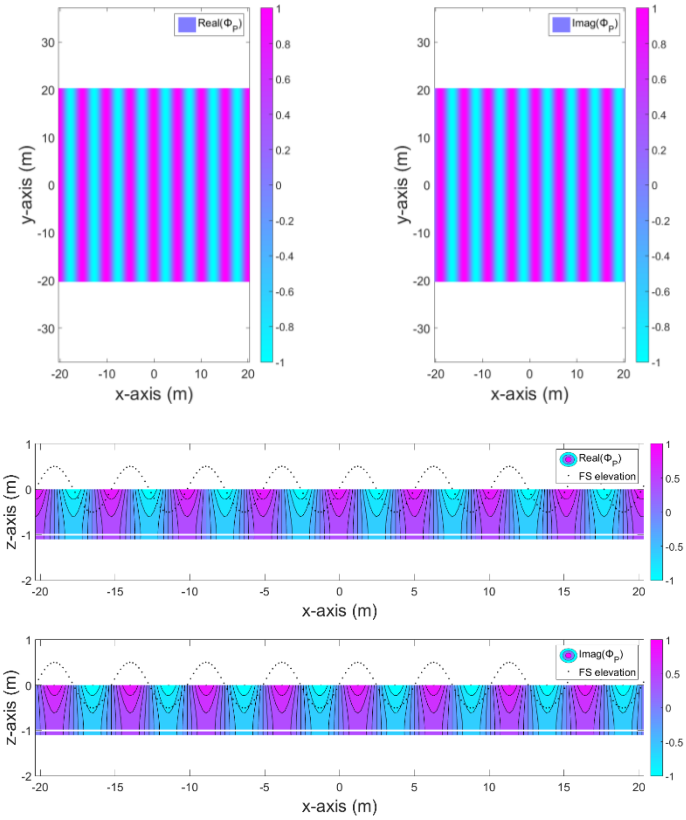

Figure 140: Propagating field (Real and Imag) by CMS (top and side view) for $\omega\sqrt{\alpha/g}$=0.5461, 0deg Flat bottom

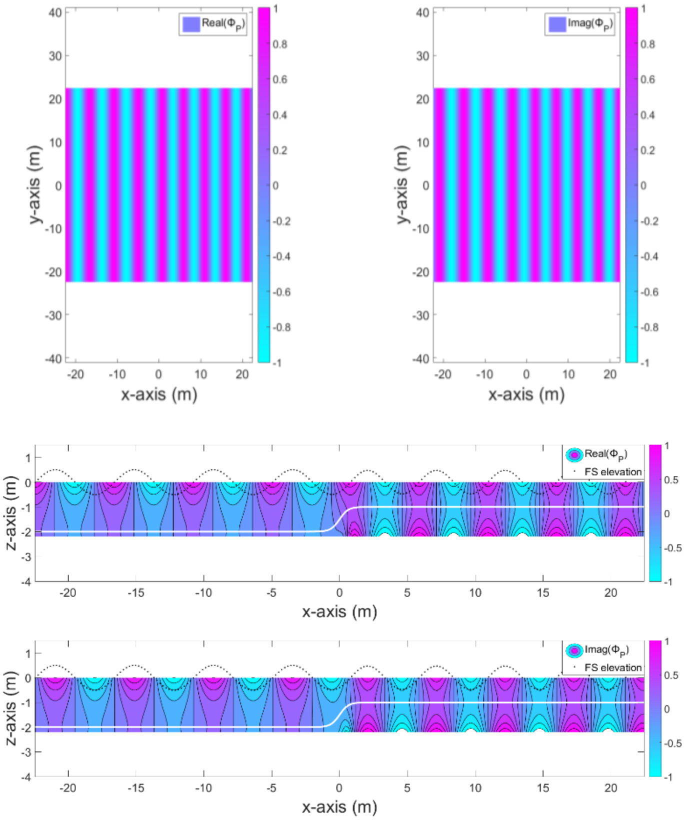

Figure 141: Propagating field (Real and Imag) by CMS (top and side view) for $\omega\sqrt{\alpha/g}$=0.5461, 0deg Variable bottom (h_1=2 m, h_3=1 m, α_{bot}=0.5)

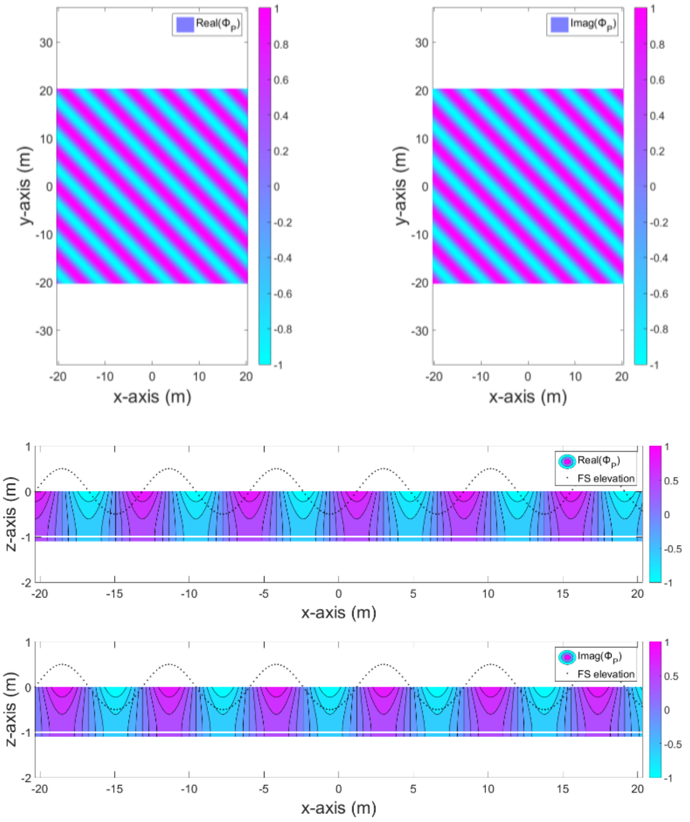

Figure 142: Propagating field (Real and Imag) by CMS (top and side view) for $\omega\sqrt{\alpha/g}$=0.5461, 45deg Flat bottom

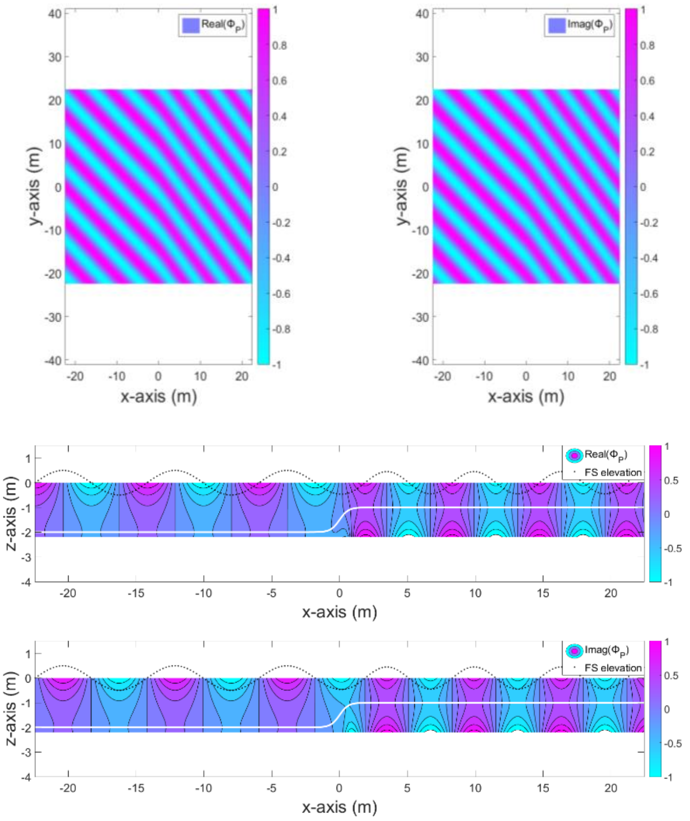

Figure 143: Propagating field (Real and Imag) by CMS (top and side view) for $\omega\sqrt{\alpha/g}$=0.5461, 45deg Variable bottom (h_1=2 m, h_3=1 m, α_{bot} =0.5)

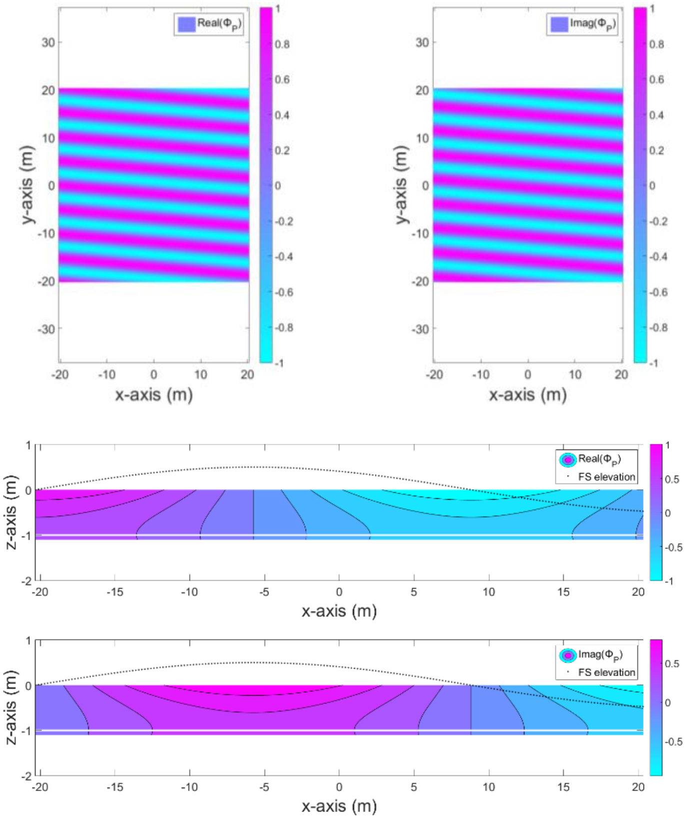

Figure 144: Propagating field (Real and Imag) by CMS (top and side view) for $\omega\sqrt{\alpha/g}$=0.5461, 85deg Flat bottom

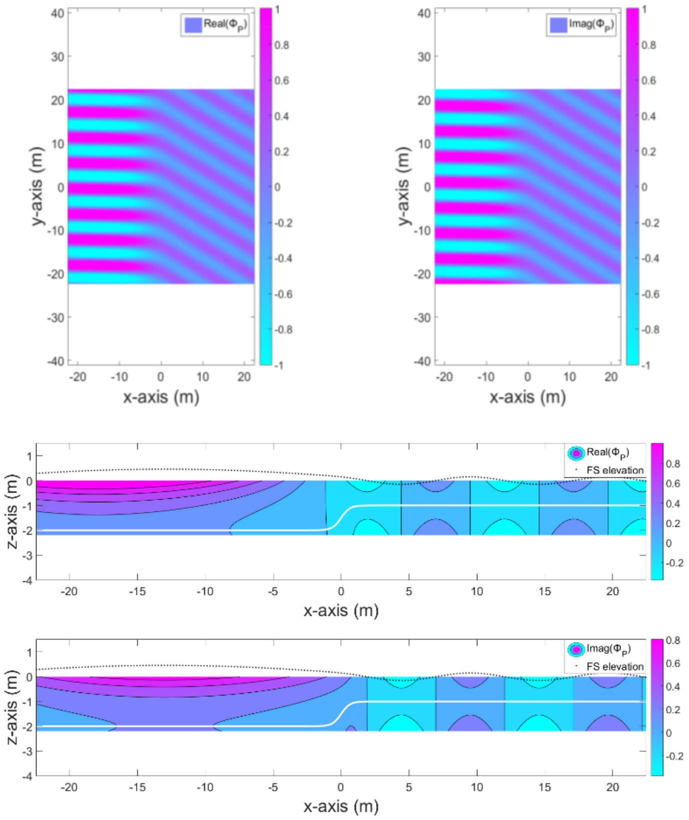

Figure 145: Propagating field (Real and Imag) by CMS (top and side view) for $\omega\sqrt{\alpha/g}$=0.5461, 85deg Variable bottom (h_1=2 m, h_3=1 m, α_{bot} =0.5)

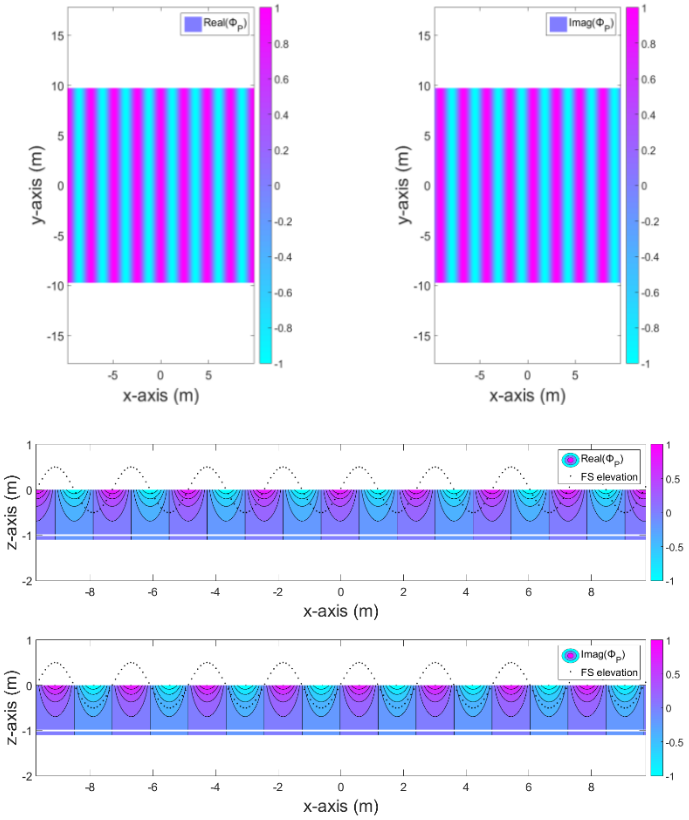

Figure 146: Propagating field (Real and Imag) by CMS (top and side view) for $\omega\sqrt{\alpha/g}$=0.8532, 0deg Flat bottom

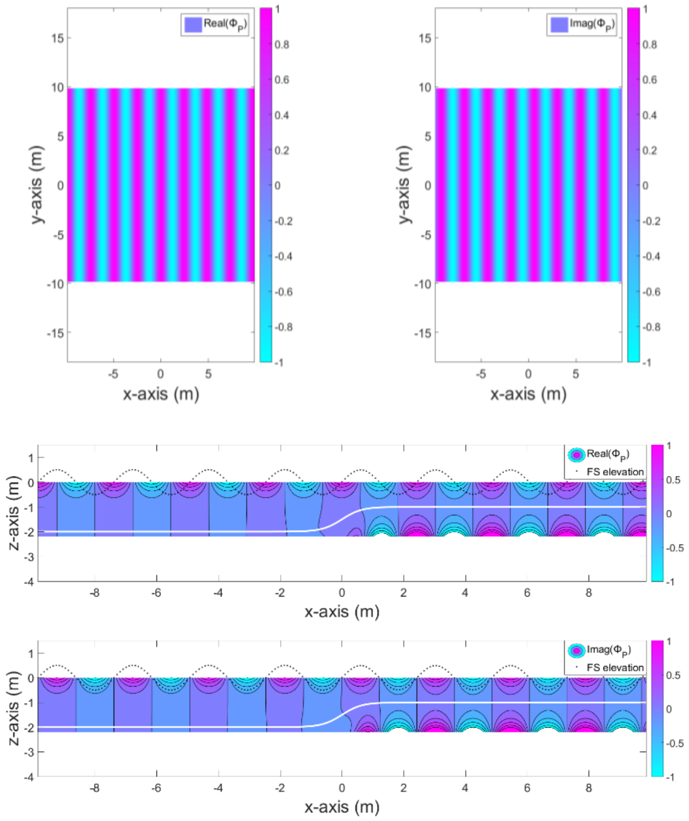

Figure 147: Propagating field (Real and Imag) by CMS (top and side view) for $\omega\sqrt{\alpha/g}$=0.8532, 0deg Variable bottom (h_1=2 m, h_3=1 m, α_{bot} =0.5)

Appendix C

Applied engineering research of a WEC

C.1 Introduction

The subject of this chapter is the analysis of a wave energy converter with a heaving buoy and energy storage to an onshore reservoir through water pumping. This analysis was completed during the author's pre-graduate thesis project [20] and is a great example of "on-hand" engineering in the field of wave energy. In here, this study will be presented in brief for reasons of completeness and in order to be available for future research, combining this applied and the previously described theoretical approaches of wave energy conversion systems.

The study is based on time-domain analysis and response evaluation of a typical cylindrical buoy heaving in linear waves. The induced forces and the power output by the device are calculated for an optimum-reference case of the buoy. Different scenarios for optimization are considered, based on different design variables, different objective functions, regular and irregular waves, by means of evolutionary algorithms and constrained by operational criteria. Sensitivity tests are included. For irregular waves, a reference site is selected and time-series data are processed for the estimation of the absorbing power by the device. Finally, an innovative proposal for the water-pump design is described in the last section.

C.1.1 Device description

The main design aspects of the proposed device are illustrated in **Fig. 148**. Further analysis of the heaving plate and the mooring system are not subject of the present study. The wave-excited oscillation of the buoy moves a connected with ball joints piston inside a hydraulic pump and with this simple principal, water can be stored as hydraulic potential to the reservoir, able to drive a hydroturbine whenever the grid demands it. This pumped storage hydro power plant is an alternative approach on the common wave-to-wire approaches and exploits the important advantages of storing energy and avoiding rejections and disposals from the grid. Therefore, the motion of this 1 DOF-device is characterized by two separate phases: the upward motion and the downward motion, presenting some crucial differences, due to the water column inside the pipe.

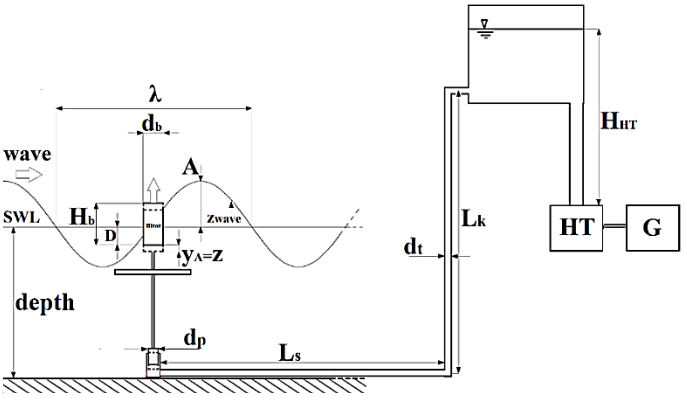

Figure 148: Simplified illustration of the proposed WEC system

Nomenclature

A	Wave amplitude
Abs_{an}	Annual WEC energy absorption
A_p	Piston cross section area
b	Damping coefficient
c	Wave phase velocity
C_d	Drag coefficient
CWR	Capture Width Ratio
D	Cylindrical buoy's draft
d_p	Piston diameter
d_{p2}	Piston diameter (second for Chapter 8)
d_b	Buoy diameter
d_t	Pipe diameter
E_{st}	Annual stored energy
E_k	Kinetic wave energy
E_p	Dynamic wave energy
E_{tot}	Total wave energy
E_{WEC}	Energy absorbed by WEC (1 period)
F	Wave frequency
F_b	Buoyancy force
F_d	Diffraction force
F_E	Amplitude of excitation force
F_e	Excitation force
F_{FK}	Froude-Krylov force
F_l	Loss force
F_r	Radiation force
F_v	Drag force
F_w	Water column force
g	Gravity acceleration
H	Wave height
$H_{1/3}$	Significant wave height
H_{cr}	Wave amplitude threshold
H_{HT}	Available water fall
H_b	Cylindrical buoy's height
J	Wave power flux
k	Wave number
L_k	Vertical pipe length
L_s	Horizontal pipe length
L_α	Total pipeline length
m_a	Added mass
m_{tot}	Total mechanism mass
P_{WAVE}	Wave power available to WEC
P_{WEC}	WEC absorbed Power
Q_t	Flow rate
Q_{tm}	Mean Flow rate
S_w	Wetted surface
T	Wave period
T_E	Wave energy period
V_{water}	Annually storage of water volume
y_A	Oscillating system displacement
y_B	Oscillating system velocity
y_E	Oscillating system acceleration
z	Vertical displacement of mechanism
Z_m	Pump-reservoir vertical distance
z_{wave}	Vertical displacement of wave
δp_{tot}	Total pressure losses
η_{sea}	Water viscosity
λ	Wave length
ρ	Water density
ω	Wave angular frequency

C.2 Mathematical model

C.2.1 Equations of motion

The mathematical formulation of this problem is based on Linear Wave Theory, introduced by Airy in 1841, which have been proved very reliable in many fluid mechanics problems.

The induced forces by the wave and by the body's motion, through the appliance of Newton's 2nd Law, are forming a system of two 2nd degree differential equations, describing the relevant phases of oscillation:

<u>*Upward motion*</u>

$$(m_{tot}+m_a)\ddot{z}=F_E\cos(\omega t)\ -b\dot{z}-\frac{1}{2}\rho C_d S_w|\dot{z}|\dot{z}+\rho g S_w(z_{wave}-z) \qquad \text{(C.1)}$$

<u>*Downward motion*</u>

$$\left(m_{tot}+m_a+\rho\ L_a\ A_p\ \frac{d_p^2}{d_t^2}\right)\ddot{z}=F_E\cos(\omega t)\ -b\dot{z}-\frac{1}{2}\rho C_d S_w|\dot{z}|\dot{z}+\rho g S_w(z_{wave}-z)-\rho g Z_m A_p-\delta_{ptot}A_p \qquad \text{(C.2)}$$

where,

- Buoyancy : $F_b=-\rho\ g\ S_w\ (z-z_{wave})$ (C.3)
- Excitation: Froude-Krylov + Diffraction : $F_e=F_{FK}+F_d=F_E\cos(\omega t)$ (C.4)
- Radiation : $F_r=-m_a\ddot{z}-b\dot{z}$ (C.5)
- Drag : $F_v=-0.5\ \rho\ C_d\ S_w\ |\dot{z}|\dot{z}$ (C.6)
- Linear friction losses : $F_l=-\delta_{ptot}A_p$ (C.7)
- Water column resistance : $F_w=-\rho g Z_m A_p$ (C.8)
- Water accelerating force : $F_{wacc}=-\rho\ L_a\ A_p\ (d_p/d_t)^2\ \ddot{z}$ (C.9)

For the evaluation of these forces (**Eqs (C.3)-(C.9)**), the involved coefficients are calculated by semi-empirical or empirical methods. These coefficients as well as the other parameters of the problem are included in **Table 14**. As shown by the previous system of **Eqs (C.1)**, **(C.2)**, during the downward motion, the resistance by the water column "trapped" inside the pipeline is now applied, along with the induced forces by the acceleration and movement of the fluid inside the tube. Obviously, the downward stroke of the piston is the power productive phase of operation.

Table 14
Fixed parameters and coefficients

Value	Variable
g=9.81	Gravity acceleration (m/s^2)
ρ=1025	Fluid density (kg/m^3)
P_{atm}=101325	Atmospheric pressure(N/m^2)
η_{sea}=9.02	Water viscosity (mPoise)
L_f=0.025	Friction factor
Z_{tot}=3.95	Total friction losses coefficient
L_s=500	Total horizontal length of tube (m)
L_k=60	Total vertical length of tube(m)
H_{HT}=76	Available water head (m)
C_d=0.5	Drag coefficient
C_A=1.0	Added mass coefficient

C.2.2 Optimization scenarios

The solution of the system of equations of motion is handled by a numerical solver based on RK 4th method. The computational code "ENALIOS" is developed in Mathworks MATLAB environment and the optimization process is carried out by the EASY software platform, developed in NTU Athens [107], able to treat SOO (Simple Objective Optimization) and MOO (Multi Objective Optimization). Four are the different scenarios of optimization, described in **Table 15**, while the algorithm's flowchart is depicted in **Fig. 149**. Absolute convergence is unfeasible and thus 1200 evaluations are set as the maximum number of iterations for the Scenarios A.1, A.2 and B, while a step of (T/70) for 10T is set for the Scenario C. The ranges for the design variables are those of **Table 16**.

Table 15
Scenarios for optimization

Scenario	DOFs	Optimization Problem Type	Objective Functions	Type of Optimum set
A.1	4 (m_{tot},d_b,d_p,d_t)	MOO	Flow Rate – Total Investment Cost	New
A.2	3 (m_{tot},d_b,d_p)	SOO	Flow Rate	New
B	4 (m_{tot},d_b,d_p,d_t)	SOO	Annual water storage	New
C	3 (d_p,d_{p2},H_{cr})	SOO	Annual water storage	Scenario B + New

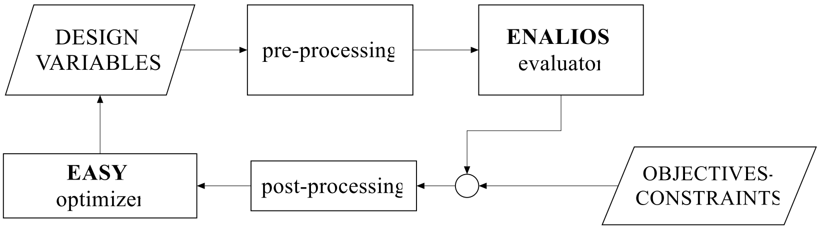

Figure 149: Total process flowchart

Table 16
Design variable ranges

Variable	Range
m_{tot}	3000-20000 kg
d_b	1-4 m
d_p	0.1-1 m
d_t	0.1-1.2 m
d_{p2}	0.1-1 m
H_{cr}	1.1-2.1 m

The objectives functions are:

- Total cost (WEC+pipeline)
- Annual Flow Rate
- Annual hydraulic energy storage

The total investment cost of the device is estimated to 8.78 m$/MW, including the WEC (R&D, manufacture process lead to a total installation cost of 2.5-6.0 m$/MW [38]) and the purchase and installation cost of a 11.5 mm thickness GRP pipe, in regard with the annual Carbon Steel prices and material reduction factors. A maintenance cost up to 0.15 m$/MW is also included. The cost of the hydropower plant (reservoir, turbine etc.) is omitted, as it is independent from the WEC design.

The optimization process is also supplemented with criteria related with safe operation and survivability of the buoy and protection from flow damages and vibrations, i.e. slamming is avoided by applying no-emergence criterion for the buoy.

C.3 Numerical results

C.3.1 Scenario A.1

The first optimization scenario has two competitive targets, the mean flow rate and the capital cost of the unit and four free design variables for regular waves of A=1.8 m and T=7 sec. As a result, a Pareto Front is obtained (**Fig. 150**), separating the area of feasible solutions with the area of unfeasible ones. The developer can then select a particular set, making a compromise of the desired values of these two competitive objective functions.

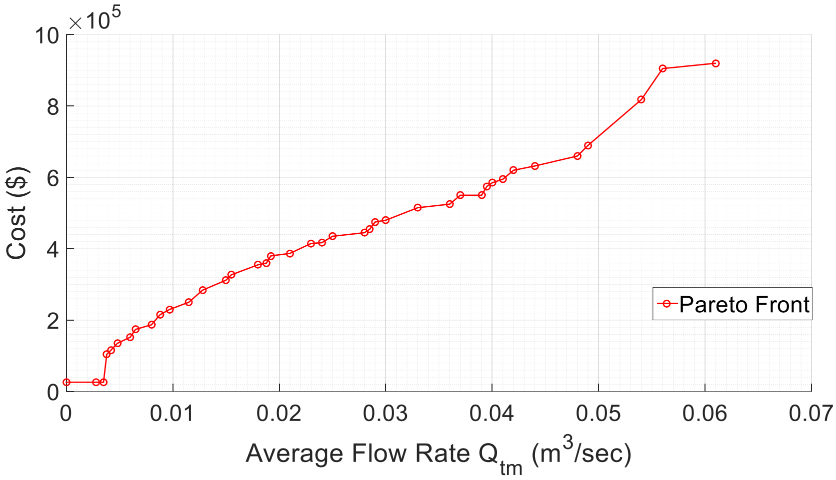

Figure 150: Scenario A.1 – Pareto Front of design-sets.

C.3.2 Scenario A.2 – Reference case

In order to obtain a single solution from the Pareto front of **Fig. 150**, the pipe diameter, is fixed at 0.6 m. The optimization now lead to the optimum set of design variables of **Table 17**.

Table 17
Optimum design variables for the reference case – Scenario A.2

Variable	Value
T	7 sec
A	1.8 m
m_{tot}	18853.40 kg
d_b	3.01 m
d_p	0.43 m
d_t	0.60 m
D	2.60 m
H_b	4.10 m

C.3.2.1 Response evaluation

For this set of parameters, the evaluation of the response of the heaving cylinder is the main objective of this section. It can be observed that the buoy follows the wave during the upwards phase, hitting a maximum amplitude above the wave, due to its inertia. However, the behavior is different in the downwards motion, where the floating buoy delays as a result of the water column resistance acting on the piston. The periodic but no harmonic behavior is obvious is the following **Fig. 151** of buoy's motion snapshots in regard to the free surface elevation.

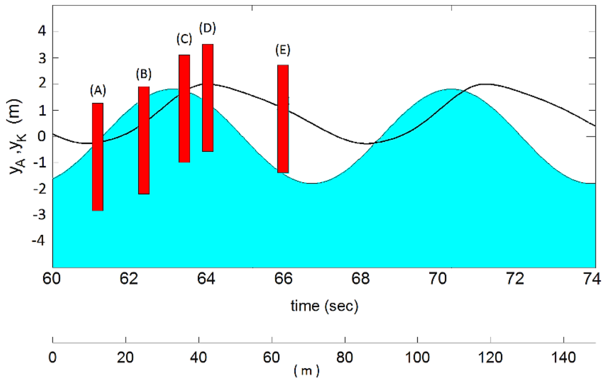

Figure 151: Relative motion of the mechanism and wave

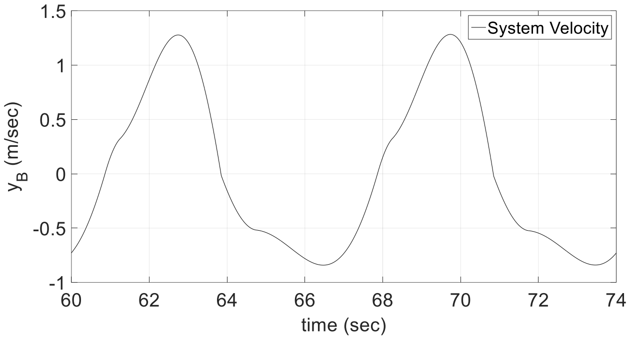

Figure 152: System velocity – Fully Periodic Response

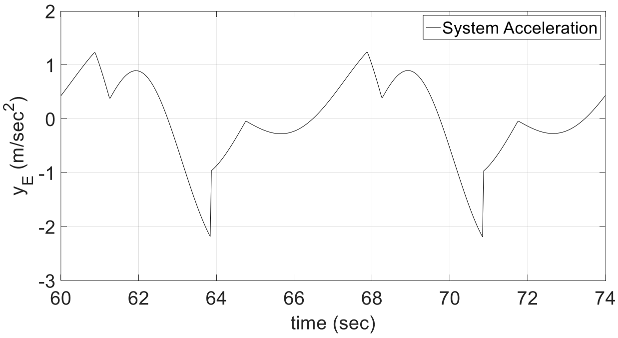

Figure 153: System acceleration – Fully Periodic Response

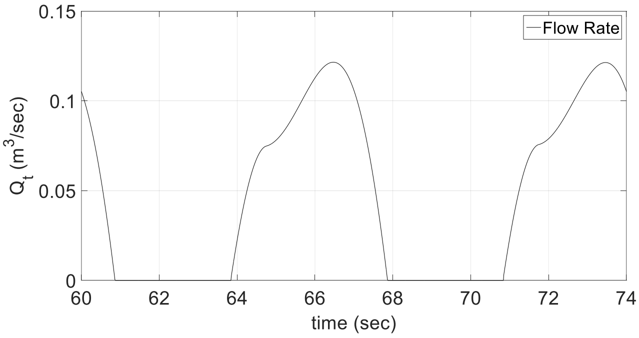

Figure 154: Flow rate at the reservoir – Fully Periodic Response

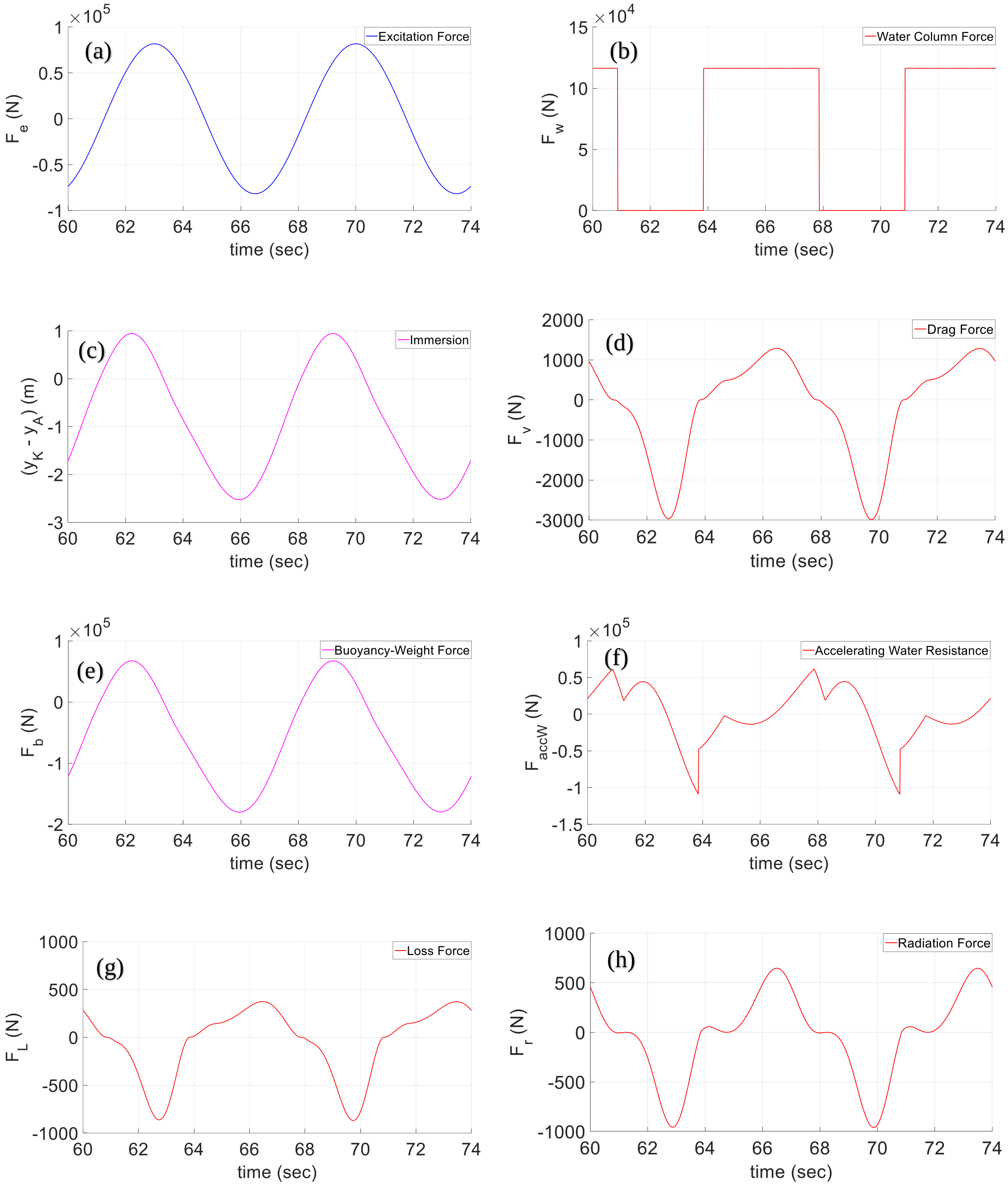

Figure 155: Plots of dynamic analysis (Upwards are positively signed): a) Excitation Force, b) Water Column Force, c) Immersion, d) Drag Force, e) Buoyancy-Weight Force, f) Accelerating Water Resistance; g) Loss Force, h) Radiation Force

The scaling is differential in *x*-axis and represents the time scale and the size-length scale. This scale-handling is the reason why the buoy appears so slender. The black curve in **Fig. 151** shows the displacement of the buoy in a way that whenever it crosses the SWL is having the design draft, which is the draft as it is calculated from the hydrostatic equilibrium. Now focusing on some specific crucial time moments of the above diagrams, conclusions can arise for the behavior of the WEC.

In position A the buoy crosses its low dead point. The velocity is equal to zero (**Fig. 152**), and therefore the flow rate is zero, as can be observed in **Fig. 154** while the deceleration hits its maximum (**Fig. 153**). At this specific moment the valve that connects the pipe and the cylinder, closes and the water column resistant force goes to zero (**Fig. 155 (b)**), while the other forces, which are velocity-depending, namely the drag force (**Fig. 155 (d)**), the radiation force (**Fig. 155 (h)**) and the friction loss force (**Fig. 155 (g)**), are nullified too.

The position B is referred to an intermediate point of the oscillation, where the wave is overtopping at maximum the design draft of the buoy, and therefore the immersion and the acting relative buoyancy force are maximum (**Fig. 155 (c), (e)**).

Position C depicts the buoy at the point of equal wave and system amplitude of oscillation. The buoyancy force now counteracts the weight of the system (**Fig. 155 (e)**), while due to the system's inertia, there is a considerable phase difference between the motions of the system and of the free surface elevation.

The buoy crosses the upper dead point at position D (**Fig. 151**), where the system's acceleration, presented in **Fig. 153**, exhibits an abrupt increase, as a result of the application of the water pipeline column back pressure. At this instant time moment the valve opens and the piston starts to pump water to the reservoir (**Fig. 154**). The system's velocity is again zero and thus all the other resisting forces are equal to zero too. In addition, the system's weight becomes now greater than the buoyancy force. (**Fig. 155 (e)**).

Position E is critical for the system behavior, because the no-emergence constraint is activated and it should not be violated and buoy marginally stays in the water (**Fig. 151**).

The flow rate strikes a maximum of almost 121 Kg/sec. This flow rate curve (**Fig. 154**) through time-integration results in a mean flow rate of 46.8 Kg/sec.

The excitation force, illustrated in **Fig. 155 (a)**, is appeared to be harmonic and in phase with the free surface elevation, which is an expected behavior for the low frequencies. The system design should aim to the minimization of the phase difference among excitation force and system velocity for the maximization of energy capture [108], a target almost achieved in this specific application.

The palm-like behavior of the water column resistance is the main reason behind the dissimilar behavior of the mechanism, due to this force's brake-like character. As shown in **Fig. 155 (b)**, this force is acting for almost 4 sec and it is neglected for a period of 3 sec, explaining the periodic but not harmonic behavior of the motion. Disturbances in the slope of most of the curves are induced by the function of the valves, which are modelled as on-off valves. The instant on-off handling "turns" on and off correspondingly a high magnitude acting force, which in turn causes this bending of the curves at specific time moments. In order to prevent such strong vibrations, the valves operation in real applications will be controlled by suitable automation systems.

C.3.2.2 Emerging buoy event

As stated previously a non-emerging criterion is applied, securing no emergence of the buoy. This non-emergence requirement was found to be the most tough-implemented constraint and the optimization procedure led the design to its limits during all scenarios, at the edge of constraint's violation. Even one change on the design parameters can drive the buoy out of the water and an example of this event, for inclusiveness reasons only, is presented in this subsection and shown in **Fig. 156**, where a buoy with 17.7% less mass than the optimum, is totally emerging from the free surface. Finally, it should be mentioned again that during the evaluation of the final results emergence is permitted for all the scenarios.

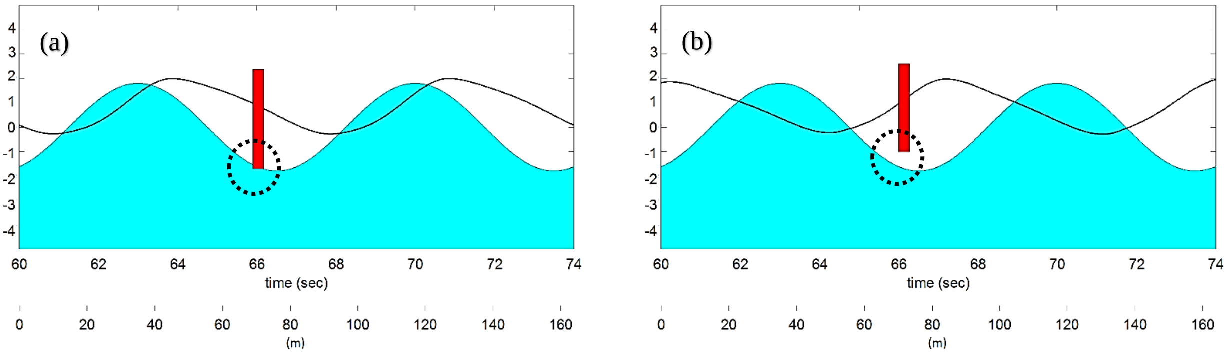

Figure 156: Snapshots of the motion created with an animation: (a) not emerging and (b) emerging.

C.3.2.3 Power Output

Calculations for the power output by this specific device had been done and concluded in very auspicious results, comparable with already installed and operating WECs [18]. The Capture Width Ratio (CWR), an indicator of efficiency for WECs, calculated as the energy absorbed from a device divided by the offered wave energy to the device per wave length, thus:

$$CWR = 100\,\frac{P_{WEC}}{P_{WAVE}} \tag{C.10}$$

where,

$$P_{WAVE} = J\,d_b \tag{C.11}$$

and the absorbed energy by the device can be evaluated as the potential dynamic energy of the system between the upper dead point (UDP) and lower dead point (LDP) for a period of oscillation:

$$P_{WEC} = \frac{E_{WEC}}{T} = \frac{m_{tot}\,g\,(\text{UDP-LDP})}{T} \tag{C.12}$$

The power flux for the considered reference wave of amplitude A = 1.8 m and period T = 7 sec is calculated as: J = 44.5 kW/m. The resulting CWR for the reference system performance is almost 45%.

C.3.2.4 Sensitivity tests

Sensitivity analysis of the optimum design variables of the system is essential for revealing the importance of each one of them and their tolerance level, which is the allowable deviation of their optimum values for maintaining the objective function near its best value.

This kind of test can be evaluated for every parameter of the system. In this brief description it will be shown only four sensitivity tests, indicative of the operation of the system and for the rest tests the reader is guided to [20].

According to **Fig. 157 (a)**, the total mass is a variable able to range inside a wide band of values with minor effects on the objective function, which is the flow rate at the reservoir, but this is limited by the non-emergence criterion. This constraint determines also the span for every parameter of design and thus the span for possible values of the buoy diameter (**Fig. 157 (b)**) and piston diameter (**Fig. 157 (c)**). The total mass and the piston diameter are shown to be well-approximated by the optimization process, while the buoy diameter is not fully converged to its optimal value, which is the peak of the relevant curve and is slightly different by the obtained value, indicated by the red marker, as shown in **Fig. 157 (b)**. Finally, the WEC can also operate safely in different wave-amplitude states as shown in **Fig. 157 (d)**, being able to achieve better flow rate levels in higher waves.

Tests like these establish the fluctuation levels of manufacturing and installation process, showing which of the parameters are more sensitive to the implemented criteria of operation and objective functions.

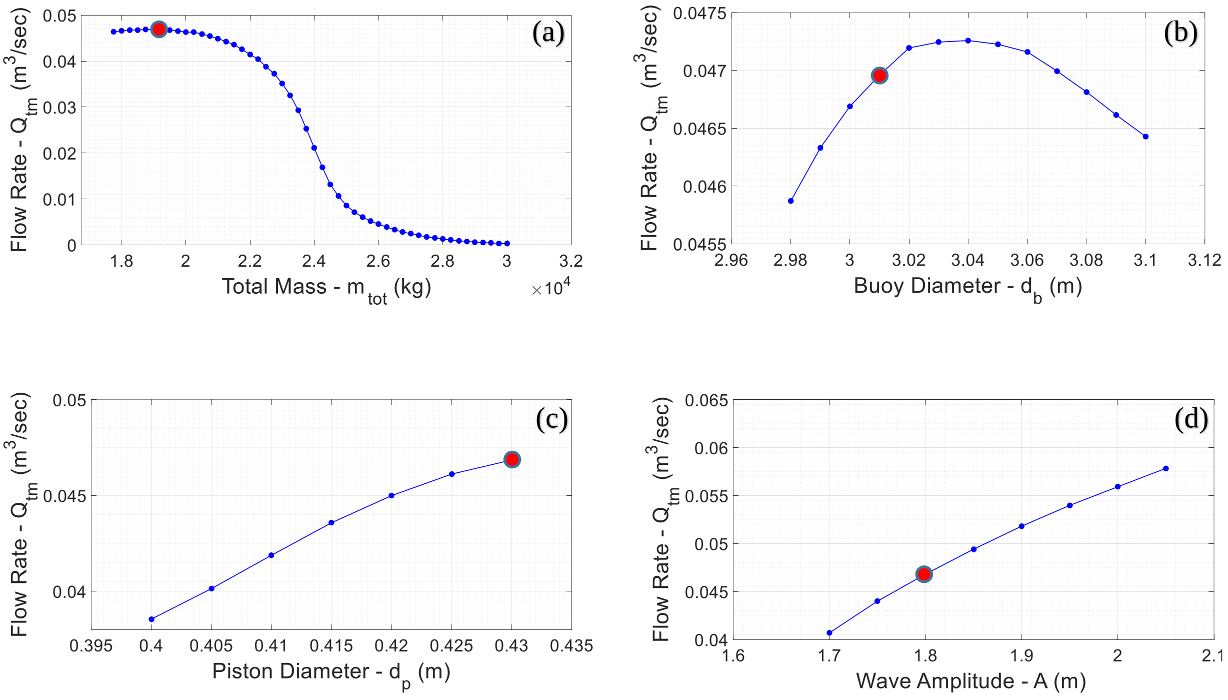

Figure 157: Parametric analysis of the effect of various design parameters:
a) Total mass, b) Buoy diameter, c) Piston diameter, d) Wave amplitude

C.3.3 *Real wave data*

C.3.3.1 Location and wave data

A more realistic approach of the device's operation evaluates the wave data time-series for Monterey Bay (36°48'36.1"N 122°08'08.6"W) ([109]). The location is shown on the map of **Fig. 158** and the time-series of Significant Wave Height-SWH and wave period-*T* for year 2015 are shown in **Fig. 159**. The sampling rate is 30 min. Based on these time series, where the deviation of the period is low, this specific sea state characterizes a swell dominated environment. As a result the period can be set as constant and the power defining parameter is the wave amplitude. The heading angle of the waves are lacking any significance, due to the axisymmetric body in heave.

Figure 158: Monterey Bay, California, USA

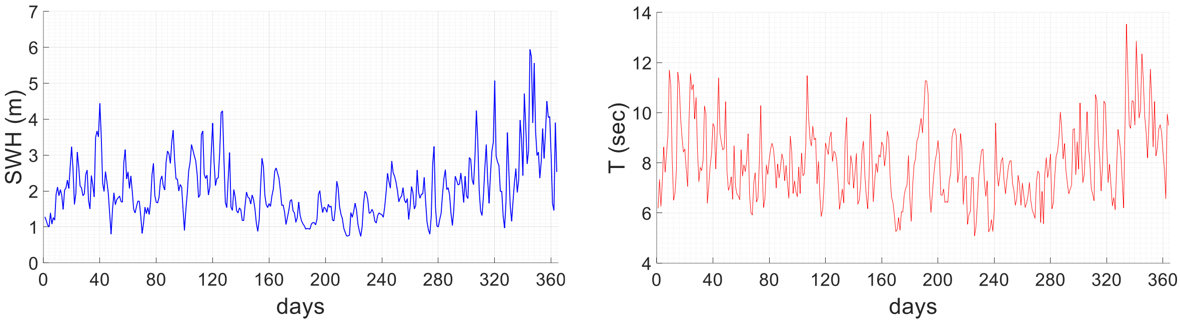

Figure 159: Time series for SWH (a) and wave period (b) in Monterey Bay during 2015 [109]

According to these time-series data, the annual power density curve for this specific site can be obtained (**Fig. 160**).

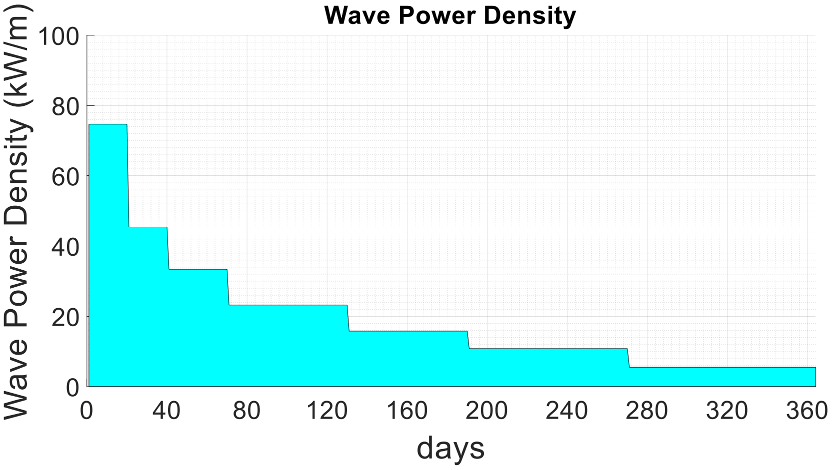

Figure 160: Annual duration curve for the wave power density, Monterey Bay 2015

C.3.3.2 Scenario B

At this time, the system is re-optimized according to the annual power density curve for Monterey Bay, US. The performance and power output by the WEC is evaluated in each one of the seven steps of this curve and the main objective in the maximization of annual cumulative water storage at the reservoir. The resulting optimum set is tabulated in **Table 18**, along with the previous Scenario A.2 and Scenario C, which follows in the next section, for reasons of comparison. It is obvious that the main design variables are alternated in this more realistic case study. The annual WEC energy absorption, also presented in **Table 18**, is the ratio of the captured by the WEC energy divided by the offered wave energy annually. The **Table 18**, proves the overestimation of WEC power output in the ideal case of regular waves, enables the comparison among the different scenarios and also manifests the superiority of an innovative proposal, following subsequently.

Table 18
Scenarios (A.2, B, C) – Design variables and energy evaluation

Variable		Scenario A.2	Scenario B	Scenario C
Total Mass (kg)	m_{tot}	18853.40	19734.10	19734.10
Buoy Diameter (m)	d_b	3.01	2.80	2.80
1st Piston Diameter (m)	d_p	0.43	0.32	0. 99
Pipe Diameter (m)	d_t	0.60	0.20	0.20
2nd Piston Diameter (m)	d_{p2}	-	-	0.32
Wave amplitude threshold (m)	H_{cr}	-	-	1.18
Average Flow Rate (m^3/s)	Q_{tm}	0.0468	0.0149	0.0192
Annual Water Storage (m^3)	V_{WATER}	1472300	468864	605798
Annual Stored Energy (MWh)	E_{st}	230.3	73.3	94.7
Annual WEC Energy Absorption	Abs_{an}	19.7 %	15.3 %	19.9 %

For the ideal harmonic waves of the Scenario A.2 energy storage by the system is exceeding up to 230.3 MWh per WEC from the provided by the sea 1168.7 MWh per WEC and thus the energy absorption in year round basis is 19.7%.

In the more realistic Scenario B, each device absorbs about 73.3 MWh out of the 477.3 MWh of provided wave energy and the average energy capture becomes 15.3%, lower than the energy absorption of Scenario A.2, because the WEC now cannot operate to its optimal design point during the whole year.

C.3.3.3 Scenario C – Double optimal adjustment

When the optimized device is installed to operate in a sea state like this described in Scenario B, its efficiency is limited by the fact that it operates in off-design points. In other words, the optimization sets the set of design variables as a compromise of different optimal operation points, and so the annual production is not maximized. Based on this principal, a concept of a mechanism combining the advantages of having two operation points is proposed. One of the most significant design variables is the piston diameter. Therefore, a device with two different operating piston diameters is considered and the system is optimized for this case. In addition, this is a not so sophisticated design and the relevant added cost is low.

From the optimization process, resulting in the relevant set of design variables of **Table 18**, is concluded that for low-waves the algorithm led the design to an increase of piston diameter in order to achieve more cross section area of scanning and as a result increase the water storage in the reservoir, despite the smaller stroke of the piston. In case of high waves, the maximization of flow rate is accomplished by a smaller piston diameter, and so smaller resistance acting on its section.

The device is schematically shown in **Fig. 161**, and its operation is explained with the **Table 19**. While the wave amplitude remains below a design value, the WEC operates like the simple one-piston device, and both piston sections pump water to the reservoir. On the other hand, when the wave height is larger than this threshold, the on-off valve No. 5 opens and the larger piston ceases to pump water, leaving the power absorption only on the operation of the piston with the smaller diameter.

As pointed out from the results of **Table 18** this conceptual approach enables the device to exploit more efficiently the waves and improve its power absorption levels. The wave amplitude threshold is equal to 1.18 m and corresponds to an appreciable period of the year. This improved design shows almost 30% higher power production in comparison with Scenario B of simple-piston device. Finally, due to its simplicity and feasibility at low cost is a promising alternative solution for efficiency improvements in the field of WECs, with even more than two optimal piston diameters.

Table 19
Valve regulation for concept design

Wave,Motion* / *Valve	**1**	**2**	**3**	**4**	**5**
Upwards Low Wave	✓	✓	✗	✗	✗
Downwards Low Wave	✗	✗	✓	✓	✗
Upwards High Wave	✗	✓	✗	✗	✗
Downwards High	✗	✗	✓	✗	✓

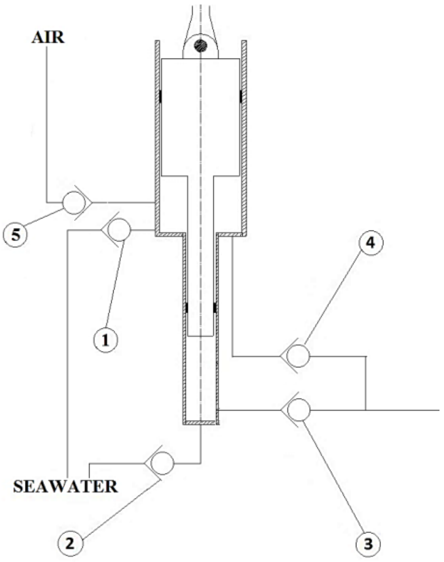

Figure 161: 2D sketch of piston-cylinder mechanism